

Hydrogen Generation in a Multi-Channel Membrane Reactor

by

Alexandre Vigneault

BSA Chemical Engineering, Université de Sherbrooke, 2001

MSc Chemical Engineering, Université de Sherbrooke, 2004

A THESIS SUBMITTED IN PARTIAL FULFILLMENT
OF THE REQUIREMENTS FOR THE DEGREE OF

Doctor of Philosophy

in

THE FACULTY OF GRADUATE STUDIES

(Chemical & Biological Engineering)

The University of British Columbia

(Vancouver)

October 2012

© Alexandre Vigneault, 2012

Abstract

A novel Multi-Channel Membrane Reactor (MCMR) has been developed for the decentralized production of hydrogen via Steam Methane Reforming (SMR). The concept alternates steam reforming gas channels to produce the hydrogen and Methane Catalytic Combustion (MCC) gas channels to provide the heat of reaction. A palladium-silver (Pd/Ag) membrane inside each reforming gas channel shifts the reaction equilibrium, and produces pure hydrogen in a single vessel.

A steady-state, non iso-thermal and two-dimensional modeling of the concept was first developed. Sensitivity analyses from the simulations indicated the importance of fast kinetics and thick catalyst coating layers ($>80 \mu\text{m}$) to avoid limitations from the catalyst. An innovative hot substrate air-spray coating method was developed, and thick layer of catalysts ($>240 \mu\text{m}$) with good adherence under sonication were obtained. A lab-made Ru MgO–La₂O₃/ γ -Al₂O₃ catalyst, with carrier and promoters pre-aged by steam, and coated on pre-oxidized Fecralloy, was found to be suitable for the reforming channel. On the combustion side, commercial Pd γ -Al₂O₃ catalysts were successfully coated on stainless steel support. Kinetics parameters were estimated for both reforming and combustion catalysts.

A proof-of-concept MCMR was designed and built. Results showed that a methane conversion of 87% was achievable with a pure hydrogen output (99.995%). The reforming experimental results were adequately predicted for a wide range of operating conditions. On the combustion side, the experimental conversions were below the model expectations, likely because of flow distribution and catalyst stability issues. It is shown that the MCMR concept has the potential to give hydrogen yield per reactor volume, and per mass of catalyst, about one order of magnitude higher than for alternate membrane reactor technologies.

Table of Contents

Abstract	ii
Table of Contents	iii
List of Tables	x
List of Figures	xiv
Acronyms	xix
List of Symbols	xxi
List of Greek Letters	xxiv
List of Subscripts	xxvi
Acknowledgments	xxviii
1 Introduction	1
1.1 The Case for Hydrogen	1
1.1.1 Climate Change and Greenhouse Gas Emissions	1
1.1.2 Life Cycle Impact Assessment	2
1.1.3 Global Hydrogen Production and Consumption	3
1.1.4 Hydrogen for Transportation	4
1.2 Hydrogen Production Pathway	6
1.2.1 Feed Sources	6
1.2.2 Reaction Pathways from Methane to Hydrogen	6

1.3	Process and Hydrogen Purification	8
1.3.1	Pressure Swing Adsorption	9
1.3.2	Preferential Oxidation	10
1.3.3	Membranes	10
1.4	Reformer Configuration	12
1.4.1	Current Large-Scale Reactor Design	12
1.4.2	Neo-conventional Reactor	12
1.4.3	Multi-channel Reactor	13
1.5	Novel Membrane Reactors	16
1.5.1	Packed Bed and Coated Tubular Membrane Reactors	17
1.5.2	Fluidized Bed Membrane Reactor	18
1.5.3	Multi-Channel Membrane Reactor (MCMR)	20
1.6	General Objectives and Strategy	20
2	Steady State Model Development	23
2.1	Introduction	23
2.2	Concept Description	26
2.3	Main Assumptions of 2-D model	26
2.4	Physical Properties	28
2.4.1	Diffusivity	28
2.4.2	Heat Capacity	30
2.4.3	Thermal Conductivity	30
2.4.4	Viscosity	31
2.5	Concentration and Partial Pressure	32
2.6	Velocity Profiles	32
2.7	Kinetics	34
2.7.1	Reforming	34
2.7.2	Combustion	39
2.8	Component Material Balance Equations	40
2.8.1	Gas Phase	42
2.8.2	Catalyst Layer	45
2.9	Energy Balances	46
2.9.1	Gas Phase	49

2.9.2	Catalyst Layer	51
2.9.3	Separator Wall	52
2.10	Conclusions	53
3	Steady State 2-D Model Simulations Results	54
3.1	Introduction	54
3.2	Model Equations and Base Case Parameters	55
3.3	Metrics	55
3.3.1	Hydrogen Production	57
3.3.2	Other Performance Indicators	59
3.3.3	Dimensionless Numbers	60
3.3.4	Sensitivity Analysis Parameters	62
3.3.5	Performance Improvement Parameters	62
3.4	Solving the Model	63
3.5	Results and Discussion	64
3.5.1	Isothermal and Non-Isothermal Base Case Simulations	64
3.5.2	Isothermal Parametric Sensitivity Analysis	71
3.5.3	Performance Improvement	76
3.6	Conclusions	81
4	Catalyst Coating: Initial Method Development	83
4.1	Introduction	83
4.1.1	Gas Phase Techniques	83
4.1.2	Liquid Phase Techniques	85
4.1.3	Surface Pretreatment	87
4.1.4	Coating Strategy	87
4.2	Materials	88
4.2.1	Metal Substrate	88
4.2.2	Modified Sol	88
4.3	Method	92
4.3.1	Sand-Blasting	92
4.3.2	Substrate Cleaning	94
4.3.3	Modified Sol Parameters	94

4.3.4	Coating Techniques	96
4.3.5	Impregnation	97
4.3.6	Analytical Instruments	97
4.3.7	Metrics	98
4.4	Results and Discussion	99
4.4.1	Metal Surface Preparation	99
4.4.2	Brush Coating, Dip Coating and Cold Substrate Air Spray Coating (Cold Spray)	102
4.4.3	Hot Substrate Air Spray Coating (Hot Spray)	102
4.4.4	Thickness Verification	110
4.4.5	Impregnation	114
4.5	Conclusions	117
5	Catalyst Coating: Final Method Development	119
5.1	Introduction	119
5.2	Material and Method	120
5.2.1	Metal Substrate	120
5.2.2	Final Coating Method	120
5.2.3	Analytical Equipment	123
5.2.4	Metrics	124
5.3	Results and Discussion	125
5.3.1	Carbon Deposition during Steaming	125
5.3.2	Surface Cracks	125
5.3.3	Rust	133
5.3.4	Successful Coating Samples	134
5.4	Conclusions	139
6	Reforming Catalyst Activity and Stability	141
6.1	Introduction	141
6.2	Material and Method	143
6.2.1	Catalyst Preparation	143
6.2.2	Micro-Reactor Configuration	143
6.2.3	Experimental Set-up	144

6.2.4	Packed Bed Model	147
6.2.5	Estimation of Kinetics Parameter	147
6.2.6	Estimation of Porosity	148
6.2.7	Analytical Equipment	149
6.2.8	Metrics	151
6.3	Results and Discussion	152
6.3.1	Preliminary Stability Test	152
6.3.2	Lab-made Ru Catalyst	152
6.3.3	Rust Effect	157
6.3.4	Start-up Procedure for Membrane	159
6.3.5	Deactivation Mechanisms	163
6.3.6	Catalyst Layer Modeling	166
6.3.7	Estimation of Jackobsen Pre-exponential Kinetic Parameter	166
6.4	Conclusions	168
7	Methane Catalytic Combustion	170
7.1	Introduction	170
7.2	Material and Method	172
7.2.1	Catalyst Preparation	172
7.2.2	Experimental Set-up	172
7.2.3	Estimation of Kinetic Parameters	174
7.2.4	Analytical Equipment	175
7.2.5	Metrics	175
7.3	Results and Discussion	176
7.3.1	Preliminary Stability Test	176
7.3.2	Stability of Pd 1%/ γ -Al ₂ O ₃ (Alfa)	176
7.3.3	Stability of Pd 5%/ γ -Al ₂ O ₃ (Alfa) and Lab-made Pd-based Catalysts	179
7.3.4	Deactivation	183
7.3.5	Estimation of Kinetic Parameters	185
7.3.6	Conclusions	190

8	Development of the Multi-Channel Membrane Reactor	191
8.1	Introduction	191
8.2	Material and Method	192
8.2.1	Reactor Design	192
8.2.2	Process Design	196
8.2.3	Catalyst Preparation	197
8.2.4	Reactor Assembly	201
8.2.5	Start-up Procedure	204
8.2.6	Operation	205
8.2.7	Analytical Equipment	206
8.2.8	Modeling Parameters and Metrics	207
8.3	Results and Discussion	212
8.3.1	Preliminary Results	212
8.3.2	Multi-Channel Reactor without Membrane	214
8.3.3	Multi-Channel Reactor with Membranes	215
8.4	Conclusions	227
9	Overall Conclusions and Recommendations	229
9.1	Conclusions	229
9.2	Recommendations	231
9.2.1	General Recommendations	232
9.2.2	Specific Recommendations	232
	References	235
A	Supplementary Coating Results	253
A.1	Brush Coating Results	253
A.2	Multi-layer Brush Coating	254
A.3	Dip Coating	254
A.4	Cold Substrate Air Spray Coating (Cold Spray)	258
A.5	Hot Spray Coating Including Metal Precursors	259
A.6	Hot Spray Coating of of Commercial Catalyst: Supplementary Results	259
A.7	Thickness vs Mass Data	265

B	Stability of Reforming Catalysts: Supplementary Results	268
	B.1 Preliminary Stability Test	268
	B.2 RK-212	268
	B.3 Early Lab-made Ni catalyst	270
	B.4 Commercial Ru 5%/ γ -Al ₂ O ₃ Catalyst	272
C	MCMR Supplementary Results	276
	C.1 Lessons Learned During Reactor Commissioning	276
	C.2 Preliminary Results	277
	C.2.1 Combustion Preliminary Results	281
	C.2.2 Reforming Preliminary Results	284
D	Micro-Reactor Supplementary Information	292
	D.1 Micro-Reactor PI&D	292
	D.2 Micro-Reactor Electrical and Control Diagram	297
E	Multi-Channel Reactor Supplementary Information	302
	E.1 MCMR PI&D	302
	E.2 MCMR Electrical Diagram	308
	E.3 MCMR Process Part Mechanical Drawings	325
	E.4 MCMR Mechanical Drawings	327
F	MATLAB Program	339

List of Tables

Table 1.1	U.S. Department of Energy Targets and Progress for Hydrogen in the Transportation Sector	5
Table 1.2	Hydrogen Fuel Quality Specifications (partial list)	9
Table 1.3	MCR Steam Reforming (A) and Catalytic Combustion (B) - Fabrication Details	14
Table 1.4	MCR Steam Reforming and Catalytic Combustion - Performance Data	15
Table 2.1	Empirical Values to Determine k and μ	32
Table 2.2	Sievert's Law Parameters	33
Table 2.3	Constants in Xu and Froment (1989) Kinetics	36
Table 2.4	Constants in Jakobsen et al. (2010) Kinetics	37
Table 2.5	Constants in Wei and Iglesia (2004) Kinetics	38
Table 2.6	Combustion Kinetic Parameters	41
Table 3.1	Base Case Parameters for Simulations, Part I	56
Table 3.2	Base Case Parameters for Simulations, Part II	57
Table 3.3	Hydrogen Flow Unit Conversion	58
Table 3.4	Isothermal and Non-Isothermal Base Case Results	65
Table 3.5	Base Case Simulation Dimensionless Numbers	70
Table 3.6	Parameter Changes for Figure 3.7A from Base Case Values of Tables 3.1 & 3.2	79
Table 3.7	Parameter Changes for Figure 3.7B from Base Case Values of Tables 3.1 & 3.2	79

Table 3.8	Non-Isothermal Base & Best Case Results and Comparison with Experimental Literature	80
Table 4.1	Boehmites Tested and their Properties	89
Table 4.2	Carriers Tested and their Properties	90
Table 4.3	Metal Precursors Tested	91
Table 4.4	Commercial Catalysts Tested	91
Table 4.5	Impregnation Solutions for Figure 4.13	115
Table 5.1	Modified Sol Parameters	122
Table 5.2	Metal Precursors; Supplier was Alfa Aesar in all cases	123
Table 5.3	Compositions of Impregnation Solutions	123
Table 5.4	Average Crack Density for Ru- and Pd-based Lab-made Catalysts Coatings	132
Table 5.5	Crack Density Results for Pd Commercial Catalyst Coatings	133
Table 6.1	Impregnation Solutions and Desired Metal Contents for Reforming Catalysts	143
Table 6.2	Co-Sorption Parameters	150
Table 6.3	Stability Conditions for Lab-made Ru-based Catalyst: Influence of Steam	153
Table 6.4	Curve Fitting Related to Figure 6.3 and Eq. (6.14) for Stability of Lab-Made Ru-based Catalyst.	155
Table 6.5	Surface Area, Pore Volume, Average Pore Diameter, and Metal Dispersion of Lab-made Ru 6%/ γ -Al ₂ O ₃ Catalyst (carrier not pre-aged by steam)	155
Table 6.6	Stability Conditions for Lab-made Ru-based Catalyst: Influence of Rust on SS 304 Support	157
Table 6.7	Curve Fitting Related to Figure 6.5 and Eq. (6.14) for Stability of Lab-Made Ru-based Catalyst.	158
Table 6.8	Membrane Start-up Steps with H ₂ –H ₂ O mixture	159
Table 6.9	Membrane Start-up Steps with H ₂ –N ₂ mixture	160
Table 6.10	Stability Conditions of Lab-made Ru-based Catalyst: Influence of Membrane Start-up Procedure	160

Table 6.11	Curve Fitting Related to Figure 6.6 and Eq. (6.14) for Stability of Lab-Made Ru-based Catalyst.	162
Table 6.12	Details of Ru-based Catalysts on XRD Spectra of Figure 6.7	162
Table 6.13	Surface Area, Pore Volume, Average Pore Size, and Metal Dispersion of Lab-made Ru Catalysts and Supports	165
Table 7.1	Impregnation Solutions and Desired Metal Contents for Combustion Catalysts	173
Table 7.2	Curve Fitting Related to Figure 7.2 and Eq. (6.14) for Stability of Pd 1% (Alfa) Catalyst	178
Table 7.3	Stability Conditions for Pd 5%/ γ -Al ₂ O ₃ (Alfa) and Lab-made Pd-based Catalysts for Figure 7.3.	179
Table 7.4	Curve Fitting Related to Figure 7.3 and Eq. (6.14) for Stability of Pd 5% (Alfa) and Pd-based Lab-made Catalysts	181
Table 7.5	Surface Area, Pore Volume, Average Pore Size, and Metal Dispersion of Pd/ γ -Al ₂ O ₃ Catalysts	182
Table 7.6	Estimated Kinetic Parameters for Pd 1% (Alfa) Catalyst: Experimental Conditions for Figure 7.7	187
Table 7.7	Estimated Kinetic Parameters for Pd 1% (Alfa) Catalyst: Linear Regression Results for Figure 7.7	187
Table 7.8	Estimated Kinetic Parameters for Experimental Conditions in Figure 7.8	189
Table 7.9	Estimated Kinetic Pre-exponential Factor, A_4 , from Figure 7.8	189
Table 8.1	Impregnation Solutions and Desired Metal Contents for Catalysts used in MCMR	200
Table 8.2	Catalyst Description for MCMR Experiment no.1, without Membrane	200
Table 8.3	Catalyst Description for MCMR Experiment no.2, with Membrane	201
Table 8.4	Catalyst Description for MCMR Experiment 3, with Membrane	202
Table 8.5	Membrane Start-up Procedure	205
Table 8.6	Experimental Operating Conditions	206

Table 8.7	Parameters for Simulations Predictions, Part I	209
Table 8.8	Parameters for Simulations Predictions, Part II	210
Table 8.9	Summary of Preliminary Results for Reforming Channel	213
Table 8.10	Membrane Effectiveness Calculations	217
Table 8.11	MCMR Experimental Results Compared with Early Simulations and Other Membrane Reactors.	226
Table 8.12	Improvement Potential for the Reforming Channel	227
Table B.1	Surface Area, Pore Volume, Average Pore Size, and Metal Dispersion of Commercial Reforming Catalysts	270
Table B.2	Stability of RK-212: Operating Conditions for Figure B.1 Part A	270
Table B.3	Stability Conditions of Ru 5% (Alfa): Modified Sol Parameters and Reduction/Start-up Conditions for Figure B.4	274
Table B.4	Curve Fitting Related to Figure B.4, and Eq. (6.14) for Stability of Ru 5% (Alfa)	274
Table C.1	Catalyst Description for MCMR Preliminary Experiments, Part I	281
Table C.2	Catalyst Description for MCMR Preliminary Experiments, Part II	282
Table C.3	Catalyst Description for MCMR Preliminary Experiments, Part III	283
Table C.4	Simulation Parameters for Preliminary Results	284

List of Figures

Figure 1.1	Hydrogen Production Pathways	7
Figure 1.2	Thesis Strategy	22
Figure 2.1	Schematic of 2-D Model	27
Figure 2.2	Schematics to Evaluate Average Velocity and to Develop Energy Balance	34
Figure 2.3	Schematic of Discretization	43
Figure 3.1	Non-Isothermal Base Case Results - Conversion, Average Temperature, Heat Flux and Molar Ratio	67
Figure 3.2	Non-Isothermal Base Case Results - Velocity and Temperature Profiles	68
Figure 3.3	Non-Isothermal Base Case Results - Molar Fraction and Catalyst Effectiveness Profiles	69
Figure 3.4	Sensitivity Analysis - Operating Parameters	73
Figure 3.5	Sensitivity Analysis - Catalyst Parameters	75
Figure 3.6	Sensitivity Analysis - Design Parameters & Diffusivity	77
Figure 3.7	Performance Improvement	78
Figure 4.1	Initial Catalyst Coating Method	93
Figure 4.2	Sand-Blasting Images	101
Figure 4.3	Surface Cleaning Issue	102
Figure 4.4	SEM Images of Brush Coating and Various Hot Spray Coatings	103
Figure 4.5	Hot Spray Coating of γ -Al ₂ O ₃ Modified Sol	106
Figure 4.6	SEM Images of γ -Al ₂ O ₃ Coatings of Various Thicknesses	107

Figure 4.7	SEM Tilted View Images of Hot Spray Coatings	108
Figure 4.8	Hot Spray Coating of α -Al ₂ O ₃ , MgAl ₂ O ₄ and CeO ₂ -ZrO ₂ Modified Sol	109
Figure 4.9	Hot Spray Coating of Commercial Pd/ γ -Al ₂ O ₃ Catalysts .	111
Figure 4.10	Temperature Cycles of Hot Spray Coatings with γ -Al ₂ O ₃ Mod- ified Sol	112
Figure 4.11	SEM Images of Tilted and Side View of Hot Spray Coating of Commercial Ru 5%/ γ -Al ₂ O ₃	113
Figure 4.12	Wet Impregnation Issues	116
Figure 4.13	Wet Impregnation on γ -Al ₂ O ₃ Support Made by Hot Spray Coating	117
Figure 5.1	Final Method for Coating Commercial and Lab-made Cata- lysts	121
Figure 5.2	Carbon Deposition during Steaming	126
Figure 5.3	Delamination and Cracking Issues after Steaming and Impreg- nation with RuNO(NO ₃) ₃ on γ -Al ₂ O ₃	127
Figure 5.4	Comparison of Sonication Test and Crack Test	128
Figure 5.5	TGA Analyses of Boehmite, Pd 5%/ γ -Al ₂ O ₃ with Boehmite, and RuNO(NO ₃) ₃ -La ₂ O ₃ / γ -Al ₂ O ₃	129
Figure 5.6	Cracks versus Cluster Formation during Hot Spraying of γ - Al ₂ O ₃	130
Figure 5.7	Presence of White Lines on Coating	131
Figure 5.8	Rust on Catalyst with SS 304 as Metal Support	135
Figure 5.9	Ru-based Catalyst on SS 304 Support at Various Stages of Coating and Catalyst Life	136
Figure 5.10	Commercial Pd-based/ γ -Al ₂ O ₃ Catalysts on SS 304 Support at Various Stages of Coating and Catalyst Life	137
Figure 5.11	Ru- and Pd-based/ γ -Al ₂ O ₃ Catalysts on Fecralloy and SS 310 at Various Stages of Coating and Catalyst Life	138
Figure 5.12	Commercial Pd 5%/ γ -Al ₂ O ₃ Catalysts on Fecralloy and SS 310 before and after MCMR run	139

Figure 6.1	Micro-Reactor Set-up	145
Figure 6.2	Micro-Reactor Process Flow Diagram	146
Figure 6.3	Stability for Lab-made Ru-based Catalyst: Influence of Steam	154
Figure 6.4	FESEM Images of Ru 6%/ γ -Al ₂ O ₃	156
Figure 6.5	Stability for Lab-made Ru–La ₂ O ₃ / γ -Al ₂ O ₃ Catalyst: Influence of Rust on Support	158
Figure 6.6	Stability of Lab-made Ru-based Catalyst: Influence of Membrane Start-up Procedure	161
Figure 6.7	XRD diagram of Lab-made Ru-based Catalyst, Fresh and Spent (after MCMR Exp.)	163
Figure 6.8	Porosity vs Pore Volume for Catalyst with Alumina Support	166
Figure 6.9	Catalyst Layer and Pores Model	167
Figure 6.10	Pre-exponential Factor A_1 - Estimation for Jackobsen Kinetics	168
Figure 7.1	Preliminary Stability Test of Pd 1%/ γ -Al ₂ O ₃ (Alfa) with 15% Boehmite	177
Figure 7.2	Stability of Pd 1%/ γ -Al ₂ O ₃ (Alfa)	178
Figure 7.3	Stability of Pd 5%/ γ -Al ₂ O ₃ (Alfa) and Lab-made Pd-based Catalyst	180
Figure 7.4	XRD Diagram of Commercial Pd 1%/ γ -Al ₂ O ₃ (Alfa) with 15% boehmite, Fresh and Spent (after MCMR Exp.)	183
Figure 7.5	XRD Diagram of Commercial Pd 5%/ γ -Al ₂ O ₃ (Alfa) with 15% Boehmite, Fresh and Spent (after MCMR Exp.)	184
Figure 7.6	XRD Diagram of Lab-made Pd-based Catalyst, Fresh and Spent (after MCMR Exp.)	184
Figure 7.7	Estimated Kinetic Parameters for Pd 1% (Alfa) Catalyst: A. Activation Energy E_4 ; B. Reaction Order for Methane α	186
Figure 7.8	Estimated Kinetic Pre-exponential Factor, A_4	188
Figure 8.1	Expanded View of MCMR Prototype	193
Figure 8.2	Top View of Temperature and Gas Sampling Locations for both Channels	194

Figure 8.3	MCMR Process Flow Diagram	195
Figure 8.4	Reactor and Process Images I	198
Figure 8.5	Reactor and Process Images II	199
Figure 8.6	Pd/Ag Membrane Installed on Bottom Flange after Experiment no.3	203
Figure 8.7	Schematic of MCMR Prototype for Simulations	208
Figure 8.8	Conversion and Temperature Profiles for MCMR Run no.1a without Membrane	215
Figure 8.9	Methane Conversion vs. Methane Flow Rate at Position no.1 for MCMR Exp. no.1, without Membrane	216
Figure 8.10	Process Response on H ₂ Production to an Increase in CH ₄ Flow	218
Figure 8.11	Process Response on Temperatures to the Start of Reforming and Combustion Methane Flows	219
Figure 8.12	Conversion and Temperature Profiles for MCMR Exp. no.3a with Membrane	220
Figure 8.13	Sensitivity on Conversion Profiles for MCMR Run no.3a	222
Figure 8.14	Conversion and Temperature Profiles for MCMR Exp. no.3b with Membrane	223
Figure 8.15	Parametric Study on Effect of S/C Ratio, Reforming Channel Pressure, and CH ₄ Flow Rate, on H ₂ Extracted to CH ₄ Feed Ratio	225
Figure A.1	Brush Coating of γ -Al ₂ O ₃ , α -Al ₂ O ₃ and RK-212 Modified Sol	255
Figure A.2	Multi-Layer Brush Coating of γ -Al ₂ O ₃ and α -Al ₂ O ₃ Modified Sol	256
Figure A.3	Dip Coating of γ -Al ₂ O ₃ and α -Al ₂ O ₃ Modified Sol Including Metal Precursors	257
Figure A.4	Scanned Images of Brush, Cold Spray and Dip Coating Samples, before and after Sonication	258
Figure A.5	Hot Spray Coating of γ -Al ₂ O ₃ Modified Sol Including Metal Precursors	260

Figure A.6	Hot Spray Coating Optical Images with Different Solvents for Modified Sol	261
Figure A.7	Hot Spray Coating of α -Al ₂ O ₃ , MgAl ₂ O ₄ and CeO ₂ -ZrO ₂ Modified Sol Including Metal Precursors	262
Figure A.8	Hot Spray Coating of Commercial RK-212 Catalyst	264
Figure A.9	Hot Spray Coating of Commercial Ru 5%/ γ -Al ₂ O ₃ Catalyst	266
Figure A.10	Coating Thickness vs Mass of Catalyst	267
Figure B.1	Stability of RK-212: Effect of Operating Conditions and Catalyst Loading	269
Figure B.2	Stability of RK-212: Comparing Crushed with Coated Catalyst	271
Figure B.3	TPR diagrams of Ni-based Catalysts	272
Figure B.4	Stability of Commercial Ru 5%/ γ -Al ₂ O ₃ (Alfa)	273
Figure C.1	Issues Encountered with MCMR, Part I	278
Figure C.2	Issues Encountered with MCMR, Part II	279
Figure C.3	Issues Encountered with MCMR, Part III	280
Figure C.4	Combustion Methane Conversion versus Time on Stream, for MCMR Exp. no.0.3	285
Figure C.5	Combustion Methane Conversion versus Time on Stream, for MCMR Exp. no.0.4 and 0.5	286
Figure C.6	Combustion Methane Conversion versus Time on Stream, for MCMR Exp. no.0.6 and 0.7	287
Figure C.7	Reforming Methane Conversion versus Time on Stream, for MCMR Exp. no.0.4	288
Figure C.8	Reforming Methane Conversion versus Time on Stream, for MCMR Exp. no.0.5	289
Figure C.9	Conversion and Temperature Profiles for MCMR Exp. no.0.4 and 0.5	290
Figure C.10	Conversion and Temperature Profiles for MCMR Exp. no.0.7	291

Acronyms

ATR Autothermal Reforming

BET Brunauer, Emmet and Teller

BJH Barrett, Joyner and Halenda

CFD Computational Fluid Dynamics

CVD Chemical Vapour Deposition

EDX Energy-Dispersive X-ray Spectroscopy

EPD Electrophoretic Deposition

FBMR Fluidized Bed Membrane Reactor

FBR Fluidized Bed Reactor

FESEM Field Emissions Scanning Electron Microscopy

FID Flame Ionization Detector

GC Gas Chromatograph

GHG Greenhouse Gas

H/C Hydrogen-to-Carbon

IPCC Intergovernmental Panel on Climate Change

LCA Life Cycle Assessment

LHV Low Heating Value

MCC Methane Catalytic Combustion

MCMR Multi-Channel Membrane Reactor

MCR Multi-Channel Reactor

MRT Membrane Reactor Technologies

P&ID Process & Instrumentation Diagram

PBMR Packed Bed Membrane Reactor

PBR Packed Bed Reactor

PEMFC Proton Exchange Membrane Fuel Cell

PSA Pressure Swing Adsorption

S/C Steam-to-Carbon

SEM Scanning Electron Microscopy

SMR Steam Methane Reforming

SS Stainless Steel

TCD Thermal Conductivity Detector

TGA Thermo Gravimetric Analysis

TPR Temperature Programmed Reduction

WGS Water Gas Shift

WHSV Weight Hourly Space Velocity

XPS X-Ray Diffraction

XRD X-Ray Diffraction

List of Symbols

- A_i Pre-exponential factor for sorption equilibrium constant K_j [various units]
- A_j Pre-exponential factor for rate coefficient k_j [various units]
- c Concentration [mol/m³]
- c_{1i} Concentration of component i after transformation (see Eq. (2.55)) [mol/m³]
- c_{2i} Concentration gradient of component i after transformation (see Eq. (2.56)) [mol/m⁴]
- c_i Concentration of component i [mol/m³]
- C_{p_i} Molar heat capacity for component i [J/(mol K)]
- \hat{C}_p Specific heat [J/(kg K)]
- D_h Hydraulic diameter [m]
- $D_{i,eff}$ Effective diffusion coefficient [m²/s]
- \mathcal{D}_{ij} Binary diffusion coefficient [m²/s]
- $D_{i,K}$ Knudsen diffusion coefficient [m²/s]
- $D_{i,mix}$ Mixture diffusion coefficient [m²/s]
- $D_{p,ave}$ Average powder (particle) diameter [μm]
- E_j Activation energy [kJ/mol]

$F_{H_2,m}$ Molar flow rate of H_2 extracted by membrane, see 3.7 [mol/s]

$F_{H_2,prod}$ Molar flow rate of H_2 produced, see 3.8 [mol/s]

F_i Molar flow rate of component i [mol/s]

H_{flux} Heat Flux (See Eq. (3.16)) [kW/m²]

H_k Half-height of channel [m]

$J_{H_2,m}$ Hydrogen molar flux through membrane [mol/(m² s)]

\vec{J}_i Component i diffusion flux [mol/(m² s)]

k Thermal conductivity [W/(m K)]

K_i Sorption equilibrium constant for component i [kJ/mol]

k_j Kinetic rate of reaction j coefficient [various units]

L Channel length [m]

Mw_i Molecular weight of species i [kg/mol]

P Pressure [bar]

Pe_L Mass Peclet number [-]

P_i Partial Pressure [bar]

\vec{q} Conduction heat flux [W/ m²]

Re Reynolds number [-]

R_g Universal gas constant: 8.314 [J/(mol K)]; $8.314 \cdot 10^{-5}$ [(bar m³)/(mol K)]

R_i Production rate of component i [mol/(m³ s)]

r_j Rate of reaction j per volume of reactor [mol/(m³ s)]

r'_j Rate of reaction j per mass of catalyst [kmol/(kg h)]

R_{pore} Average catalyst pore radius [m]

t Time on stream [h]

T Temperature [K]

T_1 Temperature after transformation (see (2.57)) [K]

T_2 Temperature gradient after transformation (see (2.58)) [K/m]

$Th_{cat,k}$ Catalyst Layer Thickness [m]

Th_m PdAg Membrane Thickness [m]

Th_s Separator Wall Thickness [m]

u Dependent parameters c_i and T , see (2.59) [various units]

v_z Axial gas velocity [m/s]

W_{cat} Catalyst mass [g]

W_k Channel width [m]

x Transverse coordinate [m]

X_{CH_4} Methane conversion [mol/mol]

x_i Mass fraction [kg/kg]

Y_{H_2} Hydrogen production intensity [various units]

y_i Molar fraction [mol/mol]

z Axial coordinate [m]

List of Greek Letters

α Exponent in Eq. 2.11 or reaction order for CH₄ in Eq. (2.50) [-]

β Exponent in Eq. 2.16 or reaction order for O₂ in Eq. (2.50) [-]

δ_k Coefficient in Eq. (2.114) [-]

$\Delta H_{rx,j}^{298K}$ Enthalpy of reaction j at 298 K, 1 bar [kJ/mol]

ΔH_{sorp} Sorption enthalpy [kJ/mol]

ΔT Transverse temperature difference (see (2.114))[K]

Δz Discretization step size in axial direction [m]

ε Catalyst porosity [-]

η_{cat} Catalyst effectiveness factor [-]

η_m Membrane effectiveness: Ratio between real flux and theoretical flux for membrane [-]

η_{react} Reactor efficiency [-]

μ Gas viscosity [Pa s]

Φ_{ij} Coefficient in Eq. (2.10) [-]

ρ Catalyst density [kg/m³]

σ_{ij} Stoichiometric coefficient of component i for reaction j [-]

σ_M Stoichiometric molar ratio between the reduced metal and the metal precursor,
see Eq. (4.4) [-]

τ Catalyst tortuosity [-]

v Pore volume [cm^3/g]

List of Subscripts

M Metal

sf Surface of micro-reactor

ave Average

b Discretization grid position in axial direction

bed Catalyst bed of a fixed reactor

c Combustion gas channel or combustion

carr Carrier

cat Catalyst layer

i Chemical component

in Inlet

j Reaction numbers, or second chemical component

k Either combustion or reforming

m Membrane

m.area Membrane area

m.sup. Membrane support

mix Mixture of gas species

o Feed conditions

out Outlet

r Reforming gas channel or reforming

s Separator wall

ske Skeleton

vol.react. Internal reactor volume

Acknowledgments

This thesis was made possible with the contributions of many people.

A first special thanks for my supervisors. Prof. John Grace has been extremely supportive throughout those years, by providing valuable advices, and critical financial and human support. I had the chance to work with Prof. Said Elnashaie, who can combine revolution and reactor modeling as no one else.

A very appreciative thank you to the thesis committee, Professors Sue Baldwin, Walter Merida, and Jim Lim, who had to go through this long thesis in a short period of time. This research was also made possible with the contribution of Prof. Tom Troczynski, allowing us to use his ceramic laboratory space, numerous equipments, and giving valuable insights. Special thanks also to Prof. Kevin Smith for his direction and knowledge with the amazing world of catalysis. Thanks to the MRT folks, with Ali Gulamhusein, Anwu Li, and Tony Boyd for all their advice.

Several students participated in this project. I would like to acknowledge the contribution of JiYeon Shin, Zaid Ahmad, Helia Yazdanpanah, Bahman Ghiasi, Kit Wong, Philipp Stoesser, Kristian Dubrawski, Dora Ip, and Nick Chow. To my fellow colleagues for their help, moral support, and good conversations, Rakib Abdur, Andres Macheta Botero, Siamak Elyasi, Laura Tremblay Boyer, Dylan Gunn, and Ali Shafiei, thank you! A special smile to my family for their on-going moral and financial support, and yes this should be my last degree in school, at least for a while. To all my friends, met through sports, activism, research, beer, and social dancing throughout those years, thank you!

I would also like to thank the company Sasol Alumina, providing at no cost various alumina powders and beads. This project was also made possible by the financial support of NSERC, FQRNT, and the Canada Fund for Innovation.

*I would like to dedicate this thesis to all of us who believe that
applying science with ethics can achieve wonderful things, et à
Louis-Philippe, Émile et Julien, car c'est un peu pour vous que je fais
tout ce travail!*

Chapter 1

Introduction

Mieux vaut 1% de pas grand chose, que 100% de rien du tout. — My mom (2011)

1.1 The Case for Hydrogen

1.1.1 Climate Change and Greenhouse Gas Emissions

In their 4th assessment, the Intergovernmental Panel on Climate Change (IPCC) reported that, to avoid climate change with devastating consequences, we need to limit global temperature rise by 2.0 - 2.4°C above the pre-industrial level. In order to achieve this target, world Greenhouse Gas (GHG) emissions need to be reduced by 50-85% from the 2000 level by 2050 (Intergovernmental Panel on Climate Change, 2007). The reduction target corresponded to a CO₂ concentration in the atmosphere of 350-400 ppm, which was already at 379 ppm in 2005 (Intergovernmental Panel on Climate Change, 2007). Trends are not encouraging, since global CO₂ concentration, measured in Mauna Loa, Hawaii, reached 392 ppm in 2011 (Earth System Research Laboratory, 2012). In 2004, 13.1% of the world emissions, or 6.4 GT CO₂ equivalent (CO₂e), were coming from the transportation sector. In Canada, 24% of GHG emissions, corresponding to 166 MT CO₂e, were emitted in 2010 by this sector, a 3.6% increase from 2005 (Environment Canada, 2012).

1.1.2 Life Cycle Impact Assessment

One option to reduce GHG emissions in the transportation sector is to use hydrogen and fuel cell technology. Hydrogen is often mistaken as a zero emission fuel, with claims referring to its combustion only producing water. Hydrogen, like electricity, is an energy carrier, and not a primary energy source. Therefore, it is important to examine hydrogen with Life Cycle Assessment (LCA) in order to understand its environmental impact.

Since hydrogen can be produced from a wide variety of feedstocks and energy sources (see Figure 1.1), then combined with fuel cell technology, LCA predictions have varied considerably in the literature (Colella et al., 2005; Granovskii et al., 2006; Schäfer et al., 2006; Dincer, 2007; Ally and Pryor, 2007).

Colella et al. (2005) showed that even with conservative assumptions (i.e. Proton Exchange Membrane Fuel Cell (PEMFC) efficiency of 46%, 10% H₂ lost by leakage), switching from internal combustion engines to hydrogen fuel cell vehicles could reduce GHG emissions by of 14 - 23%, depending on whether the hydrogen is produced from steam reforming of natural gas or electrolysis based on wind turbines. However, for hydrogen from coal without carbon sequestration, the same LCA study showed almost no reduction of GHG. In similar studies (Granovskii et al., 2006; Dincer, 2007), assuming a higher efficiency by PEMFC engine (~ 50-60%), it was found that GHG emissions could be reduced by 25-40% if H₂ was extracted from natural gas, and by up to 80-85% if H₂ was obtained from wind energy.

Most emissions from vehicles are related to the fuel consumption, rather than to vehicle manufacturing and disposal: ~73% according to (MacLean and Lave, 2003), and nearly 90% according to (Schäfer et al., 2006). Schäfer et al. (2006) also noted that in the future, the share of fuel consumption should diminish as vehicles become more energy efficient.

Schäfer et al. (2006) predicted the global warming impact for a wide range of vehicles for 2020. With likely improvement in internal combustion engine vehicles and gasoline-electric hybrid vehicles, unless hydrogen would be produced from renewable sources, they found little energy or GHG emission savings by switching to hydrogen fuel cell vehicles. Ally and Pryor (2007) studied hydrogen fuel cell

buses from a demonstration project in Perth, Australia. With available technology, conventional diesel buses were more energy efficient than fuel cell buses, and no GHG reduction benefit was found. However, with expected improvements in future fuel cell buses, the authors believed that at least a 50% reduction in GHG emissions was achievable.

In addition to global warming reductions, hydrogen in fuel cells could help improve air quality in urban area, where particulate matter, NO_x , and volatile organic compounds are concerns. Wang et al. (2008) studied different PEMFC vehicles and hydrogen delivery scenario for Sacramento, CA. Centralized H_2 production with pipeline distribution was the best scenario to reduce air pollution. Compared with advanced new gasoline vehicles, centralized H_2 production would result in 273 times less CO, 88 times less VOC, 8 times less PM10, and 3.5 times lower NO_x concentrations.

From our review of LCA studies, hydrogen in fuel cell vehicles has the potential to reduce global GHG emissions as well as other air pollutants. However, as the IPCC pointed out, no single technology could solve the entire problem (Intergovernmental Panel on Climate Change, 2007). Curbing GHG emissions will need a wide range of technological solutions, as well as much smarter land usage, political leadership, pollution pricing, education, and mentality changes.

1.1.3 Global Hydrogen Production and Consumption

In 2007 the world produced between 53 to 65 million tonnes of hydrogen. Most was consumed at refineries, surpassing ammonia production (International Energy Agency, 2007; Naqvi, 2007). Refineries were once viewed as net producers of hydrogen, but they are now major consumers. H_2 production plants are often needed to implement environmental regulations (Ferreira-Aparicio and Benito, 2005; SRI Consulting, 2010). Among other usages for hydrogen are the synthesis of methanol, resins and plastics, food processing, electronics, and annealing of steels. Only 5% of the H_2 production is sold outside the production plant and distributed as liquid or gas in tanks or by pipelines. Its use for energy purposes constitutes only a small fraction of total production (Ferreira-Aparicio and Benito, 2005).

Nearly 96% of hydrogen production is derived from fossil fuels, 49% from natural gas, 29% from liquid hydrocarbons, 18% from coal, while electrolysis and other by-product sources of hydrogen account for ~4% (SRI Consulting, 2010). Hydrogen from Steam Methane Reforming (SMR) currently sets its reference price. A study by the National Academy of Engineering (2004) shows that large-scale production of hydrogen (1,200,000 kg/day) using current SMR technology is still the most economical option to produce hydrogen (National Academy of Engineering, 2004). They estimated the production cost from large scale SMR to be US\$1.03/ kg H₂ in 2004.

1.1.4 Hydrogen for Transportation

Hydrogen is used in the production of various chemicals. Advocates of a “hydrogen economy” see hydrogen playing a new role as an energy carrier, becoming the main fuel not only for transportation, but as well for stationary power production, building heating, and mobile device power.

Transportation Economics

In 2002, world hydrogen production was equivalent to less than 10% of the world oil production (Ferreira-Aparicio and Benito, 2005), indicating the scale of investment needed for a transition to hydrogen. Table 1.1 lists various targets from the U.S. Department of Energy (DOE), together with progress achieved according to the California Fuel Cell Partnership, and technical data from Honda Motor Corp. (California Fuel Cell Partnership, 2012; American Motor Honda Co., 2012).

Electricity needed for gas and liquid storage represents, respectively, 12% and 35% of the H₂ energy content (International Energy Agency, 2007). The US National Research Council estimated that it would cost US\$0.9 and \$1.0 million to build a distributed plant producing 500 kg/day from SMR and electrolysis respectively (National Research Council, 2008).

The lack of refueling infrastructure is a major obstacle to hydrogen fuel cell market penetration. There is a small, but growing number of, demonstration fueling stations around the world. In May 2012, there were ~238 operating hydrogen refueling stations worldwide, 82 in the U.S. (8 accessible to public), and 14 in

Table 1.1: Targets and Progress for Hydrogen in the Transportation Sector (Data collected from California Fuel Cell Partnership (2012); American Motor Honda Co. (2012); International Energy Agency (2007)).

Category	Target	Progress
Fuel Cell Efficiency	60%	FCX Clarity claims 60%
Fuel Cell Durability	5000 operating hours	> 2500 operating h
Vehicle Range	480 km	FCX Clarity claims 385 km
Refueling Rate	~ 1 kg/ min ^a	~ 0.8 kg/min
Fuel Cell Cost	US\$30/ kW by 2015	US\$49/ kW in 2011 ^{b,c}
Vehicle Tank Cost	-	US\$3,000 - 4,000
Cost of Delivery Hydrogen	US\$1/ kg ^d	\$3/kg ^b
Hydrogen Cost at the Station	US\$3/ kg ^d (2015) to be revised to US\$6/ kg (2020)	From NG: US\$7.7-10.3/ kg; From electrolysis: US\$10.0-12.9/ kg

^aFCX Clarity storage tank capacity: 4 kg at 35 MPA

^bBased on projections to high-volume manufacturing or delivery

^cFCX Clarity has a 100 kW fuel cell stack

^dData were originally written in gge (USGAL gasoline equivalent), and 1 kg H₂ has about the same energy content as 1 USGAL (3.79 L) of gasoline

Canada (Fuelcells.org, 2012a,b). By comparison, there was ~12,710 retail gas stations in Canada in 2010 (CNW, 2010).

Decentralized production of hydrogen was proposed to break the bottleneck (Ogden, 2001; Ferreira-Aparicio and Benito, 2005). IHS Chemical (2003) estimated that with technology commercialized in 2003, the minimum competitive capacity for distributed vs. large centralized plant was ~10,600 - 12,700 kg H₂/day. 10,000 kg/day could supply ~2000 hydrogen fuel cell vehicles a day. Hence, there is still room for technological advancement at smaller scale (<500 kg H₂/day), the main market goal for the technology considered in this thesis.

1.2 Hydrogen Production Pathway

1.2.1 Feed Sources

Hydrogen, present in organic compounds and several inorganic compounds (e.g. water, ammonia, NaOH, H₂SO₄), can be produced as the main product or as a by-product of various chemical and biological reaction pathways (see Figure 1.1). The focus of this review is on technologies that have potential to be commercialized in a near to mid-term range, in order to supply fueling stations in a decentralized way. The main focus is on methane reforming technologies, since natural gas is most likely to stay the benchmark fuel for economic reasons, but also for thermodynamic efficiency and environmental considerations. Methane, the main component of natural gas, has the highest Hydrogen-to-Carbon (H/C) molar ratio of all hydrocarbons, therefore potentially making less CO₂ emissions per mole of hydrogen produced.

With inevitable energy losses, it makes little sense thermodynamically to use electricity alone to produce hydrogen, which will be reconverted into electricity in a fuel cell. However, for small scale production, typically up to 100 kg/day, water electrolysis has been commercialized. It has the advantage of being a well-known technology generating high purity, hydrocarbon-free hydrogen. Commercial alkaline water electrolyzers produce hydrogen with efficiency ranging from 55% - 75%, while 70% - 80% of the cost of production is attributable to electricity (International Energy Agency, 2007).

1.2.2 Reaction Pathways from Methane to Hydrogen

Various chemical reaction pathways to produce hydrogen from methane are listed below.

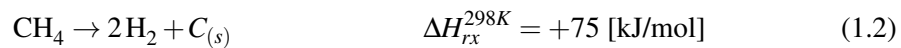
Dry Reforming:



Feed Source	Energy Source	Reaction Process
<p>Inorganic Water Ammonia Hydrogen Sulfide</p> <p>Organic Renewable Biomass Biogas, Sugar, Alcohol, Ether Fossil Natural gas, oil, Coal Alcohol, Ether</p>	<p>Heat Combustion Geothermal Solar Nuclear</p> <p>Electricity Fossil Nuclear Renewable Wind, Solar, Hydro, Geothermal, Biomass</p>	<p>Biological</p> <p>Chemical Catalysis Reforming Partial Oxidation By-product chemical process Catalytic Cracking Catalytic Decomposition Dehydrogenation</p> <p>Thermal Thermo-chemical loop Pyrolysis Gasification Decomposition</p> <p>Electro-chemical Photo-electro-chemical Plasma reforming Electrochemical reforming Electrolysis</p>

Figure 1.1: Hydrogen Production Pathways

Methane Decomposition:



Partial Oxidation:



Steam Methane Reforming:

Autothermal Methane Reforming: With Autothermal Reforming (ATR), air or oxygen is added to the methane-water mixture. The following combustion reaction occur, in addition to the SMR reactions.



If the product of interest is H_2 rather than syngas, partial oxidation and dry reforming are unlikely to be the best options. By simple mole balances, a minimum of 69% of the methane combustion energy is lost with dry reforming. Dry reforming also requires a stream of CO_2 , which may not be available. Methane decomposition could become a viable option with a strong market for solid carbon or a high price on GHG emissions. ATR can be the most efficient mode of operation since it requires the lowest total energy consumption by avoiding all heat transfer limitations (Grace et al., 2005). ATR using air dilutes the hydrogen concentration in the product stream, increasing purification cost downstream. An alternative to air would be to add an O_2 production unit to avoid N_2 dilution, but at the cost of increasing complexity. Long term stability of bi-functional catalysts for ATR can also be problematic (Grace et al., 2005). As discussed above, SMR is currently the most economical way of producing hydrogen at large scale. A major challenge at small scale is how to transfer heat as efficiently as possible.

1.3 Process and Hydrogen Purification

The conventional process to produce pure hydrogen via large-scale SMR features 5 steps (Farrauto and Bartholomew, 1997; Ferreira-Aparicio and Benito, 2005):

Table 1.2: Hydrogen Fuel Quality Specifications (partial list). For complete list, see (SAE International, 2011)

Constituent	Limits (ppm ^a)
Water	5
Total hydrocarbons ^b	2
Oxygen	5
Helium	300
Nitrogen, Argon	100
Carbon dioxide	2
Carbon monoxide	0.2
Total Sulfur	0.004
Particulate Concentration	1 mg/kg
Hydrogen Content	>99.97%

^aMole basis

^bCH₄ basis

(1) Desulfurization, to avoid poisoning of the reforming catalyst; (2) Optional pre-reforming to transform higher molecular weight hydrocarbons to methane, hence avoiding carbon formation during reforming; (3) Steam reforming; (4) High-temperature Water Gas Shift (WGS), optionally followed by low-temperature WGS, reducing the amount of CO to 1-3%; and (5) Pressure Swing Adsorption (PSA) to obtain pure hydrogen.

To be used as a fuel for PEMFC, hydrogen must meet stringent quality requirements, see Table 1.2. Few technologies exist to purify the hydrogen product stream, among them: PSA, preferential oxidation, and H₂ selective membranes.

1.3.1 Pressure Swing Adsorption

Most modern production plants use PSA for hydrogen purification. The standard process requires at least two adsorption vessels to ensure continuous operation. They are usually filled with beads of activated carbon, zeolite, molecular sieves or activated alumina (Waldron and Sircar, 2000). New systems use structured absorbents to avoid undesirable fluidization, and hence increase flow rates and reduce size and cost of the unit (Babicki and Hall, 2003). Standard operation consists of

a minimum of 4 steps: (1) adsorption of feed impurities at high pressure and collection of pure hydrogen; (2) depressurization with desorption of impurities (3) low-pressure countercurrent purge with hydrogen; and (4) pressurization with hydrogen (Waldron and Sircar, 2000). Hydrogen purity can reach 99.9999% at recovery rates from 70-90%, depending on the feed purity and off-gas pressure (Mishra and Prasad, 2011). Commercial units can handle as little as 10 Nm³/h (21 kg/day) to large-scale production of 400,000 Nm³/h (845,000 kg/day) (Xebec Absorption, 2012; Linde Group, 2012).

1.3.2 Preferential Oxidation

Preferential oxidation uses the concept of the proven catalytic converter technology from the automobile industry. The product gas from the water gas shift converter is mixed with air in a fixed bed or monolith reactor, to limit pressure drop. Catalyst is usually a noble metals (Pt, Rh, Pd), gold or CuO–CeO₂ (Farrauto and Bartholomew, 1997; Mishra and Prasad, 2011). Mishra and Prasad (2011) reported that CO levels <10 ppm can be achieved with such technology. However, the addition of air dilutes the hydrogen stream, and leads to more excess feed at the anode of the fuel cell to avoid mass transfer limitation. Preferential oxidation is probably limited to small and medium scale stationary power production, not requiring high hydrogen purity, or mobile or on-board systems constrained by system volume and weight (Ferreira-Aparicio and Benito, 2005).

1.3.3 Membranes

Membranes have the potential to be installed directly inside reformers. In-situ separation can favorably shift the limiting thermodynamic equilibrium. Adhikari and Fernando (2006) reviewed several high-temperature membranes suitable for SMR: microporous ceramic, dense metallic, and dense ceramic membranes. Although microporous ceramic membranes have relatively high hydrogen flux, their selectivity is limited, as the separation relies principally on the difference in molecular weights of the gas compounds. As the CO concentration is generally limited to less than 1 ppm in PEM fuel cells, further purification is needed. Dense metallic hydrogen membranes have the advantage of high selectivity, but lower permeability and

lower maximum operating temperature ($\sim 575^\circ\text{C}$ for Pd/Ag membrane) than microporous membranes. Dense ceramic membranes operate at high temperature and high selectivity, but lack the flux of the dense metallic and microporous ceramic membranes. The presence of pinholes in dense membranes is a major challenge.

The permeation mechanism for dense Pd-based membrane involves seven steps in series: (1) transport of hydrogen molecules to the surface of the metallic membrane; (2) reversible chemisorption of H_2 on the metal surface; (3) reversible dissolution of atomic hydrogen into the bulk metal; (4) diffusion of atomic hydrogen through the metal lattice; (5) reassociation of atomic hydrogen on the permeate-side; (6) desorption of adsorbed molecular hydrogen from the metal surface; and (7) gas transport away from the permeate-side surface. Diffusion of atomic hydrogen (step 4) is generally rate controlling. To resist the necessary pressure gradient acting as the driving force for hydrogen diffusion, a support for the membrane is generally required (Boyd, 2007).

Membrane Reactor Technologies (MRT), a UBC spin-off company, developed a $25\ \mu\text{m}$ thick planar Pd/Ag 25wt% hydrogen permselective membrane. The Pd/Ag foil is supported by a porous stainless steel sheet, separated by a ceramic layer to avoid interdiffusion between the Pd and stainless steel, lowering permeability. The major limitation with the Pd/Ag membrane is its maximum operating temperature of $\sim 575^\circ\text{C}$. At this temperature, the kinetics of the reforming reactions are relatively slow and the equilibrium conversion of methane is relatively low, compared with conventional reactor temperatures. Nonetheless, MRT membranes were successful in several research projects (e.g. Boyd (2007); Mahecha-Botero et al. (2009); Rakib et al. (2011)). This thesis also used this technology.

Research on dense Pd-based membranes seeks different alloys, better supports, and thinner membranes to enhance the H_2 flux and reduce cost. Ryi et al. (2006b) built a $4\ \mu\text{m}$ thick Pd–Cu–Ni ternary alloy membrane on a 2 mm porous nickel support. They tested the membrane up to 500°C with pressure difference across the membrane up to 3.6 bar, and no defect was detected. Su et al. (2005) made 2-6 μm Pd membranes on porous stainless steel, separated by a SiO_2 layer. Permeation measurements were made at 500°C , with a 0.5 bar pressure difference. Ryi et al. (2011) produced non-alloy, 6.8 μm thick, pinhole-free Ru/Pd composite membranes by electroless plating.

Instead of porous supports, dense silicon oxide wafers, perforated by etching, have been proposed as membrane support (Wilhite et al., 2004; Keurentjes et al., 2004; Gielens et al., 2007; Deshpande et al., 2010). Wilhite et al. (2004) made 200 nm thick Pd and Pd/Ag membranes, and operated them up to 425°C. Keurentjes et al. (2004) produced Pd/Ag membrane 0.5 and 1.1 μm thick. Pd/Ag was sputtered onto the wafer using titanium as an adhesion layer. No pinholes were detected at temperatures up to 450°C, and the pressure difference across the membrane was near 1 bar. It is not clear if those thin membranes could sustain SMR operating conditions, with more elevated temperatures and pressures.

1.4 Reformer Configuration

1.4.1 Current Large-Scale Reactor Design

Large scale conventional SMR units consist of a stack of long catalyst-filled tubes (12 m), operated at $\sim 15\text{-}25$ bar, and $\sim 850^\circ\text{C}$ (Ogden, 2001). Heat is supplied by burning natural gas or other fossil fuels in a furnace chamber surrounding the catalyst tubes. Heat transfer is limited by the permissible flux through the metal tubing, requiring expensive alloy steels. Inside the catalyst pellets, mass transfer resistance is also important, with low effectiveness factors ($<95\%$) (Adris et al., 1996).

To overcome mass and heat transfer limitations, new reactor configurations, novel catalysts, alternative reaction pathways, new heat transfer media, and separation methods are often proposed (Ogden, 2001; Ferreira-Aparicio and Benito, 2005).

1.4.2 Neo-conventional Reactor

Neo-conventional reactors typically use fixed bed reformers without radiant burners. These are hard to scale down efficiently. Heat is usually transferred by convection via pre-burned fuel gas, and the reformer tubes are U-shaped, instead of conventional straight pipes. Haldor Topsøe developed a medium-scale H_2 production plant, to produce 10,600 to 63,000 kg H_2 /day (Haldor Topsøe, 2009). UTC power commercialized a stationary heat & power unit, PureCell Model 400, that produces

400 kW of electricity and 450 kW of heat, with 90% overall fuel efficiency. This means that their reformer produces the equivalent of ~ 1300 kg H_2 /day. The unit recycles all the water generated, and no water is supplied. Their current reformer design uses fixed beds, and they are also testing plate reactor technologies (Kanuri, 2011; UTC Power, 2012).

1.4.3 Multi-channel Reactor

Multi-Channel Reactors (MCRs), also known as plate, wall, micro-channel or micro-structured reactors, have been often proposed to generate hydrogen more efficiently (e.g. (Park et al., 2005; Ryi et al., 2006a; Tonkovich et al., 2007; Seris et al., 2008; O'Connell et al., 2011; Hwang et al., 2011)). The basic idea is to imitate the compact design of a plate heat exchanger: Cold channels, where endothermic reforming reactions are taking place are juxtaposed with hot channels, where exothermic catalytic combustion is occurring.

Typical channel widths range from a few hundred microns to 3-5 mm (Tonkovich et al., 2004). Catalyst is typically coated on the channel walls, but can also be coated on metallic foam (Tonkovich et al., 2004), meshes (Ryi et al., 2006a) or in powder or pellet form (Hwang et al., 2011). MCR increases the surface area for heat exchange and enhances the hydrogen production intensity per volume of reactor. With a thin layer ($< 100 \mu\text{m}$) of coated catalyst, the catalyst effectiveness is also enhanced. Scale-up is achieved by repeating the channel pattern, so that the reaction physics and hydrodynamics stay the same (Tonkovich et al., 2005). MCRs also respond quickly to dynamic changes in feed conditions (Sohn et al., 2007). Challenges include flow distribution among channels, catalyst deactivation, hot spots, fabrication and sealing (Tonkovich et al., 2005; O'Connell et al., 2011).

Tables 1.3 and 1.4 present physical details and performance data for several MCR units used for hydrogen production via reforming of various feedstocks. In Table 1.4, reforming methane conversions from Hwang et al. (2011) exceed equilibrium values. The authors explained that this was due to their Ni sintered catalyst pellet having a membrane effect. Their design forced all gases to go through the Ni pellet. Hydrogen diffusing faster than other components shifted the equilibrium methane conversion.

Table 1.3: MCR Steam Reforming (A) and Catalytic Combustion (B) - Fabrication Details

Reference	Feed A - Catalyst	Feed B - Catalyst	Coating Method - Film Thickness	Channel Dim (Width x Height x Length) - Material - Fabrication - Sealing
Venkataraman et al. (2003)	CH ₄ - Rh-Cr ₂ O ₃ -Y ₂ O ₃ /Al ₂ O ₃	CH ₄ - Pt-Cr ₂ O ₃ -Y ₂ O ₃ /Al ₂ O ₃	Wash Coating - 10 μm	8 cm x 5 cm x 4 mm - Fecralloy - 1 mm deep corrugated plate - bolted and Fiberfrax paper gasket
Park et al. (2005)	MeOH - Cu-ZnO/Al ₂ O ₃	MeOH - Pt/Al ₂ O ₃	Al ₂ O ₃ under layer and wash coating -N/A	300 x 200 μm x 34 ^a mm - SS ^b - Wet etching - Brazing
Ryi et al. (2006a)	CH ₄ - Rh-Mg/Al ₂ O ₃	H ₂ - Pt-Zr/FeCrAlY mesh	Wash coating - N/A ^c	300 x 30 μm x 20 mm - N/A- Etching - N/A
Sohn et al. (2007)	MeOH - Cu-Zn/Al ₂ O ₃	H ₂ (start-up), MeOH - Pt/Al ₂ O ₃	Wash coating -50 μm	450 x 150 μm x 100 mm - SS - Wet etching - Clamping
Tonkovich et al. (2007)	CH ₄ - 10 wt% Rh-MgO/Al ₂ O ₃ on FeCrAlY Felt	H ₂ - Pd	Wash coating - N/A	Ref. 10.7 mm x 0.28 mm x 11.4 mm, Comb. 2.54 mm cylindrical - Inconel - N/A- N/A
Seris et al. (2008)	Nat. Gas - Noble metal (Engelhard)	H ₂ / Pd-based	Coated ceramic monolith - N/A	N/A-N/A-N/A-N/A
Hwang et al. (2011)	CH ₄ - Ni sintered powder	H ₂ (start), H ₂ + CH ₄ / Pt coated mesh	Pellet diffusion bonded - 1.2 mm	N/A- N/A- N/A- Diffusion bonding

^aEstimated^bref. = reforming, comb. = combustion, SS = stainless steel, nat. gas = natural gas^cN/A: not enough data to estimate or report

Table 1.4: MCR Steam Reforming and Catalytic Combustion - Performance Data

Reference	Reactor Size (w/out insulation) - Total H ₂ Output	Ref. ^a Feed Conversion - Purity H ₂ (dry basis)	H ₂ Output/ mass cat. kg/ (day kg _{cat})	H ₂ Output/ react. vol. kg/ (day m ³)	Efficiency Reformer ^g - External Heating
Venkataraman et al. (2003)	48-80 ^{b,c,d} ml - 0.09-0.25 ^b kg H ₂ /day	90-95% @ ~600-700°C- 74-78%	N/A ^h	700-5200 ^d	45 ^b % - Bunsen burner for start-up
Park et al. (2005)	72 ^e ml - 0.04 kg H ₂ /day	>99% conv. @ 230-260°C- 73%	N/A	590 ^e	N/A- No external heating
Ryi et al. (2006a)	50 ^f ml - 0.09 kg H ₂ /day	94% conv. @ 700°C- N/A	N/A	1780 ^f	N/A- No external heating
Sohn et al. (2007)	33 ^{b,f} mL - 0.21 kg H ₂ /day	90% conv. - 70% @ 300°C	355	6408 ^f	57% - No external heating
Tonkovich et al. (2007)	N/A- 0.06 ^b kg H ₂ /day	88% conv. @ 840°C, 12 bar - N/A	5000	N/A	N/A-N/A
Seris et al. (2008)	16 ^e L - 10.6 kg H ₂ /day	80% conv. @ 750°C, 2 bar - N/A	N/A	650 ^e	N/A- N/A
Hwang et al. (2011)	80 ^e mL - 0.04 kg H ₂ /day	95% conv. @ 610°C- N/A	N/A	470 ^e	N/A- No external heating

^acat. = catalyst, conv. = conversion, ref. = reforming, react. vol. = reactor volume

^bEstimated

^c(Venkataraman et al., 2003) has three different reactor configurations, see paper for details

^dReactor size includes some heat exchangers

^eReactor size includes heat exchangers

^fReactor size excludes heat exchangers

^gEfficiency Reformer: Low Heating Value (LHV) H₂* H₂ Flow / (LHV * Ref. Feed + LHV * Comb. Flow)

^hN/A: not enough data to estimate or report

The MCR concept allows innovative heat integration to optimize heat transfer and overall efficiency. Heat exchangers to pre-heat reforming feed and cool the products can be integrated directly to the reformer (Ryi et al., 2006a).

Some reformers have been developed for mobile device applications (Ryi et al., 2006a; Sohn et al., 2007), where fast start-up is critical. Ryi et al. (2006a) demonstrated that with a Pt-Zr coated-mesh igniter, they were able to reach their desired methanol reforming temperature in less than 1 min.

Simsek et al. (2011) compared two catalytic micro-channel configurations for syngas production (CO-H₂). They found that wall-coated micro-channel geometry led to higher methane conversions and syngas production rates than with packed catalyst in the same channel configuration.

The Institut für Mikrotechnik Mainz (IMM), Germany performed extensive experimental work on MCR technologies, including both 250 W liquefied petroleum gas and 100 W methanol fuel processors (O'Connell et al., 2011). Ztek Corporation undertook development of a small-scale reformer based on plate reactor technology (Ferreira-Aparicio and Benito, 2005). They commercialized units that likely use plate reactor technology, producing from 12 to 83 kg H₂/day at 99.99% purity. 85% efficiency from the fuel heat value is claimed (Ztek Corporation, 2005). This likely does not include parasitic losses.

1.5 Novel Membrane Reactors

Combining H₂ selective membranes with reforming reactors allows the thermodynamic equilibrium to be shifted, leading to high feed conversion, while generating pure hydrogen in a single vessel. Given the equilibrium shift and maximum temperature limitations of membranes, lower temperatures are used, reducing heat losses at small to mid production scale, and permitting less expensive stainless alloys to be employed (Grace et al., 2005).

The benefit of membrane addition in process intensification has to be weighed against slower kinetics, and the hydrogen being produced at low pressure, therefore needing to be compressed for most applications (Grace et al., 2005).

1.5.1 Packed Bed and Coated Tubular Membrane Reactors

Several Packed Bed Membrane Reactors (PBMRs) for the production of H₂ via reforming reactions have been investigated with various fuels: e.g. methane (Barbieri et al., 1997; Kikuchi, 2000; Tsuru et al., 2004; Kusakabe et al., 2006; Tong and Matsumura, 2006; Damle et al., 2008); ethanol (Yu et al., 2009; Papadias et al., 2010; Basile et al., 2008; Iulianelli et al., 2010; Tosti et al., 2010); methanol (Basile et al., 2005; Zhang et al., 2006); and liquid hydrocarbons (Chen et al., 2007a; Damle, 2009).

Methanol reforming has the advantage of lower temperatures than other fuels. For instance, Zhang et al. (2006), performed experiments with a carbon membrane reactor, from 200 to 250°C, obtaining conversion as high as 99.87% at 250°C. REB Research sells methanol membrane reformers, ranging from 0.19 kg/day (US\$13,500) to 9.6 kg/day (US\$140,000) (REB Research, 2012).

The ATR pathway has been investigated (Lin et al., 2008; Simakov and Sheintuch, 2009; Chang et al., 2010). Besides providing heat for reforming reactions, Lin et al. (2008) added oxygen to avoid unwanted reactions and carbon formation during ethanol reforming. Chang et al. (2010) developed a Pd/Ag membrane reactor for autothermal reforming of methane. With a molar ratio of 0.4 O₂/CH₄, the reactions did not need external power. O₂ was fed directly instead of air to avoid diluting the H₂ with N₂.

Dry reforming conditions have also been investigated (Galuszka et al., 1998; Coronel et al., 2011). Coronel et al. (2011) successfully tested a dry reforming membrane reactor, using 50 μm commercial Pd/Ag membrane with Rh/La₂O₃-SiO₂ catalysts. However, Galuszka et al. (1998) had their membrane destroyed by the formation of carbon filament. Cheng et al. (2009) also experienced membrane failure from carbon build-up, this time due to the partial oxidation of methane.

A typical PBMR configuration is a tubular fixed bed, with a tubular membrane inserted in the middle. Barbieri et al. (2008) located the membrane tube about half way through the entrance of the reactor. Their goal was to avoid back permeation of hydrogen at the entrance of the reactor. They claimed that they were able to reduce the size of their reactor with this configuration. De Falco et al. (2011) alternated reforming packed bed reactors with Pd membrane modules. This configuration

allows the packed beds to operate at higher temperature and provides faster kinetics and more favorable thermodynamic equilibrium. However, the process became more complex and did not lead to process intensification.

Membranes are generally not 100% selective to H₂, with small amounts of CO in the permeate. Mori et al. (2008) proposed the addition of a CO methanator on the permeate side to reduce the CO content to less than 10 ppm. However, the CH₄ content was high, from 83 to 1877 ppm (dry basis), which did not meet hydrogen purity requirement for hydrocarbons (see Table 1.2). Park et al. (2008), for the reforming of di-methyl-ether, added a water gas shift catalyst on the permeate side, leading to <20 ppm CO in the H₂ product stream.

Some authors have used different membrane separation strategies. Zou et al. (2007) separated CO₂ instead of H₂ in a water gas shift membrane reactor, filled with a Cu/ ZnO–Al₂O₃ catalyst. They obtained a H₂ stream with a CO concentration <10 ppm. Harale et al. (2010) produced a hybrid adsorbent membrane reactor by adding a CO₂ adsorbent. This reactor operated as a PSA unit, providing both H₂ and CO₂ as pure streams.

A composite membrane reactor, with catalyst directly deposited on the membrane, has been also proposed (Nomura et al., 2006; Tsuru et al., 2006, 2008). Tsuru et al. (2006) impregnated a Ni catalyst on a γ - α -Al₂O₃ tubular support, with one surface of the tube coated with microporous silica to create a catalytic membrane.

1.5.2 Fluidized Bed Membrane Reactor

Advantages and challenges of Fluidized Bed Reactor (FBR) and Fluidized Bed Membrane Reactor (FBMR) have been summarized by Grace et al. (2005) and Deshmukh et al. (2007). FBR improves heat transfer and reduces pressure drops relative to Packed Bed Reactor (PBR). Catalyst particles are much smaller than fixed bed catalyst pellets, increasing effectiveness factors from as low as \sim 0.01 to nearly 1. Fluidization also provides the possibility of replacing deactivated catalyst continuously or periodically, without shutting down the reactor. Attrition and entrainment of the catalyst are typical disadvantages associated with FBR. For FBMR, clever mechanical design and fluidization experience are needed to fit a

large number of membrane surfaces, and their associated piping, while avoiding excessive congestion. Catalyst particles can also form a film on the membrane, reducing the H₂ flux (Rakib et al., 2011).

The concept of FBMR for SMR was first proposed by Elnashaie and Adris (1989). Since then, several reactor concepts have been investigated experimentally (Adris et al., 1994; Boyd et al., 2005; Patil et al., 2007; Mahecha-Botero et al., 2011b; Rakib et al., 2011). Patil et al. (2007), using a tubular membrane consisting of a metal tube with 4-5 μm of Pd deposited on each side, obtained methane conversions from 69% at 550°C to 97% at 650°C. 650°C is a challenging temperature for Pd membranes, which generally operate in the range of 500-575°C to preserve the membrane integrity. Mahecha-Botero et al. (2011b) investigated a reactor with six planar MRT membranes for steam reforming of natural gas. The permeate yield of hydrogen over the methane fed reached ~ 2.3 , considerably less than the maximum molar ratio of 4 (excluding steam generation). However, hydrogen purity was high, exceeding 99.99% for all tests, with a relatively long cumulative experimentation time of 395 h. Rakib et al. (2011) built a FBMR for the steam reforming of methane, propane and heptane in the temperature range of 450 to 500°C. For SMR, the permeate molar yield of hydrogen over that of methane reached values as high as 3.

Autothermal conditions have also been investigated (Mahecha-Botero et al., 2008; Chen et al., 2007b). In those cases, air was split between the entrance and the exit of the reactor. The combustion reaction at the top of the reactor can provide the heat of reaction by normal catalyst recirculation in the bubbling bed. To avoid hydrogen dilution by nitrogen, some have proposed simultaneous O₂ and H₂ selective membranes (Chen et al., 2003; Rakib and Alhumaizi, 2005; Patil et al., 2007), but proof-of-concept is needed. Chen and Elnashaie (2004) proposed a circulating fluidized bed, operating at low Steam-to-Carbon (S/C) ratio, enabling extensive coking on the catalyst. The coke is then oxidized in a regenerator, providing the necessary heat for the reforming reactions. This configurations, inspired from the refinery catalyst crackers, also needs experimental proof.

Mahecha-Botero et al. (2011a) investigated a FBMR assisted by CO₂ sorption. The carbonation of CO₂ is exothermic providing a portion of the heat needed for the reforming reactions, as well as enhancing the hydrogen flux through the mem-

branes because of higher H_2 partial pressure on the retentate side. Work is needed to improve the stability of the CaO sorbent, and technical challenges have to be solved to achieve a continuous process including regeneration of the calcium oxide.

1.5.3 Multi-Channel Membrane Reactor (MCMR)

The concept of Multi-Channel Membrane Reactor (MCMR) was first applied to dehydrogenation. Franz et al. (2000) demonstrated a micro-reactor with a Pd 0.2 μm thick membrane, fabricated using e-beam deposition over a silicon wafer. The concept of MCMR applied to SMR was proposed by Goto et al. (2003), but proof of concept has been quite limited. Karnik et al. (2003) proposed a micro-reactor with Pd membrane for water gas shift. They built a unit, but only tested the flux through their membrane, which was unable to support a pressure differential greater than 1 bar. Wilhite et al. (2006) built a micro reactor with a 0.2 μm thick Pd/Ag membrane, supported on perforated silicon wafers, for partial oxidation of methanol. The $\text{LaNi}_{0.95}\text{Co}_{0.05}\text{O}_3/\text{Al}_2\text{O}_3$ catalyst was coated directly onto the membrane surface. Overall methanol conversion remained low, ranging from 44 to 63%. Varady et al. (2007) proposed Pd membrane micro-reactors to produce hydrogen from steam reforming and partial oxidation of methanol. They developed an innovative valve-less feeding system that used an ultrasonic atomizer. No clear data on methanol conversion and hydrogen purity were reported. No published experimental work has been found on the use of MCMR for SMR, and this thesis addresses this deficiency.

1.6 General Objectives and Strategy

This thesis is aimed at coupling two promising technologies for the decentralized production of hydrogen (i.e. <500 kg/day) for fuel cell usage: multi-channel reactor and permselective membrane. Several steps are involved:

- Steady-state, iso- and non iso-thermal two-dimensional reactor modeling of the MCMR;
- Coating of commercial and lab-made catalysts on a metal substrate using modified sol techniques;

- Stability, activity testing, and kinetic parameter estimations of reforming and combustion catalysts produced by the coating technique;
- Design, fabrication, commissioning, and model verification of a two-channel prototype of the MCMR, i.e. a single reforming channel, one combustion channel and a single-side planar Pd/Ag membrane.

Figure 1.2 shows the general strategy employed to build a MCMR prototype. The strategy was not linear and required many iteration loops to achieve a successful prototype. For instance, lab-made catalysts were developed because some commercial catalysts tested deactivated in an unacceptable manner. The thesis concludes with a brief discussion of what has been accomplished and what should be the next steps to obtain a commercially viable technology.

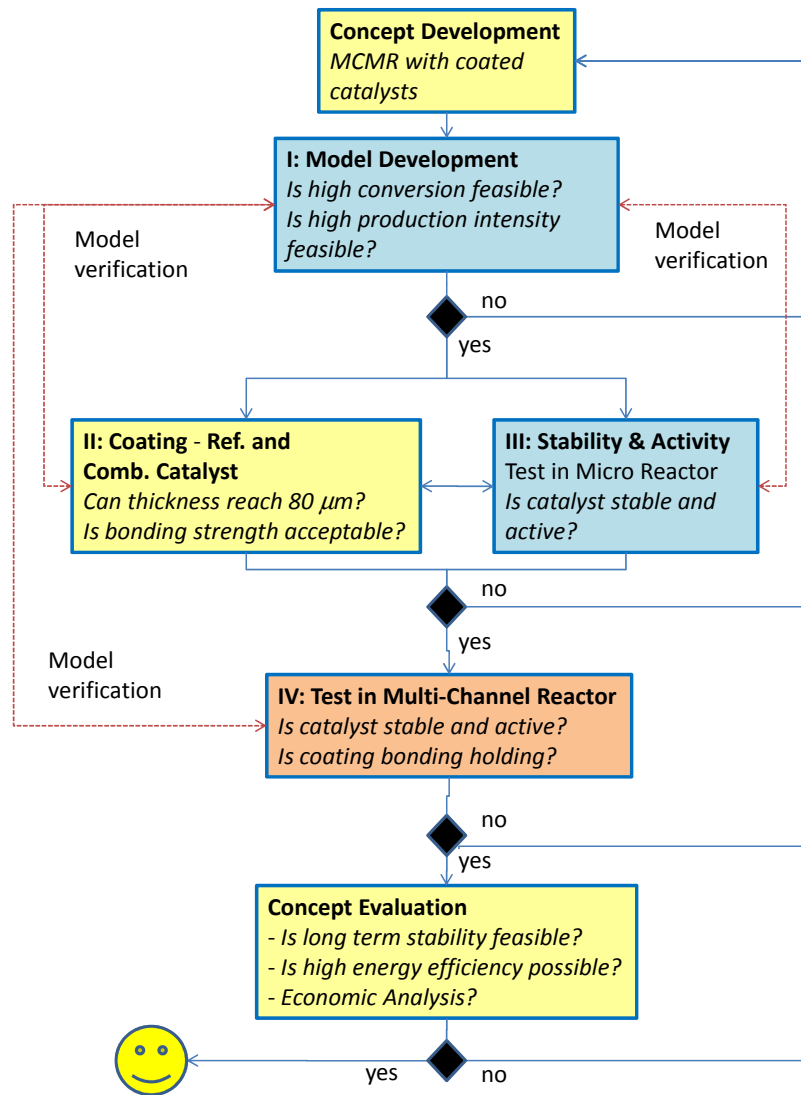


Figure 1.2: Thesis Strategy

Chapter 2

Steady State Model Development

2.1 Introduction

To produce hydrogen via Steam Methane Reforming (SMR), Goto et al. (2003) proposed to combine a Pd membrane (0.2 μm thick) with a Multi-Channel Reactor (MCR). Heat was provided by the catalytic combustion of the reforming exhaust gas in a countercurrent configuration. In their 1-D model, to avoid back permeation of hydrogen, the membrane did not start directly at the beginning of the channel. Their model included several assumptions, it assumed plug flow even though the MCR usually operates in the laminar regime; their model was isothermal, which is very unlikely for a countercurrent configuration; and they operated at a temperature of 887°C, which is much higher than the safe operating range of 500-650°C for Pd-based membranes. Alfadhel and Kothare (2005) also developed a single micro-channel 1-D model coupled with a Pd membrane to produce hydrogen based on the Water Gas Shift (WGS) reaction.

While the modeling of Multi-Channel Membrane Reactor (MCMR) for hydrogen production is limited in the literature, there have been many attempts to model the MCR, as summarized below.

Simulations have been reported with countercurrent configuration. Plate heat exchangers often operate in this mode to provide optimal heat transfer (Kolios et al., 2002). Frauhammer et al. (1999) proposed such a configuration in a 1-D model. Simulations predicted large hot spots ($>1200^\circ\text{C}$) near the entrance of the

combustion channel. To limit the formation of hot spots, Kolios et al. (2002) proposed a folded plate reactor concept to distribute the combustion fuel along the reactor length. Zafir and Gavriilidis (2004) compared co-current and countercurrent configurations. They showed that countercurrent operation led to temperature variations, both in the transverse and axial directions ($>300^{\circ}\text{C}$ in each case). On the other hand, co-current operation reduced temperature variations in both the transverse ($<25^{\circ}\text{C}$) and axial directions ($<125^{\circ}\text{C}$). Due to those large temperature variations, Kolios et al. (2004) suggested that countercurrent operation was probably impractical “for coupling high-temperature steam reforming with in situ heat generation”. However, they suggested that pre-heating of the feed and cooling of the products could still be accomplished with countercurrent flows.

Using first order exothermic and endothermic reactions, Zafir and Gavriilidis (2002) performed 2-D simulations in a co-current configuration. They showed that the inlet temperature, activation energy and pre-exponential factor strongly affected the endothermic conversion. Based on the same concept, Zafir and Gavriilidis (2003) simulated SMR and Methane Catalytic Combustion (MCC) reactions. Their results suggested an effectiveness factor of the coated reforming catalyst one order of magnitude higher than for conventional catalyst pellets. However, axial temperature variations remained large ($>200^{\circ}\text{C}$). Baratti et al. (2003) mentioned that it would be possible to minimize temperature gradients by adjusting the catalyst thickness along the reactor.

Kolios et al. (2002) pointed out the importance of optimizing the heat fluxes between the channels. Shigarov et al. (2009) made similar comments, suggesting that increasing catalyst activity (or loading) was not always the best solution. Strong combustion activity could lead to hot spot formation, whereas strong reforming activity could lead to the reformer extinction.

Encouraged by the growing power of Computational Fluid Dynamics (CFD), 2-D and 3-D modeling of MCR has been reported. Yuan et al. (2007) simulated a 3-D reforming channel with a porous catalyst layer, receiving heat from a combustion channel, assumed to be at constant heat flux. Zhai et al. (2010) conducted a 2-D CFD simulation of SMR with MCR. Only three computational domains were solved and the catalytic reactions were taken as surface reactions. One interesting observation was that reducing channel height could improve conversion, but only

to a certain limit, below which there was no further benefit.

Vaccaro et al. (2010) used the Comsol MultiphysicsTM platform to solve 2-D and 3-D models for one SMR channel coupled with one MCC channel. The two channels included catalyst and gas phase computational domains. The 3-D model results did not differ significantly from their 2-D model; co-current flow predicted higher conversion than countercurrent flow; and catalyst layer thicknesses $>50 \mu\text{m}$ did not enhance reactor performance significantly. Karakaya and Avci (2011) used the same platform and also suggested that their 2-D model was an appropriate approximation of a 3-D model. They modeled hydrogen production by steam reforming of iso-octane, coupled with MCC in a MCR. They found that increasing the wall thickness, which improved the heat distribution along the reactor length, helped obtaining better hydrogen yield.

Based on co-current and cross-flow configurations, Arzamendi et al. (2009) modeled 4 to 20 channels coupling SMR and MCC. The catalyst layer seemed to be taken as a catalytic surface reaction in the gas phase, ignoring the reduction of catalyst effectiveness due to diffusion into the catalyst layer. Computational time was nevertheless costly, with one simulation requiring from 24 to 72 h.

CFD simulations can be particularly useful to study issues related to the inlet flow distribution in MCR. Laminar flow can lead to uneven feed distribution among the channels. A review by Rebrov et al. (2011) was written on the topic.

At the early stage of our proof-of-concept development, our preoccupations were not the flow distribution or dynamic response of such system yet, but rather the feasibility of coupling Pd membranes with both SMR and MCC channels for realistic operating and design parameters. To drive the hydrogen through the membrane, the reforming channel must operate at higher pressure (e.g. 10-15 bar) than assumed in most of the simulations cited above. Temperature is also a challenge. All of these simulations operated above 800°C to favour high methane thermodynamic conversion and faster kinetics. However, with Pd membranes, depending on the suppliers/makers, maximum operating temperature ranges from 575°C (Membrane Reactor Technologies (MRT)) to 650°C (Patil et al., 2007). To limit hot spots, we chose a co-current configuration. This work sought to find whether the temperature and pressure challenges can, at least in theory, be overcome, with a high level of methane conversion and hydrogen output. Furthermore, in order to

design an experimental reactor, estimates are needed of the key design parameters (such as catalyst layer thickness, reactor length, channel height), which can only come from a suitable model.

This chapter adopts the steady-state, non-isothermal, 2-D, and co-current model developed by Zafir and Gavriilidis (2003) as a starting point. The velocity profile is assumed to be that of fully developed laminar flow, and the average velocity is determined by solving the continuity equation. This assumption avoids having to solve momentum balance equations and saves computation time. Our model adds a perm-selective Pd/Ag membrane above the reforming gas channel. It also solves both temperature and concentration profiles in the catalyst layers.

2.2 Concept Description

The concept of a single module of MCMR is illustrated in Figure 2.1. There are two channels, each including a gas phase and a catalyst layer. An impermeable separator wall separates the SMR channel and the MCC channel. The reforming heat of reaction is provided by the heat released by combustion. A Pd/Ag membrane (subscript m), located above the reforming channel, separates the hydrogen and shifts the reaction equilibrium. The flow is co-current to minimize temperature variations. The catalyst is coated for two purposes: first, to enhance the heat transfer, relying on conduction only through the separator wall; second, to minimize the pressure drops, facilitating hydrogen extraction by the membrane.

The model was made flexible, so it could be either in mode “concept” or “prototype”. In the “concept” mode, only half of the combustion channel was solved, since the other half would belong to the next set of coupled combustion and reforming channels.

We opted for a two-point boundary ordinary differential equation solver “*bvp4c*” included in the MATLABTM software, coupled with a backward finite difference discretization method, to solve the model.

2.3 Main Assumptions of 2-D model

Several assumptions were necessary to develop the model. The major ones were as follows:

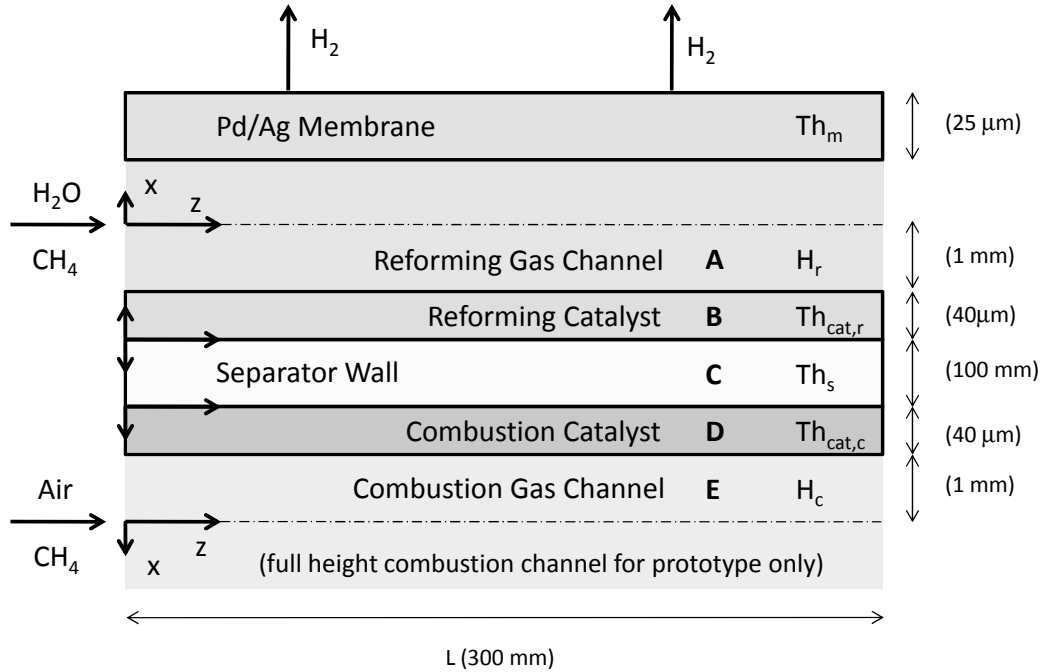


Figure 2.1: Schematic of 2-D Model, including base case dimensions, not to scale. (Subscripts: Pd/Ag membrane m ; SMR channel r ; catalyst layer cat ; separator wall s ; MCC channel c .)

General

- Ideal gas behaviour;
- Pressure drop is negligible;
- Fick's law of diffusion applies;
- Fourier's law of heat conduction applies;
- Viscous dissipation is negligible;
- No change of phase for reactants and products: carbon formation is negligible;
- Heat transfer by radiation is neglected;
- Potential and kinetic energy variations are neglected;
- Spatial derivatives of physical properties are neglected;
- No heat losses to the surroundings (adiabatic).

Gas channels

- No homogeneous reaction;
- Velocity in transverse x direction is neglected;
- Velocity profile in the axial direction z is that of fully-developed laminar flow;
- In the axial direction, molar flux by diffusion and heat transfer by conduction are neglected.

Catalyst layers

- No convection flux in both the transverse and axial directions;
- Conduction in the axial direction is negligible;
- Molar flux by diffusion in the axial direction is negligible.

Separator wall

- Conduction in the axial direction is negligible;
- Thermal conductivity is constant.

Several of those assumptions are verified in Chapter 3, Section 3.5.1.

2.4 Physical Properties

2.4.1 Diffusivity

Since we assumed Fick's law of diffusion, which is normally applied in dilute binary mixtures, we needed to make further assumptions for the diffusion coefficients $D_{i,mix}$ in a gas mixture (subscripts: chemical component i ; gas mixture mix). Two options were considered:

Option A: Zanafir and Gavriilidis (2003) assumed in their model

$$D_{i,mix} = \mathcal{D}_{ij} \tag{2.1}$$

Water (steam) and air became component j for the reforming and combustion channels respectively.

Option B: From Sherwood et al. (1975)

$$D_{i,mix} = \frac{1 - y_i}{\sum_{j,j \neq i} (y_j/D_{ij})} \quad (2.2)$$

To evaluate the binary diffusion coefficient \mathcal{D}_{ij} , we used the Fuller et al., (1969) equation in (Poling et al., 2000):

$$\mathcal{D}_{ij} = \frac{0.00143T^{1.75}}{PM_{ij}^{1/2} \left((\Sigma_v)_i^{1/3} + (\Sigma_v)_j^{1/3} \right)^2} \quad (2.3)$$

where

$$M_{ij} = 2(1/Mw_i + 1/Mw_j)^{-1} \quad (2.4)$$

P is the total pressure, Σ_v is the summation of atomic diffusion volume (see Poling et al. (2000)) and Mw_i is the molecular weight.

In both catalyst layers, the effective diffusivity $D_{i,eff}$ was assumed as a summation of resistances (Davis and Davis, 2003):

$$D_{i,eff} = \frac{\varepsilon}{\tau} \left(\frac{1}{D_{i,mix}} + \frac{1}{D_{i,K}} \right)^{-1} \quad (2.5)$$

With the tortuosity τ estimated (Reyes and Jensen, 1986), as a first approximation, as:

$$\tau = 1/\varepsilon \quad (2.6)$$

The Knudsen diffusivity $D_{i,K}$ is expressed (Bird et al., 2002) as:

$$D_{i,K} = \frac{2R_{pore}}{3} \sqrt{\frac{8R_g T_{cat}}{\pi Mw_i}} \quad (2.7)$$

where R_{pore} is the average pore radius and R_g is the universal gas constant (8.314

J/mol K).

2.4.2 Heat Capacity

The heat capacity relationship for a single component Cp_i as a function of the temperature T , neglecting pressure effect, was determined (Sandler, 1999) as:

$$Cp_i = A_i + B_iT + C_iT^2 + D_iT^3 \quad (2.8)$$

2.4.3 Thermal Conductivity

For the thermal conductivity in the gas channels, we neglected the effect of pressure and used the following relation (Bird et al., 2002) for k_{mix} of a gas mixture:

$$k_{mix} = \sum_i \frac{y_i k_i}{\sum_j y_j \Phi_{ij}} \quad (2.9)$$

where the coefficient Φ_{ij} is:

$$\Phi_{ij} = \frac{1}{\sqrt{8}} \left(1 + \frac{Mw_i}{Mw_j} \right)^{-1/2} \left(1 + \left(\frac{\mu_i}{\mu_j} \right)^{1/2} \left(\frac{Mw_j}{Mw_i} \right)^{1/4} \right)^2 \quad (2.10)$$

We obtained data to evaluate gas component thermal conductivity k_i at a reference temperature of 600 K in Lide (2004). To evaluate k_i 's at the simulation temperatures, we used the following empirical equation, based on the relation utilized by Zanfiri and Gavriilidis (2003):

$$k_i = k_i^{ref} \left(\frac{T}{T^{ref}} \right)^\alpha \quad (2.11)$$

Values of k_i^{ref} and α are provided in Table 2.1. For the separator wall, we assumed the same constant value as Zanfiri and Gavriilidis (2003):

$$k_s = 25 \quad [W/(m K)] \quad (2.12)$$

The catalyst layer is a heterogeneous phase, containing gas and solid phases.

k_{cat} depends on both phases present, and therefore on the density ρ_{cat} of the catalyst coating. For our first set of simulations, we assumed $\rho_{cat} \geq 2000 \text{ kg/m}^3$, similar to the values used by Zanfir and Gavriilidis (2003). However, measurements with our own catalyst coating later showed much lower densities ($\sim 400 \text{ kg/m}^3$). To find the thermal conductivity, Carberry et al. (1987) expressed a relation between void in porous media and the ratio between gas density and skeleton solid density. For our prototype conditions, we evaluated k_{cat} as about twice k_{mix} . Hence k_{cat} was estimated as:

$$k_{cat} = 0.4 \text{ [W/(mK)]} \quad \text{if } \rho_{cat} \geq 2000 \text{ kg/m}^3 \quad (2.13)$$

$$\text{or } k_{cat} = 2k_{mix} \quad \text{if } \rho_{cat} \approx 400 \text{ kg/m}^3 \quad (2.14)$$

2.4.4 Viscosity

Although the momentum equations are not solved in this model, the viscosity, μ of the gas mixture was needed to calculate the coefficient Φ_{ij} in (2.10) and dimensionless numbers such as the Reynolds number.

The viscosity of the mixture was estimated (Bird et al., 2002) from:

$$\mu_{mix} = \sum_i \frac{y_i \mu_i}{\sum_j y_j \Phi_{ij}} \quad (2.15)$$

We used the same method described earlier for k_i to determine component viscosity μ_i at the simulation temperature:

$$\mu_i = \mu_i^{ref} \left(\frac{T}{T^{ref}} \right)^\beta \quad (2.16)$$

Values of μ_i^{ref} and β are listed in Table 2.1.

Table 2.1: Empirical values to determine k and μ in Eqns. (2.11) and (2.16). T^{ref} is taken as 600 K.

	H ₂	CH ₄	H ₂ O	CO	CO ₂	O ₂	N ₂
α	0.7273	1.2878	1.5199	0.8414	1.1877	0.8759	0.7609
$k^{600K} * 10^{-2}$ (W/(m K))	30.9	8.41	4.71	4.57	4.16	4.81	4.40
β	1.451	1.381	0.857	1.515	1.183	1.395	1.449
$\mu^{600K} * 10^{-5}$ (Pa s)	1.44	1.94	2.14	2.91	2.80	3.51	2.96

2.5 Concentration and Partial Pressure

Based on the assumption of ideal gases, we write:

$$c = P/R_g T \quad (2.17)$$

$$P_i = y_i P \quad (2.18)$$

where c is the concentration, P_i the partial pressure of component i , and y_i the component molar fraction.

2.6 Velocity Profiles

Assuming fully developed laminar flow in the gas channel, the velocity profile in the axial direction v_z is assumed to follow the two-dimensional relation (Bird et al., 2002):

$$v_z = \frac{3}{2} v_{ave,z} \left(1 - \left(\frac{x}{H_k} \right)^2 \right) \quad (2.19)$$

Here H_k is half the height of either the reforming or combustion gas channel, represented by subscript k . To determine the average (*ave*) velocity $v_{ave,z}$ in the axial direction, fluxes coming into and out of the box indicated by dashed lines in Figure

Table 2.2: Sievert's Law Parameters

	A_m mol/(s m bar ^{0.5})	E_m J/mol
Chen et al. (2003)	2.00278e-4	15700
MRT's Pd 25wt%-Ag data	3.427e-5	9180

2.2 were integrated:

$$\int_{-H_k}^{H_k \text{ or } 0} cv_z dx|_{z=0} - \int_{-H_k}^{H_k \text{ or } 0} cv_z dx|_z + \int_0^z \int_0^{Th_{cat,k}} \sum_i R_i dx dz + \int_0^z J_{H_2,m} dz = 0 \quad (2.20)$$

Here $Th_{cat,k}$ is the catalyst layer thickness. R_i is the rate of production of component i , defined as:

$$R_i = \sum_j \sigma_{ij} r_j \quad (2.21)$$

The rate of reaction r_j is defined in section 2.7 below. σ_{ij} is the stoichiometric coefficient of component i for reaction j . $J_{H_2,m}$ is the molar flux of hydrogen through the membrane, defined based on Sievert's law:

$$J_{H_2,m} = -\eta_m \frac{A_m}{Th_m} \exp\left(\frac{-E_m}{R_g T_m}\right) \left(\sqrt{P_{H_2,r}} - \sqrt{P_{H_2,m}}\right) \quad (2.22)$$

Here Th_m is the membrane thickness, and η_m , the membrane effectiveness, is a correction factor, the ratio between the real flux and the flux predicted by Sievert's law. This value is normally obtained experimentally (see Chapter 8). We used $\eta_m = 0.5$ in our base case simulations (see Chapter 3). Different values of pre-exponential factor A_m and activation energy E_m for Pd-based membranes have appeared in the literature. This could be due to the variety of metals alloyed with Pd and different modes of fabrication and support. We used two sets of values in our simulations (see Table 2.2). The first set was employed by Chen et al. (2003), while the second set was provided by the supplier of the membranes used in our prototype reactor.

Equations (2.19), (2.21), and (2.22) into (2.20) were employed to solve for $v_{ave,z}$.

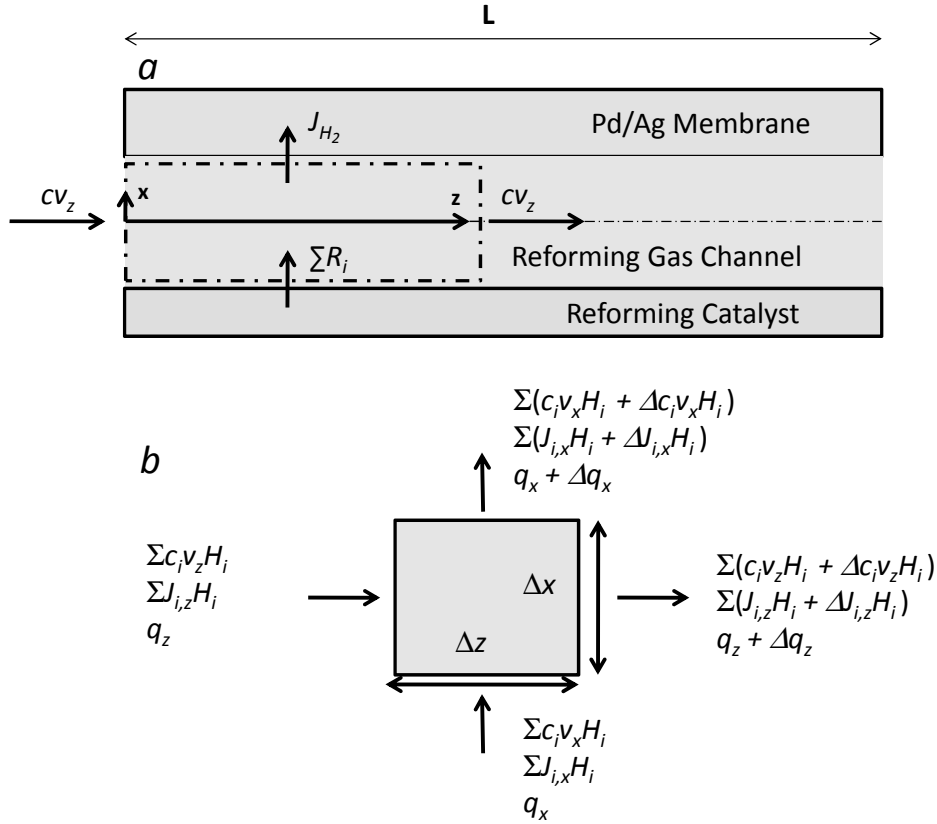


Figure 2.2: Schematics to Evaluate Average Velocity and to Develop Energy Balance: A. Integration box to evaluate average velocity; B. Energy balance over a rectangular cross-section $\Delta z \Delta x$.

2.7 Kinetics

2.7.1 Reforming

The reactions of interest in the reforming channel are:



where $\Delta H_{rx,j}^{298K}$ is the enthalpy of reaction j at 298 K and 1 bar.

Two different reforming catalysts were used in this project based on Ni and Ru. Those two catalysts have different mechanisms, requiring different kinetic expressions.

Nickel-Based Catalyst Kinetics

For a Ni-based catalyst, a study by Elnashaie et al. (1990) showed that the general rate equation based on Langmuir-Hinshelwood-Hougen-Watson approach, developed by Xu and Froment (1989) describes most accurately the kinetics for a wide range of conditions. The reforming catalyst used was Ni 15.2 wt%/ MgAl₂O₄. The rate equations per mass, r'_j , for the three reactions are:

$$r'_1 = \frac{\frac{k_1}{P_{H_2}^{2.5}} \left(P_{CH_4} P_{H_2O} - \frac{P_{H_2}^3 P_{CO}}{K_{e,1}} \right)}{Den^2} \left[\frac{kmol}{kg_{cat} h} \right] \quad (2.26)$$

$$r'_2 = \frac{\frac{k_2}{P_{H_2}} \left(P_{CO} P_{H_2O} - \frac{P_{H_2} P_{CO_2}}{K_{e,2}} \right)}{Den^2} \left[\frac{kmol}{kg_{cat} h} \right] \quad (2.27)$$

$$r'_3 = \frac{\frac{k_3}{P_{H_2}^{3.5}} \left(P_{CH_4} P_{H_2O}^2 - \frac{P_{H_2}^4 P_{CO_2}}{K_{e,3}} \right)}{Den^2} \left[\frac{kmol}{kg_{cat} h} \right] \quad (2.28)$$

where

$$Den = 1 + K_{CO} P_{CO} + K_{H_2} P_{H_2} + K_{CH_4} P_{CH_4} + K_{H_2O} P_{H_2O} / P_{H_2} \quad (2.29)$$

$$K_{e,1} = \exp \left(\frac{-26830}{T} + 30.114 \right) [bar^2] \quad (2.30)$$

$$K_{e,2} = \exp \left(\frac{4400}{T} - 4.036 \right) [-] \quad (2.31)$$

$$K_{e,3} = \exp \left(\frac{-22430}{T} + 26.078 \right) [bar^2] \quad (2.32)$$

The sorption equilibrium constant K_i and kinetic rate coefficient k_j are ex-

Table 2.3: Constants in Xu and Froment (1989) Kinetics

	A_j	Units	E_j (kJ/mol)
k_1	4.22e15	bar ^{0.5} kmol / kg _{cat} h	240.1
k_2	1.955e6	kmol / kg _{cat} h bar	67.13
k_3	1.020e15	bar ^{0.5} kmol / kg _{cat} h	243.9
	A_i	Units	$\Delta H_{sorp,i}$ (kJ/mol)
K_{CO}	8.23e-5	bar ⁻¹	-70.95
K_{CH_4}	6.65e-4	bar ⁻¹	-38.28
K_{H_2O}	1.77e5	-	88.68
K_{H_2}	6.12e-9	bar ⁻¹	-82.9

pressed as:

$$K_i = A_i \exp\left(\frac{-\Delta H_{sorp,i} * 1000}{R_g T}\right) \quad (2.33)$$

$$k_j = A_j \exp\left(\frac{-E_j * 1000}{R_g T}\right) \quad (2.34)$$

To obtain the rates of reaction per reactor volume, r_j , we need to perform the transformation:

$$r_j = r_j' \rho_{cat} k \frac{1000}{3600} \left[\frac{mol}{m_{cat}^3 s} \right] \quad (2.35)$$

Values of A_i , A_j , ΔH_{sorp} , and E_j are provided in Table 2.3. The pre-exponential factors A_j are dependent on the loading, dispersion and stability of the catalyst. They should ideally be measured experimentally. However, as shown in Chapter 6, Ni-based catalyst was not used in our prototype, but only for the first computer simulations. Therefore, we kept the same A_j 's as reported by Xu and Froment (1989).

Ruthenium-Based Catalyst

Jakobsen et al. (2010) proposed a kinetic model for a Ru 1%/ ZrO₂ catalyst. Their model is based on methane dissociative adsorption as the rate-limiting step, with

Table 2.4: Constants in Jakobsen et al. (2010) Kinetics

	A_j	Units	E_j (kJ/mol)
k_1	4.39e7	kmol/(kg _{cat} h bar)	108
k_2	400	kmol/(kg _{cat} h bar)	0
	A_i	Units	$\Delta H_{sorp,i}$ (kJ/mol)
K_{CO}	2.19e-5	1/bar	87
K_{H_2}	7.31e-6	1/bar ^{0.5}	71

CO and H₂ competing for active sites. These authors studied conditions with temperatures ranging from 425 to 575°C at 1.3 bar.

$$r'_1 = \frac{k_1 P_{CH_4} (1 - \beta_1)}{\left(1 + K_{CO} P_{CO} + K_{H_2} P_{H_2}^{1/2}\right)^2} \left[\frac{kmol}{kg_{cat} h} \right] \quad (2.36)$$

where

$$\beta_1 = \frac{P_{CO} P_{H_2}^3}{P_{CH_4} P_{H_2O}} \frac{1}{K_{e,1}} \quad (2.37)$$

Jakobsen et al. (2010) did not provide a specific expression for the water gas shift reaction, instead assuming that this reaction was fast enough to reach equilibrium at all conditions. Therefore, $r'_2 = f(r'_1)$.

We tested these assumptions in our model by assuming a large value for the rate coefficient k_2 of the water gas shift reaction (see Table 2.4).

$$r'_2 = \frac{k_2 P_{CO} (1 - \beta_2)}{\left(1 + K_{CO} P_{CO} + K_{H_2} P_{H_2}^{1/2}\right)^2} \left[\frac{kmol}{kg_{cat} h} \right] \quad (2.38)$$

where

$$\beta_2 = \frac{P_{CO_2} P_{H_2}}{P_{CO} P_{H_2O}} \frac{1}{K_{e,2}} \quad (2.39)$$

Wei and Iglesia (2004) studied the forward methane steam reforming reaction using 1.6% and 3.2% Ru on γ -Al₂O₃ and ZrO₂ supports. They performed their rate measurements between 550 and 750°C, with pressure ranging from 1 to 5 bar.

Table 2.5: Constants in Wei and Iglesia (2004) Kinetics

	A_j (kmol/(kg _{cat} h bar))	E_j (kJ/mol)
k_1	1.22e7	91
k_2	400	0

They proposed a simple rate expression:

$$r'_1 = k_1 P_{\text{CH}_4} (1 - \beta_1) \left[\frac{\text{kmol}}{\text{kg}_{\text{cat}} \text{h}} \right] \quad (2.40)$$

Wei and Iglesia concluded that C-H bond activation was the rate-limiting step, unaffected by the identity or concentration of other co-reactants or products. They did not find any dependence of the reaction rate on H₂O, and they did not study the WGS reaction. For this reason, we used the same technique as for the Jakobsen kinetics, to assure that the WGS reaction approaches very closely the chemical equilibrium, assuming a large value for the rate coefficient k_2 (see Table 2.5):

$$r'_2 = k_2 P_{\text{CO}} (1 - \beta_2) \left[\frac{\text{kmol}}{\text{kg}_{\text{cat}} \text{h}} \right] \quad (2.41)$$

Wei and Iglesia (2004) reported the pre-exponential factor A_1 for a 3.2% Ru/ γ -Al₂O₃ catalyst at 600°C, 0.25 bar CH₄, 0.25 bar H₂O, and 44.2% metal dispersion. We adjusted the units to fit our model (as shown in Table 2.5).

Berman et al. (2005) also proposed a kinetic models for a 2% Ru/ (α -Al₂O₃+ 4.8% MnO_x) catalyst. Temperatures ranged from 500 to 900°C and pressures from 1 to 7 bar. They found a negative order with respect to steam, contrary to the two previous models (Wei and Iglesia, 2004; Jakobsen et al., 2010). Their results suggested that surface hydroxyl group oxidation and carbon surface oxidation could be the rate-limiting steps. Berman et al. did not consider reaction equilibria in their equations, so we slightly modified their model for our needs. They also observed that practically all of the CO was converted to CO₂, indicating a very fast water

gas-shift reaction.

$$r_3' = \frac{k_3 P_{\text{CH}_4} (1 - \beta_3)}{\left(b_{\text{CH}_4} P_{\text{CH}_4} + b_{\text{H}_2\text{O}} P_{\text{H}_2\text{O}}^{1/2} \right)} \left[\frac{\text{kmol}}{\text{kg}_{\text{cat}} \text{ h}} \right] \quad (2.42)$$

$$r_2' = \frac{k_2 P_{\text{CO}} (1 - \beta_2)}{\left(b_{\text{CH}_4} P_{\text{CH}_4} + b_{\text{H}_2\text{O}} P_{\text{H}_2\text{O}}^{1/2} \right)} \left[\frac{\text{kmol}}{\text{kg}_{\text{cat}} \text{ h}} \right] \quad (2.43)$$

where

$$\beta_3 = \frac{P_{\text{CO}_2} P_{\text{H}_2}^4}{P_{\text{CH}_4} P_{\text{H}_2\text{O}} K_{e,3}} \quad (2.44)$$

$$b_{\text{CH}_4} = 4.42 * 10^{-6} \exp(5694.2/T) \quad (2.45)$$

$$b_{\text{H}_2\text{O}} = 8.366 * 10^{-6} \exp(4531.7/T) \quad (2.46)$$

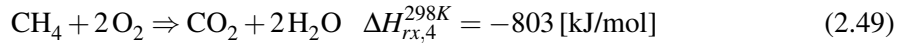
$$k_3 = 2.68 \quad [\text{kmol}/(\text{kg}_{\text{cat}} \text{ h bar})] \quad (2.47)$$

$$k_2 = 400 \quad [\text{kmol}/(\text{kg}_{\text{cat}} \text{ h bar})] \quad (2.48)$$

2.7.2 Combustion

For the combustion catalyst, we assume that only full oxidation of methane is occurring. This assumption is usually valid with a stoichiometric excess of air. However, as reported in Chapter 7, small amounts of CO were detected experimentally. Nevertheless, for simplicity, we ignored CO formation in our model.

Methane Combustion:



Pd is often considered to be the most efficient catalyst for catalytic combustion of methane (Lee and Trimm, 1995). Pd was chosen throughout this project, with

an empirical kinetic model to describe the reaction:

$$r_4 = k_4 P_{\text{CH}_4}^\alpha P_{\text{O}_2}^\beta \left[\frac{\text{mol}}{m_{\text{cat}}^3 \text{ s}} \right] \quad (2.50)$$

where

$$k_4 = A_4 \exp\left(\frac{-E_4 * 1000}{R_g T}\right) (\rho_{\text{cat } c} * 1000) \left[\frac{\text{mol}}{m_{\text{cat}}^3 \text{ s bar}^{\alpha+\beta}} \right] \quad (2.51)$$

Lee and Trimm (1995) reviewed studies of methane catalytic combustion with Pd, Pt and Rh. The reaction order α for methane ranged from 0.45 to 1.2. β varied more, from -0.5 to 1.0. Activation energies E_4 also varied widely from 52 to 199 kJ/mol.

We performed simulations with different sets of values, as summarized in Table 2.6. For the simulations in Chapter 3, we assumed values adopted by Zanfir and Gavriilidis (2003) for the kinetic combustion parameters ($\alpha = 1$, $E_4 = 90$ kJ/mol, A_4 is adapted for our work in order to respect the units chosen in Eq. (2.51)). With excess air, Zanfir and Gavriilidis (2003) assumed that the kinetics of methane combustion are independent of oxygen concentration. However, with $\beta = 0$, we found in preliminary work that it was difficult for simulations to converge for excess $\text{O}_2 < 25\%$ and with thick catalyst layers $> 100\mu\text{m}$. In those cases, simulations generated negative O_2 concentrations, with O_2 being a larger molecule than CH_4 , not diffusing as quickly as needed in the catalyst pores. Therefore, we assumed $\beta = 1$.

We later estimated the kinetic parameters, as reported in Chapter 7, in order to compare model predictions with MCMR experimental results of Chapter 8. To stay below the lower flammability limit of methane, we employed large excess of air $> 200\%$, and we neglected the effect of oxygen. Therefore, we assumed $\beta = 0$.

2.8 Component Material Balance Equations

The general equation of continuity at steady state for a component i in a mixture (adapted from Bird et al. (2002)) is:

$$-(\nabla \cdot c_i \vec{v}) - (\nabla \cdot \vec{J}_i) + R_i = 0 \quad (2.52)$$

Table 2.6: Combustion Kinetic Parameters

A_4 (kmol/(kg _{cat} s bar ^{α+β}))	α	β	E_4 (kJ/mol)	Reference
5539	1	1	90	Modification of Zanfir and Gavriilidis (2003)
1635	0.78	0	88	This work on Pd 1%/ γ -Al ₂ O ₃ (Alfa) (See Chapter 7)
4710	0.78	0	88	This work on Pd 5%/ γ -Al ₂ O ₃ (Alfa or Lab-made) (See Chapter 7)

This equation contains three terms: a convection flux vector $c\vec{v}_i$, a diffusion flux vector \vec{J}_i , and the rate of production R_i .

Assuming Fick's law of diffusion for \vec{J}_i , we obtain:

$$\vec{J}_i = -D_{i\text{mix}}\nabla c_i \quad (2.53)$$

Inserting (2.53) and expanding gradient terms while neglecting velocity component in the transverse direction, and neglecting diffusion in the axial direction, Eq. (2.52) becomes:

$$-\left(v_z \frac{\partial c_i}{\partial z} + c_i \frac{\partial v_z}{\partial z}\right) + \left(D_{i\text{mix}} \left(\frac{\partial^2 c_i}{\partial x^2}\right) + \frac{\partial D_{i\text{mix}}}{\partial x} \frac{\partial c_i}{\partial x}\right) + R_i = 0 \quad (2.54)$$

To use MATLABTM built-in functions, it was necessary to reduce the order of the differential equations to one for both concentration and temperature. To overcome this limitation, we used first order transformations in the transverse direction:

$$c_i = c_{1i} \quad (2.55)$$

$$\frac{\partial c_{1i}}{\partial x} = c_{2i} \quad (2.56)$$

$$T = T_1 \quad (2.57)$$

$$\frac{\partial T_1}{\partial x} = T_2 \quad (2.58)$$

From this point in our model development, c_i is now referred as c_{1i} , and T be-

comes T_1 . We introduced two new variables in equations (2.56) and (2.58): c_{2i} corresponding to concentration gradient of component i ; and T_2 is the temperature gradient.

We use backward difference discretization in the axial direction for any dependent parameter u :

$$\frac{\partial u_b}{\partial z} = \frac{1}{\Delta z_{b-1}} (u_b - u_{b-1}) \quad (2.59)$$

Subscript b represents the discretization grid position in the axial direction (see Figure 2.3). With discretization in the axial direction and first order transformation, Eq. (2.54) becomes:

$$\begin{aligned} & - \left(v_{z,b} \frac{1}{\Delta z_{b-1}} (c_{1i,b} - c_{1i,b-1}) + c_{1i,b} \frac{1}{\Delta z_{b-1}} (v_{z,b} - v_{z,b-1}) \right) \\ & + \left(D_{mix,b} \frac{dc_{2i}}{dx} + \frac{dD_{mix,b}}{dx} c_{2i} \right) + R_{i,b} = 0 \end{aligned} \quad (2.60)$$

Solving for $dc_{2i,b}/dx$, Eq. (2.60) becomes:

$$\begin{aligned} \frac{dc_{2i,b}}{dx} = \frac{1}{D_{mix,b}} \left\{ \left(v_{z,b} \frac{1}{\Delta z_{b-1}} (c_{1i,b} - c_{1i,b-1}) + c_{1i,b} \frac{1}{\Delta z_{b-1}} (v_{z,b} - v_{z,b-1}) \right) \right. \\ \left. - \frac{dD_{mix,b}}{dx} c_{2i,b} - R_{i,b} \right\} \end{aligned} \quad (2.61)$$

2.8.1 Gas Phase

Using equations (2.56) and (2.61), while ignoring the derivative of $D_{mix,b}$ and assuming no reaction in the gas phase, we obtain:

$$\frac{dc_{1i,b}}{dx} = c_{2i,b} \quad (2.62)$$

$$\frac{dc_{2i,b}}{dx} = \frac{1}{D_{mix,b}} \left(v_{z,b} \frac{1}{\Delta z_{b-1}} (c_{1i,b} - c_{1i,b-1}) + c_{1i,b} \frac{1}{\Delta z_{b-1}} (v_{z,b} - v_{z,b-1}) \right) \quad (2.63)$$

$$\forall i, b \neq 1$$

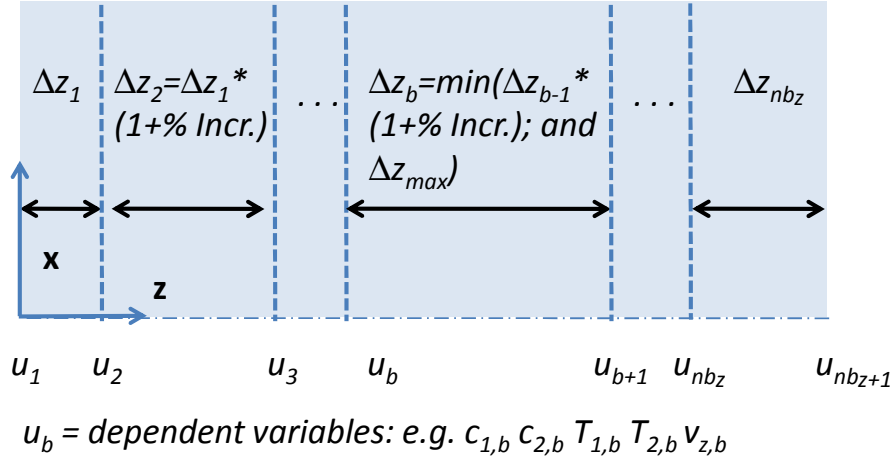


Figure 2.3: Schematic of Discretization

Boundary Conditions

Gas channel - inlet conditions ($z = 0$ and $b = 1$) At the entrance of the reactor, the concentrations c_{1i} are assumed to be constants at the feed conditions:

$$c_{1i,b=1} = c_{1i,o} \quad (2.64)$$

$$c_{2i,b=1} = 0 \quad (2.65)$$

where subscript o denotes feed conditions.

Gas channel - catalyst interface ($x = -H_k$) Performing a material balance across the interface, using Fick's law, and assuming that there are no velocities on either side of the interface, hence only diffusion fluxes, we obtain:

$$J_{i,x}|_{x=-H_k} = J_{i,x}|_{x=Th_{cat,k}} \quad (2.66)$$

$$-D_{imix} \frac{\partial c_i}{\partial x}|_{x=-H_k} = -D_{i,eff} \frac{\partial c_i}{\partial x}|_{x=Th_{cat,k}} \quad (2.67)$$

Using first order transformation and solving for $c_{2i,k,b}$, we obtain:

$$c_{2i,k,b}|_{x=-H_k} = \frac{D_{i,eff,b} c_{2i,cat,k,b}|_{x=Th_{cat,k}}}{D_{i,mix,k,b}|_{x=-H_k}} \quad (2.68)$$

$$\forall i, b \neq 1$$

Reforming gas channel - membrane interface ($x = H_r$) $\forall i$, except for H_2 , there is no flux, hence no gradient:

$$c_{2i,r,b}|_{x=H_r} = 0 \quad \forall i, b \quad (2.69)$$

For H_2 only, performing a material balance across the membrane interface, using Fick's law, discretization, first order transformation, and assuming there are no velocities on either side of the interface, we obtain:

$$J_{H_2,x}|_{x=H_r} = J_{H_2,x}|_m \quad (2.70)$$

$$-D_{H_2,mix,b} c_{2H_2,r,b}|_{x=H} = J_{H_2,x}|_m \quad (2.71)$$

Solving for $c_{2H_2,r,b}$, and inserting Sievert's law (Eq. (2.22)), we obtain:

$$c_{2H_2,r,b}|_{x=H} = \frac{1}{D_{H_2,mix,b}} \eta_m \frac{A_m}{Th_m} \exp\left(\frac{-E_m}{R_g T_{m,b}}\right) \left(\sqrt{c_{1H_2,r,b} R_g T_{1r,b}} - \sqrt{P_{H_2,m}}\right) |_{x=H_r} \quad (2.72)$$

Combustion gas channel - concept mode: half-channel ($x = 0$) We assume symmetry and hence no gradient in the transverse direction:

$$c_{2i,c,b}|_{x=0} = 0 \quad \forall i, b \quad (2.73)$$

Combustion gas channel - prototype mode: flange side ($x = H_c$) Since there is no flux, and hence no gradient, we obtain a similar boundary condition:

$$c_{2i,c,b}|_{x=H_c} = 0 \quad \forall i, b \quad (2.74)$$

2.8.2 Catalyst Layer

Using equations (2.56) and (2.61), while ignoring the derivative of $D_{imix,b}$, assuming no axial and transverse velocity occurring in the catalyst layer, and neglecting diffusion in the axial direction, we obtain this simple system of equations:

$$\frac{dc_{1i,cat k,b}}{dx} = c_{2i,cat k,b} \quad (2.75)$$

$$\frac{dc_{2i,cat k,b}}{dx} = \frac{1}{D_{i,eff,b}} (-R_{i,b}) \quad (2.76)$$

$$\forall i, b \neq 1$$

Boundary Conditions

Catalyst layer - inlet conditions ($z = 0$ and $b = 1$) At the entrance of the reactor, we assume no gradient in the catalyst layer in the axial direction, therefore:

$$c_{1i,cat k,b=1} = c_{1i,cat k,b=2} \quad (2.77)$$

Catalyst - gas channel interface ($x = Th_{cat,k}$) By continuity:

$$c_{1i,k,b}|_{x=-H_k} = c_{1i,cat k}|_{x=Th_{cat,k}} \quad b \neq 1 \quad (2.78)$$

Catalyst - separator wall separator interface ($x = 0$) There is no flux:

$$c_{2i,cat k,b}|_{x=0} = 0 \quad b \neq 1 \quad (2.79)$$

2.9 Energy Balances

The energy strategy for the one-dimensional problem used by Elnashaie and Garhyan (2003) was adapted for our 2-D simulation. Neglecting pressure drop, kinetic energy, viscous dissipation, and radiation heat transfer, an energy balance was performed on a small element $\Delta x \Delta z$ at steady state (see Figure 2.2 B):

$$\begin{aligned} & \sum_i c_i v_z H_i \Delta x + \sum_i J_{i,z} H_i \Delta x + q_z \Delta x + \sum_i c_i v_x H_i \Delta z + \sum_i J_{i,x} H_i \Delta z + q_x \Delta z = \\ & \sum_i (c_i v_z H_i + \Delta(c_i v_z H_i)) \Delta x + \sum_i (J_{i,z} H_i + \Delta(J_{i,z} H_i)) \Delta x + (q_z + \Delta q_z) \Delta x + \\ & \sum_i (c_i v_x H_i + \Delta(c_i v_x H_i)) \Delta z + \sum_i (J_{i,x} H_i + \Delta(J_{i,x} H_i)) \Delta z + (q_x + \Delta q_x) \Delta z \end{aligned} \quad (2.80)$$

Simplifying and dividing by $\Delta x \Delta z$ leads to:

$$\frac{\sum_i \Delta(c_i v_z H_i)}{\Delta z} + \frac{\sum_i \Delta(J_{i,z} H_i)}{\Delta z} + \frac{\sum_i \Delta(c_i v_x H_i)}{\Delta x} + \frac{\sum_i \Delta(J_{i,x} H_i)}{\Delta x} + \frac{\Delta q_x}{\Delta z} + \frac{\Delta q_z}{\Delta x} = 0 \quad (2.81)$$

Taking the limits when $\Delta x, \Delta z \rightarrow 0$, we obtain:

$$\begin{aligned} & \sum_i \frac{\partial(c_i v_z H_i)}{\partial z} + \sum_i \frac{\partial(J_{i,x} H_i)}{\partial z} + \sum_i \frac{\partial(c_i v_x H_i)}{\partial x} + \sum_i \frac{\partial(J_{i,z} H_i)}{\partial x} \\ & + \frac{\partial q_x}{\partial z} + \frac{\partial q_z}{\partial x} = 0 \end{aligned} \quad (2.82)$$

Expanding terms and rearranging leads to:

$$\begin{aligned} & \sum_i \left(c_i v_z \frac{\partial H_i}{\partial z} + H_i \frac{\partial c_i v_z}{\partial z} + J_{i,x} \frac{\partial H_i}{\partial z} + H_i \frac{\partial J_{i,x}}{\partial z} + c_i v_x \frac{\partial H_i}{\partial x} + H_i \frac{\partial c_i v_x}{\partial x} + J_{i,z} \frac{\partial H_i}{\partial x} + H_i \frac{\partial J_{i,z}}{\partial x} \right) \\ & + \frac{\partial q_x}{\partial z} + \frac{\partial q_z}{\partial x} = 0 \end{aligned} \quad (2.83)$$

From the component material balance Eq. (2.52):

$$(\nabla \bullet c_i \vec{v}) = -(\nabla \bullet \vec{J}_i) + R_i \quad (2.84)$$

Expanding the two gradients and multiplying both sides of Eq. (2.84) by H_i gives:

$$H_i \frac{\partial c_i v_z}{\partial z} + H_i \frac{\partial c_i v_x}{\partial x} = -H_i \frac{\partial J_{i,x}}{\partial z} - H_i \frac{\partial J_{i,z}}{\partial x} + H_i R_i \quad (2.85)$$

Inserting Eq. (2.85) into (2.83) and simplifying leads to:

$$\sum_i \left(c_i v_z \frac{\partial H_i}{\partial z} + J_{i,x} \frac{\partial H_i}{\partial z} + c_i v_x \frac{\partial H_i}{\partial x} + J_{i,z} \frac{\partial H_i}{\partial x} + H_i R_i \right) + \frac{\partial q_x}{\partial z} + \frac{\partial q_z}{\partial x} = 0 \quad (2.86)$$

For an ideal gas with no phase change:

$$\frac{\partial H_i}{\partial z} = \frac{\partial H_i}{\partial T} \frac{\partial T}{\partial z} = C p_i \frac{\partial T}{\partial z} \quad (2.87)$$

$$\frac{\partial H_i}{\partial x} = \frac{\partial H_i}{\partial T} \frac{\partial T}{\partial x} = C p_i \frac{\partial T}{\partial x} \quad (2.88)$$

Inserting Equations (2.21), (2.87) and (2.88) into (2.86) leads to:

$$\begin{aligned} & \sum_i \left(C p_i (c_i v_z + J_{i,z}) \frac{\partial T}{\partial z} + C p_i (c_i v_x + J_{i,x}) \frac{\partial T}{\partial x} \right) \\ & + \sum_i \sum_j H_i \sigma_{ij} r_j + \frac{\partial q_x}{\partial z} + \frac{\partial q_z}{\partial x} = 0 \end{aligned} \quad (2.89)$$

By definition:

$$\sum_i H_i \sigma_{ij} = \Delta H_{rx,j} \quad (2.90)$$

where:

$$\Delta H_{rx,j} = \Delta H_{rx,j}^{ref} + \int_{T_{ref}}^T \Delta C p_j \partial T \quad (2.91)$$

$$\Delta C p_j = \sum_i \sigma_{ij} C p_i \quad (2.92)$$

Inserting Eq. (2.90) into Eq. (2.89) gives:

$$\sum_i \left(C p_i (c_i v_z + J_{i,z}) \frac{\partial T}{\partial z} + C p_i (c_i v_x + J_{i,x}) \frac{\partial T}{\partial x} \right) + \sum_j \Delta H_{rx,j} r_j + \frac{\partial q_x}{\partial z} + \frac{\partial q_z}{\partial x} = 0 \quad (2.93)$$

In a more general form, Eq. (2.93) becomes:

$$\nabla T \bullet \sum_i (C p_i c_i \vec{v}) + \nabla T \bullet \sum_i (C p_i \vec{J}_i) + \nabla \bullet \vec{q} + \sum_j \Delta H_{rx,j} r_j = 0 \quad (2.94)$$

There are four heat transfer/generation terms in Eq. (2.94), representing in order: (1) transfer by convection, (2) transfer by diffusion, (3) transfer by conduction, and (4) heat generation due to reactions.

Assuming Fourier's law of conduction, we write \vec{q} as:

$$\vec{q} = -k_{mix} \nabla T \quad (2.95)$$

Expanding the gradient terms, inserting Fick's law, Eq. (2.53) and Fourier's law, Eq. (2.95), and with the same assumptions as for the material balance, i.e. neglecting the velocity component in the transverse direction, and neglecting diffusion in the axial direction, we obtain:

$$\begin{aligned} & \frac{\partial T}{\partial z} \sum_i (C p_i c_i v_z) - \frac{\partial T}{\partial x} \sum_i \left(C p_i D_{i,mix} \frac{\partial c_i}{\partial x} \right) + \left(-\frac{\partial}{\partial x} \left(k_{mix} \frac{\partial T}{\partial x} \right) - \frac{\partial}{\partial z} \left(k_{mix} \frac{\partial T}{\partial z} \right) \right) \\ & + \sum_j \Delta H_{rx,j} r_j = 0 \end{aligned} \quad (2.96)$$

With backward difference discretization in the axial direction and first order transformation, Eq. (2.96) becomes:

$$\begin{aligned} & \frac{1}{\Delta z_{b-1}} (T_{1,b} - T_{1,b-1}) \sum_i (C p_{i,b} c_{1i,b} v_{z,b}) - T_{2,b} \sum_i (C p_{i,b} D_{i,mix,b} c_{2i,b}) \\ & - \left(\frac{dk_{mix,b}}{dx} T_{2,b} + k_{mix,b} \frac{dT_{2,b}}{dx} + \frac{dk_{mix,b}}{dz} \frac{1}{\Delta z_{b-1}} (T_{1,b} - T_{1,b-1}) + k_{mix,b} \frac{1}{\Delta z_{b-1}^2} (T_{1,b} - 2T_{1,b-1} + T_{1,b-2}) \right) \\ & + \sum_j \Delta H_{rx,j} r_j = 0 \end{aligned} \quad (2.97)$$

If Eq. (2.97) is recast to solve for $dT_{2,b}/dx$, then:

$$\begin{aligned} \frac{dT_{2,b}}{dx} = \frac{1}{k_{mix,b}} \left\{ \frac{1}{\Delta z_{b-1}} (T_{1,b} - T_{1,b-1}) \sum_i (Cp_{i,b} c_{1i,b} v_{z,b}) - T_{2,b} \sum_i (Cp_{i,b} D_{imix,b} c_{2i,b}) \right. \\ \left. - \frac{dk_{mix,b}}{dx} T_{2,b} - \frac{dk_{mix,b}}{dz} \frac{1}{\Delta z_{b-1}} (T_{1,b} - T_{1,b-1}) - k_{mix,b} \frac{1}{\Delta z_{b-1}^2} (T_{1,b} - 2T_{1,b-1} + T_{1,b-2}) \right. \\ \left. + \sum_j \Delta H_{rx,j} r_j \right\} \end{aligned} \quad (2.98)$$

2.9.1 Gas Phase

Using equations (2.58) and (2.98), while ignoring the derivative of $k_{mix,b}$, ignoring the heat transfer by conduction in the axial direction, and assuming no reaction in the gas phase, we obtain:

$$\frac{dT_{1,b}}{dx} = T_{2,b} \quad (2.99)$$

$$\frac{dT_{2,b}}{dx} = \frac{1}{k_{mix,b}} \left\{ \frac{1}{\Delta z_{b-1}} (T_{1,b} - T_{1,b-1}) \sum_i (Cp_{i,b} c_{1i,b} v_{z,b}) - T_{2,b} \sum_i (Cp_{i,b} D_{imix,b} c_{2i,b}) \right\} \quad (2.100)$$

$$\forall i, b \neq 1$$

Boundary Conditions

Gas channel - inlet conditions ($z = 0$ and $b = 1$) At the entrance of the reactor, the temperature T_1 is assumed constant at the feed condition:

$$T_{1,b=1} = T_{1,o} \quad (2.101)$$

$$T_{2,b=1} = 0 \quad (2.102)$$

Gas channel - catalyst interface ($x = -H_k$) Performing an energy balance across the interface, using Fick's and Fourier's laws, and assuming velocity = 0 on either

side of the interface, we obtain:

$$\left(\sum_i J_{i,x,k} H_{i,k} - k_{mix,k} T_{2,k} \right) \Big|_{x=-H_k} = \left(\sum_i J_{i,x,cat} H_{i,cat} - k_{cat} T_{2,cat} \right) \Big|_{x=Th_{cat,k}} \quad (2.103)$$

To respect continuity, the temperatures and diffusion fluxes at this boundary must be equal, and only the temperature gradients change. Since H_i is only a function of T for an ideal gas, we can write:

$$\sum_i J_{i,x,k} H_{i,k} \Big|_{x=-H_k} = \sum_i J_{i,x,cat} H_{i,cat} \Big|_{x=Th_{cat,k}} \quad (2.104)$$

Inserting (2.104) in (2.103), using discretization and solving for $T_{2,k,b}$, we obtain:

$$T_{2,k,b} \Big|_{x=-H_k} = \frac{k_{cat} T_{2,cat}}{k_{mix,b}} \quad b \neq 1 \quad (2.105)$$

Gas channel - membrane interface ($x = H_k$) If heat losses are known:

$$\left(J_{H_2,x,r} H_{H_2,r} - k_{mix,r} T_{2,r} \right) \Big|_{x=H_r} = \left(J_{H_2,m} H_{H_2,m} - Q_{loss} \right) \Big|_m \quad (2.106)$$

Simplifying and solving for $T_{2,r}$ gives:

$$T_{2,r,b} \Big|_{x=H_r} = \frac{Q_{loss}}{k_{mix,r} \Big|_{x=H_r}} \quad b \neq 1 \quad (2.107)$$

If heat losses are negligible, then:

$$T_{2,r,b} \Big|_{x=H_r} = 0 \quad b \neq 1 \quad (2.108)$$

Gas channel - half-channel ($x = 0$) We assumed symmetry at the boundary, so that:

$$T_{2,k,b}|_{x=0} = 0 \quad b \neq 1 \quad (2.109)$$

2.9.2 Catalyst Layer

Using equations (2.58) and (2.98), while ignoring the derivative of $k_{mix,b}$, and assuming no axial or transverse velocity in the catalyst layer, we obtain:

$$\frac{dT_{1,cat k,b}}{dx} = T_{2,cat k,b} \quad (2.110)$$

$$\frac{dT_{2,cat k,b}}{dx} = \frac{1}{k_{cat k,b}} \left\{ -T_{2,cat k,b} \sum_i (Cp_{i,cat k,b} D_{i,eff,b} C_{2i,cat k,b}) + \sum_j \Delta H_{rx,j,b} r_{j,b} \right\} \quad (2.111)$$

$$b \neq 1$$

Boundary Conditions

Catalyst layer - inlet conditions ($z = 0$ and $b = 1$) At the entrance of the reactor, we assume no gradient in the catalyst layer in the axial direction, so that:

$$T_{1,cat k,b=1} = T_{1,k,b=2} \quad (2.112)$$

Catalyst - gas channel interface ($x = Th_{cat,k}$) There is no discontinuity of temperature at the interface, hence:

$$T_{1,cat k}|_{x=Th_{cat,k}} = T_{1,k,b}|_{x=-H_k} \quad b \neq 1 \quad (2.113)$$

Catalyst - separator wall interface ($x = 0$) There is a flux of energy by conduction. Using the the same development as for with the *Gas channel - catalyst*

interface above, we obtain:

$$T_{2,cat\ k,b}|_{x=0} = \delta_k \frac{k_s T_{2,s,b}}{k_{cat\ k,b}} \quad b \neq 1 \quad (2.114)$$

$$\delta_r = -1 \quad (2.115)$$

$$\delta_c = +1 \quad (2.116)$$

Because of the change in axis orientation (see Figure 2.1), we added the coefficient δ_k .

2.9.3 Separator Wall

Only conduction is occurring in this solid phase. With (2.58) and (2.98), and neglecting derivative of k_s , we obtain:

$$\frac{dT_{1,s,b}}{dx} = T_{2,s,b} \quad (2.117)$$

$$\frac{dT_{2,s,b}}{dx} = \frac{1}{\Delta z_{b-1}^2} (-T_{1,s,b} + 2T_{1,s,b-1} - T_{1,s,b-2}) \quad (2.118)$$

$$b \neq 1$$

Neglecting heat conduction in the axial direction, (2.118) become:

$$\frac{dT_{2,s,b}}{dx} = 0 \quad (2.119)$$

Boundary Conditions

Separator wall - inlet conditions ($z = 0$ and $b = 1$) At the entrance of the reactor, we assume no gradient in the separator wall in the axial direction, therefore:

$$T_{1,s,b=1} = T_{1,s,b=2} \quad (2.120)$$

Reforming catalyst interface ($x = 0$) There is no discontinuity at the interface:

$$T_{1,s,b}|_{x=0} = T_{1,cat r,b}|_{x=0} \quad b \neq 1 \quad (2.121)$$

Combustion catalyst interface ($x = Th_s$) Th_s is the thickness of the separator wall, and again, there is no discontinuity at the interface:

$$T_{1,s,b}|_{x=Th_s} = T_{1,cat c,b}|_{x=0} \quad b \neq 1 \quad (2.122)$$

2.10 Conclusions

This chapter develops the energy balance, mass balance, kinetics and physical property equations necessary to solve a 2-D MCMR model for the gas channels, the heterogeneous catalyst layers and the impermeable separator wall. Fully developed laminar flow was assumed to avoid having to solve momentum balance equations and saves computation time. The resulting set of equations, after discretization, can be solved readily using standard software. In the next chapter, we explore the results for a base case, verify the consistency of the model and several assumptions, perform an isothermal parametric sensitivity study, and explore ways to improve heat transfer between the combustion and reforming channels.

Chapter 3

Steady State 2-D Model Simulations Results

3.1 Introduction

This chapter presents the first set of simulations performed before building the prototype. Many of the base case parameters are taken or adapted from the MCR simulation of Zafir and Gavriilidis (2003), the major difference being the reforming channel, where the pressure is higher to create the necessary driving force for hydrogen to cross the membrane. We first define key indicators to evaluate the reactor performance and verify model consistency and some of the assumptions. Base case isothermal and non-isothermal simulation results are presented. Isothermal simulation can be seen as a special case of the non-isothermal simulation, where all the heat generated and the heat consumed are perfectly balanced. Base case simulations had three objectives: (1) to verify the energy and mass consistency of the model; (2) to verify some assumptions underlying the model; and (3) to obtain first insights into the performance of the MCMR concept.

Isothermal simulations were quick to perform, taking about 20 min with an Intel Zeon™ processor. We take advantage of this by performing a 15-parameters sensitivity analysis, including operating, design, catalyst and physical property parameters. Isothermal simulations decoupled the combustion and reforming channels, allowing better understanding how each parameter can improve conversion in

each channel.

In the last section of this chapter, devoted to non-isothermal simulations, we consider options to improve the reactor performance, without creating hot spots. Among the parameter adjustments, we use the technique mentioned by Baratti et al. (2003), of varying the catalyst thickness and kinetic pre-exponential factor along the reactor length. Note that at this stage of the research, we did not try to optimize the reactor, but rather to understand options which could improve performance, and provide of basis for comparison with experimental results in Chapter 8 . Many catalyst parameters, for instance (density, kinetics) need to be measured before one could attempt a practical optimization.

3.2 Model Equations and Base Case Parameters

The 2-D model equations are described in Chapter 2, where modeling options and parameters are identified. In this chapter, we adopt the “concept mode” option (only half-height of the combustion channel, see Fig. 2.1) and the adiabatic reactor ($Q_{loss} = 0$ in Eq. (2.107)). Other options, as well as the base case simulation parameters, are identified in Tables 3.1 and 3.2.

To calculate the flow of CH_4 and air in the combustion channel, we introduce in Table 3.1 two variables, the feed excesses of CH_4 and O_2 . The feed excess of CH_4 in the base case corresponds to an extra 1% of the required heat to convert 100% of the CH_4 to H_2 at standard conditions. The feed of air is determined by the stoichiometric excess of oxygen, expressed as:

$$F_{\text{CH}_4,co} = \frac{-(1 + \text{Excess}_{\text{CH}_4}) F_{\text{CH}_4,ro} \Delta H_{rx,3}^{298K}}{\Delta H_{rx,4}^{298K}} \quad [\text{mol}/s] \quad (3.1)$$

$$F_{\text{O}_2,co} = 2(1 + \text{Excess}_{\text{O}_2}) F_{\text{CH}_4,co} \quad [\text{mol}/s] \quad (3.2)$$

$$F_{\text{N}_2,co} = .79 F_{\text{O}_2,co} / .21 \quad [\text{mol}/s] \quad (3.3)$$

3.3 Metrics

Many metrics are needed to verify the model and evaluate the reactor performance:

Table 3.1: Base Case Parameters for Simulations, Part I

Parameters (Symbols)	Values (Equations)	Units
Operating Parameters		
Temperature of Feed (T_{ko})	600	°C
Pressure in Reforming Channel(P_{ro})	15	bar
Pressure on Permeate Side (P_m)	0.7	bar
Pressure in Combustion Channel (P_{co})	1.1	bar
Reforming Feed Methane Flow ($F_{CH_4,ro}$)	1.29	nL/min
Reforming Feed Steam to Carbon Ratio	3	mol/mol
Reforming Feed H ₂ Content ($y_{H_2,ro}$)	(P_m/P_{ro})	mol/mol
Combustion Feed Excess CH ₄	1% (Eq. (3.1))	mol%
Combustion Feed Excess Air/O ₂	15% (Eq. (3.2))	mol%
Catalyst Parameters		
Pore Radius ($R_{pore,k}$)	10	nm
Porosity ($\epsilon_{cat,k}$)	0.4	
Density (ρ_k)	$(2355(1 - \epsilon_{cat,k})/(1 - 0.4))$	kg/m ³
Reforming Kinetics	Xu and Froment (1989)	
Combustion Kinetics	n^{th} order (See Eq. (2.50))	
(α, β)	1, 1	
(A_4)	19.9e7	kmol/(kg s bar $^{\alpha+\beta}$)
(E_4)	90	kJ/mol
Design Parameters		
Length (L)	0.3	m
Width (W_k)	0.08	m
Catalyst Thickness ($Th_{cat,k}$)	40	μm
Separator Wall Thickness (Th_s)	0.01	m
Gas Channel Half-Height (H_k)	0.001	m

Methane conversion: X_{CH_4}

$$X_{CH_4,k} = 1 - \frac{F_{CH_4,k}|_z}{F_{CH_4,k}|_{z=0}} \quad [mol/mol] \quad (3.4)$$

Table 3.2: Base Case Parameters for Simulations, Part II

Parameters (Symbols)	Values (Equations)	Units
Membrane Parameters		
Membrane Thickness (Th_m)	25	μm
Membrane Effectiveness (η_m)	0.5	
(A_m)	2.003e-4	$\text{mol}/(\text{s m bar}^{0.5})$
(E_m)	15700	J/mol
Physical Properties		
Diffusivity	(Eq. (2.1))	
Solution Parameters		
Δz_1 (See Fig. 2.3)	0.0003	m
Δz_{max}	0.0025	m
% Increase of Δz per step	10%	
Initial Relaxation Factor Non-Iso. Sim.	0.05	
Initial Relaxation Factor Isothermal Sim.	0.3	

where F_{CH_4} , or in a general form F_i , the molar flow rate of any component i in the axial direction, is defined as:

$$F_{i,k} = W_k \int_{-H_k}^{H_r \text{ or } 0} c_{i,k} v_{z,k} dx|_z \quad [\text{mol}/\text{s}] \quad (3.5)$$

Ratio of products over methane feed:

$$\text{Ratio}_{i/\text{CH}_4} = F_{i,k}|_z / F_{\text{CH}_4,ko} \quad [\text{mol}/\text{mol}] \quad (3.6)$$

For H_2 , we could take either the total hydrogen produced (Eq. (3.7)) or the hydrogen extracted by the membrane (Eq. (3.8)).

3.3.1 Hydrogen Production

We define several measures of H_2 production:

Table 3.3: Hydrogen Flow Unit Conversion

	kg/day	mol/s	Nm ³ /h
kg/day	1	87.09	2.114
mol/s	1.148E-2	1	2.427E-2
Nm ³ /h ^a	0.4731	41.20	1
nL/min	7.886	686.7	16.67
Sft ³ /min	0.804	70.01	1.699
GJ /day	0.121	10.5	0.256
kW	1.40	122.0	3.0

^aNormal (N,n) or Standard (S) conditions are taken at 273.15 K, 1 bar

H₂ extracted by membrane: $F_{H_2,m}$

$$F_{H_2,m} = W_r \int_0^z -J_{H_2,m} dz \quad [mol/s] \quad (3.7)$$

where $J_{H_2,m}$ is defined in Eq. (2.22)

Total H₂ produced: $F_{H_2,prod}$

$$F_{H_2,prod.} = F_{H_2,r}|_z + F_{H_2,m}|_z - F_{H_2,r}|_{z=0} \quad [mol/s] \quad (3.8)$$

F_{H_2} is more commonly reported in [kg/day] or [Nm³/h]. Table 3.3 shows various conversion factors.

Specific hydrogen production: The specific H₂ production Y_{H_2} is defined as the ratio between the hydrogen extracted by the membrane (see Eq. (3.7)) and the reactor volume (*vol.react.*), mass of catalyst, or membrane area (*m.area*). How to define reactor volume is not obvious for our reactor. For instance, one could include insulation materials, pre-heaters, or flanges. In our case, we only include the internal volumes of the two channels, separator wall and membrane support volumes. This facilitates comparison of our results with other reactors, like Packed Bed Mem-

brane Reactors (PBMRs) and Fluidized Bed Membrane Reactors (FBMRs).

$$Y_{H_2, vol. react.} = \frac{87.1 F_{H_2, m} M_{wH_2}}{(2H_r + Th_s + H_c + Th_{m.sup.}/2) LW_r} \quad [kg \ H_2/day \ m^3_{react.}] \quad (3.9)$$

$$Y_{H_2, kg_{cat}} = \frac{87.1 F_{H_2, m} M_{wH_2}}{(\rho_{cat r} Th_{cat, r} W_r + \rho_{cat c} Th_{cat, c} W_c) L} \quad [kg \ H_2/day \ kg_{cat}] \quad (3.10)$$

$$Y_{H_2, m.area} = \frac{87.1 F_{H_2, m} M_{wH_2}}{LW_r} \quad [kg \ H_2/day \ m^2_m] \quad (3.11)$$

For doubled-sided MRT membranes:

$$Th_{m.sup.} = 0.00635 \quad [m] \quad (3.12)$$

where the subscript *m.sup.* denotes the membrane support.

The H₂ production per square meter of land (footprint) was also considered, but not selected because this measure is likely to be strongly scale dependent.

3.3.2 Other Performance Indicators

Catalyst effectiveness, η_{cat} :

$$\eta_{cat, j} = \frac{r_j|_x}{r_j|_{x=Th_{cat, k}}} \quad (3.13)$$

$$\eta_{cat, ave, j} = \frac{1}{Th_{cat, k} L} \int_0^L \int_0^{Th_{cat, k}} \eta_{cat, j} dx dz \quad (3.14)$$

Reactor energy efficiency, η_{react} : Reactor efficiency is defined as the ratio of the heat of combustion of the hydrogen extracted by the membrane to the total heat of combustion of the methane fed to both channels:

$$\eta_{react.} = \frac{LHV_{H_2}^{298K} F_{H_2, m}}{LHV_{CH_4}^{298K} F_{CH_4, ro} + LHV_{CH_4}^{298K} F_{CH_4, co}} \quad (3.15)$$

Reaction heat flux, H_{flux} : Reaction heat fluxes are calculated by integrating the heat produced and consumed, respectively, by the combustion and reforming reac-

tions. Ideally, reaction heat fluxes are equal in both channels to avoid hot spots and reactor extinction.

$$H_{flux,r} = \int_0^{Th_{cat,r}} \left(\sum_{j=1}^3 (\Delta H_{rx,j}^{T_{cat,r}} r_j) \right) dx/1000 \quad [kW/m^2] \quad (3.16)$$

$$H_{flux,c} = \int_0^{Th_{cat,c}} (\Delta H_{rx,4}^{T_{cat,c}} r_4) dx/1000 \quad [kW/m^2] \quad (3.17)$$

Transverse temperature, ΔT : Transverse temperatures provide an indication of the effectiveness of the heat transfer within a computational domain.

$$\Delta T_k = T_k|_{x=H_r \text{ or } 0} - T_k|_{x=-H_k} \quad [K] \quad (3.18)$$

$$\Delta T_{cat,k} = T_{cat,k}|_{x=Th_{cat,k}} - T_{cat,k}|_{x=0} \quad [K] \quad (3.19)$$

$$\Delta T_s = T_s|_{x=Th_s} - T_s|_{x=0} \quad [K] \quad (3.20)$$

3.3.3 Dimensionless Numbers

Average physical properties: To evaluate dimensionless numbers in the 2-D model, we needed to define average physical properties (e.g. ρ_{ave} , Cp_{ave}) along the axial direction. Physical properties are functions of dependent parameters u (T , P , c_i). We need to evaluate first those average dependent parameters (except for P). In the gas channels, we evaluate u_{ave} as:

$$u_{ave,k} = \frac{\int_{-H_k \text{ or } 0}^{H_k \text{ or } 0} u v_z dx}{v_{z,ave,k}} \quad [m/s] \quad (3.21)$$

In the catalyst layer and separator wall, where there is no axial velocity, we evaluate $u_{ave,k}$ based on the arithmetic mean:

Reynolds number, Re :

$$Re_k = \rho_{mix,ave,k} D_{h,k} v_{ave,k} / \mu_{mix,ave,k} \quad (3.22)$$

where:

$$D_{h,k} = 4(W_k 2H_k) / (2W_k + 4H_k) \quad [m] \quad (3.23)$$

$$\rho_{mix,ave,k} = \sum_i (c_{ave,i,k} M w_i) \quad [kg/m^3] \quad (3.24)$$

Here D_h is the hydraulic diameter, $\mu_{mix,ave,k}$ is evaluated from Eq. (2.15) at T_{ave} .

Mass Peclet number, Pe_L :

$$Pe_{L,i,k} = L v_{z,ave,k} / D_{i,mix,ave,k} \quad (3.25)$$

where $D_{i,mix,ave,k}$ is evaluated at T_{ave} .

Thermal Peclet number, $Pe_{L TH}$:

$$Pe_{L TH} = L v_{z,ave,k} \hat{C} p_{ave,k} \rho_{mix,ave,k} / k_{mix,ave,k} \quad (3.26)$$

$\hat{C} p_{ave,k}$ is the average specific heat capacity of the gas mixture:

$$\hat{C} p_{ave,k} = \sum_i (x_{i,ave,k} \hat{C} p_{i,ave,k}) \quad [J/(kg K)] \quad (3.27)$$

$$x_{i,ave,k} = (y_{i,ave,k} M w_i) / M w_{ave,k} \quad [kg/kg] \quad (3.28)$$

$$M w_{ave,k} = \sum_i (y_{i,ave,k} M w_i) \quad [kg/mol] \quad (3.29)$$

$$\hat{C} p_{i,ave,k} = C p_{i,ave,k} / M w_i \quad [J/(kg K)] \quad (3.30)$$

where x_i represents the mass fraction, $k_{mix,ave,k}$ is evaluated at T_{ave} , $y_{i,ave}$ from Eq. (2.9), and $C p_{i,ave,k}$ is evaluated at T_{ave} based on Eq. (2.8).

3.3.4 Sensitivity Analysis Parameters

In order to perform isothermal sensitivity analysis, we need to consider the overall objective of the study. Obtaining a high overall methane conversion is one possible objective. However, as seen in Table 3.4 with the isothermal simulation results, the final methane conversion in the reforming channel was already closed to 95%, giving limited space for improvement. On the other hand, on the combustion side, final conversion was lower, 82%. Base case parameters were mostly taken from Zafir and Gavrilidis (2003) and with our operating temperature well below theirs, the final methane conversion in the combustion channel was reduced. To be consistent in both channels, instead of looking at the final conversion, the sensitivity analysis focuses on the minimum length L to reach a specific conversion: to avoid an excessively long reactor, we chose 90% for the reforming channel and 70% for the combustion channel. Those two values were chosen because they were slightly lower than the isothermal base case simulation results, thereby limiting the computation time. Ordinates for the sensitivity analysis are defined as:

$$\% \text{ Change in Input Para.} = \frac{\text{New Input Para.} - \text{Base Case Input Para.}}{\text{Base Case Input Para.}} \quad (3.31)$$

$$\% \text{ Change in Min. } L \text{ for } X_{\text{CH}_4} = \frac{\text{New } L|_{X_{\text{CH}_4}} - \text{Base Case } L|_{X_{\text{CH}_4}}}{\text{Base Case } L|_{X_{\text{CH}_4}}} \quad (3.32)$$

3.3.5 Performance Improvement Parameters

In the last section of this chapter, we perform a series of simulations to improve the non-isothermal base case reactor performance. We monitor two indicators: the average reforming gas temperature ($T_{ave,r}$) and the reforming methane conversion ($X_{\text{CH}_4,r}$). $T_{ave,r}$ is chosen because it is the most critical temperature to maintain the membrane integrity. CH_4 conversion in the reforming channel is an easy parameter to understand, and, it is related directly to hydrogen production. It is also dependent on ($X_{\text{CH}_4,c}$), since low conversion in the combustion channel results in cooler temperatures, with reduced reforming performance.

3.4 Solving the Model

As mentioned in Chapter 2, we opted for a two-point boundary ordinary differential equation solver “*bvp4c*”, included in the MATLABTM software, coupled with backward finite difference discretization to solve the model. “*bvp4c*” uses orthogonal collocation on finite elements and was applied in the transverse direction. Backward finite differences were applied in the axial direction. To obtain values for the backward finite difference method, polynomials were fitted. Each discretization step was solved sequentially, from the entrance to the exit of the reactor. All integrations were performed using the trapezoidal rule. The sequential technique in the axial direction made the model quite robust, and most simulations conditions reported in this paper were obtained without special tuning. The disadvantage of the sequential technique was that second order terms in the axial direction were difficult to incorporate.

In Figure 2.1, A, B, C, D & E represent the five computational domains that must be solved for each discretization step. “*bvp4c*” required that each domain be solved individually. With each domain depending on the others, relaxation factors were used for convergence purposes. For isothermal simulations, separator Wall (C) was not needed, and only the pairs of domains, A & B and D & E, were solved. For simulations with energy balance, B,C & D domains were solved first. A & B and D & E were then solved in a second iteration loop. Complete convergence was difficult to obtain in a reasonable time while solving the second set of domains. To cope with this, we tolerated a certain level of discrepancies at the gas channel - catalyst layers boundaries, usually up to 1 K for temperatures and 0.001 for molar fractions.

Table 3.2 shows some of the solving parameters. Discretization step size Δz should be small enough that it does not influence the final results. The maximum step size was set at 0.0025 m. We verified that this value was sufficient by performing a simulation with $\Delta z_{max} = 0.0015$ m, which did not change the final result significantly (final X_{CH_4} increased by only 0.07%). We set the initial step size, Δz_1 , at the reactor entrance at 0.0003 m. The goal with Δz_1 was to obtain an X_{CH_4} after the first discretization step close to 1% in both channels.

Non-isothermal simulations took about 4 hours with an Intel ZeonTM proces-

sor, CPU 3.0 GHz with 4.0 GB of RAM. Isothermal simulations were much faster, requiring only 5 min for the combustion channel and about 15 min for the reforming channel. We were able to run four or five simulations simultaneously on one computer.

3.5 Results and Discussion

3.5.1 Isothermal and Non-Isothermal Base Case Simulations

Base case simulations had three different objectives: (1) to verify the energy and mass consistency of the model; (2) to verify some assumptions underlying the model; and (3) to obtain insights into the potential performance of the MCMR concept.

Table 3.4 shows base case results for both non-isothermal and isothermal simulations. The isothermal simulation represents a special case of the non-isothermal simulation, where the heats of reaction of both channels are perfectly balanced. The isothermal simulation performed better, with the methane conversion and hydrogen production indicators all superior to the non-isothermal case. As shown below, the non-isothermal base case suffers from an insufficient supply of heat from the combustion side, causing the reactor to cool. In the last section of this chapter, we consider some ways to improve the heat supply, and, as a result, to enhance the reactor performance.

Figure 3.1 shows various output parameters from the non-isothermal base case simulation. In Figure 3.1A, both reforming and combustion temperatures profiles are predicted to initially dip at the inlet of the reactor, then peak at ~ 0.05 m and slowly decrease until the reactor outlet. Final temperatures, ~ 780 K, are significantly lower than the inlet gas temperature of 873 K. The upper part of Figure 3.1B shows the integrated reaction heat fluxes. Those heat fluxes explain the temperatures variations in Figure 3.1A: (1) initially, the reforming heat flux is significantly higher than the combustion flux, causing the initial temperature to dip; (2) the combustion flux then becomes higher for a short length, until ~ 0.05 m, leading to peak temperatures; (3) finally, the reforming flux became slightly higher, causing the reactor to cool slowly until the outlet is reached. The initial temperature dip

Table 3.4: Isothermal and Non-Isothermal Base Case Results

Metric	Units	Value Non-Iso	Value Iso
Final $X_{CH_4,r}$	-	74.6%	94.8% ^a
Final $X_{CH_4,c}$	-	72.5%	82.2%
Final Ratio $_{H_2,m/CH_4}$	mol/mol	2.54	3.21
Final Ratio $_{H_2,prod/CH_4}$	mol/mol	3.01	3.80
$F'_{H_2,m}$	kg/day	0.42	0.52
$Y_{H_2,vol. react.}$	kg H ₂ /day m ³	1070	1350
$Y_{H_2,kg_{cat}}$	kg H ₂ /day kg _{cat}	91.8	116
$Y_{H_2,m area}$	kg H ₂ /day m ² _m	17.3	21.8
η_{react}	-	63.8%	N/A
$\eta_{catr,ave,1}$	-	90.1%	86.3%
$\eta_{catc,ave,4}$	-	81.2%	76.2%
Average Residence Time of Ref's	s	3.24	3.20
Average Residence Time of Comb's	s	0.162	0.156

^aWithout membranes, thermodynamic equilibrium at isothermal base case conditions would limit $X_{CH_4,r}$ to 28%.

can be observed in previous MCR models based on a counter-current configuration (Kolios et al., 2002; Zafir and Gavriilidis, 2004).

In Figure 3.1A, although the difference between the temperature maxima and minima in the axial direction reaches almost 100 K, average transverse temperature differences between the reforming and combustion channels are <10 K. Moreover, in the lower part of Figure 3.1B, temperature differences within each domain (gas channels, catalyst layers and wall) are usually <10 K, indicating good heat transfer. Catalyst layer ΔT 's are, as expected, much smaller than the gas channel ones, not surprising given that their thicknesses are 25-50 times smaller.

One can observe a counter-intuitive result in Figure 3.1A: towards the exit of the reactor, the reforming gas average temperatures are predicted to exceed the catalyst combustion average temperature. Several observations help to explain this behaviour. First, reaction heat fluxes towards the exit became small and other heat transfer mechanisms, e.g. convection, can dominate. Second, the reforming gas channel height is twice that of the combustion channel, and the total molar

flow rate in the reforming channel is also about twice as large. The reforming gas channel has a higher resistance to changes in temperature, leading to larger ΔT 's in the transverse direction (Figure 3.1B) and more resistance to change in average temperatures in the axial direction (Figure 3.1A).

From Figure 3.1C, one can compare $Ratio_{i/CH_4}$ with X_{CH_4} in Figure 3.1A. Our model respects the expected stoichiometric ratios: in the combustion channel, $Ratio_{H_2O/CH_4,c}$ is twice the $Ratio_{CO_2/CH_4,c}$, and $Ratio_{CO_2/CH_4,c}$ is equivalent to $X_{CH_4,c}$; in the reforming channel $Ratio_{H_2prod/CH_4,r}$ is about four times $X_{CH_4,r}$, and $(Ratio_{CO_2/CH_4,r} + Ratio_{CO/CH_4,r})$ is equivalent to $X_{CH_4,r}$.

Figure 3.2 shows 2-D velocity and temperature profiles. Velocities for both combustion and reforming channels follow similar trends, but variations are predicted to be larger on the reforming side. In both channels, the peak temperatures, observed in parts C & D, decrease the gas density while increasing the gas velocities. In the reforming channel, mole generation due to reactions, combined with withdrawal of moles by the membrane, add to the velocity variations. Isotherms in the catalyst layers (parts E & F) show less curvature than in the gas channels (parts C & D), indicating faster heat transfer.

Figure 3.3 shows H_2 (parts A & B) and CH_4 (parts D & E) molar fraction 2-D profiles, as well as catalyst effectiveness, η_{cat} (parts C & F) in both reforming and combustion channels. In the reforming channel (right side of the figure), with 40 μm thick coating in the base case, the catalyst effectiveness remains high, generally >0.8 . H_2 molar fraction gradients in the transverse direction are apparent in the gas channel, suggesting that H_2 extraction by the membrane or H_2 diffusion limits the reactor performance. On the combustion side, the catalyst effectiveness behaves differently, with lower values (~ 0.5) at the reactor entrance. Slower O_2 diffusion in the catalyst layer, may explain this observation. CH_4 iso-molar-fraction lines in the combustion gas channel are relatively straight (part D), indicating low mass transfer resistance.

Verification of Assumptions

Based on results of the non-isothermal base case simulation, this section considers some of the model assumptions adopted in Chapter 2.

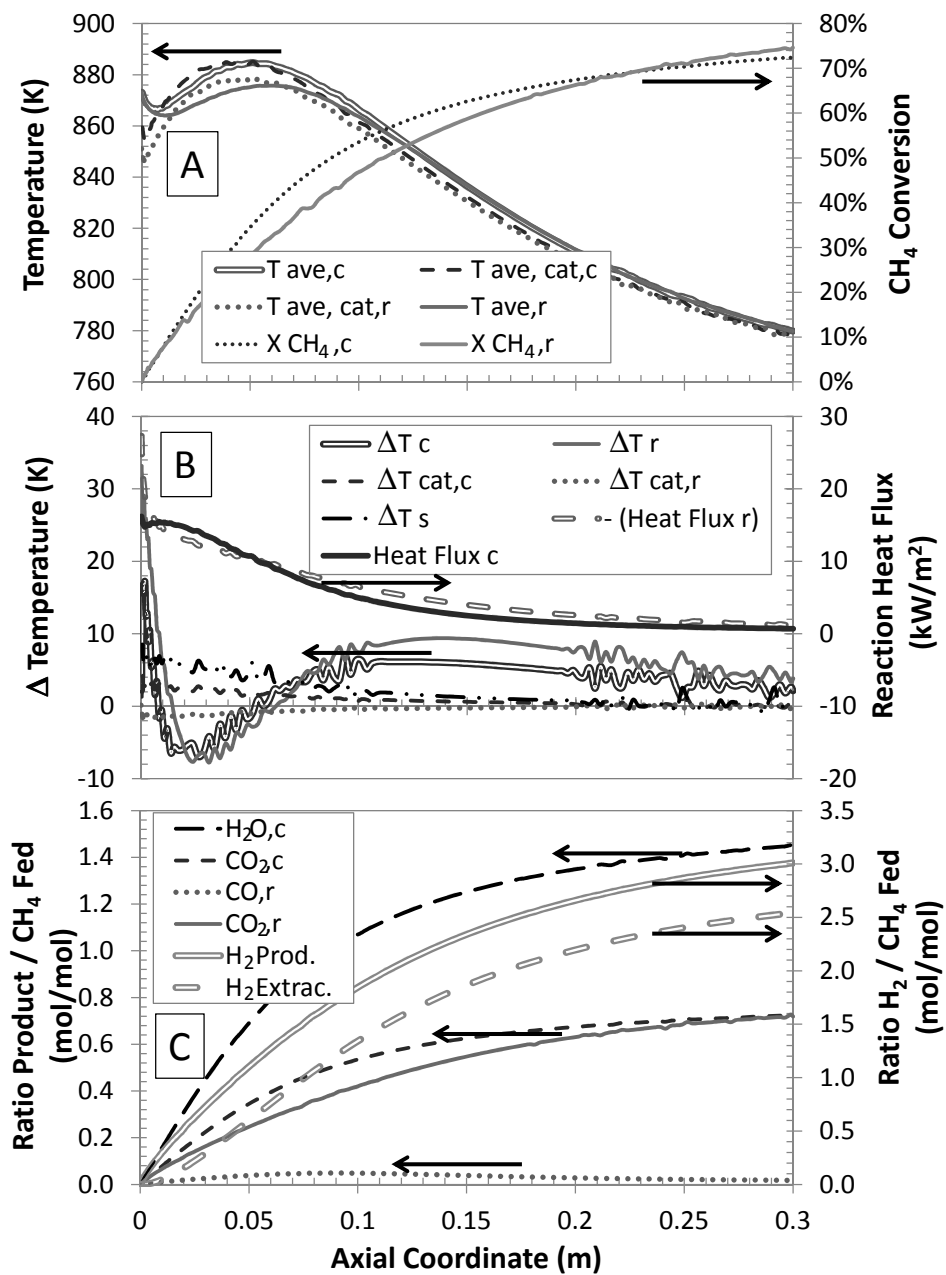


Figure 3.1: Non-Isothermal Base Case Results - A: X_{CH_4} & Average Temperature Profiles; B: Transverse ΔT & Reaction Heat Fluxes; C: $Ratio_{i/CH_4}$. (For base case parameters, see Table 1.)

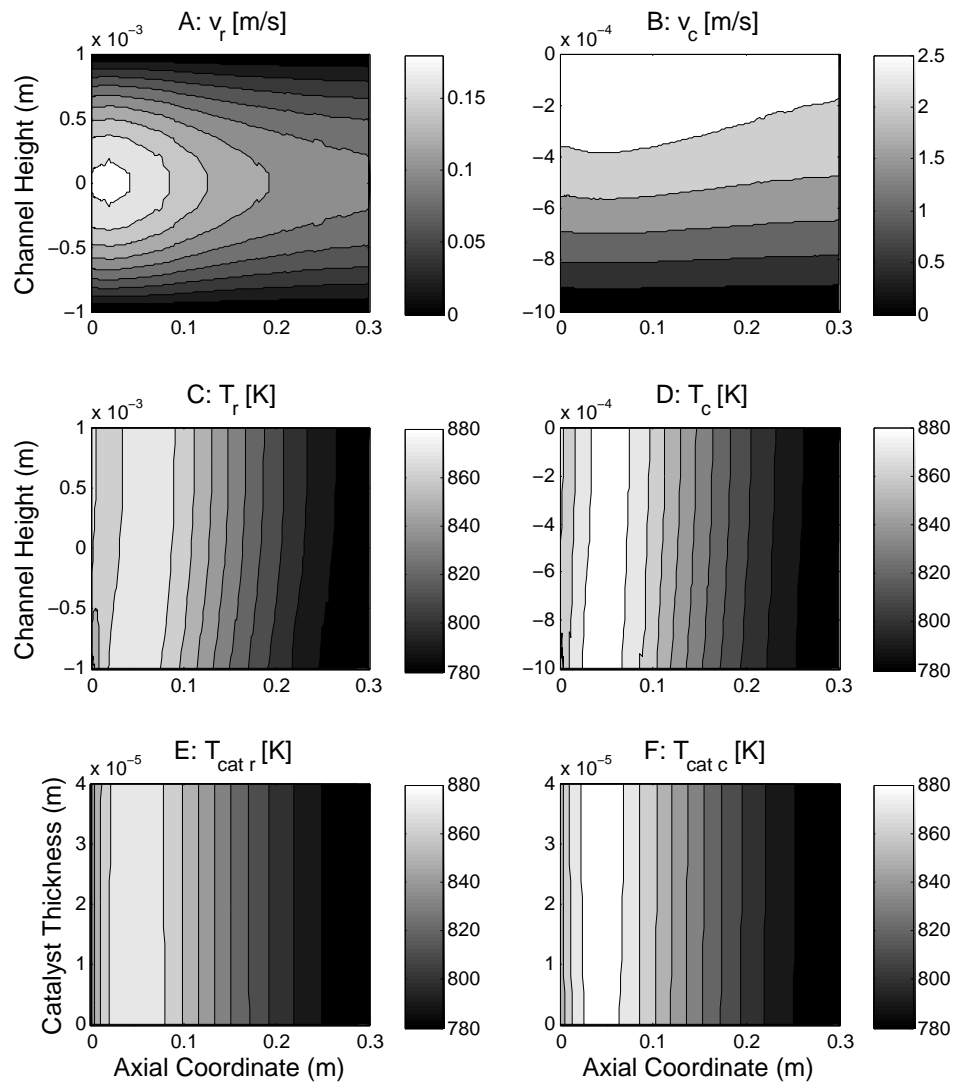


Figure 3.2: Non-Isothermal Base Case Results - Velocity and Temperature Profiles

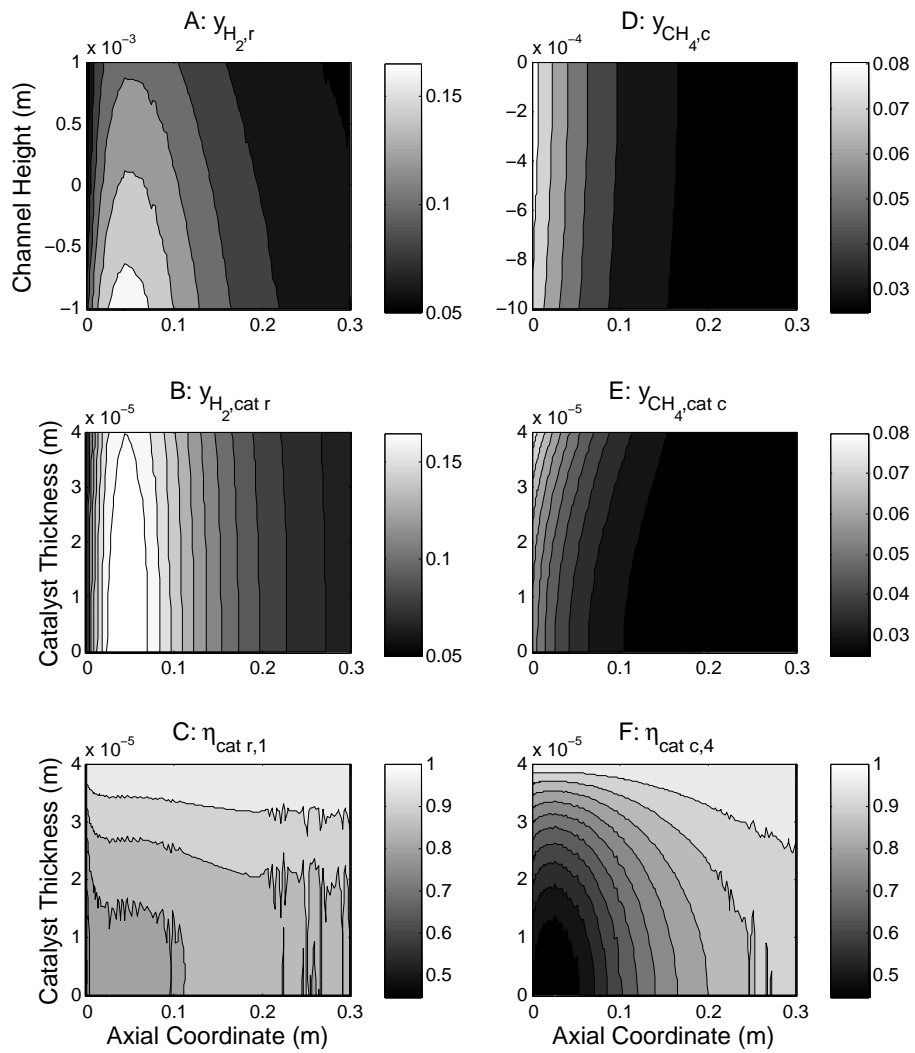


Figure 3.3: Non-Isothermal Base Case Results - Molar Fraction and Catalyst Effectiveness Profiles

Table 3.5: Base Case Simulation Dimensionless Numbers

	Values Non-Iso		Values Iso
	Inlet ^a	Outlet	Outlet
Re_r	54	47	39
$Pe_{L,H_2,r}$	962	720	587
$Pe_{L,TH,r}$	3280	2600	2100
Re_c	31	38	33
$Pe_{L,CH_4,c}$	4420	4780	4410
$Pe_{L,TH,c}$	4600	5150	4760

^aInlet dimensionless numbers are the same for both Non-Iso and Isothermal simulations

Gas channels: Table 3.5 shows dimensionless numbers for the gas channels. The low Re numbers, all <55 , confirm laminar flow in both channels. The entrance length to produce fully-developed laminar flow ($0.06 * Re * D_{h,k}$) was evaluated <13 mm in both channels, or $<4.5\%$ of the total reactor length. $Pe_{L,CH_4,c}$ values are high (>4000), but $Pe_{L,H_2,r}$ values are <1000 , indicating some axial dispersion of H_2 by diffusion, which is not taken into account in the model. However, $Pe_{L,H_2,r} >500$, so that adding a diffusion term in the axial direction at this stage of the project was deemed to be unnecessary. In both channels, $Pe_{L,TH}$ is mostly >1000 , indicating, as assumed, that axial heat transfer by conduction is negligible.

Spatial derivatives of the physical properties were also assumed to be negligible. Using data from the simulation, we back-calculated the heat convection term and the terms including the thermal conductivity derivative in the axial direction in Eq. (2.98). The derivative term was ~ 3 orders of magnitude smaller than the convective heat flux term, supporting this assumption.

Catalyst layers: Both mass diffusion and heat conduction in the axial direction were assumed to be negligible. Based on model predictions, we back-calculated concentration and temperature gradients in both the transverse and axial directions. The axial concentration gradient was ~ 5 orders of magnitude smaller than the corresponding transverse concentration gradient. Similarly, the axial heat conduction gradient was ~ 4 orders of magnitude smaller than the transverse heat conduction

gradient, again supporting the assumptions.

It was assumed that the derivative of $D_{i,mix}$ was negligible. We compared the following two terms by back calculations in the catalyst layers:

$$D_{i,mix} \left(\frac{d^2 c_i}{dx^2} \right) \text{ vs } \frac{d D_{i,mix}}{dx} \frac{d c_i}{dx}$$

The second term, including the spatial derivative of $D_{i,mix}$, was ~ 3.5 orders of magnitude smaller than the first term, again supporting our assumption.

Separator wall: For the separator wall, thermal conduction in the axial direction was assumed to be negligible. Back calculations showed that the driving forces for conduction in the axial and transverse directions were of the same order of magnitude. Our solving strategy, solving each discretization step sequentially starting at the entrance of the reactor, makes it difficult to take into account second order heat transfer terms in the axial direction. Ideally, all reactor equations would be solved simultaneously. Conduction in the axial direction would diffuse the heat, reducing temperature variations. By neglecting axial heat conduction, we might exacerbate hot spots, which we want to avoid to preserve the membrane. Therefore, our simulations are believed to provide conservative estimates regarding the formation of hot spots.

3.5.2 Isothermal Parametric Sensitivity Analysis

Predictions from the isothermal parametric sensitivity analysis are presented in Figures 3.4, 3.5 and 3.6. The y-axis is inverted so the upper quadrants show improvements in reactor performance (i.e. decreases in minimum reactor length to achieve a desired methane conversion, corresponding to increases in methane conversion and hydrogen production). For simplicity in this section, instead of mentioning the “Minimum length to achieve a specific conversion”, we use the generic terms “performance” and “conversion”. We discuss in this section the parameter adjustments that could improve the reactor performance and link these changes with practical considerations.

Figure 3.4 shows sensitivity results regarding some operating parameters. Tem-

perature was the most sensitive parameter in both channels. One might be tempted to increase the reactor temperature to increase performance. However, as mentioned in Chapter 2, Pd/Ag membranes have serious temperature limitations. Unless Pd-based membrane working $>600^{\circ}\text{C}$ can be developed, higher temperature would not be desired. Furthermore, more expensive alloys would likely be required to reactors to operate at those conditions. Higher pressures led to higher performance in both channels, but to a lesser extent than higher temperatures. By Le Châtelier's principle and without any membrane, since there is a net production of moles in the SMR reactions, increasing the reforming pressure reduces the conversion. However, increased pressure also increases the driving force for the hydrogen permeation, explaining the slight overall increase in performance with increasing pressure. Despite this advantage, higher pressure also brings challenges. First, the membrane may not withstand increases in pressure (MRT membranes have an upper limit of 25 bar). Second, higher pressures require thicker material requirements for the reactor, leading to higher equipment cost and longer start-up times. As shown in Figure 3.4A, it was also possible to enhance conversion by lowering the pressure on the permeate side, indicating that H_2 extraction might be a major factor limiting the reactor performance. Lowering permeate pressure generally does not increase significantly the cost of the reactor, but would increase parasitic losses, e.g. for compression of product H_2 .

Figure 3.4 also shows linear effect of varying flow rates, while maintaining the same stoichiometric ratios, on the performance in both channels. Increasing flow rates decreased proportionally the conversions. In light of those results, one can confirm that mass transfer resistance was not limiting the reactor performance in the gas channel. The limited influence of the steam-to-carbon ratios in reforming and of the excess air on the combustion side further supports this assumption. Decreasing the flow rates is not an attractive option: although it increases conversion, it reduces the hydrogen yields Y_{H_2} . Practical issues would likely set feed parameters. Steam-to-carbon ratio >3 is usually required to avoid carbon formation with Ni-based catalysts, and a large excess of air might be required on the combustion side to stay below the methane lower flammability limit.

Figure 3.5 shows the influence of parameters related to the catalyst layers. Activation energies are predicted to have the strongest effect in both channels. The

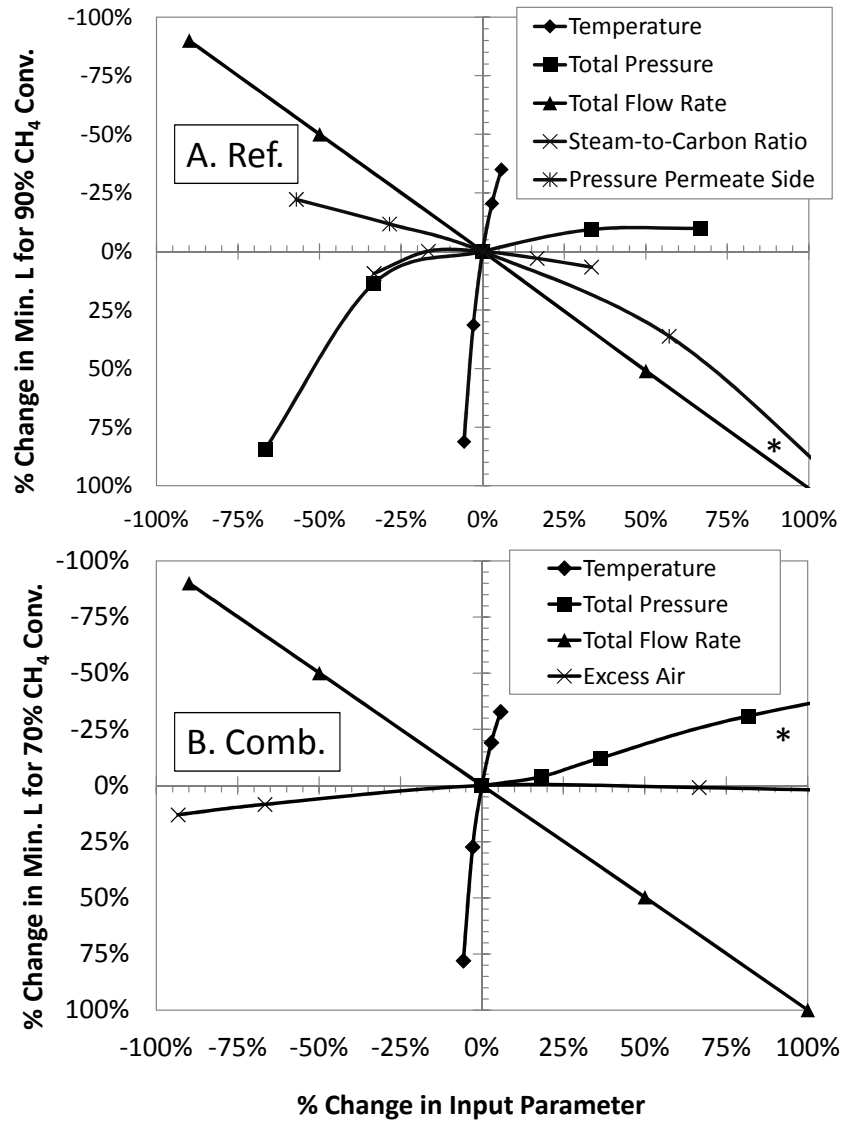


Figure 3.4: Sensitivity Analysis around Base Case Values of Tables 3.1 & 3.2 - Operating Parameters: A. Reforming Channel; B. Combustion Channel (* Some values are off chart.)

only way to influence this parameter would be to change the catalyst itself. Pre-exponential factors could improve performance, especially on the combustion side. The prediction that the reforming channel was less influenced by this parameter, again indicates that H_2 extraction was a major performance limiting factor, not the catalyst. Pre-exponential values are functions of the metal catalyst loading and may vary considerably. Those results suggested that a careful selection of metal loading in the catalyst would be required to balance the heat consumption and production. Shigarov et al. (2009) made similar observations, and suggested that increasing catalyst activity (or loading) is not always the best solution. Strong combustion activity could cause hot spots, whereas strong reforming activity could cause extinction. The importance of pre-exponential factors also suggests that catalyst deactivation is a major challenge.

Increasing pore radius showed a moderate influence on the combustion side and a negligible effect on the reforming. These observations are related to the catalyst effectiveness factors showed in Figures 3.3C & D, where the combustion effectiveness factor was lower than the reforming one near the entrance of the reactor. Pore radius, as well as porosity, are functions of the catalyst support and hence cannot be easily altered.

Figure 3.6 shows the effect of some other reactor design parameters and the effect of diffusivity on reactor performance. In Figure 3.6A, a thinner membrane improved conversion, confirming once again that membrane extraction of H_2 is limiting the performance. However, when designing the prototype, pinhole free planar membranes thinner than $25 \mu\text{m}$ were not commercially available. In other words, membrane thinner than those used in the base case would be unlikely to produce fuel cell grade hydrogen. Half-channel heights are predicted to have little influence on the combustion reaction. However, the half-height significantly affects the reforming performance. As mentioned above, the reforming channel height was assumed to be twice that of the combustion channel. The molecules then had twice the distance to travel and based on Fick's law, the diffusion flux is inversely proportional to the square of the distance traveled. Since the H_2 must diffuse across the reforming channel to be extracted, the effect of reforming channel height can be rationalized. Hence, reducing the half-channel height is one option to improve performance, subject to machining tolerances and fabrication methods. Figure 3.6

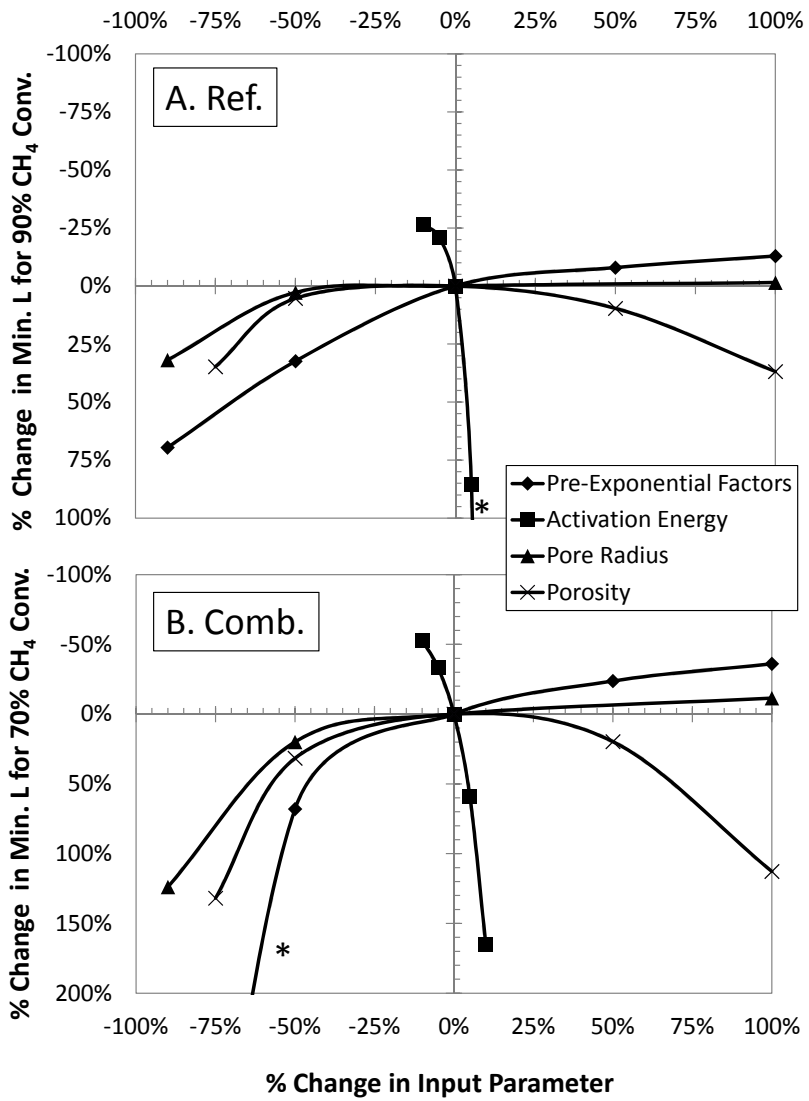


Figure 3.5: Sensitivity Analysis around Base Case Values of Tables 3.1 & 3.2
 - Catalyst Parameters: A. Reforming Channel; B. Combustion Channel
 (* Some values are off chart.)

indicated a small benefit of increasing the catalyst thickness layers, up to about twice the size of the base case thickness (from 40 to 80 μm). The results also showed that the diffusivity is unlikely to limit the performance, at least over the range tested.

3.5.3 Performance Improvement

Figure 3.7 shows results of a series of non-isothermal simulations. The y-axis displays both average reforming gas temperature ($T_{ave,r}$) and the reforming methane conversion ($X_{\text{CH}_4,r}$). The non-isothermal base case results show that the methane conversion predicted in the combustion channel is less than in the reforming one (see Table 3.4). As a result, not enough heat is transferred to the reforming side. In Figure 3.7A, key combustion channel parameters are modified (see Table 3.6) from their base case values, with the goal of transferring more heat. In Figure 3.7B, as proposed by Baratti et al. (2003), we varied the combustion catalyst layer thickness and the kinetic pre-exponential factor A_4 along the reactor length, with the combustion catalyst layer of Figure 2.1 divided into six intervals, each 50 mm long. Table 3.7 presents the parameter changes from the base case scenario.

All parameters varied in Figure 3.7A improved the conversion. However, increasing the pressure and augmenting A_4 both led to a hot spot >900 K near the reactor entrance. In contradiction to the isothermal simulation (see Figure 3.4), reducing all the flow rates by 25% did not increase the conversion proportionally. This could be explained by the reforming reactions and hydrogen extraction benefiting most from flow reduction, causing further cooling and slower combustion. A cooler reactor leads to lower final conversions. In Figure 3.7B, methane conversion improved again, this time with the variable catalyst parameters strategy. Increasing A_4 after two intervals was more effective than increasing the catalyst thickness after two intervals. Combining the two variations was even better, with conversion improving 10% without hot spot formation. The best conversion ($>90\%$), was obtained, without hot spots, by combining A_4 and thickness variations with increased excess methane flow.

Table 3.8 summarizes the performance improvements between our non-isothermal base case simulation and the best case in Figure 3.7, as well as membrane reactor

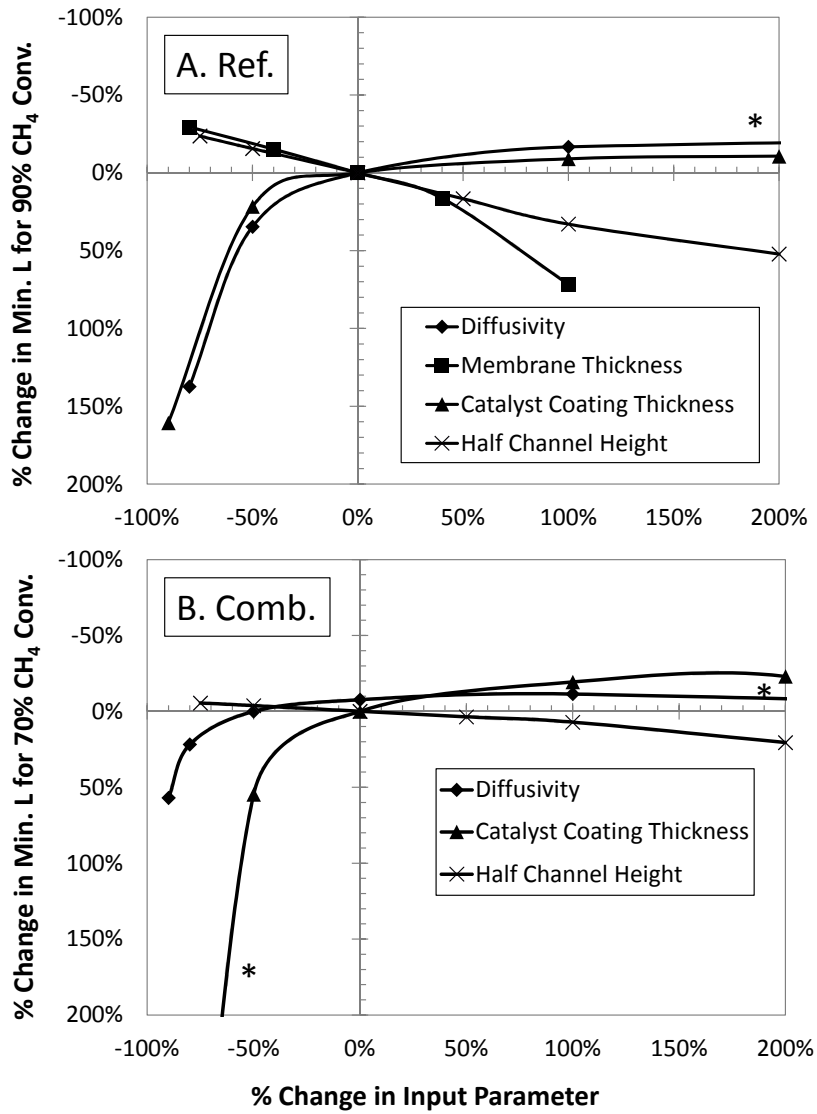


Figure 3.6: Sensitivity Analysis around Base Case Values of Tables 3.1 & 3.2 - Design Parameters & Diffusivity: A. Reforming Channel; B. Combustion Channel (* Some values are off chart.)

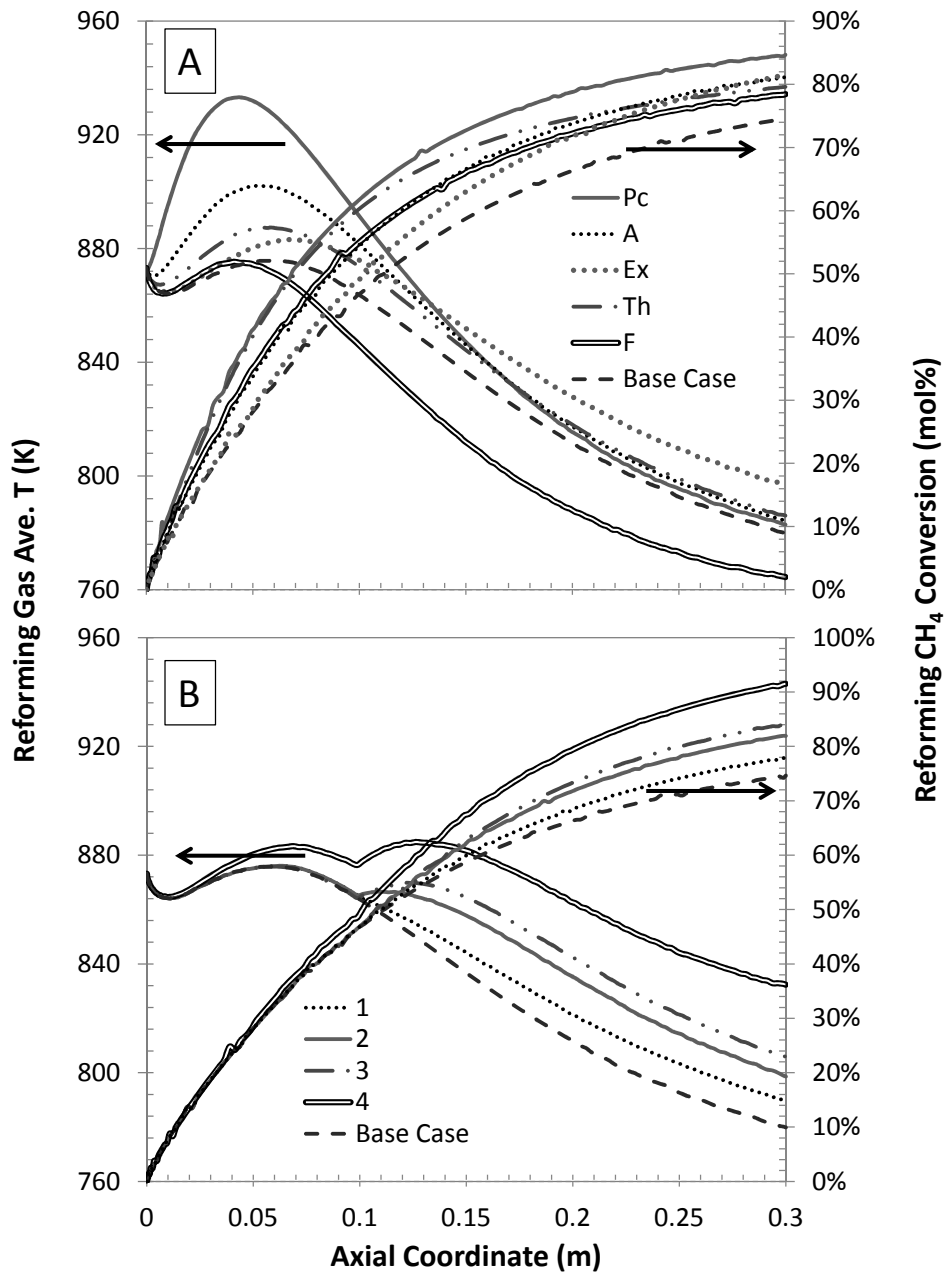


Figure 3.7: Performance Improvement Trials - A. Constant Catalyst Properties along the Reactor Length; B. Variable Catalyst Properties ($Th_{cat,c}$, A_4) along the Reactor Length.

Table 3.6: Parameter Changes for Figure 3.7A from Base Case Values of Tables 3.1 & 3.2

Label	Parameter Changed	Value	Units
A	A_4 Multiplication Factor	1.5	-
Ex	Combustion Feed Excess CH_4	15	mol%
F	Inlet Flow Rates (Ref. and Comb.) Multiplication Factor	0.75	-
Pc	Combustion Pressure (P_c)	1.6	bar
Th	Combustion Catalyst Thickness ($Th_{cat,c}$)	60	μm

Table 3.7: Parameter Changes for Figure 3.7B from Base Case Values of Tables 3.1 & 3.2

Label	Combustion Catalyst Thickness ($Th_{cat,c}$) per Interval (μm)	A_4 Multiplication Factor per Interval	Combustion Excess CH_4 (mol%)
1	40-40-60-60-60-60	N/A ^a	N/A
2	N/A	1-1-2-2-2-2	N/A
3	40-40-60-60-60-60	1-1-2-2-2-2	N/A
4	40-40-60-60-60-60	1-1-2-2-2-2	15

^aN/A= Same as base case

experimental work reported in the literature. Care is needed when comparing, as operating conditions differed widely, some values are rough estimates (denoted by \sim) and, as shown in later chapters, experimental results are generally lower than simulation predictions. However, some general observations are possible: (1) The MCMR has the potential for higher production per reactor volume and per mass of catalyst; (2) the production per membrane area will likely be similar to other membrane technologies; and (3) as long as pin-holes are absent, thinner membranes are desirable.

The best case η_{react} 76.3%, is lower than desirable, despite the improvements,

Table 3.8: Non-Isothermal Base & Best Case Results and Comparison with Experimental Literature

	Base Case	Best Case	FBMR ^a	FBMR ^b	FBMR ^c	PBMR ^d
Final X_{CH_4r} -	74.6%	91.5%	70%	73%	73%	80%
Final X_{CH_4c} -	72.5%	88.0%	N/A	N/A	N/A	N/A
Final Ratio $_{H_2,m}/CH_4$ mol/mol	2.54	3.12	2.5	3.0	1.3	N/A
Final Ratio $_{H_2,prod.}/CH_4$ mol/mol	3.0	3.68	3	N/A	N/A	N/A
$F'_{H_2,m}$ kg/day	0.42	0.51	0.4	1.82	2.27	0.03
$Y_{H_2,vol. react.}$ kg H ₂ /day m ³	1070	1311	~40	~160	~200	420
$Y_{H_2,kg_{cat}}$ kg H ₂ /day kg _{cat}	91.8	90.0	~0.2	~2.5	~3.1	2
$Y_{H_2,m area}$ kg H ₂ /day m _m ²	17.3	21.2	2	6.81	8.50	15
η_{react}	63.8%	76.3%	N/A	N/A	37%	N/A

^a(Rakib et al., 2011) 773 K, 6 bar, 0.5 bar permeate side, Th_m : 25 μ m, electric heating

^b(Mahecha-Botero et al., 2008) 823 K, 10 bar, 0.3 bar permeate side, Th_m : 25 μ m, electric heating

^c(Mahecha-Botero et al., 2008) 823 K, 10 bar, 0.3 bar permeate side, Th_m : 25 μ m, auto-thermal

^d(Tong et al., 2005) 823 K, 3 bar, sweep flow equivalent to 0.3 bar, Th_m : 6 μ m, electric heating

note the efficiency does not include parasitic and heat losses. In Table 3.8, reactor efficiency calculations for auto-thermal conditions showed low efficiency, likely due to reactor heat losses. Even though operating temperature of 823 K is much lower than in conventional reforming, heat losses were still important for the scale studied (~ 2 kg H₂/day). In order to have acceptable reactor efficiency with SMR, the scale of production may need to be at least one to two orders of magnitude higher. To improve the MCMR efficiency significantly, one avenue would be to recycle the reforming gas exhaust as a combustion fuel. Reforming conversion could be controlled so that the retentate gas would contain enough energy to supply the required heat, after condensing and separating the steam. This strategy could also save membrane surface area, since a conversion of $\sim 88\%$ would leave enough methane and unextracted hydrogen to supply the reforming heat requirement. With the isothermal base case conditions, η_{react} could then reach 90% according to our calculations.

3.6 Conclusions

This Chapter presents isothermal and non-isothermal simulation results from the 2-D, steady-state reactor model developed in Chapter 2. For the base case simulations, the non-isothermal case underperformed the isothermal case, due to a lack of heat generated from the combustion reaction. Except for the entrance of the reactor, transverse temperature variations within computational domains could be kept below 10 K. Base case key indicators showed mass and energy consistency. Most model assumptions were verified with dimensionless number calculations and back calculations of heat and mass transfer driving forces. Future model improvements would benefit from incorporation of second-order axial heat transfer terms for the separator wall.

Isothermal sensitivity analysis was carried out involving 15 parameters varied one at a time around the base case values. This sensitivity analysis indicated a limited number of parameter adjustments practically available to increase the reactor performance from the base case scenario. Among these, the most promising were: increasing operating pressure in both channels; lowering permeate pressure on the reforming side; increasing pre-exponential factors and coating thickness on the combustion catalyst; and reducing the half-channel height of the reforming channel. The predictions indicate that H_2 membrane extraction is the major factor limiting reforming performance, whereas catalyst activity is the major factor limiting performance in the combustion channel.

Several combustion channel parameters were varied in an effort to improve the reactor performance. Without rigorous optimization, it was possible to obtain methane conversion ($>90\%$) without the formation of hot spots. Axial temperature variations were reduced from ~ 100 K in the base case to ~ 10 K in the best case. Performance could be improved significantly by a combination of varying the pre-exponential factor (metal loading) and catalyst thickness along the length of the reactor, while increasing the methane flow rate on the combustion side. Compared with other membrane reactor technologies, MCMR has the potential to have 1 to 2 orders of magnitude higher hydrogen production per reactor volume and per mass of catalyst.

Results in this chapter were promising enough to prompt the design and con-

struction of an MCMR prototype reactor. The next two chapters focus on catalyst coating, with a specific goal of obtaining a stable coating thickness $>80 \mu\text{m}$.

Chapter 4

Catalyst Coating: Initial Method Development

4.1 Introduction

Previous chapters of this thesis developed the concept of the Multi-Channel Membrane Reactor (MCMR). This concept requires both reforming and combustion catalysts to be coated on a flat metal substrate. Sensitivity simulations on an isothermal base case, performed in Chapter 3, suggest that the reactor performance could benefit from a relatively thick layer of catalyst, up to $\sim 80 \mu\text{m}$ thick. We review in this Introduction various coating techniques described in the literature, with special attention to techniques with the potential to achieve thick coating layers.

4.1.1 Gas Phase Techniques

Low Temperature Plasma

Production of catalyst by low temperature plasma was reviewed by Liu et al. (2002). Plasma, an ionized gas, can produce a strong and thick carrier or catalyst deposit on metal or ceramic substrate. Powder is heated to near or above its melting point in a plasma torch, and accelerated by a plasma gas stream toward the substrate. The particle diameter is usually between 5 and 60 μm (Liu et al., 2002). Ismagilov

et al. (1999) coated γ -Al₂O₃ and α -Al₂O₃ particles on a Ti support. SEM images showed coating thickness >100 μ m, but surface areas were low, <1 m²/g. One of the advantages of plasma deposition is that no further heat treatment is necessary, saving time and energy. However, operating cost can be high, due to the gas and energy consumption, and operation generally requires highly trained labour.

CVD and Variations

In conventional Chemical Vapour Deposition (CVD), a substrate is exposed to a volatile precursor, which reacts on the substrate surface, to form a solid product (Seshan, 2002). CVD generally produces nanometer thick coating only, and requires a relatively expensive and complex deposition chamber, and/or vacuum system (Meille, 2006). Because CVD does not generate enough surface area to achieve sufficient reactor productivity, Meille (2006) discarded the technique as a suitable method for catalyst production.

Choy (2003) provided an exhaustive review of CVD techniques and variations, partially based on his own work. Among the techniques reviewed is Aerosol-assisted CVD. This consists of dissolving catalyst chemical precursors into an organic solvent. The precursor solution is atomized and delivered into a heated zone, where the solvent is rapidly evaporated or combusted. The chemical precursors undergo subsequent decomposition and/or chemical reaction near, or on, a heated substrate to deposit the desired film. One variant of the technique is Electrostatic spray-assisted vapor deposition, where the atomized droplets are sprayed across an electric field, enhancing chemical deposition efficiency (>90%). Using this technique, a 250 μ m thick Y₂O₃–ZrO₂ film was produced on a Ni-alloy substrate.

Choy and Seh (2000) also reported on a technique named Flame-assisted vapor deposition, called Flame spray deposition by Thybo et al. (2004). The technique consists of mixing organo-metallic precursors into water and combustible organic solvent. During deposition, the precursor solution is atomized and propelled by compressed air into an open flame from a Bunsen burner. The precursors are then converted into nanometer-sized metal or metal-oxide particles. Choy and Seh (2000) produced 100 μ m thick Ni–Al₂O₃ coatings, whereas Thybo et al. (2004) reported Au/TiO₂ coatings up to 150 μ m. A disadvantage of the technique

is that the flame temperature is hard to control, causing a potential reproducibility problem.

4.1.2 Liquid Phase Techniques

EPD

Electrophoretic Deposition (EPD) consists of the application of an electric field between electrodes, making charged particles in suspension migrate to the oppositely charged substrate, causing discharge, and formation of a film (Seshan, 2002). The cathode is generally the substrate to be coated, while the anode is either an aluminum or stainless steel foil (Meille, 2006). Ferrari et al. (2006) coated $\text{Al}_2\text{O}_3\text{-ZrO}_2$ films with EPD, reaching 50 μm . Ceramic films, close to 300 μm thick, were reported by Besra and Liu (2007).

Suspension

The suspension technique, also called slurry, consists in mixing a powder (catalyst support or catalyst itself), an organic binder (usually an organic polymer), an acid, and a solvent (Meille, 2006). Films are prepared by either wash, spin, dip, air spray, or brush coating on a substrate. The coated substrate is then dried and calcined to remove the water and organic material, and to develop the final ceramic structure.

Particle size is an important factor affecting coating adherence on the substrate. Agrafiotis et al. (1999), using washcoating on cordierite honeycombs, reported that particles in the range of 2 μm led to much more adherent layers than 17 or 52 μm particles. Germani et al. (2007) successfully coated on stainless steel micro channels 10-50 μm thick layers of γ alumina powder ($D_{p,ave}$ 3 μm) and Cu-ZnO/ Al_2O_3 commercial catalyst ($D_{p,ave}$ 28 μm). Methylhydroxyethyl cellulose as binder and no acid led to the best catalyst activity and adhesion.

Valentini et al. (2001) created 5-80 μm thick films of $\gamma\text{-Al}_2\text{O}_3$ using dip coating on aluminum slabs and $\alpha\text{-Al}_2\text{O}_3$ tubes. Adherence was not clearly reported for their 80 μm thick coating. (Meille et al., 2005) reported coating layers 1-200 μm thick using a $\gamma\text{-Al}_2\text{O}_3$ suspension, including a dispersant agent. Adherence was not clearly reported for their thicker coatings (~ 200 μm).

Sol-Gel Technique

A sol is a dispersion of solid particles in a liquid where the particles are small enough to remain suspended indefinitely by Brownian motion. A gel is a substance that contains a continuous solid skeleton enclosing a continuous liquid phase (Brinker and Scherer, 1990). The sol-gel technique consists of mixing an organo-metallic precursor of the material to deposit with a suitable solvent. Additives can be added to control the viscosity and surface tension of the sol-gel. Enough time must be allowed for the sol to age, allowing gelation. The more complex the oligomers formed, the thicker the coating, but the risk of cracks is then higher (Meille, 2006). The sol-gel technique generally produces layers around 10 μm thick. Cini et al. (1991) coated $\gamma\text{-Al}_2\text{O}_3$ film on a $\alpha\text{-Al}_2\text{O}_3$ tubes. They reported films up to 100 μm thick, however cracks could not be avoided with layers thicker than 10 μm .

Modified Sol-Gel Technique

The modified sol-gel technique can be seen as a hybrid between the suspension and sol-gel techniques. Calcined ceramics are dispersed in the sol-gel matrix to prevent large strain in conventional sol-gel films, occurring during heat treatment. Commercial catalyst powder can substitute for ceramic, but sol particles can block partially active sites and reduce catalyst activity (Meille, 2006). Sidwell et al. (2003) used this technique to coat a commercial Pd 5 wt% $\gamma\text{-Al}_2\text{O}_3$ onto a cast-alumina disk. Boehmite was used as sol agent with acetone as the solvent. The mixture was sprayed in thin layers, and a flow of nitrogen partially removed the solvent between each layer. The process was continued until the film thickness reached 90 μm .

Modified sol-gel techniques are commonly used in micro-channel reactor technologies. For instance, Sohn et al. (2007) obtained a 50 μm alumina coating for their methanol fuel micro-reactor by mixing $\alpha\text{-Al}_2\text{O}_3$ powder, aluminum isopropoxide, ethanol, water and nitric acid. Peela et al. (2009) obtained good coating adherence properties, measured by sonication, with $\gamma\text{-Al}_2\text{O}_3$ coating. The modified sol, containing $\gamma\text{-Al}_2\text{O}_3$ powder, polyvinyl alcohol, and boehmite, was washcoated on a stainless steel micro-channel to obtain coatings ~ 65 μm thick.

4.1.3 Surface Pretreatment

Surface pretreatment can be applied to increase the adherence of a catalyst layer, almost independently of the coating technique.

Thermal oxidation: Thermal oxidation consists of creating a thin oxide layer ($\sim 1 \mu\text{m}$ thick) by thermal treatment in air. It is usually applied to a Fecralloy substrate (Fe 72% Cr 22% Al 5.0%) above 840°C (Meille, 2006). Enger et al. (2008) used the thin oxide layer to impregnate RhCl_3 in a Multi-Channel Reactor (MCR) for partial oxidation of methane and propane.

Chemical treatment: Surface roughness can also be affected with chemical treatment. Depending on the nature of the metal support, by immersing the metal substrate into a strong acid or base, etching and/or surface oxidation can occur (Meille, 2006; Valentini et al., 2001).

Mechanical treatment: Sand-blasting can also be used to create surface roughness (Hawthorne et al., 2004), and it is applicable to any metal substrates that can withstand the mechanical stress of the process. However, it is limited to areas within the line of sight.

Primer application: Some authors (Valentini et al., 2001; Park et al., 2005; Peela et al., 2009) reported using sol-gel technique to create a thin oxide layer, as a primer for a second thicker layer. For instance, Park et al. (2005) used an alumina primer on stainless steel, before coating a commercial $\text{Cu/ZnO/Al}_2\text{O}_3$ catalyst.

4.1.4 Coating Strategy

After reviewing different coating techniques, we selected the modified sol approach for several reasons: (1) It allows the coating of both lab-made and commercial catalysts. (2) The equipment required is relatively inexpensive (e.g. compared to plasma technique) and available at UBC. (3) Solid material and solvent (usually water) are relatively inexpensive and non-toxic. (4) UBC has some expertise in coating alumina with modified sol (Hawthorne et al., 2004).

Coating methodology is often under-reported in the multi-channel/ micro reactor literature, where authors give minimal details of their procedure or the effects of coating parameters. In this chapter, we show most of the results obtained during our quest to develop a methodology for coating lab-made and commercial reforming and combustion catalysts. The next chapter focuses on solving coating issues related to the catalysts selected for the MCMR prototype.

4.2 Materials

4.2.1 Metal Substrate

Experiments were generally conducted on austenitic Stainless Steel (SS) 304, no. 4 finish plates. Metal thickness was generally gauge 24 (0.635 mm), but gauges 22 (0.792 mm) and 20 (0.953 mm) were also tested. Fecralloy (Fe 72% Cr 22% Al 5.0% Y 0.1% Zr 0.1%) plates, 1 mm thick (GoodFellow), which allow thermal treatment for surface oxidation, were also tried. Most plates were sheer cut to 39.5 mm x 39.5 mm.

4.2.2 Modified Sol

Boehmites

Various boehmites (AlOOH) (see Table 4.1) were mixed with water to create a sol. Initially, experiments were conducted with the Soltonerde P2 boehmite, but after the initial stock was exhausted, we could not buy the same product again, since the company had been purchased by Sasol. Sasol Disperal P2 was found to be the closest product available. Sasol Disperal P3 has the characteristic of not having nitrate, but instead acetate, as a dispersion agent. Unless specified otherwise below, Sasol Disperal P2 was used.

Carrier

Table 4.2 shows properties for the various carriers tested in this chapter. $\alpha\text{-Al}_2\text{O}_3$ is a common support for reforming catalyst. We used two types of $\alpha\text{-Al}_2\text{O}_3$, one from Sasol and the other one from Alcoa. Alcoa sold their alumina division to

Table 4.1: Boehmites Tested and their Properties

Name (Code Name)	Supplier	Particle size	BET Sur- face Area m ² /g	Al ₂ O ₃ content wt%	Nitrate Content wt%
Soltonerde P2 (Co)	Condea	< 25 μm : 31% <45 μm : 70%	287	73.1	3.5
Disperal (P0)	Sasol	< 25 μm : 69% <45 μm : 83%	181	78.1	-
Disperal P2 (P2)	Sasol	< 25 μm : 40% <45 μm : 83%	287	74.4	3.5
Disperal P3 (P3)	Sasol	< 25 μm : 4.5% <45 μm : 11%	320	67.8	6.9 (Ac- etate)

Brenntag Specialties, and alumina A-16 was not always available for testing. γ -Al₂O₃ has a much higher surface area than α -Al₂O₃, but undergoes a phase change at $\sim 850^\circ\text{C}$ in air (Gitzen, 1970), making it less likely to be used in conventional Steam Methane Reforming (SMR). However, since our Pd/Ag membrane must be operated below 600°C , γ -Al₂O₃ was considered as option. We also investigated alternatives to alumina: magnesium aluminate spinel (MgAl₂O₄), known for its thermal and chemical stability (Guo et al., 2004), and ceria oxide (CeO₂), which is known to act both as promoter and carrier (Laosiripojana and Assabumrungrat, 2005).

Promoter and Catalyst Precursors

Table 4.3 lists all promoter and catalyst precursors covered in this chapter. Ni is commonly used as an SMR catalyst (Twigg, 1997). It is relatively inexpensive compared to noble metals. Noble metals (Rh, Ru, Ir) are, however, more active than Ni per unit mass (Berman et al., 2005). They are also more resistant to carbon deposition and sulfur poisoning. Their cost is usually prohibitive in conventional SMR, but since MCMR has the potential to use much less catalyst, as discussed in Chapter 3, noble metals can be considered. In this work, we tested Ru, being significantly less expensive than Rh.

Mg, Mn, Ca and K are common promoters for SMR, while using Ni as catalyst.

Table 4.2: Carriers Tested and their Properties

Name (Code Name)	Supplier	Density ^a	$D_{p,ave}$ ^a	BJH Pore Volume	BET Surface Area
		g/cm ³	μm	ml/g	m ² /g
A-16SG α -Al ₂ O ₃ (A-16)	Alcoa, Brenntag Specialties	2.19	0.4	0.05	9.5
Ceralox α -Al ₂ O ₃ (Ceral)	Sasol Alumina	2.2	0.27	0.04	7.8
Baikalox CR125 γ -Al ₂ O ₃ (CR125)	Baikowski	0.15	0.3	0.78	105
Cerium (IV) oxide (CeO ₂)	Alfa Aeser		5	0.007	0.68
Magnesium Aluminate Spinel (MgAl ₂ O ₄)	Atlantic Equipment Engineers		1-5	0.002	0.54

^aSupplier Data

Promoters are used to increase the pH of the carrier. Acidic sites promote coke formation and polymerization (Twigg, 1997).

For Methane Catalytic Combustion (MCC), Pd is known to be the most active catalyst (Lee and Trimm, 1995), and it is also less expensive than Pt, which is also used for MCC. A more affordable alternative CeO₂–ZrO₂ was also investigated. This has shown some activity for MCC (Bozo et al., 2000).

Commercial Catalyst

Table 4.4 lists all commercial catalysts tested for coating. RK-212 was received in pellet form and was mechanically crushed and sieved. To obtain particle size “ $\ll 25 \mu\text{m}$ ”, we passed $<45 \mu\text{m}$ powder 3-4 times through a mechanical crusher (Fritsch, Disk Mill PULVERISETTE 13) with a minimum distance between the two crushing disks.

Binder

In a limited number of experiments, a binder was added to the modified sol. In this work, we used polyethyleneimine, branched (MW = 10,000) from Alfa Aeser.

Table 4.3: Metal Precursors Tested

Name (Code Name)	Supplier	Purity
Catalyst Precursors		
Nickel(II) nitrate hexahydrate (Ni Nitr.)	Alfa Aesar	98%
Ruthenium(III) chloride hydrate (RuCl ₃)	Alfa Aesar	99.9% , Ru 38% min
Ruthenium(III) nitrosyl nitrate (Ru Nitr.)	Alfa Aesar	Ru 31.3% min
Palladium(II) nitrate hydrate (Pd Nitr.)	Alfa Aesar	99.9%
Copper(II) nitrate hemi(pentahydrate) (Cu Nitr.)	Alfa Aesar	98%
Promoter Precursors		
Calcium nitrate tetrahydrate (Ca Nitr.)	Alfa Aesar	99%
Magnesium nitrate hexahydrate (Mg Nitr.)	Alfa Aesar	98%
Potassium nitrate (K Nitr.)	Sigma-Aldrich	99%+
Manganese(II) nitrate tetrahydrate (Mn Nitr.)	Alfa Aesar	98%+
Zirconium dichloride oxide octahydrate (ZrCl ₂)	Alfa Aesar	99.9%

Table 4.4: Commercial Catalysts Tested

Names (Code Name)	Supplier	Composition wt%	Particle Size μm	BJH Pore Volume ml/g	BET Surface Area m ² /g
RK-212 (RK-212)	Haldor Topsoe	Ni 15%, MgO ^a 25-30%, K ₂ O 1-2%, CaO 1-4%	various sieved size: \ll 25 - <63	0.06	14.3 - 8.3
#11749 Ru 5%/ γ -Al ₂ O ₃ (Ru 5%)	Alfa Aesar	Ru ~5%		1.3	225
#11711 Pd 1%/ γ -Al ₂ O ₃ (Pd 1%)	Alfa Aesar	Pd 1 %		0.58	189
#11713 Pd 5%/ γ -Al ₂ O ₃ (Pd 5%)	Alfa Aesar	Pd 5 %		0.45	145

^aMgO is in the form of MgAl₂O₄

4.3 Method

Figure 4.1 shows the various steps and options for all catalyst coatings investigated in this chapter. There were three main stages, with an optional fourth one. First, a metal substrate was sand-blasted to create roughness on the surface, and to give physical support for the catalyst. If Fecralloy was used, calcination could be performed to create a layer of aluminum oxide on the surface. The surface had to be cleaned to avoid contamination from dust and grease.

The second stage consisted of preparing the modified sol and applying it to the metal substrate. The modified sol was composed of a solvent (usually distilled water), boehmite, a carrier or commercial catalyst, and a small amount of acid to adjust the pH, generally <5-6. Optionally, metal catalyst and promoter precursors were added. The modified sol was ball-milled overnight. The pH usually changed after the ball-milling and was readjusted before coating. We tested four different coating techniques: brushing, dip coating, cold substrate and hot substrate air-spray (also named “cold spray” and “hot spray”) coating.

In the third stage, coated plates were first dried at 65°C for 10+ min and then calcined at 650°C overnight. The calcination step transformed boehmite into γ -Al₂O₃ and the metal precursors into their oxide form. Since our MCMR is expected to operate below 600°C, calcination aims at pre-aging the carrier or catalyst as well. Multi-layer coating could be achieved by repeating stages 2 & 3 as many times as needed. Impregnation of metal catalyst or promoter precursors may be done in an additional (fourth) stage.

4.3.1 Sand-Blasting

Sand-blasting was performed inside a specially designed glove box, which includes a compressed air spray gun and a vacuum to extract the dust. The sand used was brown alumina (Manus Abrasives) at various particle sizes: from coarse particles (grit # 4) to finer particles (grit # 80). The air blasting pressure could be varied from 0 to 6.9 barg (100 psig). For most cases, grit # 80 with 3.5 barg (50 psig) blasting pressure, was employed. After the sand-blasting, the plates were manually flattened.

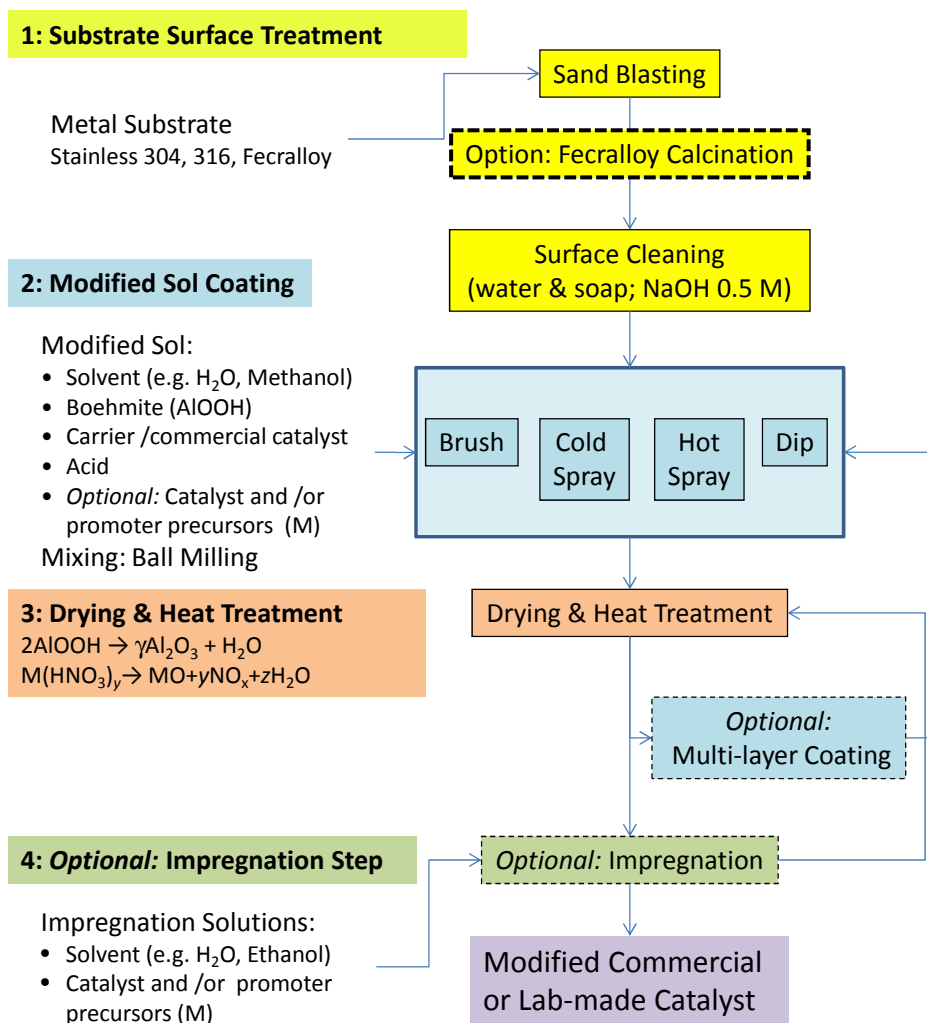


Figure 4.1: Initial Catalyst Coating Method

4.3.2 Substrate Cleaning

Sand-blasting and plate flattening can introduce dust and oily contaminant on the substrate surface. Various methods were tested to remove contaminant, with various cleaning solutions (distilled water, water with detergent, acetone, NaOH solution), aided by scouring sponges, gloves, or sonic bath. In this chapter, water with detergent or ~ 0.5 M NaOH solution, followed by a distilled water rinse, was generally employed.

4.3.3 Modified Sol Parameters

Carrier or commercial catalyst molar concentration (mol/L): This parameter affects directly the viscosity of the modified sol. Therefore, the coating thickness obtained with brush or dip coating is a function of this parameter. For commercial catalysts, since the exact content is not always known, the molar concentrations reported below are based on the molecular weight of their carrier.

Boehmite content (wt%): Boehmite content plays a role in determining the bonding between the carrier or commercial catalyst particles, as well as in the bonding between the particles and metal substrate. We define this parameter as:

$$\text{Boeh. Content} = \frac{\text{Mass Boehmite}}{\text{Mass Boeh.} + \text{Mass Carr. or Comm. Cat.}} * 100 \text{ [wt\%]} \quad (4.1)$$

pH: The pH of modified sol was mainly adjusted with nitric acid, before and after ball milling. Some attempts were also made with formic and acetic acid. Unless specified otherwise, pH data reported in figures are taken after the adjustment made after ball milling, using nitric acid.

Metal content (wt%): Metal catalyst and promoter precursors can be added directly to the modified sol or later, via impregnation. If added with the sol, their concentrations were adjusted to obtain a specific mass fraction after calcination and/ or reduction. We report in all figures the desired final mass fractions (oxidized form for promoters, reduced form for catalysts) rather than precursors metal

concentrations. It is assumed that all nitrates, chlorides and hydrates were totally removed after calcination.

CeO₂/ZrO₂ mole ratio: For CeO₂-ZrO₂ coatings, we used a constant CeO₂/ZrO₂ mole ratio of 3, based on Bozo et al. (2000). ZrO₂ was obtained from ZrCl₂, mixed directly into the CeO₂ modified sol.

Ball Milling

The modified sol was ball milled overnight. Alumina balls of different sizes (1/16 to 0.25”(1.58 to 6.35 mm)), represented about half of the modified sol mass, were added to a container used for ball milling, while about a quarter of the container remained empty.

Life Time of Modified Sol

Modified sol did not age well, and adherence results could differ significantly one week after ball milling. pH tended to increase over time. Cristiani et al. (2005) reported two pathways for acid consumption; surface charging and dissolution:



To keep properties constant, it was best to use the modified sol immediately after ball milling.

Modified Sol Description in Figure Legends

Legend items can be described as follows (Note that some items can be omitted if they have the default value): [Boehmite content, wt%], [Boehmite Code Name (default is P2)], [Carrier Concentration, mol/L], [Carrier code Name], [pH after ball milling and adjustment], [optional items: presence of binder; particle sieved size; acid used (default is nitric acid); solvent (default is distilled water); sonication time, min (default is 15 min)]. To save space, some parameters omitted in the legend are specified in figure captions.

4.3.4 Coating Techniques

Brush Coating

Brush coating was conducted by simply painting the modified sol on the metal substrate using a regular foam brush, available in hardware stores. Thread brushes, and different painting rolls were also tried during screening tests, but results were unsatisfactory, leading to poor coating uniformity.

Dip Coating

Dip coating consisted of dipping the metal substrate in a beaker filled with modified sol. A lab-made apparatus, consisting in an electric motor with its shaft attached to a string, and a voltage regulator to control the rotational speed, allowed the withdrawal of the dipped sample at constant speed, 0.2 to 8.3 mm/s.

Cold Substrate Air-Spray Coating (Cold Spray)

Cold spray coating was conducted by spraying the modified sol using an air spray gun (Graco, Delta Spray, model 239-71XEO2A). This spray gun utilizes compressed air at ~ 1.7 barg (25 psig). The sol was sprayed by quickly sweeping the gun above the substrate. Between each sweep, air was blown over the substrate to evaporate excess water.

Hot Substrate Air-Spray Coating (Hot Spray)

Hot spray coating consisted of spraying the modified sol with the same technique as for the cold spray, while the metal substrate was heated by a plate heater. The temperature of the heater ($> 100^\circ\text{C}$, up to 180°C) was not controlled, but remained above the water boiling point throughout the spraying. Each sweep allowed a very thin layer of catalyst to be coated, while most of the water contained in the modified sol evaporated instantaneously.

4.3.5 Impregnation

Wet impregnation

Wet impregnation consisted in immersing the catalyst plate, containing the metal support, the carrier and previously impregnated metals, into a solution of metal precursor(s). Plates were left in solutions for 2 to 24 h at ambient temperature. Screen tests were also performed at 65°C, but led to excess metal deposition on the carrier surface. Excess liquid was removed by gravity by tilting the plate of a $\sim 80^\circ$ angle. Drying was performed in stages. First, plates were allowed to air dry for ~ 2 h; second, plates were put in an oven at 110-120°C for a time ranging from 4 h to overnight. Dried samples were then calcined at 650°C overnight for 24 h.

Impregnation Solutions Parameters

The metal M precursors (M Nitr.) concentrations were estimated according to the following equations:

$$[\text{M Nitr.}] = \frac{x_M}{x_{\text{carr}} \nu_{p,\text{carr}}} \frac{1}{M_{\text{WM}}} \frac{1}{\sigma_M} * 1000 * \text{Corr.} \quad [\text{mol/L}] \quad (4.4)$$

where x_M is the desired metal mass fraction in the catalyst; x_{carr} is the estimated carrier mass fraction (*carr*); ν_{carr} is the carrier pore volume; σ_M is the stoichiometric molar ratio between the reduced metal and the metal precursor; and *Corr.* is a correction factor based on Energy-Dispersive X-ray Spectroscopy (EDX) measurement or analytical balance of the final metal content. *Corr.* was usually ~ 0.75 .

4.3.6 Analytical Instruments

SEM-EDX

Scanning Electron Microscopy (SEM) images were obtained by a Hitachi 2-3000N. Images were taken with an acceleration voltage of 20 kV, at 1.5×10^{-3} Pa. EDX instrument (Advanced Analysis Technologies), used a silicon-lithium X-Ray detector, with resolution of 133 eV. The magnification was usually set at 350x while measuring composition with EDX. Samples were Au–Pd sputtered to overcome

the electrical insulation of the ceramic material.

Surface Area - Pore volume - Pore size

A Micromeritic ASAP 2020 analyzer was used with nitrogen to measure the Brunauer, Emmet and Teller (BET) surface area, Barrett, Joyner and Halenda (BJH) desorption average pore size and BJH desorption pore volume.

Optical microscope

To obtain coating surface images, a Nikon Eclipse MA200 microscope was used, combined with a Nikon DS-Fi1 camera, having a resolution of 2560 x 1920 pixels.

4.3.7 Metrics

In this chapter, coating quality was characterized by two variables: the coating adherence and coating thickness.

Coating Adherence

Coating adherence was determined by the coating resistance to erosion by cavitation. We measured the dried mass of the catalyst before and after immersion in a sonic bath (Esma Ultrasonic System E386) during 15 min, and calculated the % mass losses. This technique, also named sonication, was also used by earlier authors (Germani et al., 2007; Stefanescu et al., 2007). In this work, we set the acceptable limit at 20 wt% loss.

Each point in plots featuring the “Mass Loss vs Average Thickness” corresponds to thickness and adherence measured on one sample.

Coating Thickness

To measure the coating thickness, a thickness meter was used, Positector 6000-1 by Defelsko, based on the eddy current principle. The thicknesses reported in this chapter are averages of five measured values on each plate after coating and calcination. Four points are near the corners and one at the center of the plate. The meter is zeroed by taking a reading on a clean and flat plate of the same material.

The sand-blasting of the plates induces a “thickness” reading on the meter, which we called “profile noise”. That value was significant, ranging from 20 to $\sim 100 \mu\text{m}$, depending on the roughness achieved by sand-blasting. It was not obvious what roles the profile noise played on the measured coating thickness, with the effect seeming to depend on the coating technique.

We made several conservative estimates to cope with this issue. For all hot spray coating and dip coating samples, we simply subtracted the average profile noise values from the average measured thicknesses. For single layer brush coating, the measured thickness was often smaller than the profile noise. For coatings with similar sol content, and with constant geometric surface area of the plates (length * width), we proceeded as follows. First, we plotted measured thickness versus mass of catalyst. We then performed a linear regression and subtracted the y-axis intercept, $\sim 20 \mu\text{m}$, from the coating thickness reading. With some brush coating samples, we could not find a correlation between the measured thickness and catalyst mass. In those cases, instead of thickness, we plotted the ratio between the mass of catalyst and the geometric surface area of the plates.

For multi-layer brush coating, we did the same subtraction as for single layer coating. However, some thickness data were erroneous, with the thickness becoming thinner with increasing catalyst mass. We then took the thickness and catalyst mass after coating the final layer, and we estimate proportionally the thickness of previous layers knowing the mass of the catalyst.

4.4 Results and Discussion

4.4.1 Metal Surface Preparation

Sand-Blasting

The goal of the sand-blasting is to create maximum roughness on the surface of the plate, while keeping it as flat as possible. Larger particle size (lower grit number) and higher blasting pressure result in more surface roughness, but create more stress on, and deformation of the metal plates. By trial and error, we realized that it was not possible to achieve simultaneously the two goals, and all plates had

to be manually flattened after blasting.

After trial and error, we chose grit # 80, 3.4 barg (50 psig) blasting pressure, and 24 gauge plates. Sand with grit numbers 4 to 56 required higher air pressure, >4.1 barg (60 psig), to flow through the gun, leading to plate deformations that were very difficult to fix manually. Thicker plates (gauges 20 or 22) did not solve the deformation issue, with the plates being much harder to flatten manually.

Figure 4.2 shows the metal substrate before and after sand-blasting. From the tilted view (Part C), we estimated the height of the roughness features, as $\sim 10 \mu\text{m}$. The noise profile reading on this plate was $\sim 80 \mu\text{m}$. This confirmed that our subtracting the noise profile from the coating thickness readings was reasonable.

For the Fecralloy samples (right-hand side), it can be observed (between Part E and F) that the heat treatment at 1000°C for 10 h reduced the roughness of the alloy surface. In future work, heat treatment could be optimized. For instance, Jia et al. (2007) showed that oxidation at 900°C created on the surface a larger number of alumina whiskers than oxidation at 1000°C .

Surface Cleaning

Surface cleaning quickly became a significant step in the process. Figure 4.3 shows contamination on the coating, resulting from improper surface cleaning. The cleaning method evolved slowly during the project. Initially, brushing with tap water with a small amount of soap, followed by a rinse of distilled water was considered sufficient. However, with this method, we regularly had to discard samples because of contamination. We later used a 0.5 M NaOH solution that removed most oily contaminants. However, NaOH solution can affect the anti-corrosion properties of stainless according to electrochemical equilibria diagrams (Pourbaix, 1974). As a final procedure, mostly used in the next chapter, we rinsed the plates with tap water and clean gloves to remove apparent dust, put the plates in a sonic bath with distilled water for 15 min to remove encrusted dust particles, followed by a further 15 min sonic bath with acetone to remove oily contaminants. Plates were then dried at 65°C in an oven before coating.

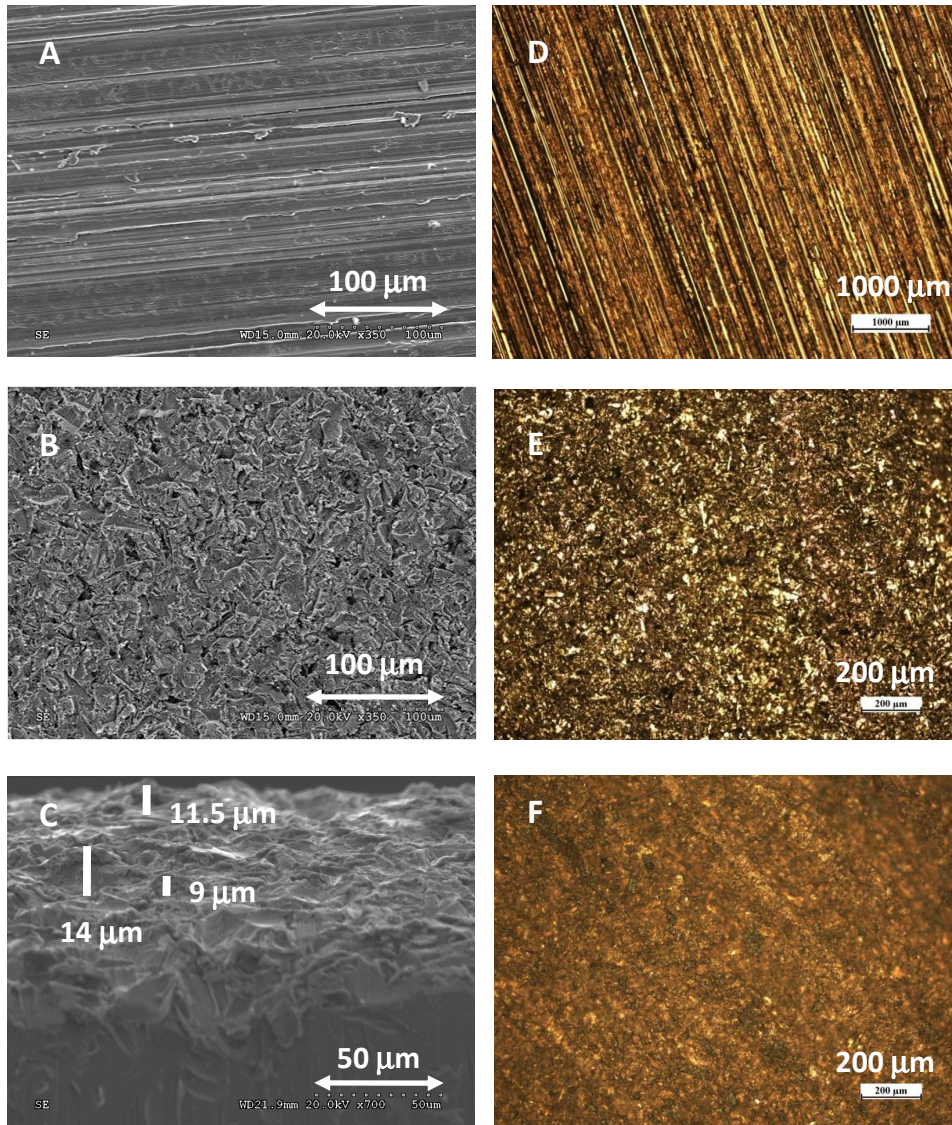


Figure 4.2: Sand-Blasting Images. Left side - SEM images of SS 304 plates: A. Before sand-blasting; B. After sand-blasting; C. After sand-blasting, tilted view. Right side - Optical microscope images of Fecralloy: D. Before sand-blasting; E. After sand-blasting; F. After calcination at 1000°C for 10 h, in static air.

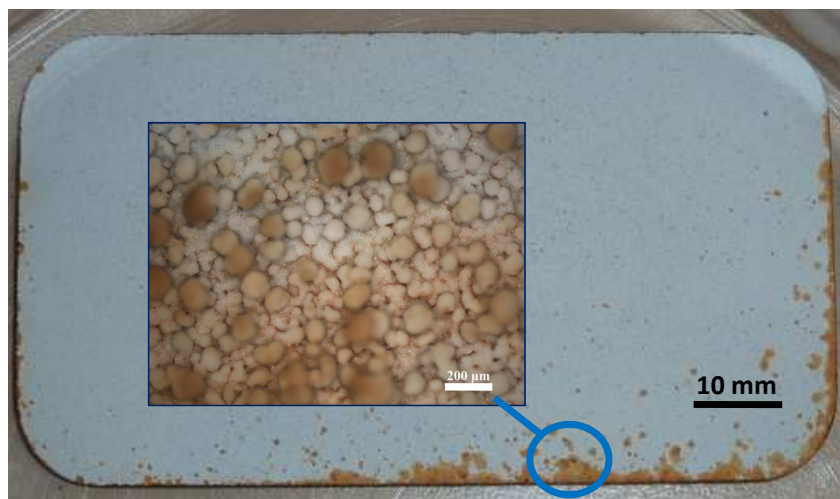


Figure 4.3: Surface Cleaning Issue

4.4.2 Brush Coating, Dip Coating and Cold Substrate Air Spray Coating (Cold Spray)

Brush coating and dip coating were a limited success, and results are provided in the Appendix A. In summary, brush coating gave good adherence with some modified sol, but insufficient thicknesses. Figure 4.4A displays a SEM image of a brush coating sample. Multi-layers brush coating could eventually solve the thickness requirement, but was overly time-consuming. With dip coating, although some samples showed thickness $>80 \mu\text{m}$, adherence quality was unsatisfactory. No satisfactory results were obtained with cold spray coating.

4.4.3 Hot Substrate Air Spray Coating (Hot Spray)

Of all the techniques tested, hot spray coating was the most promising. Figure 4.4, Parts B-F show SEM images of hot spray coatings obtained from various modified sol compositions. One could observe on those images large variations of 3-D surface structures. The following sections present experimental hot spray coating

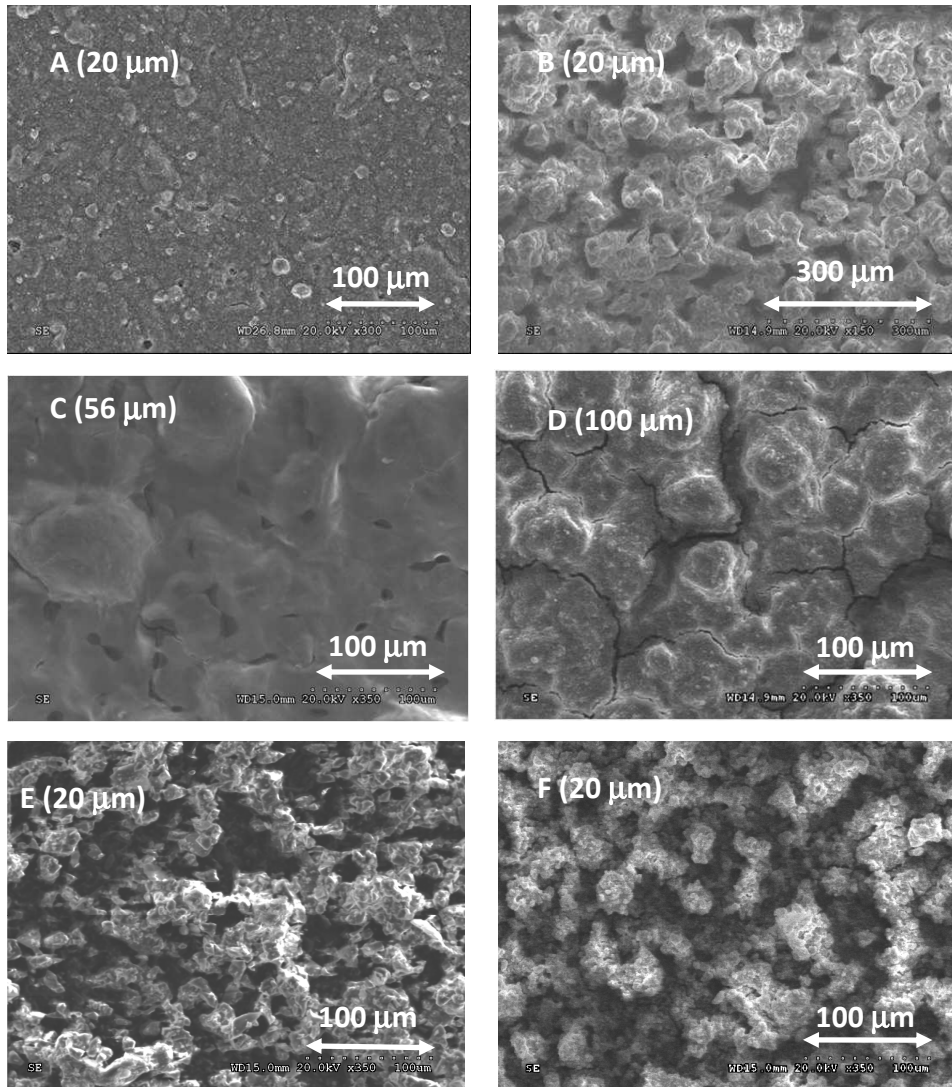


Figure 4.4: SEM Images of Brush Coating and Various Hot Spray Coatings (coating thickness): Brush Coating A. Ni-MgO/ γ -Al₂O₃; Hot Spray Coating B. γ -Al₂O₃; C. Ni-MgO/ α -Al₂O₃; D. Ni-MgO CaO K₂O/ γ -Al₂O₃; E. MgAl₂O₄; F. RK-212.

work conducted over a wide range of conditions.

Hot Spray of Carrier

Figure 4.5 shows coating results with $\gamma\text{-Al}_2\text{O}_3$. Many successful coatings achieved thickness $>80\ \mu\text{m}$, almost reaching $240\ \mu\text{m}$, while a significant number of samples failed the adherence threshold. More samples succeeded in Fig. 4.5B, where $\gamma\text{-Al}_2\text{O}_3$ concentration was generally lower than the results plotted in Fig. 4.5A.

Results were collected over a period of two years, and some conditions might have changed (e.g. operator skills, $\gamma\text{-Al}_2\text{O}_3$ powder manufacturer lot, hot spray air pressure). Hence, trends must be treated with caution. Nevertheless, we can report some general observations: as seen in part B, lower $\gamma\text{-Al}_2\text{O}_3$ concentration $\sim 1\ \text{mol/L}$ reduced variability in adherence results; low pH values of 2 were not necessary to make the coating successful; higher value of boehmite content, $\geq 30\ \text{wt\%}$, can improve the bonding quality.

Some samples in Part A were inserted in the sonic bath for 60 min instead of the regular 15 min time. Three out of four samples were above the threshold quality limit, but samples with the same modified sol content exhibited a significant variations, and their thicknesses were $\sim 50\%$ smaller. Therefore, it is not possible to identify the effect of sonic bath, but common sense suggests that more time in the sonic bath would result in more mass losses.

Figure 4.6 shows how the physical appearance of the $\gamma\text{-Al}_2\text{O}_3$ coatings change while the thickness of the coatings increase. $\gamma\text{-Al}_2\text{O}_3$ coatings form clusters that grow in size while the thickness increases.

Some thickness measurements were taken before and after the calcination step. The measured thicknesses shrunk on average by 11% and the mass was lower by 3-5%. Similar behaviour was observed with Pd 5%/ $\gamma\text{-Al}_2\text{O}_3$ coatings ($\sim 10\%$ thickness reduction). Mass and thickness reduction could be the consequence of phase change from boehmite to $\gamma\text{-Al}_2\text{O}_3$. Thickness standard deviation on the five measurements on each plate was on average $4.4\ \mu\text{m}$ (for 67 plates).

The hot spray coating of $\gamma\text{-Al}_2\text{O}_3$ was the most successful coating pathway covered in this work. For this reason, combined with its valuable high surface area, we selected this coating method to produce our reforming catalyst. In the

next chapter, we present work to reduce the variability in coating bonding quality, which has consequences on further impregnation steps.

Figure 4.7 shows SEM images from a tilted perspective. Part A shows the complex surface structure of a γ -Al₂O₃ coating, while B.1 and B.2 show the structure of a commercial Pd 5%/ γ -Al₂O₃. Pd 5% results are discussed in section 4.4.3.

Figure 4.8 shows coating results with α -Al₂O₃, MgAl₂O₄ and CeO₂-ZrO₂ as carriers. α -Al₂O₃ was the only carrier that produced coatings with acceptable bonding quality. However, more tests are needed for coating thickness of $\sim 80 \mu\text{m}$. Neither MgAl₂O₄ nor CeO₂-ZrO₂ carriers produced coatings with both acceptable thickness and adherence.

For α -Al₂O₃ coating (Part A), observations were similar to those with γ -Al₂O₃, regarding modified sol parameters: lower carrier concentration, higher boehmite concentration ($\geq 20 \text{ wt}\%$) favour adherence, while low pH might not be necessary. Even though results with α -Al₂O₃ were encouraging, we did not investigate further coatings with α -Al₂O₃, since results with γ -Al₂O₃ were considered superior.

Particle sizes for MgAl₂O₄ and CeO₂ were most likely too large and might lack surface area for hot spray coating (see Table 4.2). When we tested their physical properties, we found that those powders were not porous, and hence, were not suitable for impregnation. For this reason, we terminated experiments with those two carriers.

Hot Spray Including Metal Precursors

As shown on Figure 4.1, catalyst and promoter precursors could either be introduced directly in the modified sol or by impregnation, after the coating and calcination of the carrier. However, in Chapter 6, we show that introducing the metal precursors with the modified sol did not lead to active and stable catalysts. Coating results are presented in Appendix A.5. In brief, most samples failed the adherence quality test. For this poor adherence results, combined with poor activity reason, spray coating, including metal precursors, was not investigated further.

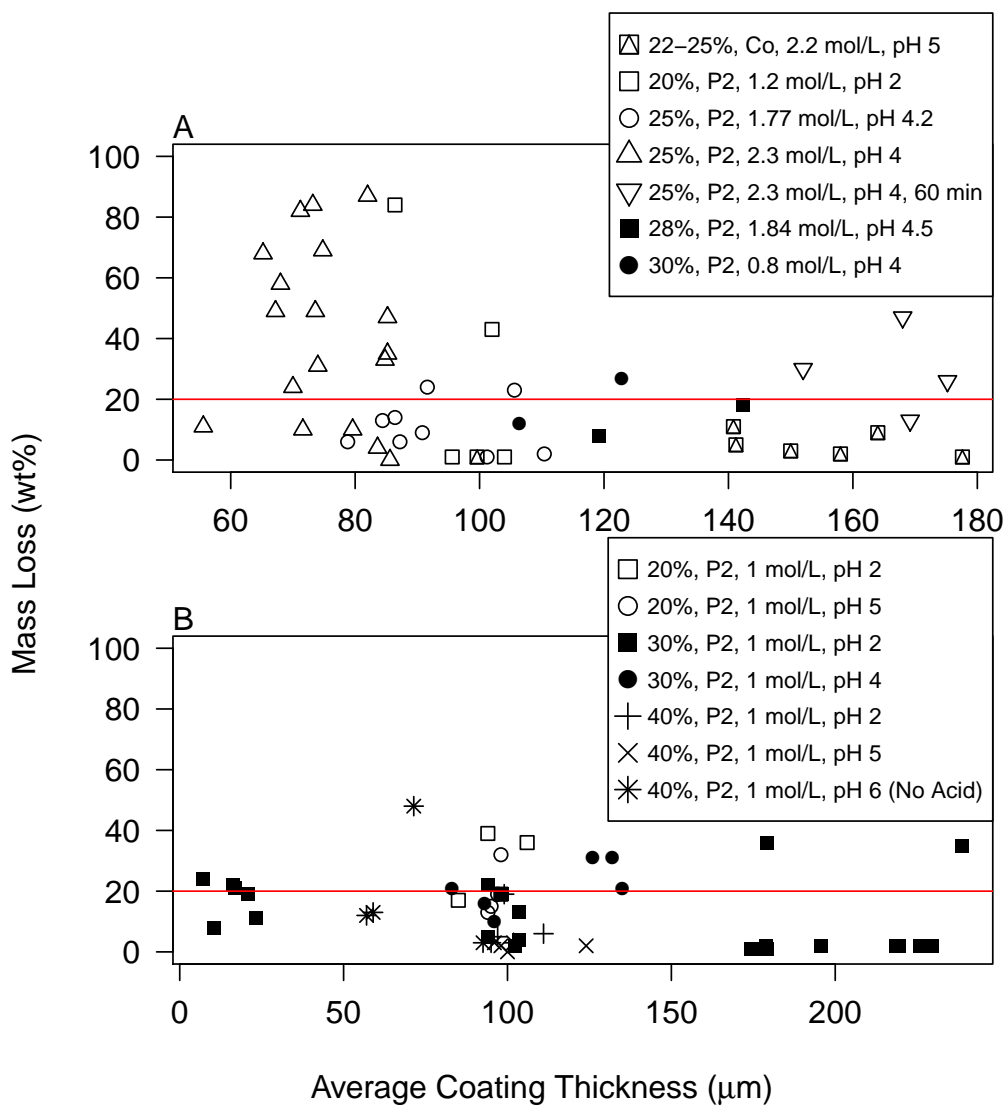


Figure 4.5: Hot Spray Coating of $\gamma\text{-Al}_2\text{O}_3$ Modified Sol, Mass Loss vs Average Thickness: A. Various sol parameters; B. Constant carrier concentration. Line representing the 20% mass loss limit is shown.

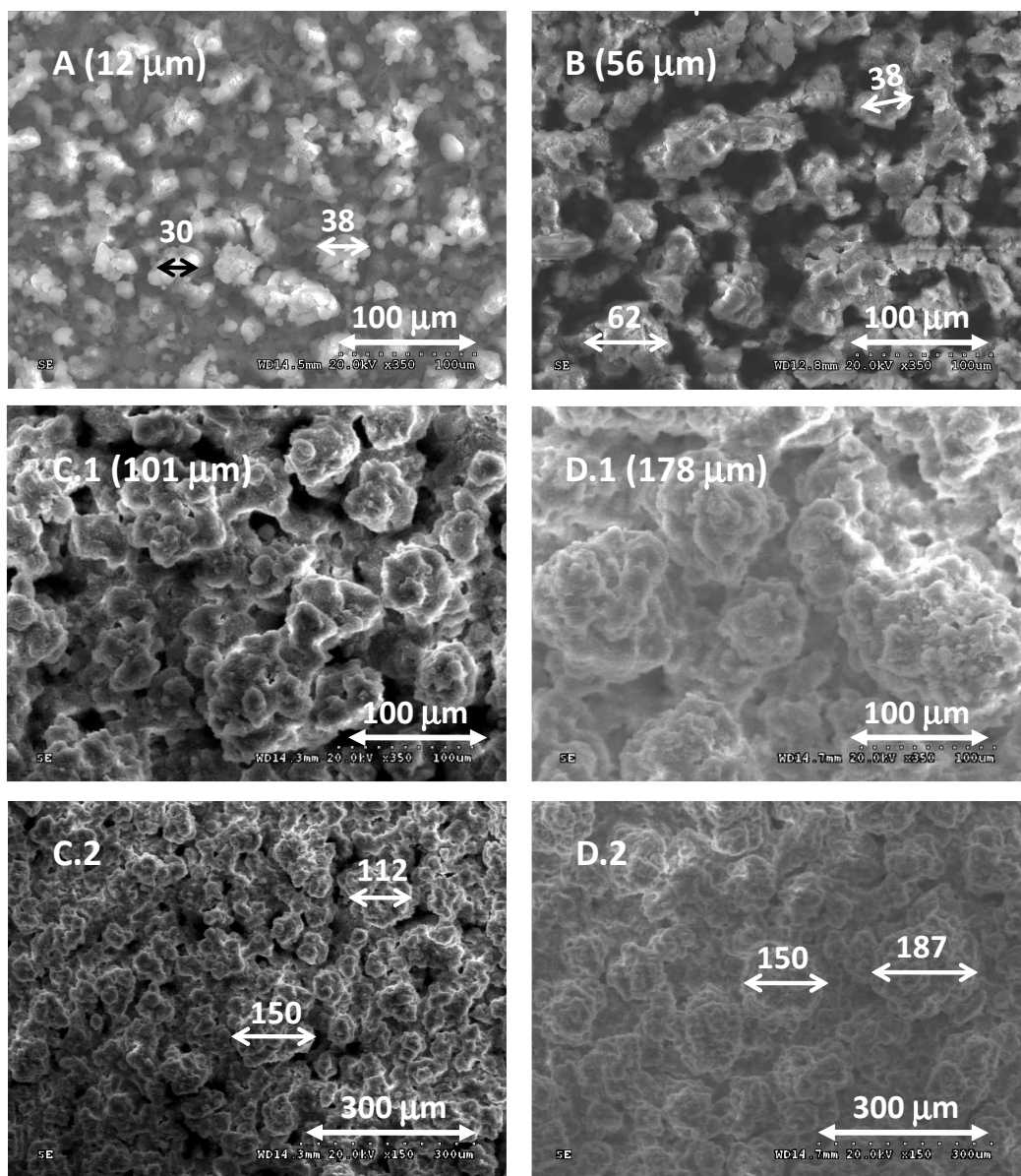


Figure 4.6: SEM Images of γ - Al_2O_3 Coatings of Various Thicknesses (coating thickness). Sol parameters: 25% boeh., 2.3 mol/L, pH 4.

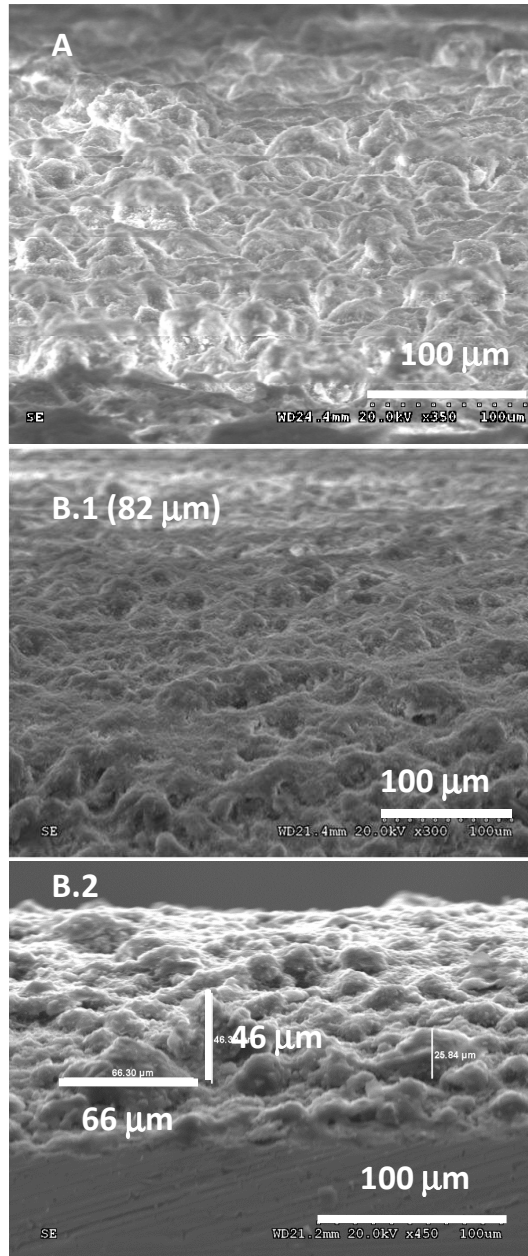


Figure 4.7: SEM Tilted View Images of Hot Spray Coatings: A. $\gamma\text{-Al}_2\text{O}_3$; B. Pd 5%/ $\gamma\text{-Al}_2\text{O}_3$ (coating thickness).

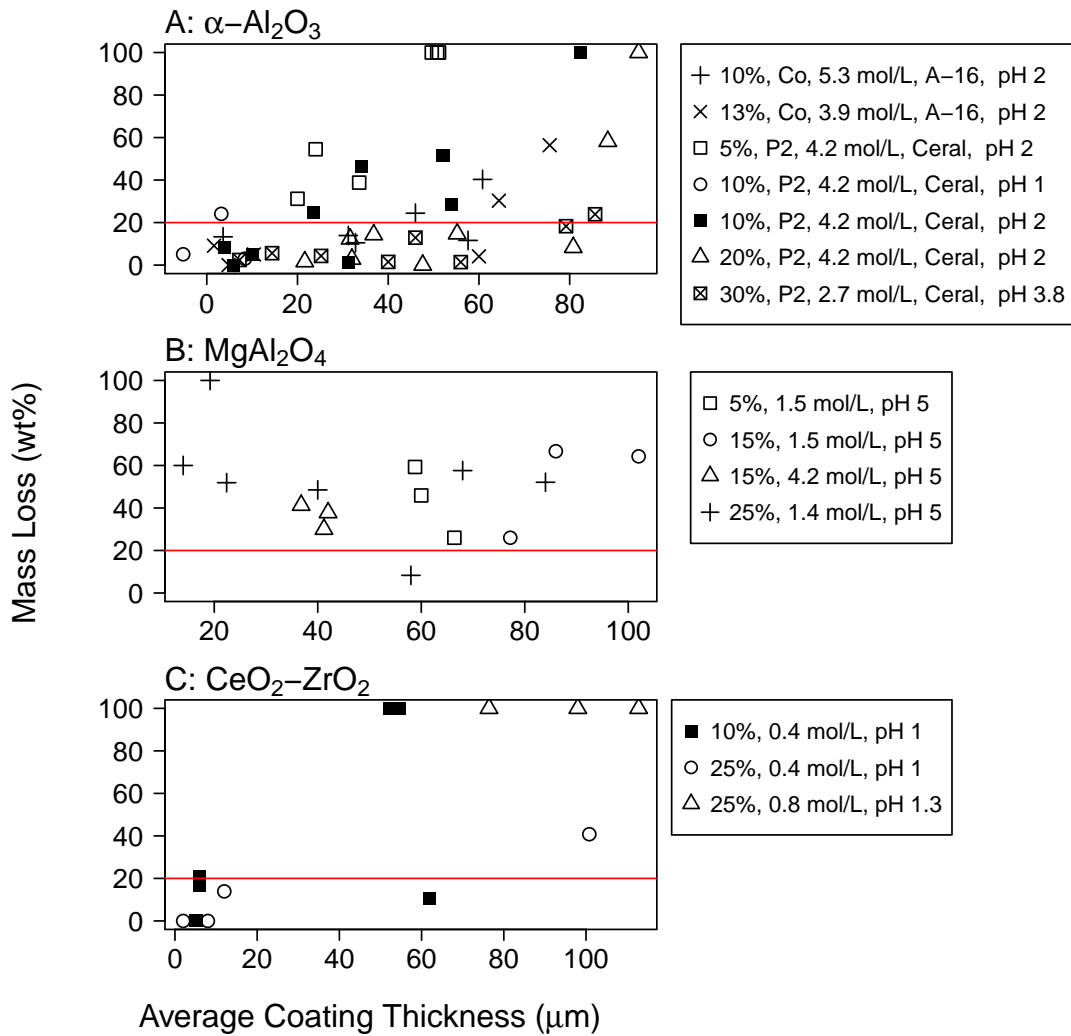


Figure 4.8: Hot Spray Coating of α -Al₂O₃, MgAl₂O₄ and CeO₂-ZrO₂ Modified Sol, Mass Loss vs Average Thickness. Line representing the 20% mass loss limit is shown.

Hot Spray of Commercial Catalyst

Hoping to save time by using ready-to-use catalysts, we also tested various commercial catalysts. The reforming catalyst tested were not selected for the MCMR prototype, and the results are presented in the Appendix A.6. In summary, Ru/ γ -Al₂O₃ catalyst showed good results as well. However, Chapter 6 show that nitric acid adversely affects the activity and stability of this catalyst. Coating of RK-212, a Ni-based/ MgAl₂O₄ catalyst would be possible, but only for sieved particle sizes <25 μ m.

As mentioned in the introduction, Pd was selected as the combustion catalyst. Figure 4.9 shows results with Pd 1 wt% / γ -Al₂O₃ (Part A) and Pd 5 wt% / γ -Al₂O₃ (Part B). Results were in general very positive. Both catalysts achieved good results at 15% boehmite, 0.25 mol/L and pH 5. Furthermore, nitric acid did not adversely affect on the catalyst stability and activity, as shown in Chapter 7. Hence, this modified sol composition was selected for the MCMR prototype.

Temperature Cycles

The MCMR could go through a series of temperature cycles throughout the life of the catalyst. Resistance to temperature cycles was investigated with γ -Al₂O₃ coating, and results are reported in Figure 4.10. After two and three temperature cycles, all adherence tests were excellent, with <10% mass losses. Those results suggested, for catalysts using γ -Al₂O₃ as carrier, that temperature cycles would not be a major issue with respect to coating adherence.

4.4.4 Thickness Verification

Some attempts were made to confirm the thickness meter measurements with SEM images. Figure 4.11 shows SEM images of two commercial Ru 5% / γ -Al₂O₃ coatings. Part A shows one edge of the plate, after polishing. The thickness at the edge was smaller than the measured average thickness at 90 μ m. One could expect that the edge value would be below the average one. Therefore, the thickness measurement could not be confirmed with this image.

Part B is a cross-sectioned view, near the middle of plate. To obtain this image, the sample was covered with epoxy, and then cut with a metal saw. The highly

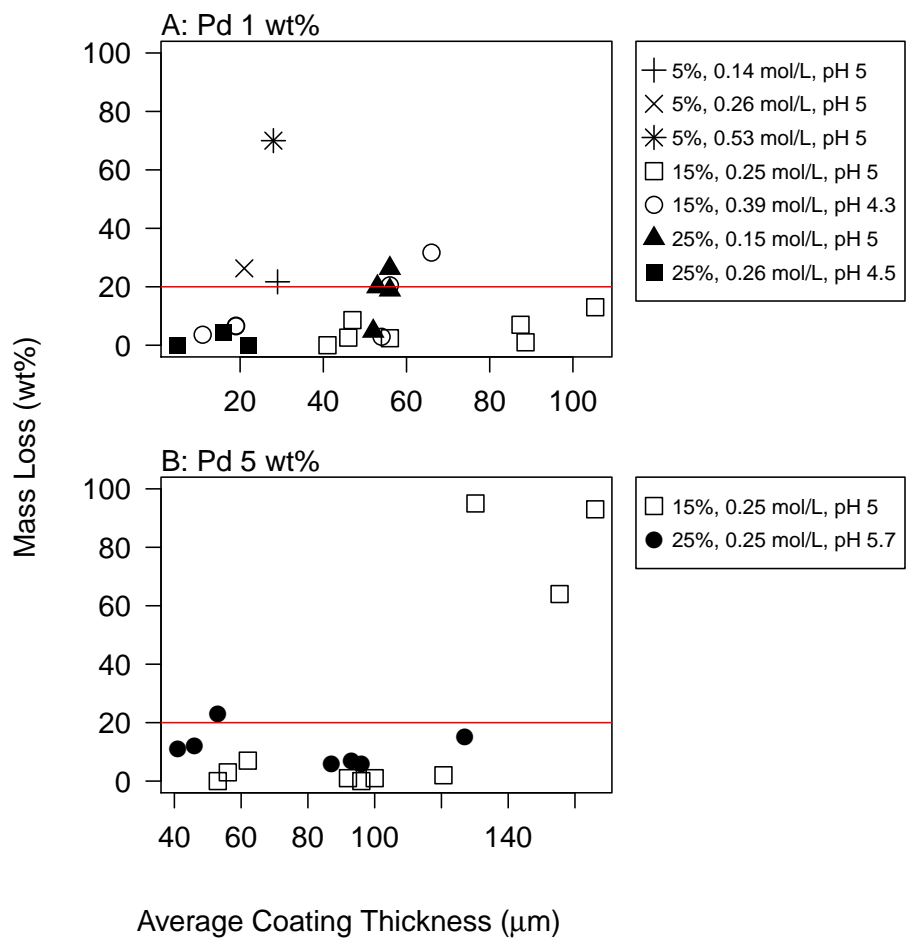


Figure 4.9: Hot Spray Coating of Commercial Pd/ γ -Al₂O₃ Catalysts, Mass Loss vs Average Thickness: A. Pd 1wt%; B. Pd 5 wt%. Line representing the 20% mass loss limit is shown.

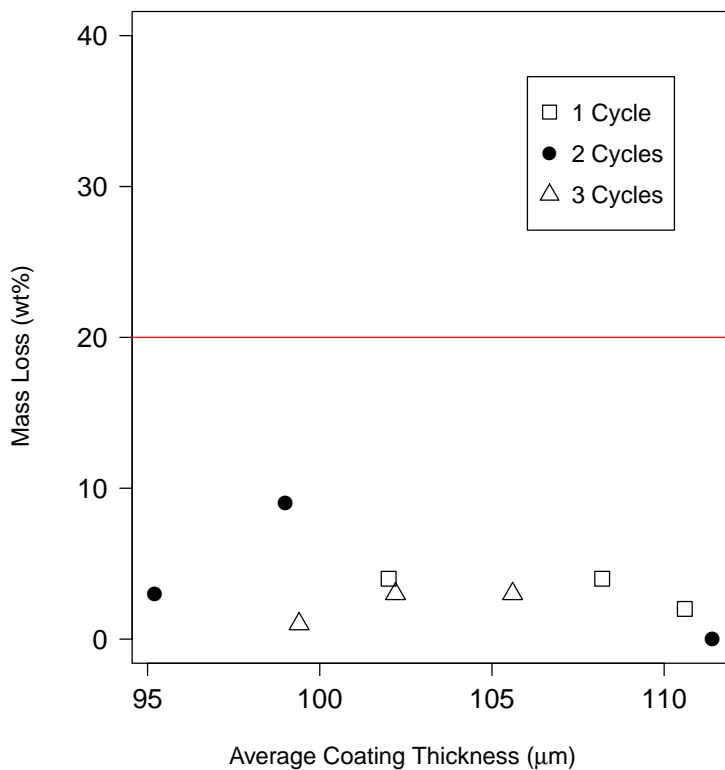


Figure 4.10: Temperature Cycles of Hot Spray Coatings with $\gamma\text{-Al}_2\text{O}_3$ Modified Sol, Mass Loss vs Average Thickness. Sol parameters: 40% boeh. P2, 1 mol/L, pH 5 (no acid); Temperature cycle: Ambient to 650°C in ~ 2 h, hold at 650°C overnight, cool to ambient in ~ 4 h. Line representing the 20% mass loss limit is shown.

porous nature of the $\gamma\text{-Al}_2\text{O}_3$ support made the epoxy unstable under the SEM vacuum. As seen on the right-hand side, the epoxy covered the catalyst layer. Also, it appears that cutting the catalyst plate damaged the catalyst layer, and chunks of stainless steel can be seen mixed with the catalyst. Nevertheless, coating thicknesses measured on the image (114 μm) are close to the average thickness obtained with the meter (120 μm) (after profile noise subtraction).

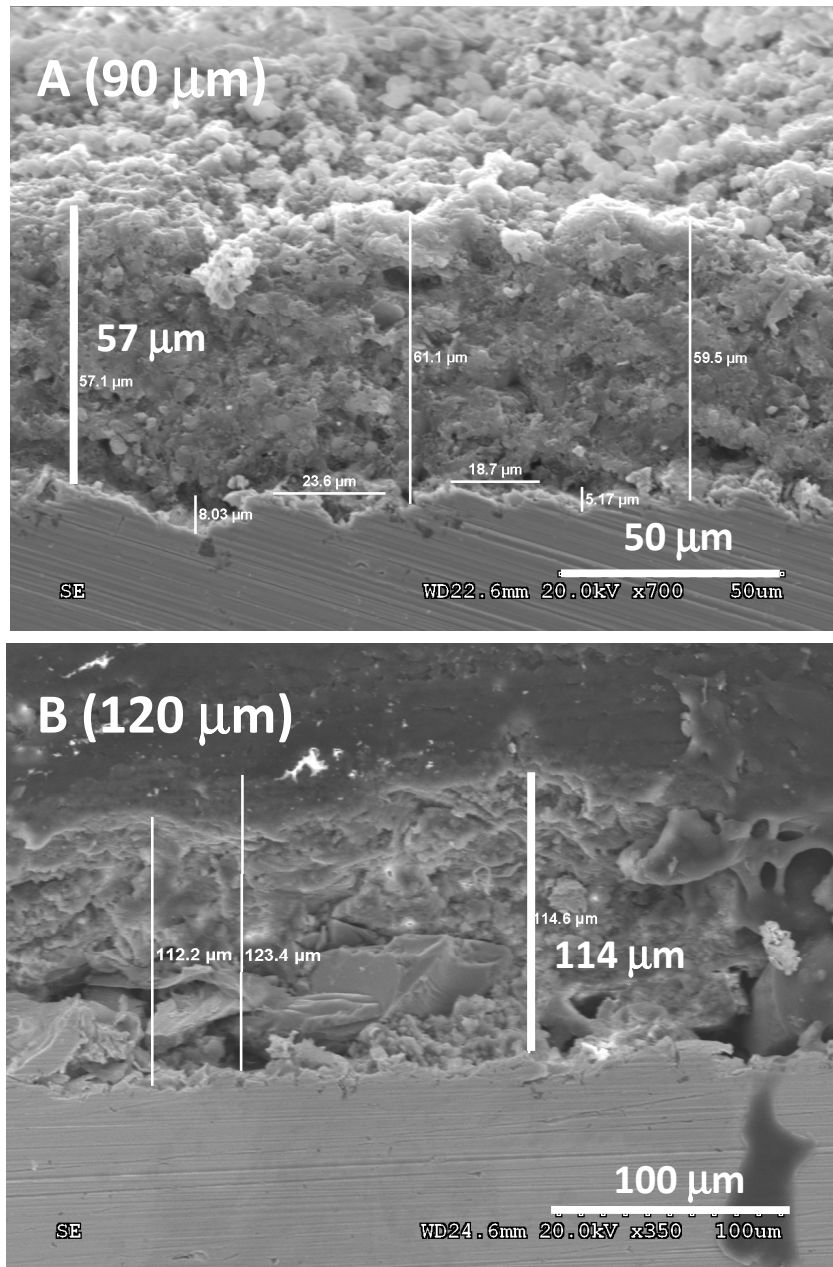


Figure 4.11: SEM Images of Tilted and Side View of Hot Spray Coating of Commercial Ru 5% / γ -Al₂O₃: A. Tilted view of one coating edge; B. Cross-section view of catalyst coating in epoxy cast.

4.4.5 Impregnation

Impregnation can be used to insert promoter and catalyst precursors in subsequent step(s) after carrier coating and calcination. In this section we report preliminary results.

Impregnation issue

Many issues that occurred during impregnation are presented on Figure 4.12.

Cracks: Cracks often occurred during the impregnation. Fig. 4.12A shows a case where a serious network of cracks developed during the process. The solvent added significant stress on the coating. Reducing the number of cracks, that can lead to catalyst delamination, is a key subject of the next chapter.

Metal precursor solubility: Some metal precursors may not be soluble in the chosen solvent. This problem occurred with Pd nitrate that forms PdO in contact with water. In Fig. 4.12B, PdO crystals can be seen on the surface of the γ -Al₂O₃ coating.

Carrier unwanted solubility: In Fig. 4.12C, it can be observed that ethanol solvent dissolved the γ -Al₂O₃ carrier on the edges of the plate. Drying restored the white appearance of the alumina. We were concerned that the pore structure of the γ -Al₂O₃ coating could be affected by dissolution. Since we did not have this issue with water, we did not study this potential problem further.

Metal precursor corrosion on metal support: Figs. 4.12D, E & F are related to the same issue. We believe that chloride anions in RuCl₃ were corroding the stainless 304 support, causing delamination of the catalyst. EDX analysis showed chlorine content up to 8% still present in the catalyst after heat treatment, indicating the difficulty of eliminating this element. In Fig. 4.12E, corrosion is clearly visible on the right side of the metal plate. The corrosion could disturb the bonding between the alumina and stainless. Part F shows an optical microscope image of the coating section not lifted in Part D; large cracks are seen. This issue made us switch to

$\text{RuNO}(\text{NO}_3)_3$ as Ru precursor. Coating results for it are presented in the next chapter.

The delamination due to corrosion gave us some insight about the bonding between the alumina and stainless steel. Mechanical adhesion with the sand-blasting is not sufficient. Hydrogen bonds and weak electrostatic interaction, (Van der Waals forces) could be disturbed by the iron oxidation.

Adherence Testing

Figure 4.13 shows thicknesses and mass losses with various impregnation solutions on $\gamma\text{-Al}_2\text{O}_3$ coatings. Table 4.5 presents the impregnation solution concentrations. Samples with “Sol B” coating, containing 40% boehmite generally performed better than “sol A”, containing only 30% boehmite. Impregnation time did not show a clear winner, but tests with copper indicated that shorter impregnation times better preserve the coating adherence. In the next chapter, we consider causes of coating failures during the impregnation process in greater detail.

Table 4.5: Impregnation Solutions for Figure 4.13

Code Name	Desired Metal Content wt%	Solution Concentration mol/L
Ni-Mg Ca K	Ni 7.9% MgO 1.5% CaO 1.5% K_2O 1.5%	Ni Nitr 1.2; Mg Nitr 0.6; Ca Nitr 0.35; K Nitr 0.32.
Mg	MgO 3%	Mg Nitr 1.1
Cu	CuO 2%	Cu Nitr 0.15

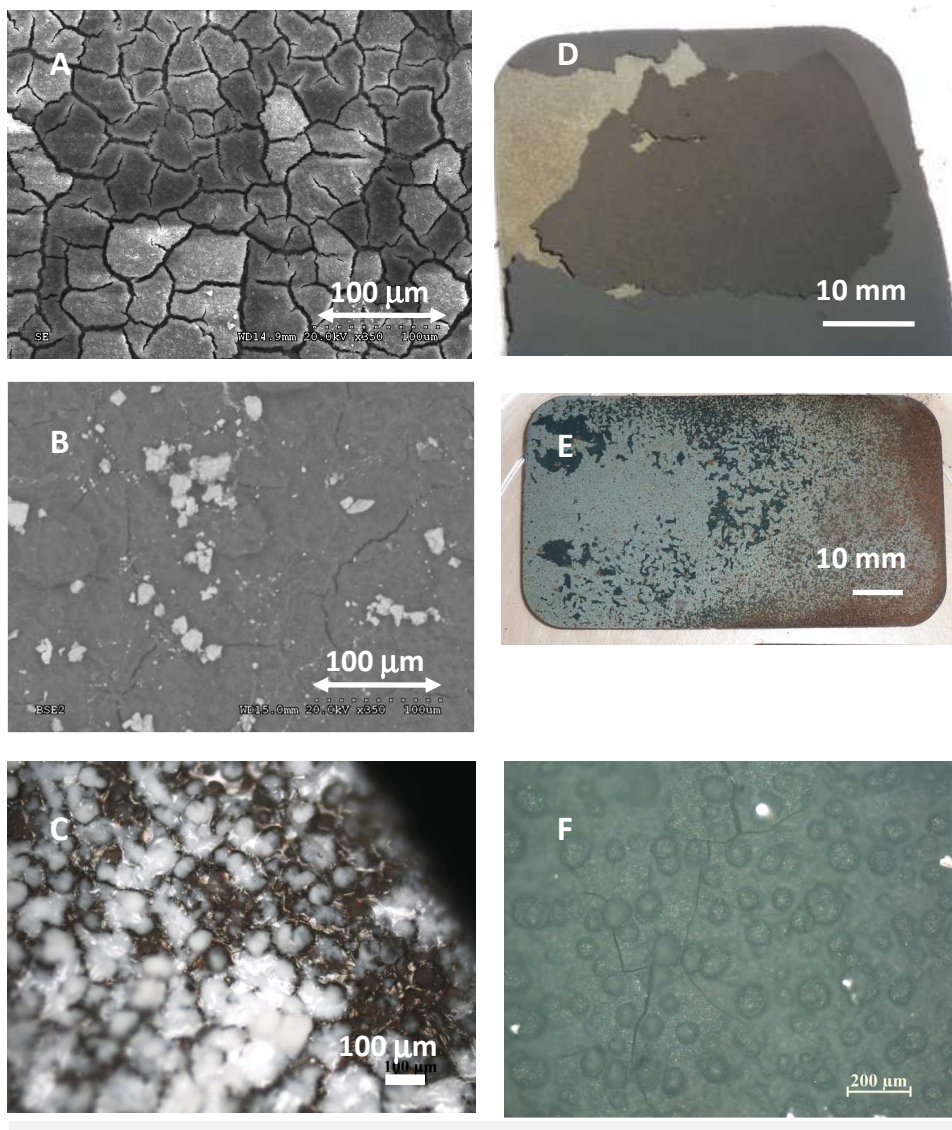


Figure 4.12: Impregnation Issues: A. SEM image of Cu Nitrate on brush coated α - Al_2O_3 ; B. SEM image of Pd Nitrate on γ - Al_2O_3 ; C. Optical image of γ - Al_2O_3 , using ethanol as solvent for impregnation; D. Ru (from RuCl_3)/ γ - Al_2O_3 \sim 3 days after calcination; E. Ru (from RuCl_3)/ γ - Al_2O_3 \sim 1 week after calcination; F. Optical microscope image of coating section not lifted in D.

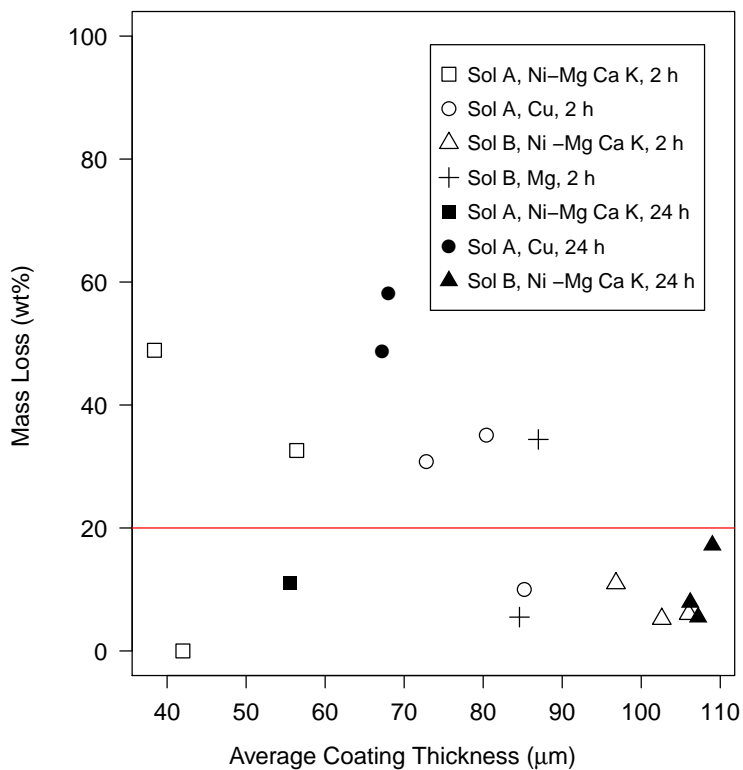


Figure 4.13: Wet Impregnation on $\gamma\text{-Al}_2\text{O}_3$ Support Made by Hot Spray Coating, Mass Loss vs Average Thickness. Modified Sol parameters: Sol A. 25% boeh., 2.3 mol/L, pH 4; Sol B. 40% boeh, 1 mol/L, pH 5 (no acid); See Table 4.5 for impregnation solutions. After impregnation, samples were dried at 65°C for 10+ min, and calcined at 650°C for 24h. Line representing the 20% mass loss limit is shown.

4.5 Conclusions

The work reported in this chapter sought a method to coat SMR and MCC catalysts on metal supports. To be successful, the coatings needed good adherence, measured by sonication, and a coating layer thickness $>80 \mu\text{m}$.

Among the coating techniques tested, hot spray coating was the most promis-

ing. With modified sol containing γ -Al₂O₃, thicknesses up to 240 μ m were obtained, while adherence results were well below the 20% mass losses limit. The coating thickness had a strong effect on the surface structure, with clusters growing along with the thickness. γ -Al₂O₃ coating resisted heat cycles well, making it a strong candidate for the MCMR.

Hot spray coating with α -Al₂O₃ gave encouraging results, but more tests are needed with thickness ≥ 80 μ m. Coating with other carriers, CeO₂ and MgAl₂O₄, did not lead to satisfactory results, likely because of the larger particle size and poor surface area. Introducing promoter and catalyst precursors with the modified sol did not give successful coatings.

Hot spray coating of commercial catalysts with γ -Al₂O₃ as carrier were successful. Pd/ γ -Al₂O₃ coatings were successful enough to be selected as the combustion catalyst for our MCMR prototype. Ru/ γ -Al₂O₃ catalyst also showed good results as well. Coating of RK-212, a Ni-based/ MgAl₂O₄ catalyst would be possible, but only for sieved particle sizes < 25 μ m.

Some observations were made also on the modified sol parameters. Water plays an essential role in the bonding process, switching solvent to methanol has an adverse effect. Acid addition is essential to most coating adherence. However, the pH requirement varies according to the carrier or commercial catalyst. pH is varied in modified sol, indicating that the carrier or metals consumed acid. Therefore, the modified sol should be utilized as soon as possible after ball milling. Boehmite content has a strong influence on the adherence. The optimal content is a function of the type of carrier.

Impregnation of the promoter and/or catalyst precursors led to many challenges, especially formation of cracks and corrosion of the metal support, leading to delamination.

Thickness measurements with eddy current probes were affected by roughness on the metal surface. The measured “noise profile” should be subtracted from the thickness measurements.

Finally, proper cleaning is essential to avoid contamination.

Chapter 5

Catalyst Coating: Final Method Development

5.1 Introduction

In Chapter 4, we obtained thick coating layers ($>80\ \mu\text{m}$) with good adherence under sonication using $\gamma\text{-Al}_2\text{O}_3$ powder and Pd/ $\gamma\text{-Al}_2\text{O}_3$ commercial catalyst. Starting with $\gamma\text{-Al}_2\text{O}_3$ as carrier for the reforming catalyst, promoters and metal catalyst still need to be impregnated. Preliminary testing in Chapter 4 indicated that cracks and delamination often occurred during impregnation. The sonication method to test catalyst adherence in the previous chapter destroyed the samples. As we moved towards the MCMR prototype and considering the time required to produce a fully-functional catalyst (2-3 weeks), a non-destructive method was needed to assess adherence.

Most methods to measure adherence are destructive, e.g. the scratch test, pull-off test and tape test (Chalker et al., 1991). This chapter explores a proxy for adherence measurement: counting the number of cracks with an optical microscope. This is a simplification of the “Crack density function” method (Berndt and Lin, 1993), which incorporated both the number of cracks and their size.

Chapter 4 focused on finding a method to coat a thick catalyst layer with good adherence. With information from catalyst stability testing in a packed bed micro-reactor (Chapter 6) and preliminary testing with the MCMR prototype (Chapter

8), it became clear that coating and catalyst activity testing needed be performed simultaneously. This avoided active catalysts that cannot be coated or catalyst coatings that are not active.

5.2 Material and Method

5.2.1 Metal Substrate

Experiments were conducted on various steel plates: austenitic SS 304, no. 4 finish, gauge 24 (0.635 mm); SS 310, gauge 24 (0.635 mm); and Fecralloy 0.5 mm thick (from GoodFellow). Some plates were sheer cut to 39.5 mm x 39.5 mm. Plates intended for the MCMR were water jet cut to 50.55 mm x 89.15 mm (1.990" x 3.510"), with rounded corners, radius 9.525 mm (0.375"), see Appendix E.4.

5.2.2 Final Coating Method

Figure 5.1 shows the various steps for coating commercial or lab-made catalyst. There were three main stages for commercial catalyst and four additional stages for lab-made catalyst. First, a metal substrate was sand-blasted with brown alumina, grit #80, using compressed air at 3.5 barg. For Fecralloy, calcination was performed at 1000°C for 10 h in static air to create an alumina oxide surface layer. The plate was then manually flattened, then cleaned in two steps: first the plate was immersed for 15 min in a sonic bath containing acetone, followed by a second 15 min bath containing deionised water.

The second stage consisted of preparing the modified sol and applying it to the metal substrate. The modified sol was comprised of distilled water, boehmite Disperal P2 (Sasol), and Baikalex CR125 γ -Al₂O₃ powder (Baikowski), or commercial catalyst (Pd 1%, Pd 5%/ γ -Al₂O₃, Alfa Aesar). The properties of boehmite, carrier, and commercial catalysts are listed in Tables 4.1, 4.2 and 4.4. Nitric acid was added to adjust the pH to ~5 before and after overnight ball-milling. Table 5.1 lists the modified sol parameters employed in this chapter. Hot substrate air spray coating (hot spray) was used throughout, with the technique explained in Section 4.3.4.

Depending on the carrier or commercial catalyst concentrations, the time re-

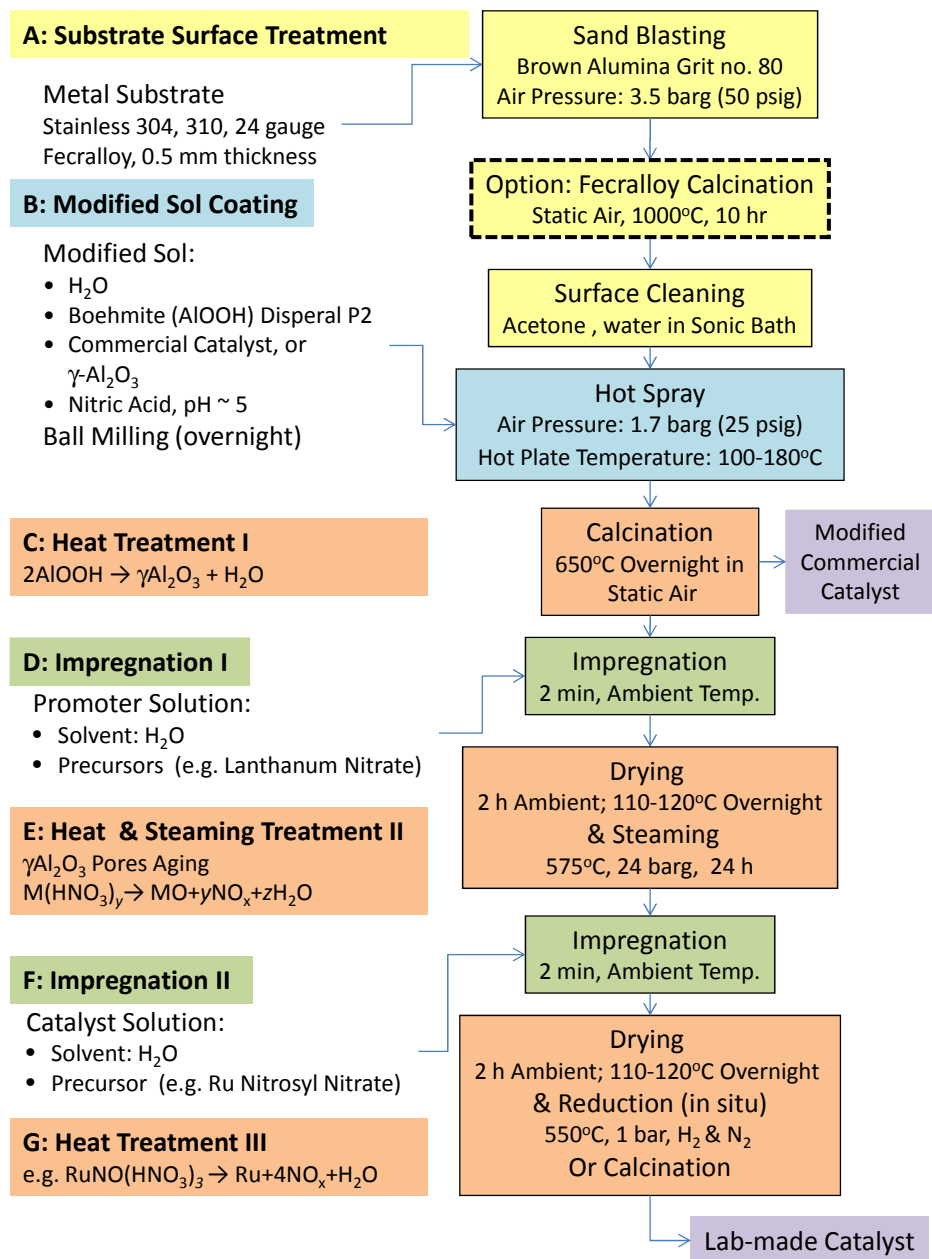


Figure 5.1: Final Method for Coating Commercial and Lab-made Catalysts

Table 5.1: Modified Sol Parameters

Coating	Boehmite Content ^a wt%	Carrier Concentration ^b mol/L	pH
γ -Al ₂ O ₃	40	0.5-0.75-1	~5
Pd 1%	15	0.25	~5.5
Pd 5%	15	0.25	~5.5

^aSee Eq. (4.1)

^bBased on the molecular weight of γ -Al₂O₃

quired to coat one plate varied significantly. At 1 mol/L, it took ~20-30 min per reactor plate to reach 200 μ m, whereas at 0.25 mol/L it could require >60 min per plate to reach the same thickness.

In the third stage and first heat treatment, coated plates were first dried at 65°C for 10+ min and then calcined at 650°C overnight. This concluded the procedure for commercial catalyst.

For lab-made catalyst, a modified incipient wetness impregnation method for promoter precursors was performed as follows: (1) Metal precursor(s) solution was added dropwise to the top of the coated plate, until it was saturated and a liquid layer formed above the coating surface. (2) After 2 min soaking at room temperature and gentle shaking, excess liquid was removed by tilting the plate at an angle of ~ 80° for ~5 min. Drying was performed in stages. First, plates were air-dried for ~2 h; second, plates were held in an oven at 110-120°C overnight. Tables 5.2 and 5.3 list precursors employed and solution concentrations.

For the second heat treatment, catalyst plates were inserted into the reforming channel of the MCMR prototype (as described in Chapter 8). Plates were steamed for 24 h at ~24 bar and 575°C. The sample was then impregnated with the catalyst precursor solution, following the same incipient wetness procedure as described above.

Final heat treatment for the reduction of the reforming catalyst was generally performed in-situ, i.e. during the MCMR start-up procedure, with a mixture of N₂ and H₂ gases. The start-up procedure is explained in detail in Chapter 8. Combustion Pd-based catalyst was calcined at 600°C in static air for 5.5 h.

Table 5.2: Metal Precursors; Supplier was Alfa Aesar in all cases

Name (Code Name)	Purity
Catalyst Precursors	
Ruthenium(III) nitrosyl nitrate, Ru 31.3% min (RuNO(NO ₃) ₃)	-
Palladium(II) nitrate, solution, Pd 4-5 wt% (Pd(NO ₃) ₂ Sol.)	-
Promoter Precursors	
Magnesium nitrate hexahydrate (Mg(NO ₃) ₂)	98%
Manganese(II) nitrate tetrahydrate (Mn(NO ₃) ₂)	98%+
Lanthanum(III) nitrate hexahydrate (La(NO ₃) ₃)	99.9%

Table 5.3: Compositions of Impregnation Solutions

Desired Metal Content ^a wt%	Solution Concentration ^b mol/L
Promoters	
La ₂ O ₃ 6%	La Nitr. 0.27
La ₂ O ₃ 4% MgO 4%	La Nitr. 0.18; Mg Nitr. 0.72
La ₂ O ₃ 4% MgO 2% MnO 2%	La Nitr. 0.18; Mg Nitr. 0.36; Mn Nitr. 0.28
Catalyst	
Ru 6%	Ru Nitr. 0.51
Pd 5%	Pd Nitr. Sol. (as received)

^aMeasured Metal Content can vary by $\pm 2\%$

^bSolution concentrations determined with the help of Eq. (4.4)

5.2.3 Analytical Equipment

Optical microscope

Optical images were taken with a Nikon Eclipse MA200 microscope, combined with a Nikon DS-Fi1 camera, having a resolution of 2560 x 1920 pixels.

TGA

Thermo Gravimetric Analysis (TGA) was performed with a TGA-50 from Shimadzu. About 20 mg of powder were deposited in a ceramic crucible. Under a

N₂ flow of ~60 ml/min, from ambient conditions, the temperature was raised to 110°C at 20°C/min and held for 30 min. At a rate of 10°C/min, the temperature was then elevated to 800°C and held for 30 min.

5.2.4 Metrics

Crack density

As a proxy to measure coating adherence without destroying the sample, we define a crack density as follows: the number of cracks are counted at five locations on plates using optical microscope images at a magnification of 10X, corresponding to an area of 1.9 mm² per location, or 9.5 mm² in total. Four images were taken near the plate corners, and one at the middle. At each location, the number of cracks was counted up to 10. Beyond 10, cracks tended to intersect with each others to form a network, making counting difficult. The five counts were averaged to obtain a “crack density”. Any sample with one or more “10” reading was automatically given an overall “10” (failed) as a final value, regardless of the actual average. This method is a simplification of the “Crack density function” method (Berndt and Lin, 1993), which incorporates both the number of cracks and their size. The crack density test has the advantage of not destroying the sample. We recognize that it gives information which differs from the sonication test, and therefore may be an imperfect replacement.

Coating Thickness

To measure the coating thickness, a Positector 6000-1 thickness meter, by Defeslko, based on the eddy current principle, was employed. The thicknesses reported in this chapter are averages of five measured values on each plate after coating and calcination. Four points were taken near the corners and one at the center of the plate. The meter was zeroed by taking a reading on a clean flat plate of the same material. Sand-blasting of the plates induces a “thickness” reading on the meter, which we call “profile noise”. The average profile noise was simply subtracted from the average measured thicknesses. For samples where Fecralloy was the support, the thickness meter could not measure thickness, due to the magnetic

property of the alloy. In that case the thicknesses were estimated from the mass of the catalysts, with the same modified sol composition (see Appendix A.7).

5.3 Results and Discussion

5.3.1 Carbon Deposition during Steaming

Pre-aging of the carrier by steaming resulted in some carbon deposition challenges. Figure 5.2 shows coated plates after steaming. Carbon is readily visible on Part A.1 and could be removed by calcination at 650°C as shown in Part A.2, although some carbon remained. Part B.1 shows the effect of adding La_2O_3 , which effectively suppresses carbon deposition.

The carbon likely originated from the Grafoil™ gasket used in the MCMR prototype. Another potential source could be the silicone used in the early plate assembly procedure. Steaming and reactor assembly procedures were therefore modified to avoid carbon deposition: (1) Continuous N_2 flow was applied during start-up and shut down to flush any deposited carbon from the Grafoil gasket; and (2) Silicone was only used on the gasket and outside the reforming channel.

5.3.2 Surface Cracks

The impregnation of Ru after steaming was unsuccessful at first. On the first attempt, five of ten plates showed severe coating delamination, as shown in Figure 5.3 Part A. Numerous cracks could also be observed through the microscope on the section of the coating that did not delaminate (Part B). Furthermore, some coating plates, that did not delaminate during the impregnation process, lost material during the MCMR run (Part C).

As the coating method was getting longer, with the addition of steaming and impregnation stages, a non-destructive method was needed to measure coating adherence, as an alternative to sonication. We then measured crack density, as described above.

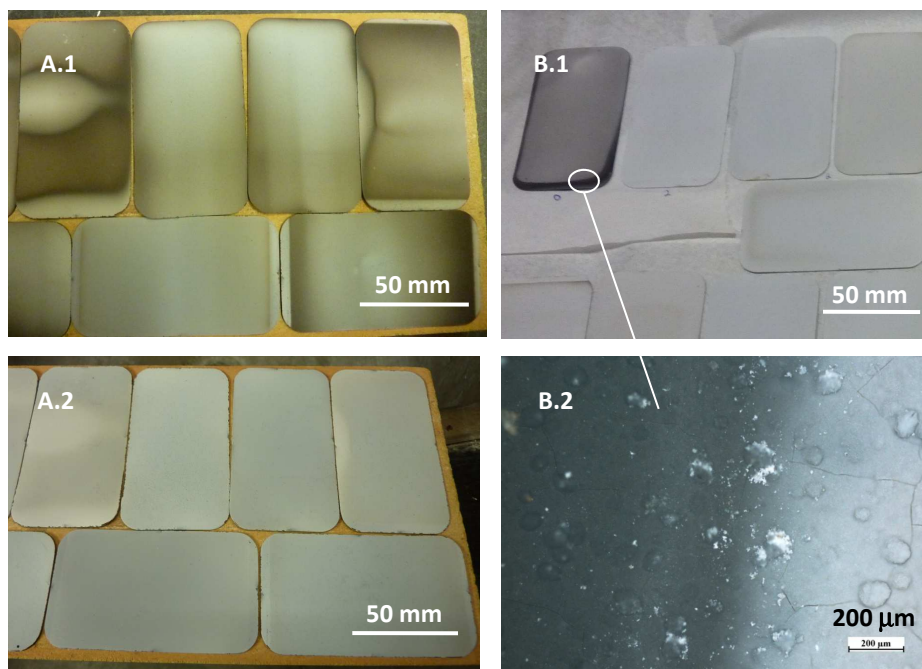


Figure 5.2: Carbon Deposition during Steaming: (A.1) $\gamma\text{-Al}_2\text{O}_3$ after steaming; (A.2) After calcination of plates in (A.1); (B.1) La_2O_3 5%/ $\gamma\text{-Al}_2\text{O}_3$ after steaming (top left plate does not have La_2O_3); (B.2) Optical microscope image of $\gamma\text{-Al}_2\text{O}_3$ plate after steaming.

Crack Density Test Verification

Figure 5.4 compares average crack densities with mass losses after sonication for a $\gamma\text{-Al}_2\text{O}_3$ coating. Crack densities and sonication show consistency. The plate with the maximum crack density value of 10 lost nearly 50% of its mass under sonication, while a low crack density of 2.3 led to a mass loss of only 5% .

Source of Crack Formation

Several assumptions could be made to explain crack formation. In fact, cracks could occur at every step of the coating process.

Early assumptions were that boehmite phase change, or combustion of nitrate compounds during calcination, could be the origin of the cracks. Figure 5.5 shows TGA plots for boehmite, boehmite with Pd 5%/ $\gamma\text{-Al}_2\text{O}_3$ powder, and

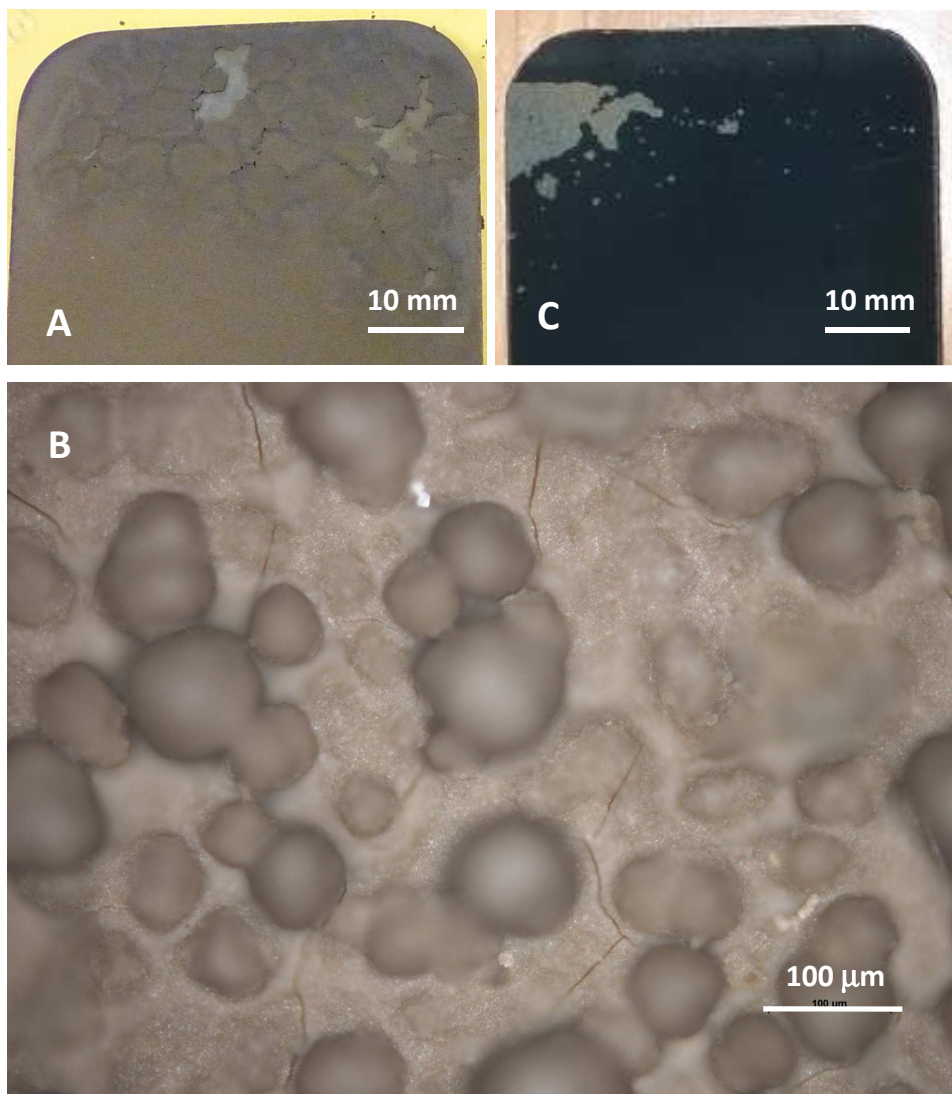


Figure 5.3: Delamination and Cracking Issues after Steaming and Impregnation with $\text{RuNO}(\text{NO}_3)_3$ on $\gamma\text{-Al}_2\text{O}_3$: (A) Catalyst delamination during impregnation step; (B) Microscope image after impregnation and drying; (C) Catalyst delamination after two MCMR runs.



Figure 5.4: Comparison of Sonication Test and Crack Test: Images show corresponding plates after coating material removal due to sonication. Numbers give (mass loss wt% / average crack density).

$\text{RuNO}(\text{NO}_3)_3\text{-La}_2\text{O}_3$ 8%/ $\gamma\text{-Al}_2\text{O}_3$. This plot indicates that boehmite changes phase at $\sim 400^\circ\text{C}$ and that $\text{RuNO}(\text{NO}_3)_3$ decomposed at $\sim 250^\circ\text{C}$. The Pd 5%/ $\gamma\text{-Al}_2\text{O}_3$ plot has two peaks, the second one corresponding to boehmite phase change. The origin of the first is not clear. The nitric acid in the modified sol might generate compounds that decompose at $\sim 250^\circ\text{C}$. As demonstrated below, phase change and nitrate removal were not found to be critical in crack formation, and the heat treatment procedures were therefore not changed.

Figure 5.6 gives the first hint on the source of crack formation. Cracks, as in Part A, were less likely to occur when clusters were abundant, as in Part B. Some clusters could be removed by simply rubbing the coating surface with ones fingers (Part C). However, even with this apparent weakness, samples could keep their material throughout the coating process and MCMR runs.

Figure 5.7 gives a second hint on the source of cracks. The white lines on Part A are weak spots that may lead to future cracks, as shown in Part B. Those white lines were generally observed after the first calcination step of the $\gamma\text{-Al}_2\text{O}_3$ coating. These white lines could lead to water infiltration during impregnation,

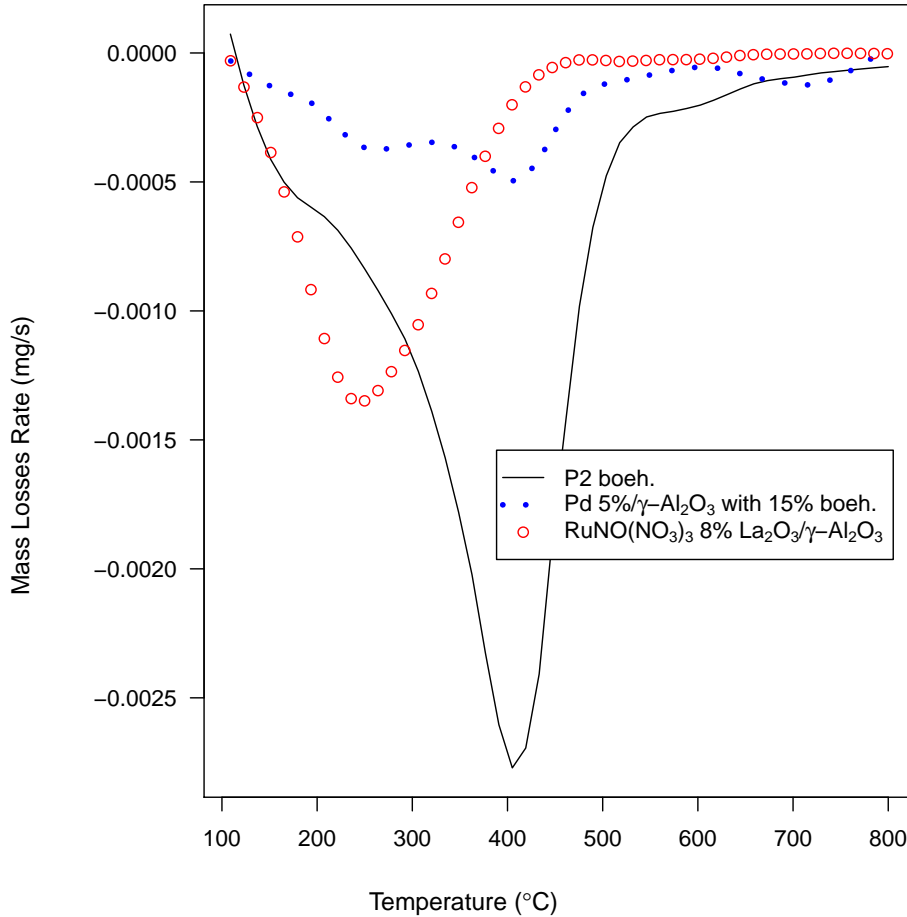


Figure 5.5: TGA analyses of boehmite, Pd 5%/ γ -Al₂O₃ with 15% boehmite, and RuNO(NO₃)₃-La₂O₃/ γ -Al₂O₃. Lines are smoothed.

creating stress on the coating that could lead to cracks and delamination.

With the experience gained throughout several hot spray coatings, it was realized that cluster formation and white line avoidance were linked to water evaporation during the coating. Aside from compressed air pressure, no other hot spray coating parameters were quantified or controlled. However, it was observed qualitatively that to avoid cracks, water must evaporate instantly while spraying the modified sol. With our equipment for spray coating, best practices include: (1) To

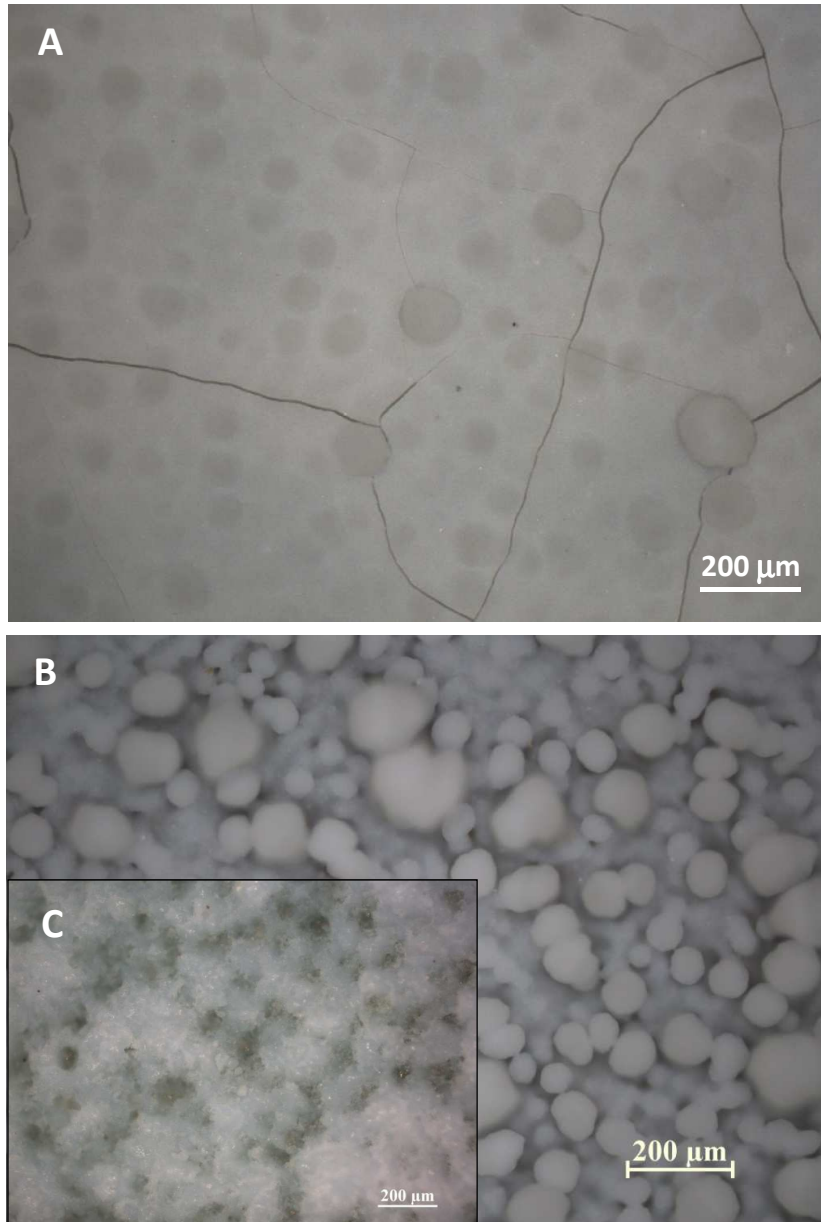


Figure 5.6: Cracks versus Cluster Formation during Hot Spraying of γ - Al_2O_3 : (A) Large cracks visible with few clusters; (B) No cracks visible with many clusters; (C) No cracks visible, with clusters manually removed.

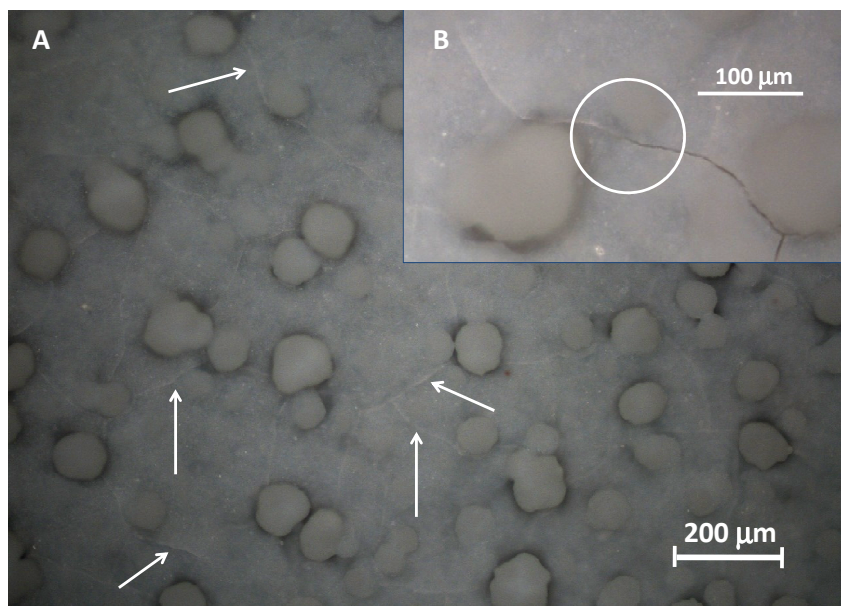


Figure 5.7: Presence of White Lines on γ -Al₂O₃ Coating after Calcination:
 (A) Several white lines visible, with arrows pointing at some of them;
 (B) White line becomes a regular crack.

avoid large droplets of modified sol reaching the plate, it is best to avoid pointing the spray gun directly at plates at the start of a sweep. (2) The modified sol mist should be adjusted to reach the plate perpendicularly. (3) The mist flow rate needs to be adjusted to see no changes in colour on the plate; and (4) Plates should be rotated periodically to improve coating uniformity, while pausing to ensure that the plate temperature always exceeds the water boiling point.

Crack Density Measurements

Table 5.4 presents crack density results for lab-made catalyst coatings at various stages of the coating method and catalyst life in chronological order. As more insight about the source of cracks and how to avoid them was obtained, fewer measurements were required.

The first column shows that cracks can appear after the first calcination step. The second column indicates that lowering the carrier concentration of the modi-

Table 5.4: Average Crack Density for Ru- and Pd-based Lab-made Catalysts: Unbracketed numbers on a scale of 0-10 give average number of cracks counted on an area of 9.5 mm². Bracketed numbers are numbers of plates tested. Plates with crack density >2 were generally discarded before they reached the next coating step. Carrier concentration in modified sol is 0.5 mol/L, except where indicated. Catalyst compositions are approximate.

Step	Ru 5% (0.75 mol/L ^a)	Ru 5%	Ru 5% - La ₂ O ₃ 6%	Ru 5% - La ₂ O ₃ 6% on Fecralloy, Evap. Monit. ^b	Ru 5% - or Pd 5% - La ₂ O ₃ 6% on SS 310, Evap. Monit.
Before γ -Al ₂ O ₃ Calcination	0.06 (8)	0.00 (5)	- (-)	- (-)	- (-)
After γ -Al ₂ O ₃ Calcination	3.38 (38)	0.03 (32)	- (-)	0.00 (2)	0.00 (2)
After Promoter Impregn. & Drying	1.73 (3)	N/A	- (-)	- (-)	- (-)
After Steaming	1.18 (16)	0.63 (6)	0.15 (25)	0.00 (3)	0.00 (4)
After Catalyst Impregn. & Drying	6 (11)	5.88 (5)	1.20 (13)	0.00 (1)	0.00 (1)
After MCMR Run	5.52 (5)	- (-)	- (-)	0.00 (2)	0.00 (3)

^aCarrier concentration in modified sol

^bEvap. Monit.: water evaporation rate during spraying was monitored

fied sol eliminated cracks after the first calcination, but did not guarantee adherence after Ru impregnation. In the third column, La₂O₃ was added as promoter. Results suggested that La₂O₃ helps maintain coating integrity throughout the steaming and Ru impregnation stages. However, improving operator coating skills, might have also played a role. In the last two columns, the evaporation rate of water during the hot spray coating was monitored, as explained above. We had essentially eliminated crack formation at this point.

The learnings gained from the lab-made catalyst coating to the commercial Pd

Table 5.5: Crack Density Results for Pd Commercial Catalyst Coatings: Scale 0-10. Bracketed numbers are numbers of plates tested.

	Pd 1 wt% on SS 304	Pd 5 wt% on SS 304	Pd 5 wt% on SS 310 and Fecralloy
Before Calcination	- (-)	0.00 (6)	- (-)
After Calcination	0.00 (3)	0.03 (6)	0.00 (2)
After MCMR Run	- (-)	0.00 (4)	0.00 (2)

5% coating were applied, with the powder concentration kept low in the modified sol at 0.25 mol/L, and the water evaporation rate observed carefully. Table 5.5 shows that cracks were then avoided throughout the coating process and MCMR experiments.

If the hot spray coating is performed correctly, it is not expected that the support material (SS 304, SS 310 or Fecralloy) will significantly affect coating adherence.

5.3.3 Rust

Figure 5.8 shows plates, with various coating composition, all with visible rust stains. We paid attention to this issue after it was suspected that rust was inhibiting the Ru-based catalyst, as shown in Chapter 6. However, there was no evidence that rust affected the Pd-based combustion catalyst. The presence of rust or iron oxide was first observed after an unsuccessful MCMR run with RK-212 (Part A). The iron presence was confirmed with EDX measurement.

Rust appeared at different rates. The SMR environment accelerated the appearance of rust. Rust was observed immediately after the MCMR run (Parts A & B.1). The rust occurred at a much slower rate for plates that went no further than steaming (see Figure 5.1). Plates in Part C.1 displayed little or no rust stains immediately after steaming. However, after 8 months, as can be seen on the image, iron oxide had diffused slowly through the coating layer and reached the surface. Combustion catalyst plates (Part D) were also affected by rust, but less so and at a slower rate than the reforming ones. Scratching catalyst off the plates revealed rust stains on the metal support itself (Part B.2 & C.2), confirming that the rust came

from the support (SS 304), from outside contamination.

$\gamma\text{-Al}_2\text{O}_3$ coating plates that were not subjected to steaming were not affected by rust, even though they were experienced to 650°C calcination. However, RK-212 plates encountered rust formation without experiencing steaming or the SMR environment. Therefore, we speculate that the presence of steam might be needed to trigger rust diffusion through $\gamma\text{-Al}_2\text{O}_3$, whereas only time is needed to see rust if other metal elements are present.

To stop the diffusion of iron oxide, two alternative steel alloys, SS 310 and Fecralloy, were tested. Fecralloy was calcined prior to coating as explained above. We did not see any corrosion issues with Fecralloy throughout the coating and utilization process, but a small amount of stains started being visible on SS 310 a few weeks after the steaming step. Therefore, we selected Fecralloy as support for the reforming catalyst. Since Pd-based catalyst was not as strongly affected by rust, SS 310 was used in the combustion channel of the MCMR.

5.3.4 Successful Coating Samples

Figure 5.9 shows images of lab-made Ru-based catalyst on SS 304 support. Figure 5.10 presents commercial Pd-based catalyst on SS 304. Some carbon deposition was often observed on the combustion catalyst surface after the MCMR run. This carbon could be removed by calcination at 650°C. The source of the carbon was likely Grafoil gasket decomposition during start-up and shutdown. The procedure was eventually changed to ensure continuous air flow through the channel to flush away any carbon.

Figures 5.11 and 5.12 show images of lab-made and commercial catalyst on Fecralloy and SS 310. As discussed in Chapter 4, Figure 4.2, the Fecralloy surface, contains visible linear furrows, likely from the rolling manufacture process. These furrows influence the position of the clusters, as seen in Figure 5.11 Part A.

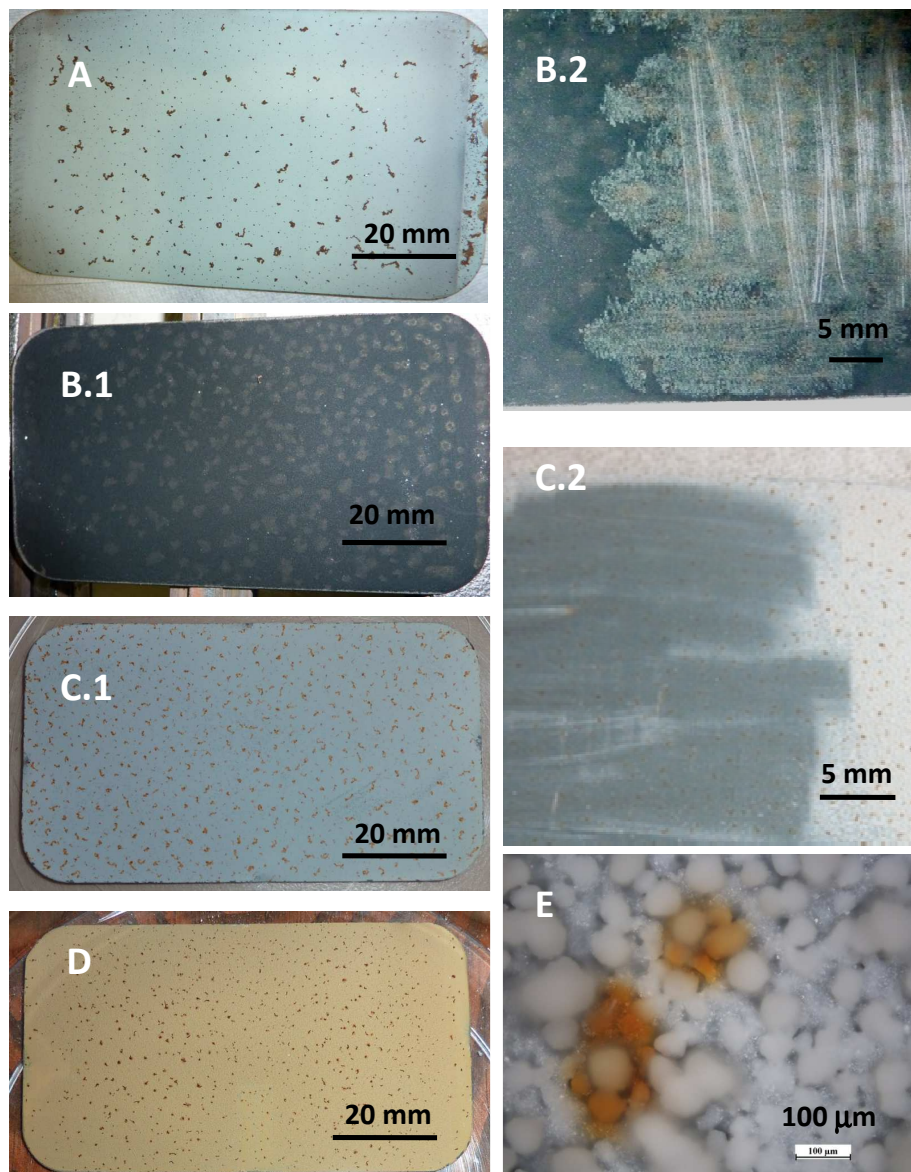


Figure 5.8: Rust on Catalyst with SS 304 as Metal Support: (A) RK-212 (Ni/MgAl₂O₄) spent (~2 days after run) ; (B.1) Ru 6%/ γ -Al₂O₃ spent (~2 days after run); (B.2) Close-up on (B.1) after catalyst partially scratched off; (C.1) La₂O₃ 6%/ γ -Al₂O₃ (8 months after coating); (C.2) Close-up on (C.1) after catalyst partially scratched off; (D) Pd 1%/ γ -Al₂O₃ spent (8 months after run); (E) γ -Al₂O₃ on optical microscope (3 months after steaming).

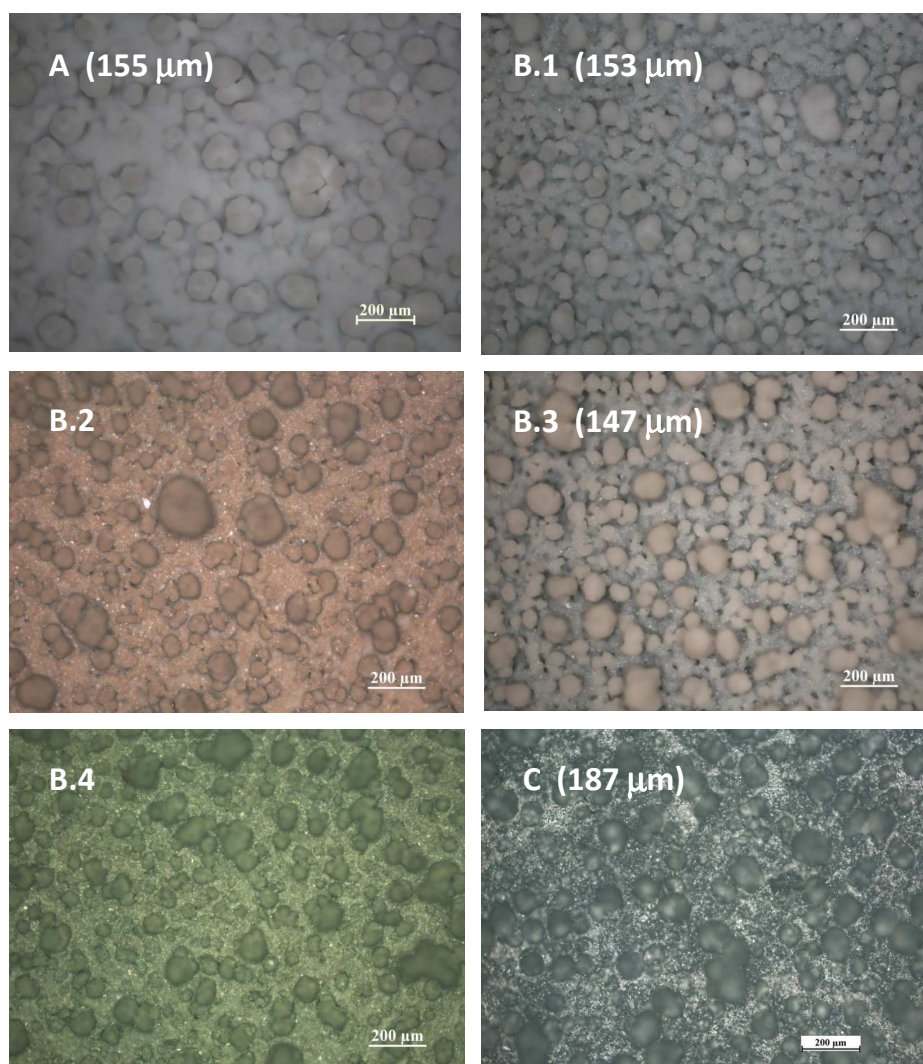


Figure 5.9: Ru-based Catalyst on SS 304 Support at Various Stages of Coating and Catalyst Life (coating thickness): (A) $\gamma\text{-Al}_2\text{O}_3$ before calcination; (B.1) $\gamma\text{-Al}_2\text{O}_3$ after calcination; (B.2) After La- Mg- Mn- nitrates impregnation & drying; (B.3) After steaming; (B.4) After $\text{RuNO}(\text{NO}_3)_2$ impregnation & drying; (C) After MCMR run. ((A) & (C) images are from different plates than (B's) but shared the same coating method and modified sol parameters: 0.5 mol/L, 40 wt% boeh., pH 5.)

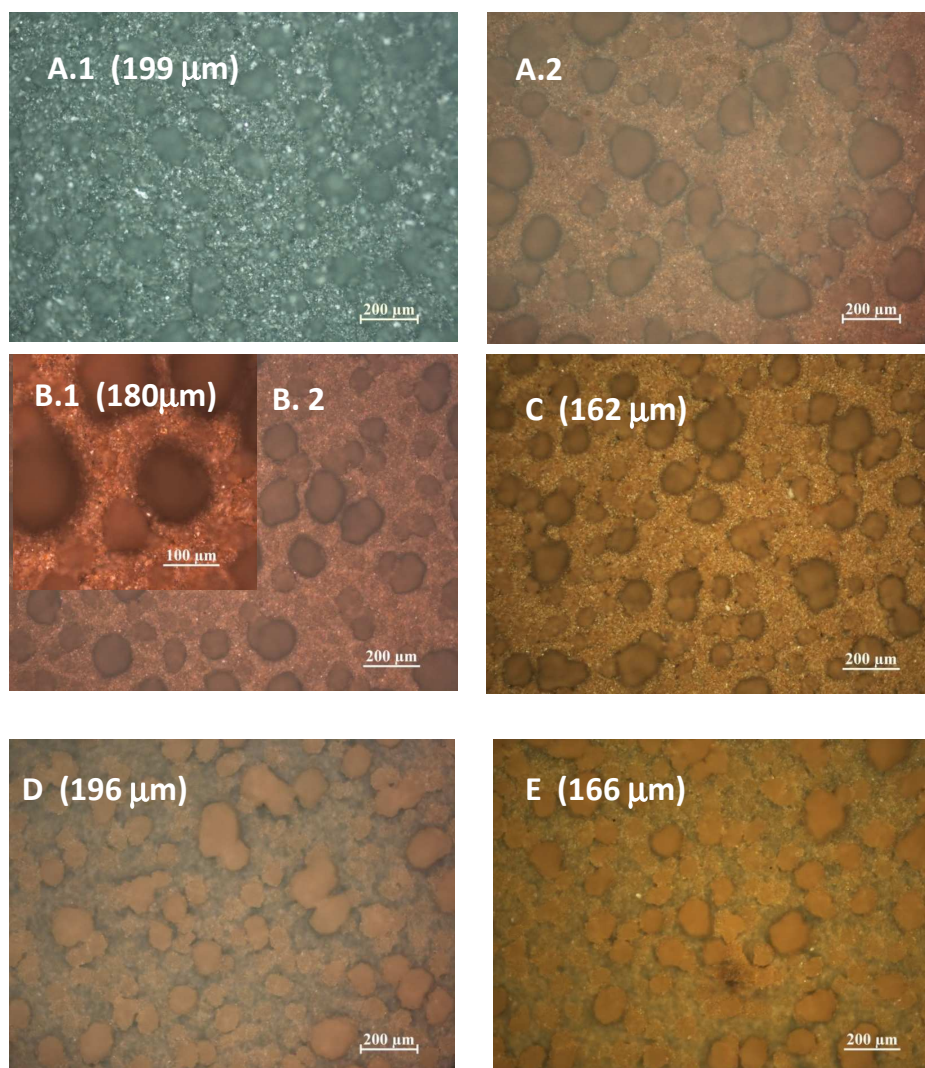


Figure 5.10: Commercial Pd-based/ γ -Al₂O₃ Catalysts on SS 304 Support at Various Stages of Coating and Catalyst Life (coating thickness): (A.1) Pd 5% before calcination; (A.2) After calcination; (B.1) & (B.2) Pd 5% After MCMR run; (C) Pd 5% after run and regeneration (calcination at 650°C); (D) Pd 1% after calcination; (E) Pd 1% after MCMR run.

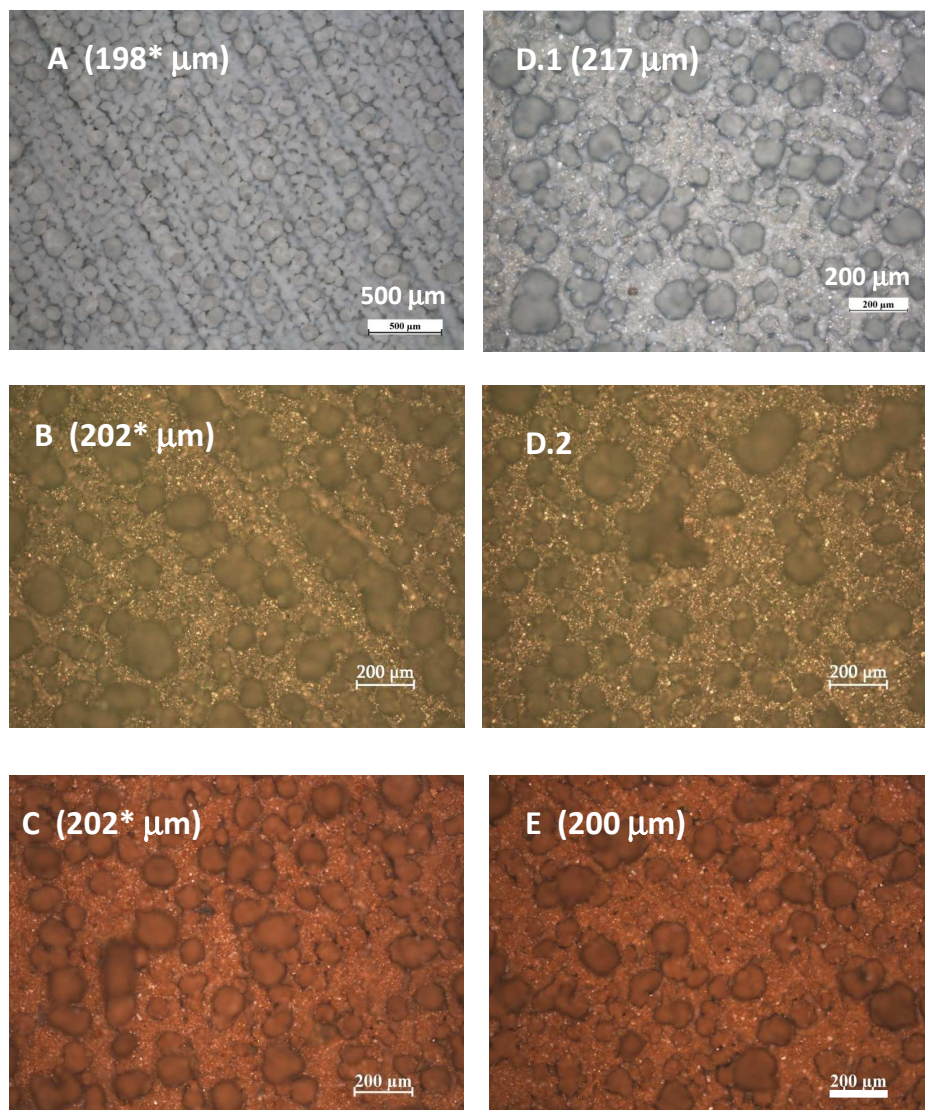


Figure 5.11: Ru- and Pd-based/ γ - Al_2O_3 Catalysts on Fecralloy (left side) and SS 316 (right side) at Various Stages of Coating and Catalyst Life (coating thickness): (A) γ - Al_2O_3 after calcination; (B) Ru 8% La_2O_3 3% MnO 2% MgO 2% after Ru impregnation & drying; (C) Pd 5.6% La_2O_3 6% after MCMR run; (D.1) Ru 7% La_2O_3 6% after Ru impregnation & drying; (D.2) Sample (D.1) After MCMR run; (E) Pd 5.3% La_2O_3 4% MgO 4% after MCMR run. (* Estimated, see Coating Thickness Section)

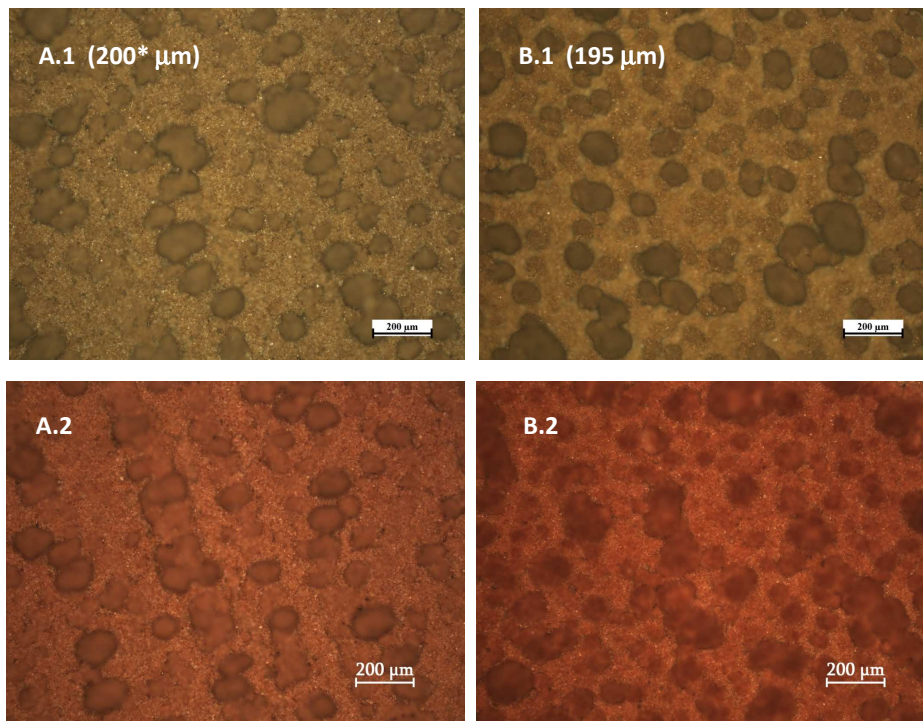


Figure 5.12: Commercial Pd 5%/ γ -Al₂O₃ Catalysts on Fecralloy (left side) and SS 310 (right side) before and after MCMR run (coating thickness): Top Row: After Calcination and before MCMR run; Bottom Row: After MCMR run. (* Estimated, see Coating Thickness Section)

5.4 Conclusions

This Chapter describes a successful coating method for reforming and combustion catalysts, lab-made or commercial, on various metal supports. A crack density test provided a non-destructive method to evaluate coating adherence, with results consistent with the sonication test. Crack formation and coating delamination during impregnation were linked to the presence of white lines, precursors to cracks, on the coating surface, and to the absence of clusters. Cracks could be avoided by lowering carrier or commercial catalyst concentration in the modified sol, and

by monitoring the rate of water evaporation during hot spray coating. Water must evaporate instantly while spraying the modified sol. La_2O_3 was an effective promoter to avoid carbon deposition during steaming. Rust appeared on most coatings on SS 304 as support. Rust diffusion could be reduced by using SS 310, and arrested completely by using Fecralloy as the metal support.

Chapter 6

Reforming Catalyst Activity and Stability

6.1 Introduction

Steam Methane Reforming (SMR) is traditionally performed with Ni-based catalysts (Twigg, 1997). Nickel has the advantage of being relatively inexpensive compared to more active noble metals. However, as shown in Chapter 3, the multi-channel reactor configuration, compared with a packed bed reactor, could lower the catalyst loading by more than one order of magnitude. Hence noble metals were considered as alternative catalysts. Ruthenium and rhodium are the most active reforming catalysts per unit of weight (Nielsen and Hansen, 1993). However, Rh is approximately an order of magnitude more expensive than Ru on the spot market (eBullion Guide, 2012). For this reason, ruthenium was tested as an alternative to nickel.

Several catalyst deactivation mechanisms can occur in an SMR environment:

1. Sintering is a loss of catalytic activity due to a loss of active surface area (Fogler, 2004). Steam and pressure accelerate sintering (Twigg, 1997). There are two types of sintering: pore sintering, where the pores of the catalyst support close, and metal sintering, where active metal sites agglomerate.
2. Fouling occurs when carbon material is deposited on the surface of the cat-

alyst (Fogler, 2004). Fouling is common with steam reforming on Ni-based catalyst. High Steam-to-Carbon (S/C) molar ratio (>3) are generally used to avoid this issue. Noble metals are more resistant to carbon formation, allowing a lower S/C molar ratio to be used (Nielsen and Hansen, 1993).

3. Poisoning is the process where molecules become irreversibly chemisorbed onto the active sites. Sulfur, naturally present in many petroleum feedstocks is a common catalyst poison (Fogler, 2004).

Catalyst stability can be improved by adding promoters to the carrier. Among them, MgO, MnO, and La₂O₃ are known to suppress carbon formation, active metal particles sintering and oxidation (Berman et al., 2005). Earth alkaline metals (Mg, Ca) neutralize the acidity of the support, helping to suppress cracking and polymerization (Twiggs, 1997).

Catalyst preparation, removal of the salts from the metal precursors, pre-aging, and catalyst activation need to be performed carefully. Jakobsen et al. (2010) prepared a Ru/ ZrO₂ catalyst with extensive aging of the catalyst, treated for 336 h at 750°C, 11 bar and a steam-to-H₂ molar ratio of 1. Before kinetic experiments in the 425-575°C range, the temperature was raised to 850°C under a hydrogen flow. Li et al. (2009) showed that calcination in air for 4 h at 500°C adversely affected a Ru/ Al₂O₃ catalyst for the steam reforming of kerosene.

This Chapter is the bridge between coating experiments covered in Chapters 4 & 5, and the Multi-Channel Membrane Reactor (MCMR) experiments, presented in Chapter 8. We present in this Chapter activity and stability tests performed on the packed bed micro-reactor, with both fresh catalysts from the coating trials and catalysts spent during the MCMR runs. Full description of these runs and their operating conditions are provided in Chapter 8. These post-run results are included here so that all of the micro-reactor material related to reforming is presented in one place. They also highlight some deactivation mechanisms that only occur in the MCMR.

Table 6.1: Impregnation Solutions and Desired Metal Contents for Reforming Catalysts

Desired Metal Content ^a wt%	Solution mol/L
Promoters	
MgO 3%	Mg Nitr. 0.54
La ₂ O ₃ 6%	La Nitr. 0.27
La ₂ O ₃ 4% MgO 4%	La Nitr. 0.18; Mg Nitr. 0.72
La ₂ O ₃ 4% MgO 2% MnO 2%	La Nitr. 0.18; Mg Nitr. 0.36; Mn Nitr. 0.28
Catalyst	
Ru 6%	Ru Nitr. 0.51

^aMeasured metal content can vary of $\pm 2\%$

6.2 Material and Method

6.2.1 Catalyst Preparation

Tests on both commercial and lab-made catalysts are reported in this chapter. Coating methodologies and material employed were described in Chapters 4 and 5. Since many coating options were presented in those chapters, we list specific coating parameters in tables and figures below. After coating and heat treatment or MCMR runs, catalyst particles or pieces were scratched off the metal plates, ground with a mortar and pestle to obtain fine powders, then inserted into the micro-reactor following a procedure described below.

For lab-made Ru-based catalysts, impregnation solution concentrations are listed in Table 6.1.

6.2.2 Micro-Reactor Configuration

Figure 6.1 illustrates the configuration of the micro-reactor. The reactor consisted of 95 mm (3/8") OD SS 316 tube. From 0.002 to 0.25 g of catalyst was diluted with γ -Al₂O₃ powder ($D_{p,ave}$ 80 μ m, BASF HiQ-7S19cc) for a total weight of 1.0 g. Two layers of glass wool maintained the particles in place, while alumina beads \varnothing 0.4-0.6 mm (SEPR Ceramic) kept the catalyst bed at an even height. A thermocouple was inserted inside the bed to monitor the temperature, allowing the

temperature to be controlled by a PID controller.

6.2.3 Experimental Set-up

Figure 6.2 shows a simplified process flow diagram of the micro-reactor unit, including some key control instruments. A detailed Process & Instrumentation Diagram (P&ID) is included in Appendix D.1. The functioning of the unit can be summarized as follows: Water is pressurized with N_2 and, after being pre-heated to produce steam, it is mixed with CH_4 and H_2 at the desired ratios. There is also an additional air line for Methane Catalytic Combustion (MCC) studies. All feed streams are controlled with mass flow controllers. Downstream of the micro-reactor, water is removed by a condenser, and gas products are split into two streams, one going to the Gas Chromatograph (GC), the second being vented.

The micro-reactor has one thermocouple inside the bed (subscript *bed*) (see Figure 6.1) and one on the outside surface of the reactor tube (subscript *sf*). Two pressure transducers measure the inlet (P_{in}) and outlet (P_{out}) pressures. All temperatures reported below are reactor temperatures (T_{bed}), whereas the pressures are averages of P_{in} and P_{out} .

In case of emergency shutdown, triggered manually or automatically by a flow, temperature or pressure alarm, the system is flushed with N_2 , while all other feed lines are isolated with solenoid valves. A detailed electrical and control diagram is found in Appendix D.2.

Gases used for the SMR experiments were purchased from Praxair: CH_4 (99% purity), H_2 (99.995+% purity), and N_2 (99.995+% purity). Deionized water was utilized to produce the steam.

Start-up

Catalysts were reduced from 1 h to overnight, at 550-600°C and 0 barg at the reactor outlet, with a H_2 flow rate of 42 Nml/min. Once the reduction was completed, N_2 was used to adjust the pressure at the desired level, and the steam flow was started. ~15 min later, the methane flow was started. It took ~1 h to remove all the hydrogen originating from the start-up and reduction procedure.

The start-up procedure needed some modifications to simulate MCMR start-

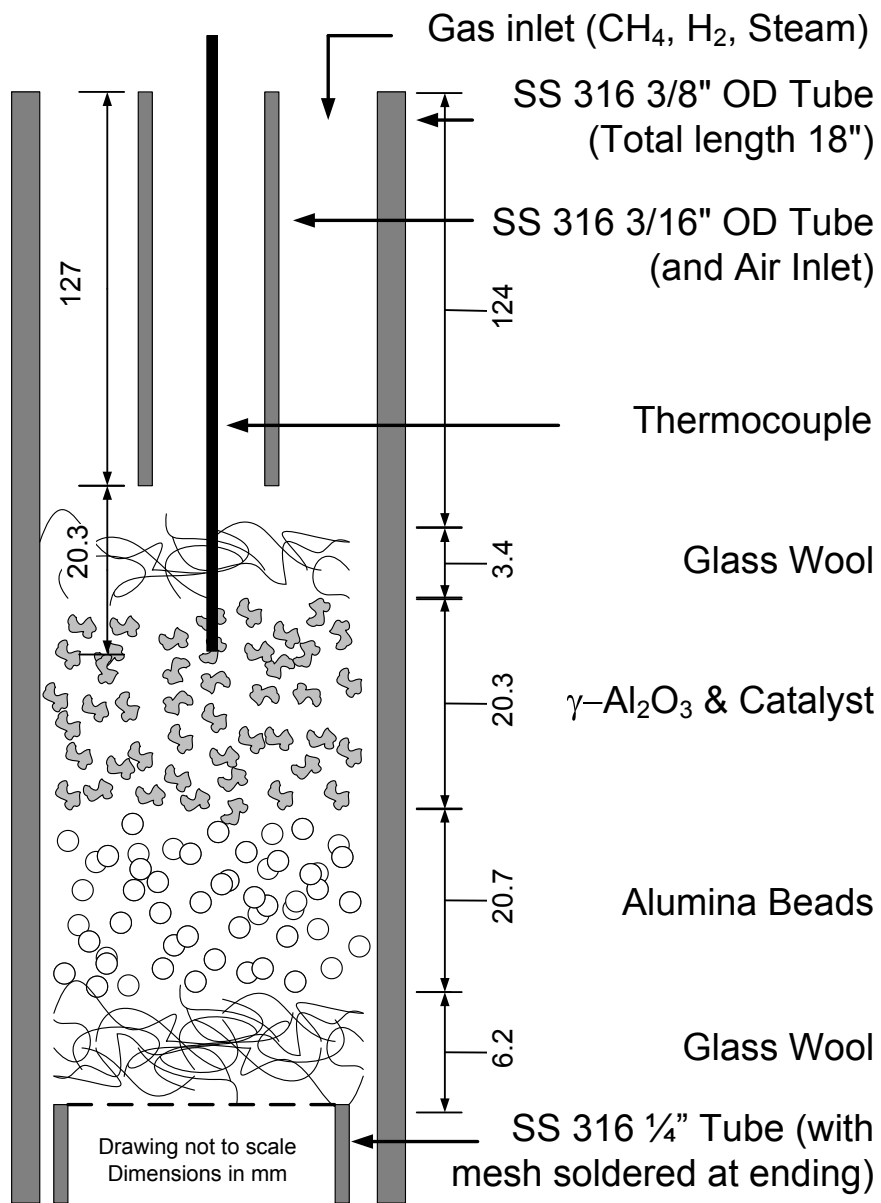


Figure 6.1: Micro-Reactor Set-up

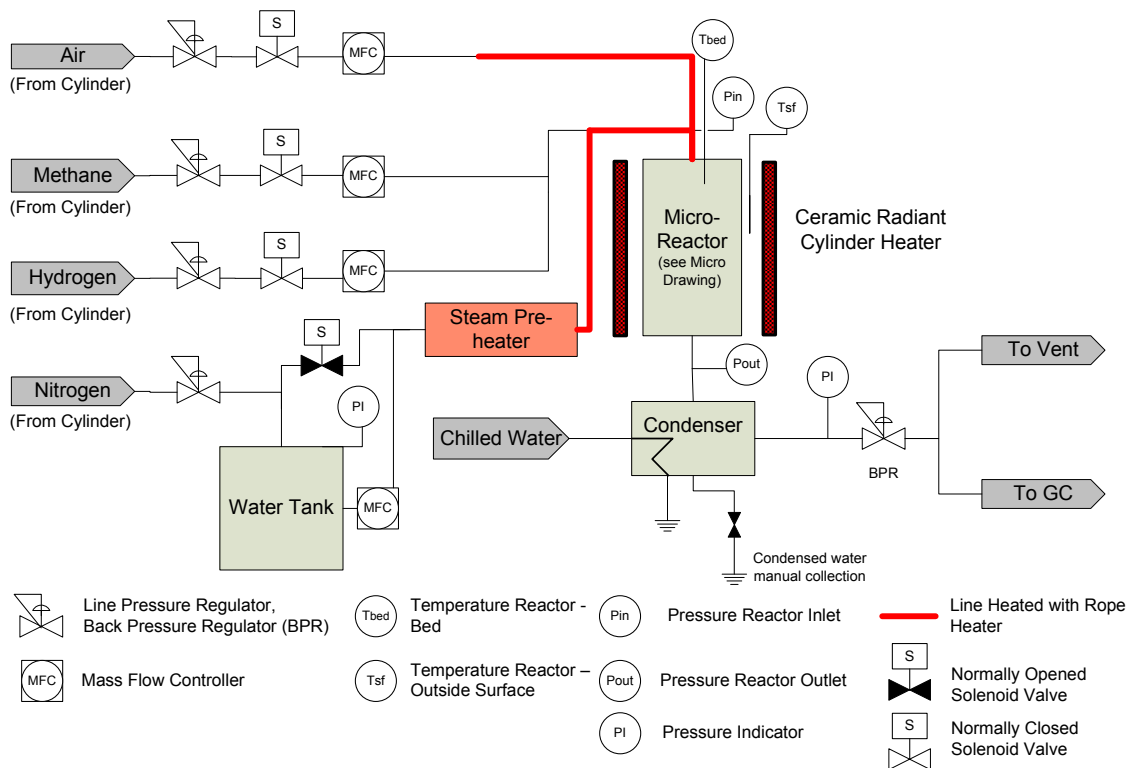


Figure 6.2: Micro-Reactor Process Flow Diagram. For detailed PI&D, see Appendix D.1.

up conditions. The Pd/Ag membrane requires specific H₂ partial pressures when ramping the temperature. In Section 6.3.4 below, trial and error tests were performed to activate the catalyst while respecting, insofar as possible, the membrane requirements.

Operation

The micro-reactor was operated at temperature of 550-600°C, average pressure 6 - 11 bar, methane flow rate 100-105 Nml/min, S/C 2.5-4, and a Hydrogen-to-Carbon (H/C) molar ratio of 0-1.4. Catalyst loading varied from 0.002 g, for Ru lab-made catalyst, to 0.25 g for RK-212.

The average pressure drop through the packed bed was small: <0.2 bar for

experiments at an average pressure of 11 bar. For most of the lab-made Ru catalysts, the Weight Hourly Space Velocity (WHSV), based on the total flow rate, was $\sim 8000 \text{ h}^{-1}$. The reactor surface (or skin) temperature differed significantly from the reactor temperature. For example, when the methane conversion was 30% at a reactor temperature of 550°C , the surface temperature could be as high as 640°C . If the catalyst was not active, the surface temperature was $\sim 20\text{-}30^\circ\text{C}$ higher than the reactor temperature.

6.2.4 Packed Bed Model

Figure B.1 compares micro-reactor results with predictions of a packed bed model using Xu & Froment kinetics (see Chapter 2, Section 2.7). The model is a simplified packed bed reactor, neglecting pressure drop, temperature variation, and external and internal mass transfer resistances, leading to:

$$\frac{dF_i}{dW_{cat}} = -R_i \quad (6.1)$$

where R_i is the rate of production of component i as defined in (2.21), and W_{cat} is the mass of the catalyst. MATLABTM software with the ordinary differential equation function “ode15s” was utilized to solve the model. Equation (6.1) is integrated over the mass of the catalyst. Inlet flow rates, reactor temperature, and average pressure are used as inputs and initial parameters to solve the model.

The methane conversion as a function of the mass of catalyst was calculated as:

$$X_{\text{CH}_4} = 1 - F_{\text{CH}_4} / F_{\text{CH}_4,o} \quad (6.2)$$

6.2.5 Estimation of Kinetics Parameter

Chapter 2 detailed the Jacobsen’s kinetic model for a Ru 1% / ZrO₂ catalyst. The pre-exponential factor, A_1 , was estimated by assuming that the micro-reactor acts as a differential reactor, and average properties between the inlet and outlet of the

micro-reactor were calculated, leading to:

$$A_1 = \frac{r'_1 \left(1 + K_{CO} P_{CO,ave} + K_{H_2} P_{H_2,ave}^{1/2} \right)^2}{\exp\left(\frac{-E_1 * 1000}{R_g T}\right) P_{CH_4,ave} (1 - \beta_1)} \quad \left[\frac{kmol}{kg_{cat} h} \right] \quad (6.3)$$

where

$$r'_1 = X_{CH_4,out} * F_{CH_4,in} \quad \left[\frac{kmol}{kg_{cat} h} \right] \quad (6.4)$$

$$P_{i,ave} = (y_{i,in} * P_{in} + y_{i,out} * P_{out}) / 2 \quad [bar] \quad (6.5)$$

β_1 is defined in Eq. (2.37), while K_j is defined by Eq. (2.34) and Table 2.4. E_1 is found in Table 2.4. Subscripts *in* and *out* refer to the inlet and outlet of the micro-reactor.

6.2.6 Estimation of Porosity

The porosity, ε , is needed to calculate the effective diffusivity in the catalyst layer of the MCMR model, developed in Chapter 2 (see Eq. (2.5)).

$$\varepsilon = V_{pore} / V_{cat} \quad (6.6)$$

Dividing (6.6) by W_{cat} / W_{cat} leads to:

$$\varepsilon = \frac{V_{pore} / W_{cat}}{V_{cat} / W_{cat}} \quad (6.7)$$

We next introduce:

$$W_{ske} = W_{cat} \quad (6.8)$$

$$V_{cat} = V_{ske} + V_{pore} \quad (6.9)$$

$$v = V_{pore} / W_{cat} \quad [cm^3 / g] \quad (6.10)$$

where subscript *ske* refers to the carrier skeleton properties. Inserting Eqs. (6.8), (6.9) & (6.10) into Eq. (6.7), we obtain:

$$\varepsilon = \frac{\nu}{\frac{V_{ske} + V_{pore}}{W_{cat}}} \quad (6.11)$$

$$\varepsilon = \frac{\nu}{1/\rho_{ske} + \nu} \quad (6.12)$$

For alumina, $\rho_{ske} \approx 3900 \text{ kg/m}^3$; for ν measurements, see Section 6.2.7 below. Note that ν units must be adjusted to be used in Eq. (6.12).

6.2.7 Analytical Equipment

FESEM

Field Emissions Scanning Electron Microscopy (FESEM) images were obtained from a Hitachi S-4700 FESEM. Images were taken with an acceleration voltage ranging from 2.3 to 4.0 kV at $7 \times 10^{-4} \text{ Pa}$. Samples could be Au–Pd sputtered to overcome the electrical insulation of the ceramic material.

Gas Chromatograph

The gas product composition was analyzed with a Shimadzu GC-14B, equipped with both a Thermal Conductivity Detector (TCD) and a Flame Ionization Detector (FID). The GC includes three packed columns in series: Porapak-N (80/100 mesh, 3 m), Porapak-Q (80/100 mesh, 3 m) and MS-5A (60/80, 2.25 m). Argon is both the carrier gas and the TCD reference gas, at flow rates of $\sim 22 \text{ Nml/min}$. For CO_2 , CH_4 and CO detection, the FID detector was used for sample concentrations below $\sim 3 \text{ vol\%}$. For more concentrated samples, as well as other gases, the TCD detector was used. Oven temperature started at 60°C for $\sim 10 \text{ min}$, ramped 7.5°C/min to 105°C , and was kept constant until the program finished. The FID temperature was set at 200°C and the TCD at 160°C .

Table 6.2: Co-Sorption Parameters

Step	Gas Comp (vol%)	Flow (ml/min)	Temp. Target (°C)	Temp. Rate (°C/min)	Hold Time (min)
Preparation					
1	10% H ₂ -Ar	50	120	10	30
2	10% H ₂ -Ar	50	400	20	30
3	He	50	50	-	30
CO - Pulse					
4	10% CO-He	1.81 umol/dose	50	-	-

Metal Dispersion (CO-Sorption)

A Micromeritics AutoChem II analyzer measured the metal catalyst dispersion. About 0.1-0.2 g of catalyst was inserted into the sample tube. Gas and temperature settings are listed in Table 6.2. We assumed a 1:1 mole ratio between the Ru or Ni sites and the CO absorbed.

TPR

Temperature Programmed Reduction (TPR) profiles were recorded on a Micromeritics AutoChem II analyzer equipped with a TCD. The following protocol was used: About 0.1-0.2 g of catalyst was inserted into the sample tube. For sample preparation, a stream containing 10% O₂ in helium flowed at of 50 ml/min, while the temperature was ramped at 20°C/min until 700°C was reached, and then held for 30 min. The sample was next cooled quickly to 40°C. A cold trap (liquid nitrogen and isopropyl alcohol) was installed to prevent reaction byproducts from reaching the detector. The TPR recording was started, with the temperature ramped at 20°C/min to the desired final temperature (700-900°C), with a 10% H₂ in argon gas flow of 50 ml/min. A stoichiometric ratio of 1.0 between H₂ and Ni is assumed in the reducibility calculations.

XRD

Catalyst X-Ray Diffraction (XRD) spectra were obtained with a D8 Advanced powder X-ray diffractometer. The device uses Cu radiation and a NaI scintillation detector. The scanning speed was 8-9 s/step at a step size of 0.05°/step.

Surface Area - Pore volume - Pore size

A Micromeritic ASAP 2020 analyzer was used with nitrogen to measure the Brunauer, Emmet and Teller (BET) surface area, Barrett, Joyner and Halenda (BJH) desorption average pore size, and BJH desorption pore volume.

6.2.8 Metrics

Methane Conversion

The micro-reactor methane conversion was calculated from the reactor outlet dry composition:

$$X_{\text{CH}_4} = \frac{y_{\text{CO}_2} + y_{\text{CO}}}{y_{\text{CH}_4} + y_{\text{CO}_2} + y_{\text{CO}}} \quad [\text{mol/mol}] \quad (6.13)$$

Deactivation

For experiments with the same operating conditions, exponential curve fitting was performed for comparison purposes only. It was not intended as a rigorous deactivation model. X_{CH_4} vs time on stream t was fitted by:

$$X_{\text{CH}_4} = a * e^{-bt} + c \quad (6.14)$$

where $(a + c)$ is proportional to the initial activity of the catalyst. b is related to the deactivation rate, and c is an indication of the residual activity of the catalyst.

6.3 Results and Discussion

6.3.1 Preliminary Stability Test

The first stability tests were related to early coating attempts, as explained in Chapter 4. Crushed RK-212, RK-212 with boehmite, lab-made Ni catalyst, and commercial Ru catalyst were tested first. None of those catalysts were active and/or stable enough to be successful in the MCMR. Detailed stability results are presented in Appendix B.

In summary, RK-212 was not stable enough for the MCMR. However, experiments with this catalyst demonstrated the importance of providing an appropriate amount of catalyst in the micro-reactor to avoid thermodynamic equilibrium from hiding deactivation. Lab-made Ni-based catalysts, prepared with the initial coating method presented in Chapter 4, were not active. TPR analyses suggested that high temperature $>700^{\circ}\text{C}$ is required to reduce this catalyst, making it undesirable. The commercial Ru/ $\gamma\text{-Al}_2\text{O}_3$ catalyst showed superior stability compared to the RK-212 catalyst. However, application of nitric acid during the coating had strong negative effects on both the initial activity and stability. Since nitric acid is essential to our modified-sol coating technique, this catalyst was not investigated further. However, stability test with commercial Ru catalyst exposed the importance of activations conditions. Calcination in air and reduction with H_2 at elevated pressure (11 bar) both had strong negative effects on initial activity and stability.

6.3.2 Lab-made Ru Catalyst

The first lab-made Ru-based catalyst coatings were prepared according to the initial procedure explained in Chapter 4, with the promoters and ruthenium impregnated in two different steps, after hot spray coating and calcination of the $\gamma\text{-Al}_2\text{O}_3$ support. Learnings from the commercial Ru catalyst experiments were also applied with the lab-made catalysts not calcined, but only reduced in-situ in the micro-reactor.

Figure 6.3 presents the first results with lab-made Ru catalyst. In part A, all lab-made catalyst (curves B,C & D) performed better than the commercial one (curve A). Catalyst containing MgO (curves C & D) was stable under the condi-

Table 6.3: Stability Conditions for Lab-made Ru-based Catalyst: Influence of Steam. Catalyst Composition and Steam Conditions for Figure 6.3. Modified sol: 40% boeh., 0.75 mol/L, pH 5 (nitric acid); Metal support: SS 304.

Label	Composition (wt%)	Ru Precursor	Note	Steaming Conditions
A	Ru 5% (Alfa)	N/A	for comparison	N/A
Without Steam				
B	Ru 5%	RuNO(NO ₃) ₂	-	N/A
C	Ru 5% MgO 5%	RuNO(NO ₃) ₂	-	N/A
D	Ru 5% MgO 3%	RuCl ₃	-	N/A
With Steam				
E	Ru 5% MgO 3%	RuNO(NO ₃) ₂	-	21 bar, 11 h, 550°C (Support and Metal Catalyst)
F	Ru 5%	RuNO(NO ₃) ₂	Spent: after MCMR run	Run Conditions: 21 bar, S/C: 2.5, H/C: 0, 5 h
G	Ru 5%	RuNO(NO ₃) ₂	Catalyst loading 0.01g	23 bar, 11 h (Support only)

tions studied. Note that for curve (C), a steep drop in conversion occurred at ~20 h. This drop coincided with a sudden pressure change, caused by the purging of the water condenser. The pressure change might have displaced the catalyst bed. Catalyst in curves (C) & (D) were made of RuCl₃ and RuNO(NO₃)₂ respectively, showing that the type of Ru precursor did not influence the activity. However, as presented in Chapter 4, the coating was unstable when using RuCl₃. RuNO(NO₃)₂ was therefore selected for further testing. Table 6.4 lists the curve fitting results.

Steam Effect

The first trials with the MCMR prototype were at ~20 bar, almost twice than the maximum pressure tested in the micro-reactor, ~11 bar. Figure 6.3 Part B, shows the decline in conversion with high pressure steam. Catalyst in curve (F) was scratched off a plate after an unsuccessful trial in the MCMR (See Chapter 8).

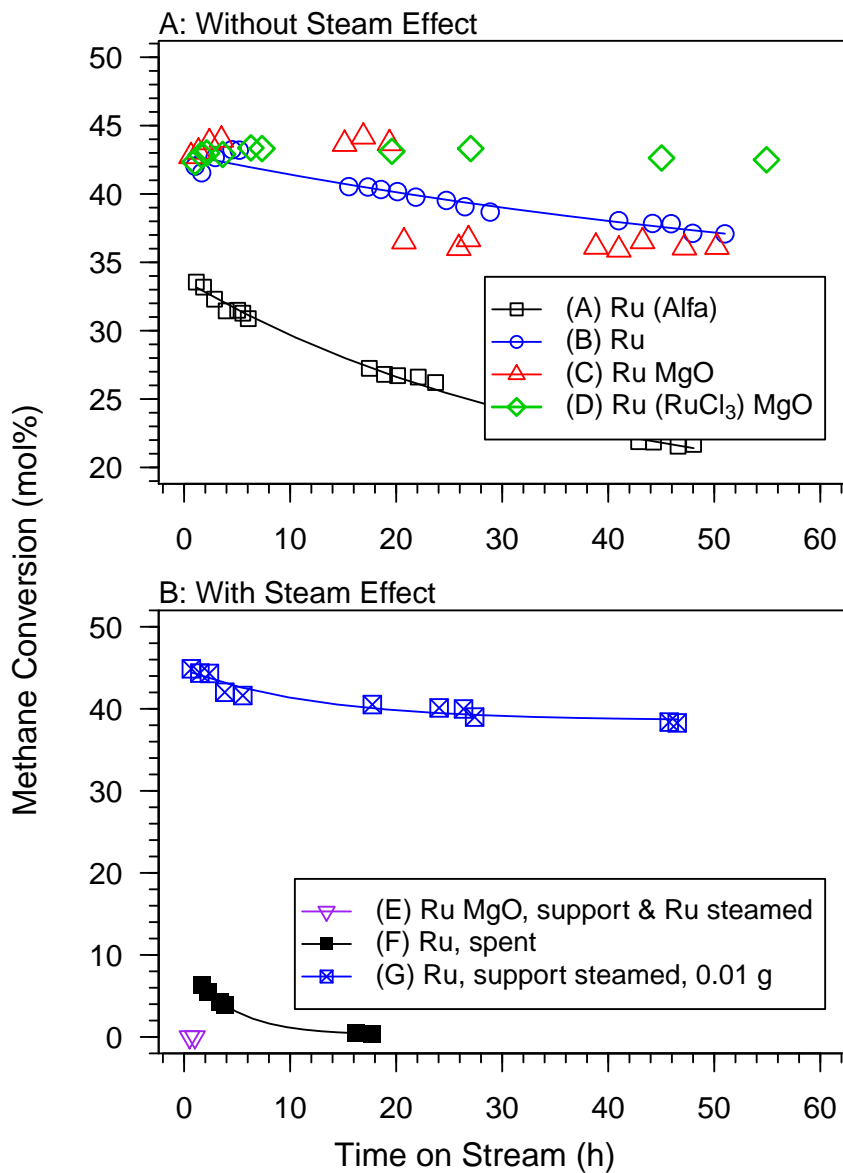


Figure 6.3: Stability Test for Lab-made Ru-based Catalyst, Influence of Steam: Methane Conversion vs Time on Stream. Reforming Conditions: 550°C, 11 bar, S/C: 2.5, H/C: 0, CH₄ flow: 100 Nml/min; Catalyst loading (except where specified): 0.02 g. Reduction & Start-up: H₂ flow: 42 Nml/min, ramped at 5°C/min, hold for 1 h at 600°C. Data fitted with Eq. (6.14). Table 6.3 shows changes in catalyst preparation.

Table 6.4: Curve Fitting Related to Figure 6.3 and Eq. (6.14) for Stability of Lab-Made Ru-based Catalyst.

Label	a	b	c	a+c	R ²
A	16.8	0.0272	16.9	33.7	0.994
B	11.3	0.0141	31.6	42.9	0.93
C	Stable over conditions studied				
D	Stable over conditions studied				
E	Activity too low				
F	8.88	0.232	0.26	9.1	0.999
G	6.20	0.0799	38.6	44.8	0.93

Table 6.5: Surface Area, Pore Volume, Average Pore Diameter, and Metal Dispersion of Lab-made Ru 6%/ γ -Al₂O₃ Catalyst (carrier not pre-aged by steam)

	Surface Area m ² /g	Pore Volume cm ³ /g	Ave. Pore Dia. nm	Metal Dispersion mol %
Fresh	126	0.52	13.5	5.3%
Spent	103	0.51	16.5	2.7%

Activity was severely affected.

Steam was suspected to be a factor in the deactivation, and several analyses were therefore performed to identify the problem. Figure 6.4 shows FESEM images before and after the MCMR run. Part C (fresh) and Part D (spent) have the same magnification; no noticeable structural change can be observed. The issue seemed to be at a scale smaller than detectable on those FESEM images. Macro pore sintering (>50 nm) and extensive carbon fouling could be discounted as possible reasons.

Table 6.5 shows the surface area, pore volume, average pore diameters, and CO-sorption data before and after the MCMR run. While the pore volume stayed constant, the average pore size increased, indicating that smaller pores sintered during the MCMR experiments. The metal dispersion also dropped by 50%, indicating that both metal and pore sintering may have occurred at the same time.

In order to resolve the issue, high-pressure (~20 bar) steam was contacted with

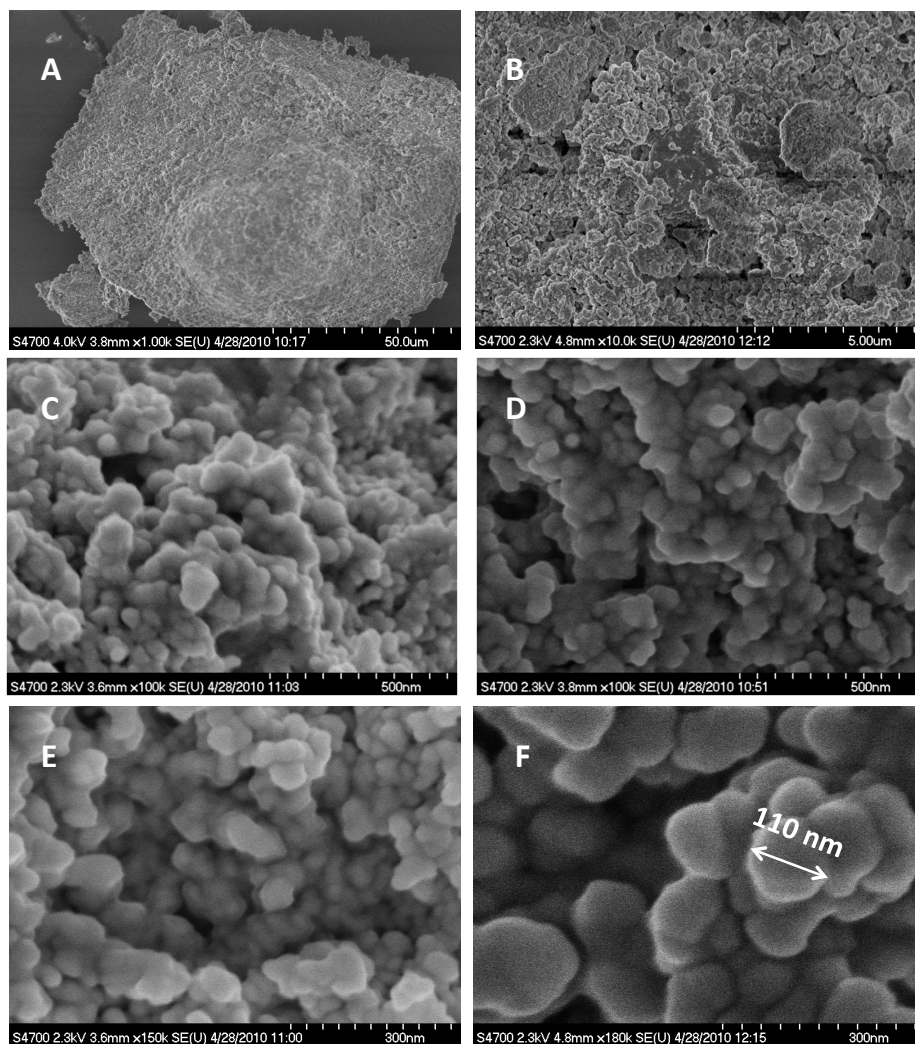


Figure 6.4: FESEM Images of Ru 6%/ γ -Al₂O₃ (carrier not steamed): A,D spent catalyst; B,C,E,F fresh catalyst. Modified sol: 40% boeh., 0.75 mol /L, pH 5.

Table 6.6: Stability Conditions for Lab-made Ru-based Catalyst, Influence of Rust on SS 304 Support for Figure 6.5. γ -Al₂O₃ support with La₂O₃ steamed 24 h, 23 bar, 590°C. Modified Sol: 40% boeh., 0.75 mol/L, pH 5 (nitric acid).

Label	Composition (wt%)	Note
A	Ru 8% La ₂ O ₃ 5%	No rust, fresh, Fecralloy support ^a
B	Ru 6% La ₂ O ₃ 6%	Rusty ^b , fresh, repeat 1
C	Ru 6% La ₂ O ₃ 6%	Rusty ^b , fresh, repeat 2
D	Ru 5% La ₂ O ₃ 3%	Rusty, spent: after MCMR run

^aData taken from Figure 6.6 for comparison purpose

^bRust appeared while leaving plate with catalyst support at ambient temperature for 4 months after the steaming step. Ru impregnation was then made on that rusty support.

the carrier prior to impregnation with RuNO(NO)₃. The catalyst in curve (G) on Figure 6.3B had its carrier pre-aged with steam and showed high activity, but still showed some deactivation. Hence, promoters are likely still needed. In the next sections, La₂O₃, known to help stabilize γ -Al₂O₃ (Schaper et al., 1983), and proven to be effective in suppressing carbon formation in Chapter 4, was added. We also added to some catalyst ~2-4% MgO, which has been shown to be beneficial for stability in Figure 6.3A, and ~2% MnO, used by Berman et al. (2005).

6.3.3 Rust Effect

Our first trial with Ru–La₂O₃ on hydro-aged γ -Al₂O₃ in the MCMR was successful (see Chapter 8). However, there were issues repeating the experiments with fresh catalyst and also while reusing the catalyst plates that appeared to be active at the end of a previous run.

As in Chapter 5, rust appeared on many samples under different conditions with SS 304 as metal support. It was suspected that the rust affected the activity of the Ru catalyst.

Figure 6.5 examines the rust issue. Only 0.002 g of catalyst were loaded into the micro-reactor in order to observe faster deactivation. Spent catalyst (curve D), recovered after the MCMR run, was completely inactive. Curve (A) represents rust-free fresh catalyst. Curves (B) & (C) belongs to the same fresh catalyst, where rust was visible on the surface of the plate. The residual activity factors “c” on Table

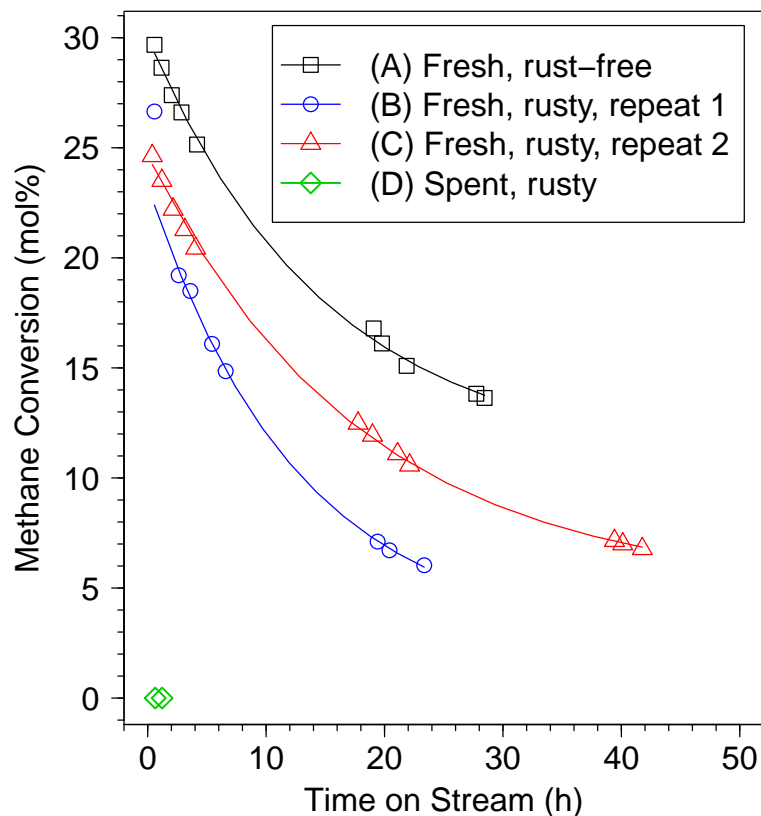


Figure 6.5: Stability for Lab-made Ru–La₂O₃/ γ -Al₂O₃ Catalyst, Influence of Rust on Support: Methane Conversion vs Time on Stream. Start-up conditions: H₂ flow: 42 Nml/min, ramped 6.3°C/min, hold at 600°C for 1 h. Reforming Conditions: 550°C, 11 bar, CH₄ flow: 100 Nml/min; S/C: 2.5, H/C: 0; Catalyst loading: 0.002 g. Data fitted with Eq. (6.14). Table 6.6 provides details on the catalysts studied.

Table 6.7: Curve Fitting Related to Figure 6.5 and Eq. (6.14) for Stability of Lab-Made Ru-based Catalyst.

Label	a	b	c	a+c	R ²
A	19.2	0.0661	10.8	30.0	0.998
B	20.6	0.0795	2.74	23.3	0.999
C	19.7	0.0556	4.92	24.7	0.999
D	Activity null				

Table 6.8: Membrane Start-up Steps with H₂–H₂O mixture (starting at room temperature)

Step	Temperature		Flow Rates		P _{ave} bar	P _{H₂} bar
	Ramp (°C/min)	Final Value (°C)	H ₂ O (g/h)	H ₂ (Nml/min)		
1	6.3	400	69	10	6	0.04
2	6.3	450	29	10	6	0.10
3	6.3	500	12	14	6	0.32
4	6.3	550	12	14	6	0.32
5	-	550	0	0	11	0.00

6.7 suggest a loss of activity for “rusty” catalysts. However, more tests would be needed to prove the difference statistically.

Rust stains on spent catalyst were larger than those on rusty supports (see Chapter 4, Figure 5.8 Parts C.1 vs B.1). The extent of iron oxide coating could explain the difference of activity between fresh & spent rusty catalysts.

To the best of our knowledge, there is limited indication that iron oxide could deactivate Ru catalyst, acting as a poison. Arena (1992) suggested that a Ru/Al₂O₃ catalyst for glucose hydrogenation could have been deactivated by iron build-up on the catalyst, but other compounds like sulfur were also present.

As described in Chapter 5, the rust issue was solved by changing the metal support. Fecralloy proved to be effective, whereas SS 310 reduced rust diffusion, but did not stop it completely. With Fecralloy as metal support, the MCMR was finally able to produce pure hydrogen, as shown in Chapter 8.

6.3.4 Start-up Procedure for Membrane

The regular reduction and start-up procedure consisted of feeding pure hydrogen while ramping the micro-reactor temperature. In order to maintain the integrity of the Pd/Ag membrane, tight control on hydrogen partial pressure was required during the MCMR start-up. We observed in previous sections that the start-up procedure can influence catalyst activity. The micro-reactor was employed to develop a procedure acceptable for both the membrane and for catalyst activity. Tables 6.8 and 6.9 show trial procedures, using steam and nitrogen respectively. The membrane start-up procedure is finalized in Chapter 8.

Table 6.9: Membrane Start-up Steps with H₂–N₂ mixture (starting at room temperature)

Step	Temperature		Flow Rates		P _{ave} bar	P _{H₂} bar
	Ramp (°C/min)	Final Value (°C)	N ₂ (Nml/min)	H ₂ (Nml/min)		
1	6.3	400	356	10	1.5	0.04
2	6.3	500	225	10	1.5	0.06
3	6.3	550	180	43	1.5	0.29
4	6.3	550	180	43	11	2.12
5	-	550	0	43	11	0.00

Table 6.10: Stability Conditions of Lab-made Ru-based Catalyst: Influence of Membrane Start-up Procedure for Figure 6.6. Modified Sol: 40% boeh., 0.5 mol/L, pH 5 (nitric acid). γ -Al₂O₃ carrier and promoters steamed for 24 h, at 23 bar, and 590°C on Fecralloy (except where specified).

La- bel	Composition (wt%)	Note / Start-up Conditions
Regular Reduction & Start-up^a		
A	Ru 8% La ₂ O ₃ 5%	-
B	Ru 8% La ₂ O ₃ 5%	SS 304 as metal support
C	Ru 8% La ₂ O ₃ 5%	SS 304 as metal support
D	Ru 7% La ₂ O ₃ 4% MgO 4%	
Start-up Modified for Membrane		
E	Ru 7% La ₂ O ₃ 4% MgO 4%	Steam & N ₂ mix ^b
F	Ru 7% La ₂ O ₃ 4% MgO 4%	Heated at 600°C for 1 h with N ₂ , cooled to 350°C, pressurized to 6 bar, H ₂ –H ₂ O mix start-up (Tab. 6.8)
G	Ru 7% La ₂ O ₃ 4% MgO 4%	Heated at 625°C for 1 h with N ₂ , cooled to 350°C, follow by H ₂ –N ₂ mix start-up (Tab. 6.9)
H	Ru 7% La ₂ O ₃ 4% MgO 4%	H ₂ –N ₂ mix start-up (Tab. 6.9)

^aRegular Reduction & Start-up: H₂ flow: 42 Nml/min, ramped 6.3°C/min, hold for 1 h at 600°C.^bRatio Steam / N₂ not measured

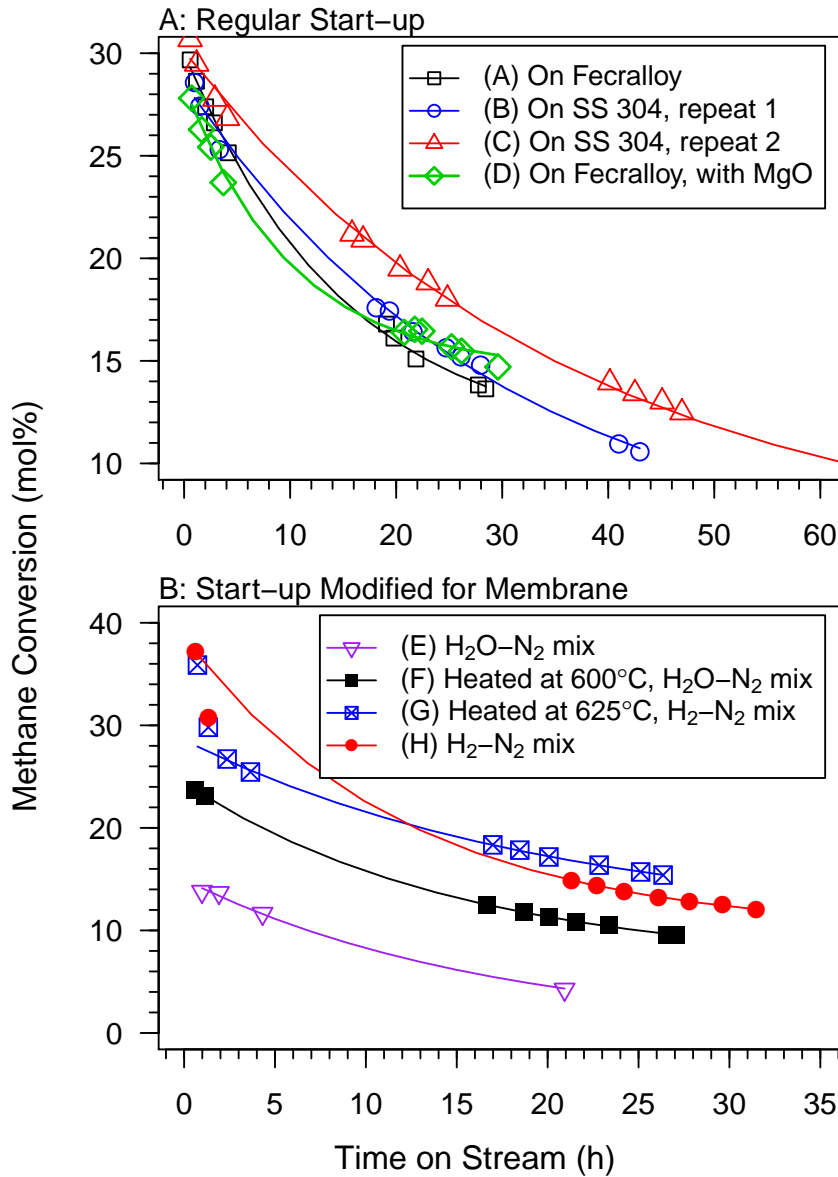


Figure 6.6: Stability of Lab-made Ru-based Catalyst, Influence of Membrane Start-up Procedure: Methane Conversion vs Time on Stream. Reforming Conditions: 550°C, 11 bar, CH₄ flow: 100 Nml/min; S/C: 2.5, H/C: 0; Catalyst loading: 0.002 g. Data fitted with Eq. (6.14). Table 6.10 shows changes in catalysts and start-up conditions.

Table 6.11: Curve Fitting Related to Figure 6.6 and Eq. (6.14) for Stability of Lab-Made Ru-based Catalyst.

Label	a	b	c	a+c	R ²
A	19.2	0.0661	10.8	30.0	0.998
B	23.4	0.0335	5.19	28.6	0.996
C	24.6	0.0274	5.56	30.1	0.998
D	13.9	0.0986	14.5	28.4	0.996
E	15.0	0.0594	0.0	15.0	0.996
F	17.8	0.0662	6.59	24.4	0.9998
G ^a	18.2	0.0490	10.4	28.6	0.9997
H ^a	28.7	0.0819	9.89	38.5	0.998

^aFirst two data points skipped, where stronger deactivation than the exponential model fit occurred.

Table 6.12: Details of Ru-based Catalysts on XRD Spectra of Figure 6.7. Modified sol: 0.5-0.75 mol/L, 40% boeh., pH 5; Ru from RuNO(NO₃)₃.

Label	Composition (wt%)	Steaming	Fresh/Spent	Note
A	Ru 5%	no	fresh	calcined
B	Ru 5%	no	spent	
C	Ru 7% La ₂ O ₃ 5%	yes	fresh	
D	Ru 6% La ₂ O ₃ 6%	yes	spent	
E	Ru 4% La ₂ O ₃ 6%	yes	spent	

Figure 6.6 Part A shows stability results with the regular reduction and start-up procedure for a Ru–La₂O₃ catalyst. All catalysts showed similar initial activity, while Table 6.11 indicated some variations in the rate of deactivation and residual activity. Variations are more apparent in Figure 6.6 Part B. Start-up with steam (curves E & F) affected the Ru activity, while start-up with H₂–N₂ mixtures (curves G & H) gave activity results similar to those in Part A. Even with pre-reduced catalyst (curve F), the activity was affected by steam. Based on these results, a H₂–N₂ mixture was selected for the MCMR start-up.

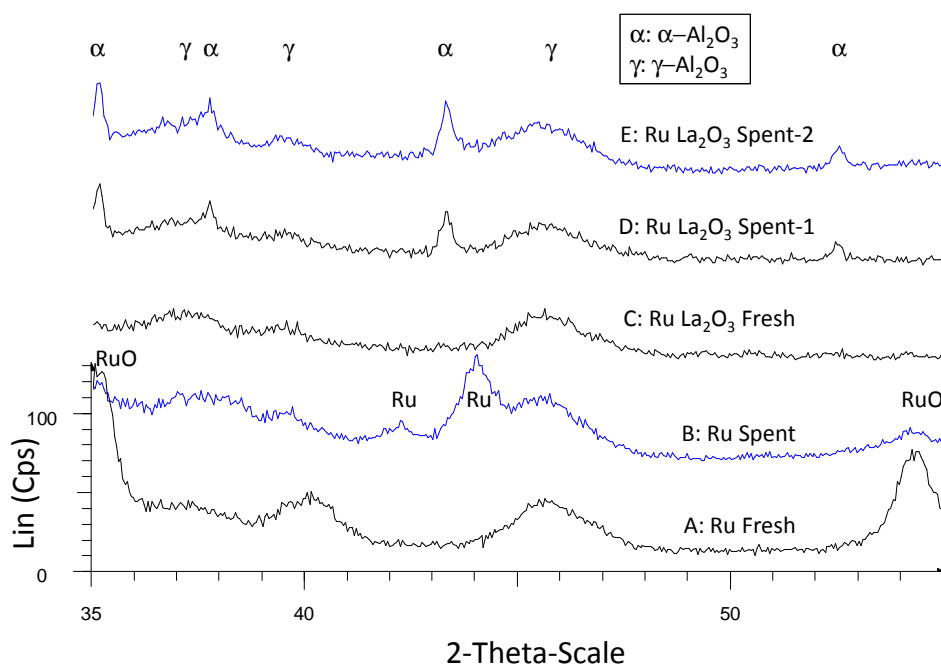


Figure 6.7: XRD diagram of Lab-made Ru-based Catalyst, Fresh and Spent (after MCMR Exp.). See Table 6.12 for details on the catalysts.

6.3.5 Deactivation Mechanisms

This section tries to explain the catalyst deactivation decays presented in this chapter, using both fresh catalysts and catalysts spent during the MCMR experiments. Figure 6.7 presents XRD spectra of lab-made Ru-based catalysts. Spectra (A) and (B) are for early lab-made catalysts, with the support not steamed, no promoters, and the $\text{RuNO}(\text{NO}_3)_3$ calcined. The presence of large Ru and RuO peaks indicates poor Ruthenium dispersion. Poor dispersion was already observed in Table 6.5 with a similar catalyst. It was previously noted that during calcination, Ru could be oxidized to RuO_4 and vaporise. The large RuO peaks could also indicate that the calcination caused severe metal sintering. Poor dispersion was obtained also by Li et al. (2009), while a calcined Ru 1%/ Al_2O_3 catalyst had a dispersion of only 2.8%, compared to 55.9% for the same catalyst without calcination.

Spectra (C), (D), and (E) represent active catalysts with La_2O_3 as promoter. No Ru peaks are visible, indicating good dispersion for both fresh and spent catalysts. The two spent catalysts show the appearance of $\alpha\text{-Al}_2\text{O}_3$, indicating a phase change that would cause inevitable pore sintering. In air, $\gamma\text{-Al}_2\text{O}_3$ would only change to $\alpha\text{-Al}_2\text{O}_3$ around 800°C (Gitzen, 1970). The steam itself, during the hydro-aging of the carrier and promoters, did not cause a phase change (spectrum C). However, the SMR environment seems to have promoted the phase change at a much lower temperature than air, since the MCMR operated at a maximum temperature of 575°C in the reforming channel.

Table 6.13 summarizes surface area, pore volume, average pore diameter data for the catalyst support and various catalysts. As expected, steaming reduced the surface area, slightly lowered the pore volume and increased the average pore diameter.

Even though we observed some phase changes on XRD spectra (Figure 6.7), this did not translate into significant drops in pore volume. However, the slight decrease in surface area, and increase in average pore sizes, indicated some pore sintering.

The presence of rust did not seem to affect either the pores or the metal dispersion. The catalyst with a rusty support had a slightly higher dispersion than the rust-free one. Iron oxide might not be a conventional poison, but the presence of iron oxide could, nevertheless, change the electro-negativity of the Ru affecting the absorption/ desorption processes necessary for the SMR reactions.

Promoters helped maintain high metal dispersion. The catalysts without promoters saw their metal dispersion drop on average from 38 to 6.5%, while catalysts with promoters maintained at least half of the dispersion of the fresh samples. There are not enough data to draw conclusions about the optimal promoter concentrations and compositions. This could be a topic for future work.

Porosity Estimation

Based on Eq. (6.12), the porosity is plotted vs pore volume in Figure 6.8 for the range of pore volume data reported previously.

Table 6.13: Surface Area, Pore Volume, Average Pore Size, and Metal Dispersion of Lab-made Ru Catalysts and Supports

	Surface Area m ² /g	Pore Volume cm ³ /g	Ave. Pore Size nm	Metal Dispersion mol %
Catalyst Support				
γ -Al ₂ O ₃ BaikaloX CR125	104	0.78	28.6	N/A ^a
Boehmite Disperal P2 ^b	260	0.5	-	N/A
γ -Al ₂ O ₃ with 40% boeh. after calcination	154	0.55	12.3	N/A
La ₂ O ₃ 7%/ γ -Al ₂ O ₃ after steaming	92	0.52	19.1	N/A
La ₂ O ₃ 3% MgO 3%/ γ -Al ₂ O ₃ after steaming	93	0.49	17.9	N/A
La ₂ O ₃ 4% MgO 2% MnO 2%/ γ -Al ₂ O ₃ after steaming (rusty)	96	0.49	17.7	N/A
Lab-made Ru-based Catalyst/ γ-Al₂O₃ (γ-Al₂O₃ and promoters steamed)				
Ru 7% (fresh)	117	0.50	14.7	38%
Ru 7% (spent) ^c	89	0.48	20.0	6.5%
Ru 6% La ₂ O ₃ 6% (fresh)	93	0.39	14.9	42%
Ru 6% La ₂ O ₃ 6% (rusty support, fresh)				48%
Ru 7% La ₂ O ₃ 5% (spent) ^c	93	0.46	17.5	17%
Ru 7% La ₂ O ₃ 4.6% (spent) ^c	88	0.44	17.8	22%
Ru 7.5% La ₂ O ₃ 4% MgO 4% (fresh)	106	0.41	12.7	34%
Ru 7% La ₂ O ₃ 4% MgO 4% (spent) ^f	88	0.40	16.3	27%
Ru 7.5% La ₂ O ₃ 4% MgO 4% (spent) ^f	98	0.43	15.8	N/A ^b
Ru 7% La ₂ O ₃ 4.6% MgO 2.3% (spent) ^d	94	0.41	16.0	N/A ^b
Ru 8% La ₂ O ₃ 3.2% MnO 1.6% MgO 1.6% (spent) ^e	97	0.42	16.0	22%

^aN/A: Not applicable, or not measured, due to insufficient sample available or faulty instrument

^bSupplier data, after activation at 550°C

^cAfter Exp. no.0.4 (See Section C.2.2)

^dAfter Exp. no.1 (See Table 8.6)

^eAfter Exp. no.2 (See Table 8.6)

^fAfter Exp. no.3 (See Table 8.6)

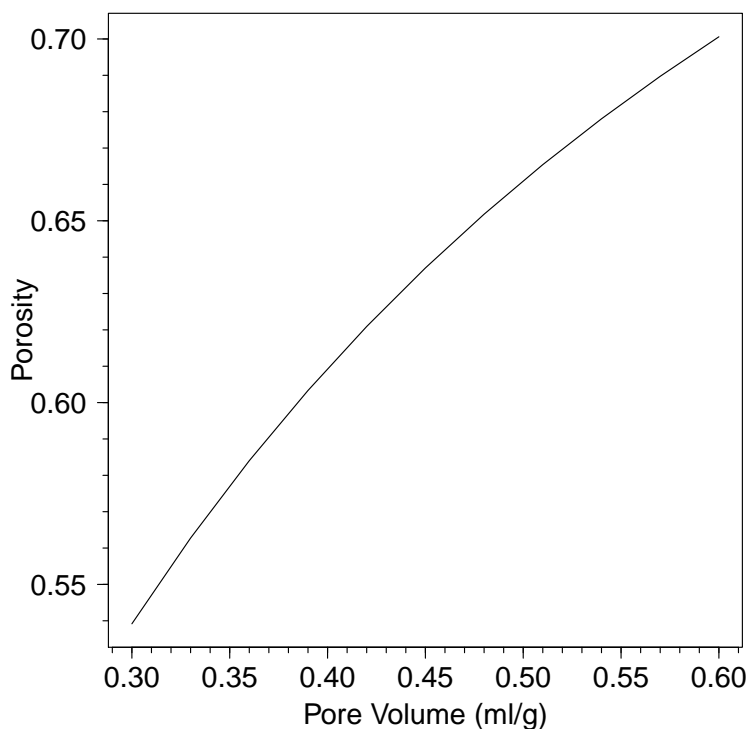


Figure 6.8: Porosity vs Pore Volume for Catalyst with Alumina Support

6.3.6 Catalyst Layer Modeling

With the information gained in previous chapters, we can discuss the validity of the catalyst and pore model developed in Chapter 2. Figure 6.9 illustrates the simulation model (Part A) and an improved model (Part B), based on microscope images, $\gamma\text{-Al}_2\text{O}_3$ particle size data, pore volume and pore diameter measurements. Note that our pore volume measurements only include pore diameters between 2 and 150 nm, and a fraction of the inter-particle voids in Part B.2 might be included in the measured pore volumes.

6.3.7 Estimation of Jackobsen Pre-exponential Kinetic Parameter

Figure 6.10 shows the estimated Jackobsen kinetic pre-exponential factor based on our experimental data. Our estimation is very similar to published data (Jakobsen et al., 2010), even though their catalyst was different (Ru 1%/ ZrO₂). The curves

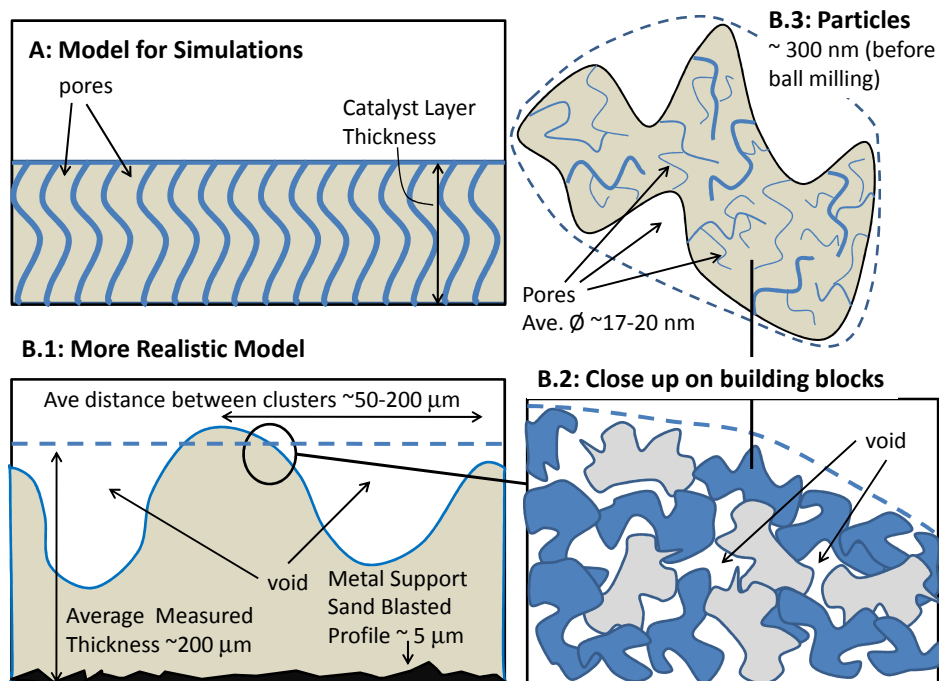


Figure 6.9: Catalyst Layer and Pores Model: A. As Simulated; B. Improved Model. Drawings not to scale.

seem to settle around a ratio of 1. The challenge with our MCMR experiments is that the catalyst was unstable during the first 24 h, a time of the same order as the time of operation.

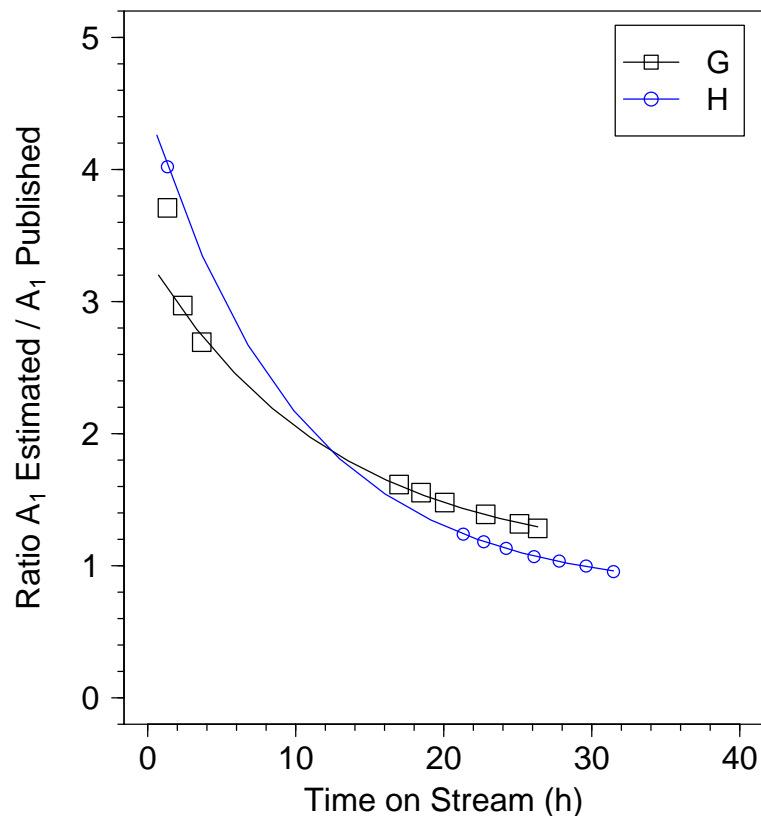


Figure 6.10: Pre-exponential Factor A_1 - Estimation for Jackobsen Kinetics: Ratio between Estimated Value (Eq. (6.3)) over Published Value (Jakobsen et al., 2010) vs Time on Stream. Data are taken from Figure 6.6 curves (G), & (H) and fitted with Eq. (6.14).

6.4 Conclusions

Micro-reactor activity experiments allowed various reforming catalysts to be tested for their suitability in the MCMR prototype, the development of a start-up procedure for the MCMR, and the estimation of the pre-exponential kinetic parameter.

A lab-made Ru-based catalyst had better activity and stability than a commercial Ru catalyst, and was selected for the MCMR. Aging of the support with steam was necessary to avoid total catalyst deactivation. Rust appeared to poison the Ru

catalyst. Fecralloy, initially oxidized in air, effectively stopped rust diffusion from the metal support. Steam should be avoided during start-up of the MCMR since it negatively affected the initial activity. A H_2-N_2 gas mixture was able to activate the catalyst and imitate MCMR start-up conditions.

MgO and La_2O_3 improved the stability of the lab-made Ru catalyst. Insufficient data were collected to reach conclusions on the effectiveness of MnO , as well as the optimal concentrations for the promoters. XRD analyses showed a phase change from $\gamma-Al_2O_3$ to $\alpha-Al_2O_3$. Average pore size generally increased during MCMR runs, confirming that pore sintering was a deactivation mechanism. Fitted pre-exponential factors were similar to those reported by Jakobsen et al. (2010).

Based on microscope images and catalyst physical properties, an improved pore model was obtained, but model equations to describe it is still needed.

Chapter 7

Methane Catalytic Combustion

7.1 Introduction

Catalytic combustion allows the production of heat at lower temperature than homogeneous combustion, leading to less generation of nitrogen oxides and fewer constraints on reactor design (Zanfir and Gavriilidis, 2003; Chauhan et al., 2009). Noble metals (Pd, Pt, Rh) and their oxides are often used as catalysts for this application (Chauhan et al., 2009). Less costly alternatives have also been investigated. For instance, Terribile et al. (1999) studied $\text{CeO}_2\text{--ZrO}_2$ catalysts, some doped with Mn and Cu; Zou et al. (2011) investigated LaMnO_3 perovskite; and Thaicharoen-sutcharittham et al. (2009) looked at NiO/CeZrO_2 . However, for methane combustion, palladium is generally seen as the most efficient catalyst (Lee and Trimm, 1995; Chauhan et al., 2009).

The general pattern of catalytic combustion of hydrocarbons can be described as follows (Lee and Trimm, 1995): As temperature is increased, oxidation is initiated at a temperature that depends on the hydrocarbon and the catalyst; after the ignition, conversion increases exponentially with temperature until the reaction becomes mass transfer controlled, also called the “light off” point.

Deactivation mechanisms were summarized in Chapter 6. Fouling, pore and metal sintering, and poisoning, can also occur with MCC. With Pd-based catalyst, another deactivation mechanism could be the change in oxidation states. There is controversy in the literature about which of the reduced or oxidized palladium

state (Pd or PdO) is more active (Lyubovsky and Pfefferle, 1999). Some authors suggested that Pd is not or less active, and can be a source of deactivation at temperatures above 700°C, where metallic Pd particles are formed from PdO (Colussi et al., 2009). Gao et al. (2008) suggested that deactivation could also come from the transition from PdO to PdO₂. Hellman et al. (2012) used density functional theory and in-situ surface XRD to identify and characterize atomic sites yielding high methane conversion. Assuming that the rate-limiting step is the breaking of the first C-H bond, they found that PdO sites in the crystal plane (101) and metallic Pd sites in the crystal plane (211) gave the lowest activation energies. Since controlling the crystal structure of palladium can be difficult and is rarely reported, the Hellman et al. (2012) findings give some hints about the source of the controversy.

Promoters can be added to stabilize the Pd oxidation state and reduce the rate of metal sintering. For instance, Ozawa et al. (2003) added of Nd₂O₃ and La₂O₃ to Al₂O₃, effectively slowing the transformation from PdO to Pd and preventing PdO particle growth.

Pd-catalysed combustion kinetics is also subject to controversy since interactions with the support, catalyst preparation, gases used for catalyst pre-treatment, partial pressure of oxygen, temperature, oxidation state and crystal structure, can all affect the kinetics (Lee and Trimm, 1995; Lyubovsky and Pfefferle, 1999; Hellman et al., 2012). Lee and Trimm (1995) reviewed studies of methane catalytic combustion with Pd, Pt and Rh. For palladium, the reaction order for methane ranged from 0.5 to 1; for oxygen, the order from 0 to 0.1. Activation energy also varied widely from 52 to 138 kJ/mol. Water is often recognized as an inhibitor (Ciuparu et al., 2001). Some kinetic models include water and give it a negative order (Groppi et al., 2001).

We present in this chapter activity and stability tests performed in the packed bed micro-reactor, with both fresh combustion catalysts from the coating trials and catalysts spent during the MCMR runs. Full description of these runs and their operating conditions are provided in Chapter 8. These post-run results are included here so that all of the micro-reactor material related to combustion is presented in one place. We also estimate kinetic parameters for the Pd-based catalysts used in the MCMR.

7.2 Material and Method

7.2.1 Catalyst Preparation

Commercial and a limited amount of lab-made oxidation catalysts were tested. Coating methodologies and materials are described in details in Chapters 4 and 5. In brief, for commercial catalyst, Disperal P2 boehmite (Sasol) was mixed in distilled water with the commercial catalyst powder. Boehmite represented 15% of the total solid mass. The concentration of the catalyst powder was 0.25 mol/L (based on molecular weight of alumina). The mixture was ball milled overnight, and the pH was adjusted with nitric acid to ~ 5 before and after the ball milling. The modified sol was air-spray coated onto a stainless metal substrate, after being heated to $>100^\circ\text{C}$, and previously sand-blasted. Once the thickness of the coating was judged acceptable, the samples were calcined overnight in static air at 650°C .

For lab-made catalyst, Baikalox CR125 $\gamma\text{-Al}_2\text{O}_3$ (Baikowski) was mixed with the boehmite, which represented 40% of the total solid mass. The concentration of the $\gamma\text{-Al}_2\text{O}_3$ powder was 0.5 mol/L. After the air-spray coating and calcination, promoters were impregnated using a modified incipient wetness procedure. Plates were flooded with the impregnation solution, and excess solution was removed after 2 min. The mixture was air dried for 2 h, and heated at 110°C overnight in static air. Impregnation solution concentrations are listed in Table 7.1. The support and promoters were steamed and heated under pressure at 25 bar and 575°C for 24 h. Pd was then impregnated following the same procedure as for the promoters. Plates were calcined at 600°C in static air for 5.5 h.

After the heat treatment, for “fresh” samples, or after MCMR runs, for “spent” samples, catalysts were scratched off the metal plates, and ground with a mortar and pestle to obtain a fine powder. 1.7 to 2.0 mg of catalyst were diluted in $\gamma\text{-Al}_2\text{O}_3$ powder (BASF HiQ-7S19cc) to obtain a total of 1 g. The solid mixture was inserted into the micro-reactor, following the procedure described in Chapter 6.

7.2.2 Experimental Set-up

A simplified process flow diagram of the micro-reactor unit was provided in Figure 6.2, and a detailed P&ID is included in Appendix D.1. The functioning of the unit

Table 7.1: Impregnation Solutions and Desired Metal Contents for Combustion Catalysts

Desired Metal Content ^a wt%	Solution mol/L
Promoters	
La ₂ O ₃ 6%	La Nitr. 0.27
La ₂ O ₃ 4% MgO 4%	La Nitr. 0.18; Mg Nitr. 0.72
Catalyst	
Pd 5%	Pd Nitr. Sol. Pd 4-5% w/w (Alfa Aesar, as received)

^aMeasured metal content can vary by $\pm 2\%$ from the desired value

for the catalytic combustion experiments can be summarized as follows: Air was pre-heated to 300-380°C with rope heaters, before being mixed with CH₄ to the desired composition. All feed streams are controlled with mass flow controllers. Downstream of the micro-reactor, water was removed with a condenser, and gas products were split into two streams, one going to the GC, the other being vented.

The micro-reactor has one thermocouple inside the bed and one on the outside surface of the reactor tube. Pressure transducers measure the inlet (P_{in}) and outlet (P_{out}) pressures. All temperatures reported in the results section below are reactor temperatures (T_{bed}), whereas the pressures are averages of P_{in} and P_{out} .

Gases used for the MCC experiments were purchased from Praxair: CH₄ (99% purity), air (extra dry grade), and N₂ (99.995+% purity).

Start-up and Operation

Start-up was difficult for the MCC. Uncontrolled temperature jumps, when reaching the light-off point were common, and could trigger automatic shut down of the unit. The start-up was performed as follows to minimize temperature jumps: Air was fed to the reactor at 200 Nml/min, and atmospheric pressure (P_{out}), while the temperature was increased at 10°C/min from ambient temperature to 400°C. Air flow was then increased to 1000-1900 Nml/min and methane flow was started (30-37 Nml/min), to obtain the desired inlet composition of 2-3% CH₄ in air. The pressure was then increased to the desired value (average pressure from 3.8 to 8.4 bar). After the pressure stabilized, the temperature was increased at 2-3°C/min to 510°C.

After reaching this temperature, if a higher temperature was needed, the ramping rate was reduced to 1°C/min until the final desired temperature (550-575°C) was reached.

The P&ID temperature controller often needed manual adjustment >510°C to stabilize the temperature at the desired set point: unlike the reforming reaction, MCC requires less heating, since the combustion is exothermic.

Due to the large excess of air sought, resulting in large air flow, pressure drops through the packed bed were significant: for instance, for an average pressure of 5.7 bar, the pressure drops was 1.3 bar. WHSV varied from 38,000 to 71,000 h⁻¹. The reactor surface (or skin) temperature differed significantly from the reactor temperature. For example, when methane conversion was 10% at a reactor temperature of 575°C, the surface temperature could reach be as high as 665°C.

7.2.3 Estimation of Kinetic Parameters

As in Chapter 6, we estimated kinetic parameters by assuming that the micro-reactor was acting as a differential reactor. Kinetic parameters were evaluated for methane conversions less than 15%, to avoid mass transfer limitations. Initially, catalysts were subject to considerable deactivation, but after 24-48 h, the catalysts were more stable, and kinetics measurements were then performed.

Chapter 2 provided an empirical n^{th} order kinetic model to describe the combustion reaction (Eqs. (2.50), (2.51)). To stay below the CH₄ explosion limit, a large stoichiometric excess of air (240-415%) was provided. The effect of oxygen on the kinetics was neglected ($\beta = 0$ in Equation (2.50)). Experimentally, we determined the rate of reaction as:

$$r_4'' = X_{CH_4,out} * F_{CH_4,in} \left[\frac{kmol}{kg_{cat} s} \right] \quad (7.1)$$

By varying the temperature, with constant flow rates and pressure, taking the natu-

ral logarithm of r_4'' in Eq. (2.50), we obtain:

$$\ln(r_4'') = \ln \left(A_4 \exp \left(\frac{-E_4 * 1000}{R_g T} \right) P_{CH_4,ave}^\alpha \right) \quad (7.2)$$

$$= \left(\frac{-E_4 * 1000}{R_g T} \right) + \left(\ln(A_4) + \ln \left(P_{CH_4}^\alpha \right) \right) \quad (7.3)$$

From the slope of a plot of $\ln(r_4'')$ versus $(1/T)$, we can extract the activation energy E_4 .

By varying the total pressure of the system, while keeping flow rates constant, we can obtain several values of $P_{CH_4,ave}$. Taking the natural logarithm of r_4'' , we obtain:

$$\ln(r_4'') = \alpha \ln(P_{CH_4,ave}) + \ln \left(A_4 \exp \left(\frac{-E_4 * 1000}{R_g T} \right) \right) \quad (7.4)$$

The slope of $\ln(r_4'')$ versus P_{ave} represents the reaction order α .

Finally the pre-exponential factor A_4 is evaluated with:

$$A_4 = \frac{r_4''}{\exp \left(\frac{-E_4 * 1000}{R_g T} \right) P_{CH_4,ave}^\alpha} \left[\frac{kmol}{kg_{cat} s bar^\alpha} \right] \quad (7.5)$$

E_4 and α were evaluated with experiments on commercial Pd 1%/ γ -Al₂O₃ (Alfa). A_4 was estimated for Pd 1% and 5%/ γ -Al₂O₃ (Alfa), and for lab-made Pd La₂O₃–MgO/ γ -Al₂O₃ catalysts.

7.2.4 Analytical Equipment

All instrumentations utilized in this chapter is described in Chapter 6.

7.2.5 Metrics

Equations (6.13) and (6.14)), from Chapter 6 were used to evaluate the methane conversion and to fit the stability data with an exponential decay relationship.

7.3 Results and Discussion

7.3.1 Preliminary Stability Test

To investigate a less costly alternative to Pd, tests with CeO₂ powder, and CeO₂–ZrO₂–Al₂O₃ from the coating procedure (see Chapter 4) were initially performed. No significant conversion was observed, although previous researchers, e.g. Terribile et al. (1999) reported some success with CeO₂. We showed in Chapter 4 that our purchased CeO₂ was non-porous, so a lack of active sites could explain the lack of activity. No further work were performed on the CeO₂-based catalysts, since tests with Pd-based catalysts were successful, as shown below.

7.3.2 Stability of Pd 1%/ γ -Al₂O₃ (Alfa)

Figure 7.1 shows the stability of Pd 1%/ γ -Al₂O₃ (Alfa) with 15% boehmite. Two different deactivation mechanisms could be observed. First, there was a similar exponential decay deactivation behaviour as observed with the reforming stability tests presented in the previous chapter. However, with the combustion catalyst, some of the deactivation was reversible, a finding not observed with reforming catalysts. After unplanned shutdowns (denoted by “*” in Fig. 7.1A), causing the reactant flows to stop and N₂ to purge the unit, the conversion came closed to its initial level, but quickly deactivated again in a similar exponential decay pattern.

Meanwhile, CO concentration (Fig. 7.1B) increased with the decreasing CH₄ conversion. CO concentration also increased with increasing temperature and pressure. Water is known to inhibit the combustion reaction (Groppi et al., 2001), and it can take a significant time for the surface water concentration and the gas phase water concentration to reach equilibrium (Ciuparu et al., 2001). We speculate that water molecules could not desorb from the Pd sites as quickly as the methane dissociated, causing incomplete methane combustion, and CO formation.

Figure 7.2 shows the effect of the coating on the activity and stability of Pd 1%/ γ -Al₂O₃ (Alfa). Curves (A), (B) & (C) are for freshly coated catalysts, whereas curve (D) is the “as received” catalyst from the supplier. The curve fitting results in Table 7.2 show that the initial activity ($a + c$) and residual activity (c) for the coated catalysts were lower than for the “as received” catalyst, but the deactivation

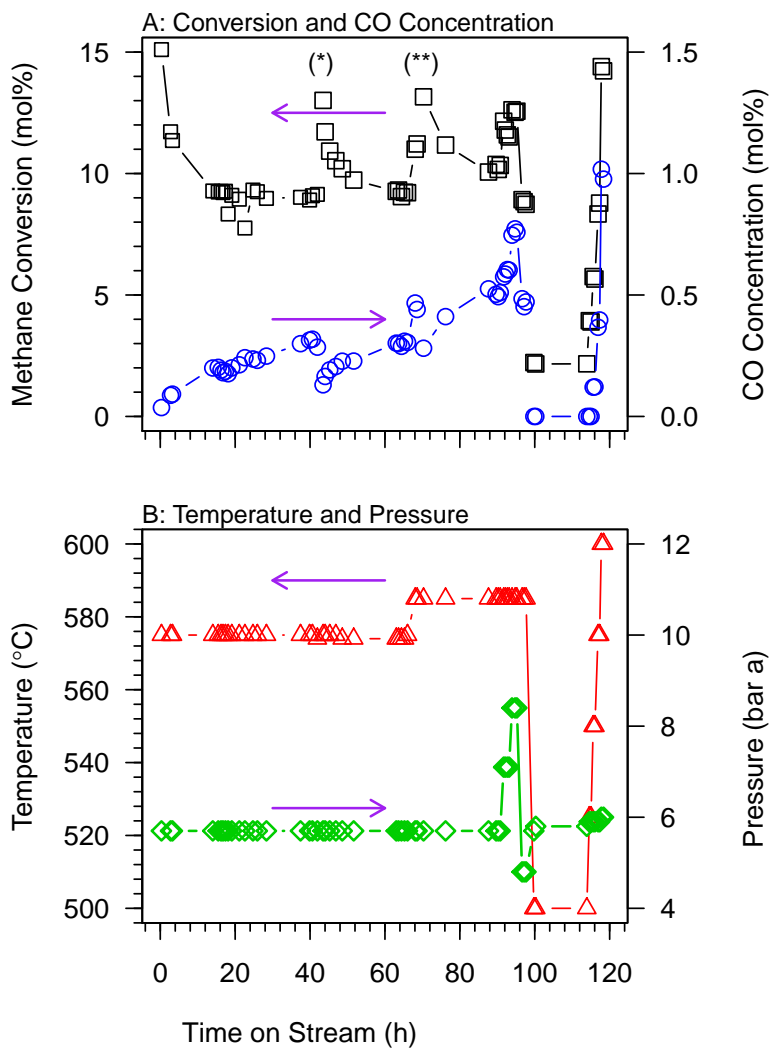


Figure 7.1: Preliminary Stability Test of Pd 1% / γ -Al₂O₃ (Alfa) with 15% Boehmite: A. Methane Conversion and CO Concentration vs Time on Stream; (*) 10 min shut down (**) 20 min shut down. B. Temperature and Pressure vs Time on Stream. Catalyst Loading: 0.002 g. Inlet Conditions: CH₄ Flow: 37.3 Nml/min, 3% in air.

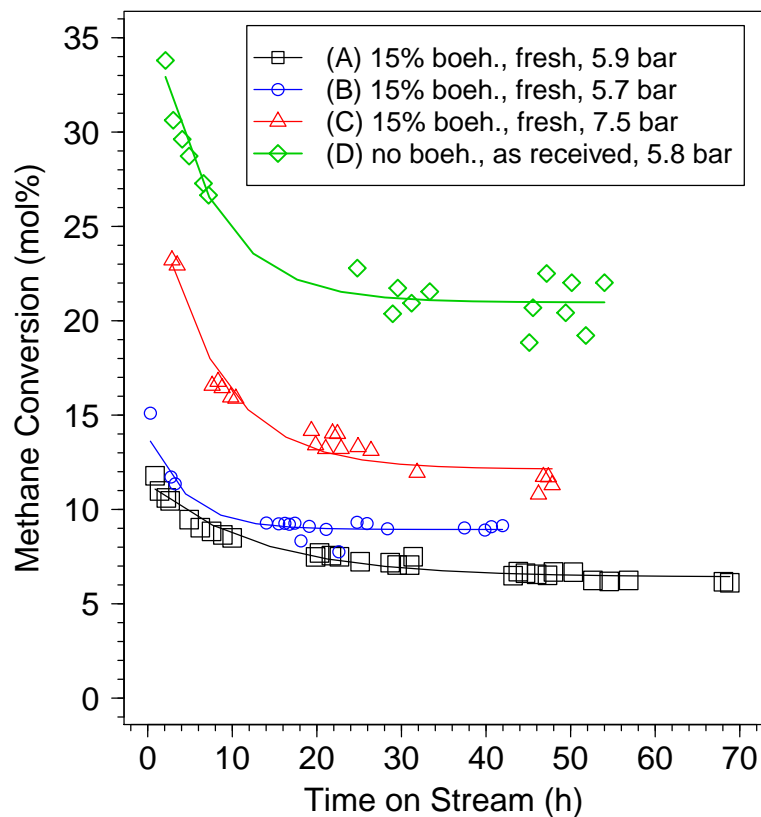


Figure 7.2: Stability of Pd 1%/ γ -Al₂O₃ (Alfa): Methane Conversion vs Time on Stream. Catalyst Loading: 0.0017 g (excluding boehmite). Inlet Condition: CH₄ flow 37 Nml/min, 2 mol% in air; 575°C. Data fit with Eq. (6.14). Catalyst description (boehmite content) and average pressure are listed in the legend.

Table 7.2: Curve Fitting Related to Figure 7.2 and Eq. (6.14) for Stability of Pd 1% (Alfa) Catalyst

Label	Description	a	b	c	a+c	R ²
A	15% boeh. (fresh), 5.9 bar	4.99	0.078	6.42	11.4	0.96
B	15% boeh. (fresh), 5.7 bar	5.02	0.218	8.94	14.0	0.82
C	15% boeh. (fresh), 7.5 bar	16.2	0.138	12.1	28.3	0.95
D	No boehmite, as received, 5.8 bar	16.3	0.147	21.0	37.3	0.94

Table 7.3: Stability Conditions for Pd 5%/ γ -Al₂O₃ (Alfa) and Lab-made Pd-based Catalysts for Figure 7.3.

Label	Catalyst	Fresh / Spent	Note
A	Pd 5% (Alfa) with 15% boeh.	Fresh	7.4 bar
B	Pd 5% (Alfa) with 15% boeh.	Spent	-
C	Pd 5% (Alfa) with 15% boeh.	Fresh	-
D	Pd 4.5% La ₂ O ₃ 6%	Fresh	
E	Pd 5% La ₂ O ₃ 4% MgO 4%	Spent ^a	SS 310 support, rust visible. Repeat 1
F	Pd 5% La ₂ O ₃ 4% MgO 4%	Spent	Same as (E), Repeat 2

^aMCMR run: 16.5 h on stream at 555-575°C, 3.8 bar, 3-3.5% CH₄ in Air.

rate (b) did not differ significantly.

It might appear that boehmite would cover some of the active sites for the reaction, but CO-sorption analyses, contradicted this assumption, with both samples, as received and coated, exhibited metal dispersion virtually identical at ~28% (see Table 7.5). Nevertheless, all samples were active after 40 h and relatively stable, making them good candidates for the MCMR.

Ahmad (2011), based on data in Figure 7.2, suggested that the deactivation could be fitted with a second-order decay model, commonly used for sintering.

7.3.3 Stability of Pd 5%/ γ -Al₂O₃ (Alfa) and Lab-made Pd-based Catalysts

Figure 7.3 presents results for a commercial (Part A) and lab-made (Part B) Pd 5%/ γ -Al₂O₃ catalysts. Table 7.4 shows the exponential curve fitting results. All fresh catalysts in this section were found suitable for the MCMR.

Curves (A) and (C) are both for fresh catalysts, but (A) is for a higher pressure,

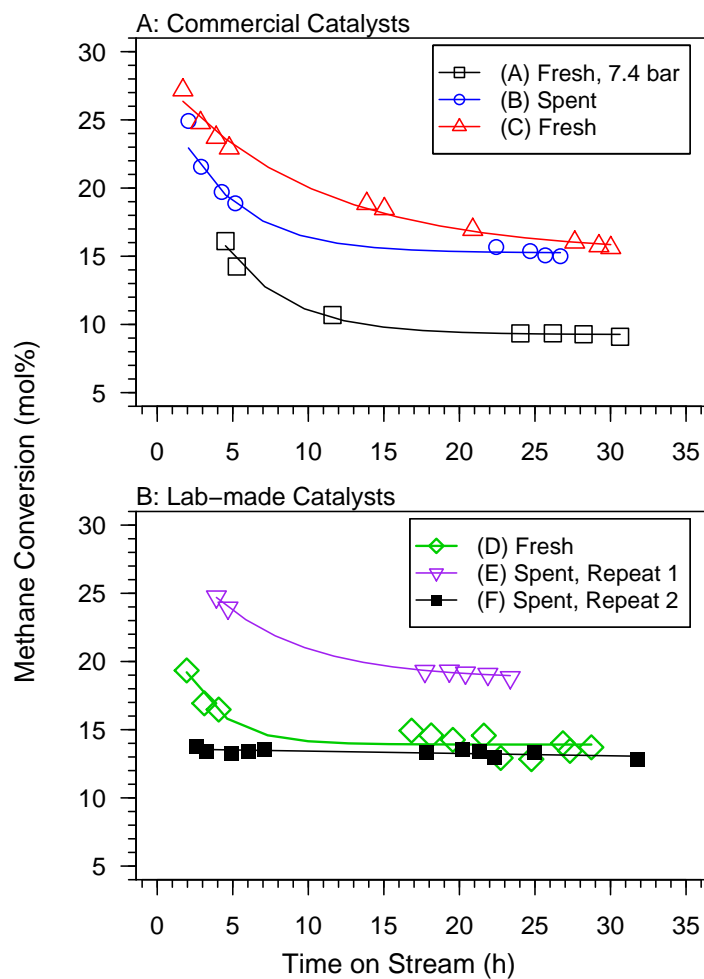


Figure 7.3: Stability Test with Pd 5% / γ -Al₂O₃ (Alfa) and Lab-made Pd-based Catalyst, Fresh and Spent Catalysts after MCMR runs: Methane Conversion vs Time on Stream. Catalyst Loading: 0.002 g; Inlet Conditions: CH₄ flow 30 Nml/min, 3 mol% in air, 510°C, 3.8 bar (unless otherwise noted in legend). Data fit with Eq. (6.14). Catalysts are described in the Legends, with more information in Table 7.3.

Table 7.4: Curve Fitting Related to Figure 7.3 and Eq. (6.14) for Stability of Pd 5% (Alfa) and Pd-based Lab-made Catalysts

Label	a	b	c	a+c	R ²
A	19.0	0.237	9.26	28.2	0.991
B	12.7	0.242	15.2	27.9	0.993
C	13.2	0.101	15.2	28.4	0.990
D	11.2	0.383	13.9	25.1	0.88
E	11.3	0.163	18.7	30.1	0.999
F	13.6	0.0013	0.0	13.6	0.43

7.4 bar instead of 3.8 bar. Initial activities ($a + c$) were similar, but deactivation (b) was stronger at higher pressure. Not shown on this graph was the CO concentration, which went up to ~ 1200 ppm at higher pressure, but was close to the detection limit at 3.8 bar, < 20 ppm.

The activity of the spent catalyst, curve (B), was unexpected. In Table 7.5, the metal dispersion dropped from 14% to 2% from fresh to spent catalyst. Pore volume analyses showed a significant drop in pore volume and surface area, while the pore size remained stable. However, the activity of the spent catalyst (B) was similar to that of the fresh sample for the same operating conditions (C). Catalyst activity might not be very sensitive to metal dispersion. Hellman et al. (2012) suggested that a relatively thick film of PdO favours methane dissociation, also indicating that high metal dispersion might not be essential.

For initial and residual activities, fresh lab-made catalyst (curve D) were slightly lower than for the fresh commercial catalyst at the same conditions (curve C). The added promoters (initially intended for reforming catalyst), and pre-aging by steam, did not enhance the catalyst performance compared to the commercial catalyst. Catalysts corresponding to curves (E) & (F) had some rust on the support, but this did not seem to affect the activity and stability, unlike the Ru-based catalyst for reforming (Chapter 6). Curve (F) had further unexpected behaviour, being mostly stable during the stability test, and giving poor fitting.

We experienced some issue with our GC at that time that might have hidden differences between the samples tested in this section. However, the catalyst deac-

Table 7.5: Surface Area, Pore Volume, Average Pore Size, and Metal Dispersion of Pd/ γ -Al₂O₃ Catalysts.

	Surface Area m ² /g	Pore Volume cm ³ /g	Ave. Pore Size nm	Metal Dispersion mol%
Commercial Catalyst				
Pd 1% (Alfa) (as received)	189	0.58	9.4	28%
Pd 1% (Alfa) with 15% boeh. (fresh)	159	0.46	8.7	27%
<i>StandDev (with 3 samples)</i>	<i>15</i>	<i>0.05</i>	<i>0.11</i>	
Pd 1%(Alfa) with 15% boeh. (spent) ^a	133	0.44	10.7	1.3%
<hr/>				
Pd 5% (Alfa) (as received)	145	0.45	9.3	14%
Pd 5% (Alfa) with 15% boeh. (fresh)	139	0.41	9.2	14%
Pd 5% (Alfa) with 15% boeh. (spent) ^{b,c}	93	0.28	9.9	1.9%
<hr/>				
Lab-made Catalyst				
Pd 4.3% La ₂ O ₃ 6% (fresh)	92	0.46	18.3	14%
Pd 5.3% La ₂ O ₃ 4% MgO 4% (spent) ^d	84	0.40	17.8	N/A ^e
Pd 4.4% La ₂ O ₃ 3.5% MgO 3.5% (spent) ^d	88	0.43	18.3	N/A ^e
Pd 5.6% La ₂ O ₃ 6% (spent) ^d	87	0.46	17.8	N/A ^e

^aAfter Exp. no. 0.3 & 0.4 (See Section C.2.1)

^bAverage of 2 samples, except for Metal Dispersion, where there was only one sample.

^cAfter Exp. no.2 (See Table 8.6)

^dAfter Exp. no.3 (See Table 8.6)

^eN/A: Not Measured

tivation observed in the MCMR in Chapter 8 cannot be explained by a significant decrease in catalyst activity alone.

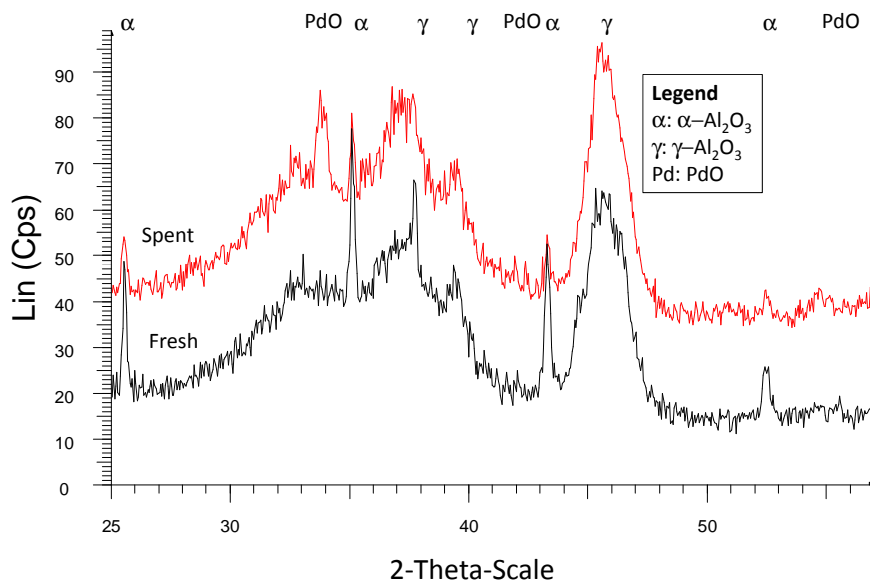


Figure 7.4: XRD Diagram of Commercial Pd 1%/ γ - Al_2O_3 (Alfa) with 15% Boehmite, Fresh and Spent (after MCMR Exp. no.0.3, see Table C.2).

7.3.4 Deactivation

This section tries to explain the catalyst deactivation decays presented in this chapter, using both fresh catalysts and catalysts spent during the MCMR experiments. Figure 7.4 presents XRD spectra for Pd 1% (Alfa) fresh and spent catalysts. α - Al_2O_3 is present in the fresh sample, but peaks did not grow or were even reduced in spent sample. One PdO peak appeared in the spent spectrum, but it was not backed up by two other peaks that should normally have also appeared. In Table 7.5, for Pd 1% samples, surface area dropped for the spent sample, while pore size increased, indicating some pore sintering. Metal dispersion decreased dramatically from 27 to 1.3%, but we cannot conclude at this stage whether metal sintering was significant due to the absence of clear peaks in the XRD spectra.

Figure 7.5 presents XRD spectra for Pd 5% (Alfa) fresh and spent catalysts. There is a clear growth in α - Al_2O_3 peaks, indicating a beginning of phase change, possibly causing pore sintering. PdO peaks remained stable. In Table 7.5, both sur-

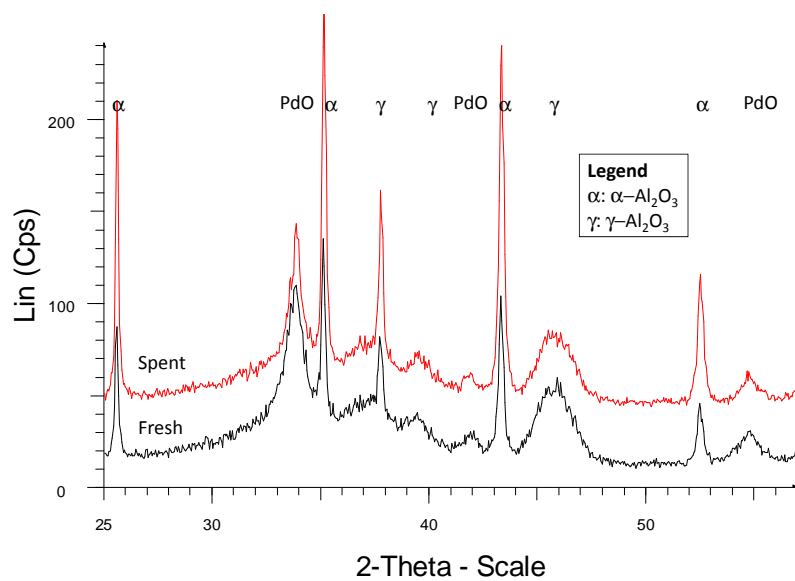


Figure 7.5: XRD Diagram of Commercial Pd 5%/ γ -Al₂O₃ (Alfa) with 15% Boehmite, Fresh and Spent (after MCMR Exp. no.2, see Chapter 8).

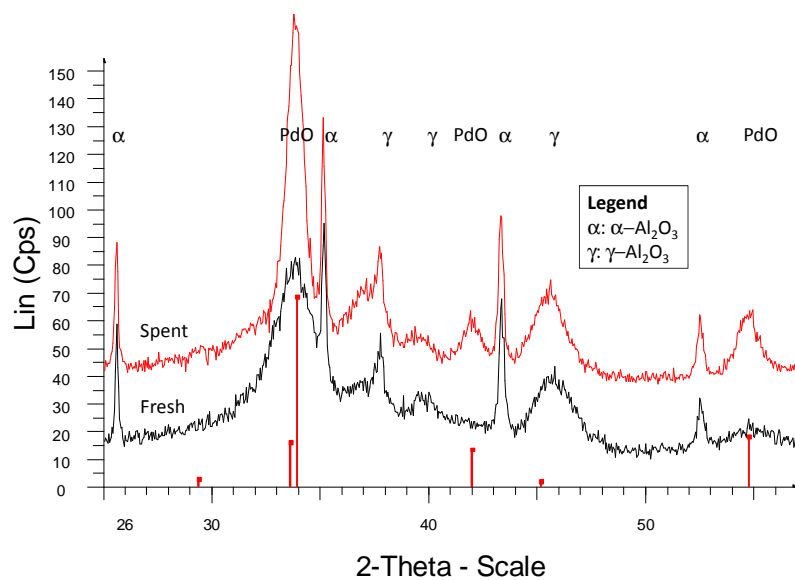


Figure 7.6: XRD Diagram of Lab-made Pd-based Catalyst, Fresh (Pd 4.3% La₂O₃ 6% γ -Al₂O₃) and Spent (after MCMR Exp. no.3, see Chapter 8, Pd 5.3% La₂O₃ 4% MgO 4% γ -Al₂O₃).

face area and pore volume dropped significantly, confirming pore sintering, likely causing the drop in metal dispersion.

Figure 7.6 shows XRD spectra for lab-made Pd 5% La₂O₃–MgO/ γ -Al₂O₃. No growth in α -Al₂O₃ peaks is observed, but rather a growth in PdO peaks, indicating metal sintering. In Table 7.5, the surface area, pore volume and average pore size were stable. It can then be concluded that the steam-aged support, with promoters, was stable under the MCC conditions. However, promoters might have had an adverse effect of the Pd site stability. More work is clearly needed to improve the stability of the the lab-made Pd-based catalyst.

7.3.5 Estimation of Kinetic Parameters

Activation Energy E_4 and Reaction Order for Methane α

Using Pd 1% (Alfa) catalyst, Figure 7.7 shows data obtained in order to calculate the activation energy E_4 and the reaction order for methane, α . Table 7.7 presents the slopes from the linear regressions, as well as the calculated kinetic parameters. The kinetic parameters are in the range of those reported in the literature (Lee and Trimm, 1995). The error in α is large, possibly indicating temperature dependence of the coefficient.

The A_4 value for Pd 1% (Alfa) was ~ 3 times smaller than for Pd 5% (Alfa). However, the experimental scatter for the Pd 5% samples was large. Lab-made catalyst had A_4 similar to the commercial Pd 5% catalyst.

Pre-exponential Factor, A_4

Figure 7.8 presents the data used to estimate the pre-exponential Factor, A_4 , for the Pd-based catalysts tested in this chapter. Table 7.8 details the experimental conditions, and Table 7.9 presents the A_4 results. The catalysts and rate of reaction seemed to stabilize after ~ 30 -40 h, allowing the use of the residual fitting parameter c from Eq. (6.14) to estimate A_4 .

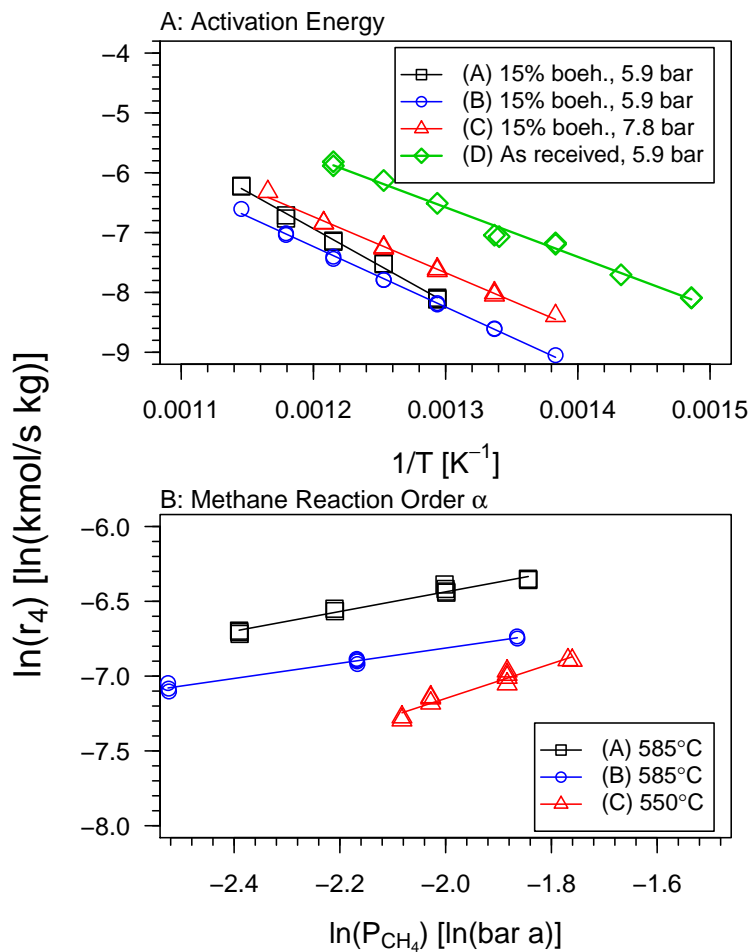


Figure 7.7: Estimated Kinetic Parameters for Pd 1% (Alfa) Catalyst: A. Activation Energy E_4 ; B. Reaction Order for Methane α . Catalyst Loading: 2.0 mg (except for curve (D) at 1.7 mg). Inlet Condition: CH₄ flow: 37 Nml/min, 2 mol% in air; Pressure, temperature and catalyst details are listed in Table 7.6. Linear regression results appear in Table 7.7.

Table 7.6: Estimated Kinetic Parameters for Pd 1% (Alfa) Catalyst: Experimental Conditions for Figure 7.7

Label	Catalyst	Constant Pressure for Part A bar	Temperature Variation for Part A °C	Pressure Variation for Part B bar	Temperature for Part B °C
A	Pd 1%, 15% boeh.	5.9	500-600	4.8-8.4	585
B	Pd 1%, 15% boeh.	5.9	450-600	4.1-8.0	585
C	Pd 1%, 15% boeh.	7.8	450-585	4.5-7.4	550
D	Pd 1% (as received)	5.9	400-550		N/A

Table 7.7: Estimated Kinetic Parameters for Pd 1% (Alfa) Catalyst: Linear Regression Results for Figure 7.7

Label	Activation Energy E_4		Reaction Order for Methane α		
	Slope	R^2	Label	Slope	R^2
A	-12320	0.995	A	0.66	0.98
B	-10110	0.998	B	0.51	0.98
C	-9374	0.995	C	1.16	0.94
Average E_4 (kJ/mol)	-10600		Average (α)	0.78 ^a	
Std. Error (kJ/mol)	88 ^a		Std. Error	0.39	
D	-8274	0.990			
E_4 (kJ/mol)	69				

^aAs an alternative, multivariate non-linear regression for all of the data gave a reaction order α of 0.83, and an activation energy of 96 kJ/mol.

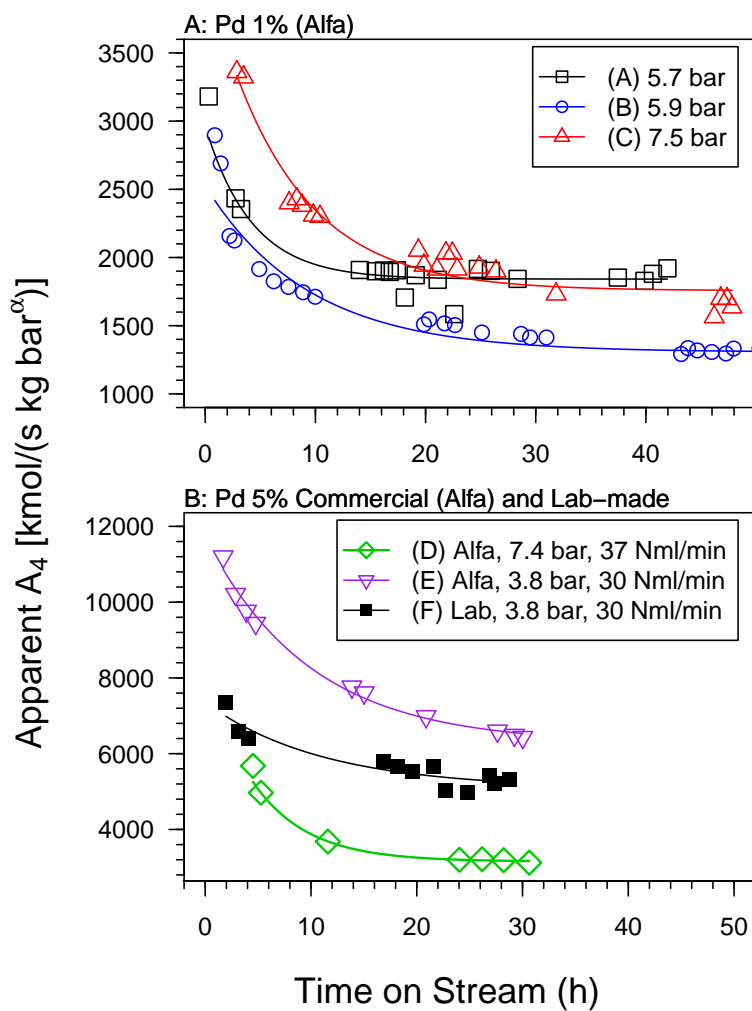


Figure 7.8: Estimated Kinetic Factor, A_4 . Data fitted with Eq. (6.14). Experimental conditions are listed in Table 7.8.

Table 7.8: Estimated Kinetic Parameters for Experimental Conditions in Figure 7.8

Label	Catalyst	Temperature °C	Ave. Pressure bar	CH ₄ Flow Nml/min	% CH ₄ in Air mol%	WHSV h ⁻¹
A	Pd 1% (Alfa), 15% boeh.	575	5.7	37	2.0	71,000
B	Pd 1% (Alfa), 15% boeh.	575	5.9	37	2.0	71,000
C	Pd 1%(Alfa), 15% boeh.	575	7.5	37	2.0	71,000
D	Pd 5% (Alfa), 15% boeh.	510	7.4	37	3.0	47,000
E	Pd 5% (Alfa), 15% boeh.	510	3.8	30	3.0	38,000
F	Pd 4.5% La ₂ O ₃ 6%	510	3.8	30	3.0	38,000

Table 7.9: Estimated Kinetic Pre-exponential Factor, A₄, from Figure 7.8

Label	Catalyst	A ₄ kmol/(s kg bar ^α)	R ²
A	Pd 1% (Alfa), 15% boeh.	1842	0.82
B	Pd 1% (Alfa), 15% boeh.	1306	0.93
C	Pd 1%(Alfa), 15% boeh.	1757	0.95
	<i>Average</i>	<i>1635</i>	
	<i>Std. Error</i>	<i>326</i>	
D	Pd 5% (Alfa), 15% boeh.	3153	0.999
E	Pd 5% (Alfa), 15% boeh.	6267	0.990
	<i>Average</i>	<i>4710</i>	
	<i>Std. Error</i>	<i>3052</i>	
F	Pd 4.5% La ₂ O ₃ 6%	5080	0.88

7.3.6 Conclusions

Micro-reactor experiments allowed combustion catalysts to be tested for their suitability in the MCMR prototype, as well as estimation of kinetic parameters.

Commercial Pd 1% and 5% γ -Al₂O₃ catalysts (Alfa Aesar) as well as lab-made Pd 5% La₂O₃-MgO/ γ -Al₂O₃, were found to be suitable for the MCMR prototype. The activity of the catalysts was generally stable after 24-48 h on stream.

In the stability experiments on Pd 1% (Alfa) catalyst, reversible deactivation was observed, and CO concentration increased with increasing temperature, pressure and time on stream. Inhibition by water molecules is likely to have been the cause of the reversible deactivation.

XRD spectra and pore analyses suggest that pore sintering was the major source of deactivation for the two commercial Pd catalysts, while metal sintering was more important for the lab-made Pd La₂O₃-MgO catalyst. Further work is needed to improve the stability of the catalysts.

For the Pd 1% (Alfa) catalyst, the activation energy E_4 was evaluated to be 88 kJ/mol, and the reaction order for methane α was estimated to be 0.78. The pre-exponential factor for commercial Pd 1% catalyst was about three times less than for the commercial and lab-made Pd 5% catalysts.

Chapter 8

Development of the Multi-Channel Membrane Reactor

8.1 Introduction

In Chapter 1, the importance of developing small-scale hydrogen production technologies (<500 kg/day), to enable the market penetration of hydrogen powered vehicles, was highlighted. Several technologies with potential to achieve this objective economically were reviewed. In Chapter 2, the concept of a Multi-Channel Membrane Reactor (MCMR) was presented, combining a Multi-Channel Reactor (MCR) and perm-selective palladium-silver (Pd/Ag) membrane technologies. The MCMR alternates Steam Methane Reforming (SMR) gas channels to produce hydrogen with Methane Catalytic Combustion (MCC) gas channels to provide the reforming heat of reaction. Pd/Ag membranes, located in the reforming gas channel, shift the reaction equilibrium, and produce pure hydrogen in a single vessel. The concept was proposed by Goto et al. (2003), but proof-of-concepts are limited. No previous experimental work has been published on MCMR using SMR.

This chapter presents the design, commissioning and results of a MCMR prototype. Results are compared with predictions from the 2-Dimensional (2-D) model

developed in Chapters 2 and 3. Reforming and combustion catalysts were coated on metal plates, with the innovative air-spray hot substrate coating method developed in Chapters 4 and 5. The activity and stability of those catalysts were tested in Chapters 6 and 7, with Ru and Pd-based catalysts on γ -Al₂O₃ support selected for the reforming and combustion channels respectively.

8.2 Material and Method

8.2.1 Reactor Design

Figure 8.1 presents an expanded view of the MCMR prototype. The core component of the design is the separator. In addition to transferring heat from the combustion to the reforming channel, the separator had several functions: (1) To distribute the feed and remove gas products; (2) to hold the catalyst plates with five recesses located on each side; (3) to monitor reforming and combustion temperature profiles on four locations on each side; and (4) to host four sampling tubes on each side to collect and measure gas compositions along the reactor.

The reforming frame created a space between the separator and the membrane to provide the reforming channel. Experiments were conducted both without and with membranes. The Pd/Ag 25 μ m thick membrane, was provided by Membrane Reactor Technologies (MRT) and was fabricated using an electroless plating technique. A dummy membrane with the same dimensions as the Pd/Ag membrane was used to preserve the desired channel height when there was no membrane. In order to avoid hot spots on the combustion side, an optional frame was designed to distribute the air evenly along the reactor, as suggested by Tonkovich et al. (2004). However, a hot spot was never an issue in practice, so the combustion frame was never used as intended.

Once assembled, from the extremities of the flanges, the reactor measured 500 mm x 254 mm x 125 mm. Internal channel volumes were \sim 50 ml for both channels. Sealing was by GrafoilTM gaskets with Tang 316/316L inserts. All parts were tightened with 18 bolts going through the flanges. Mechanical drawings are provided in Appendix E.4.

The MCMR was monitored by 16 thermocouples: 8 located inside each car-

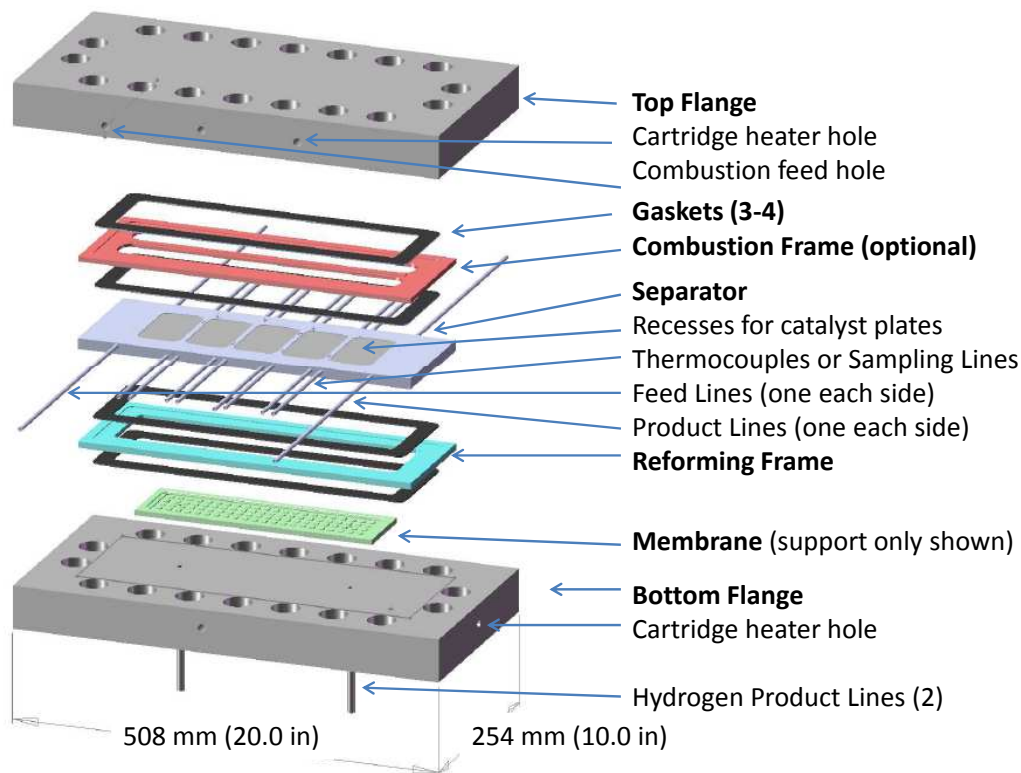


Figure 8.1: Expanded View of MCMR Prototype

tridge heater, inserted in the two flanges; and 8 divided equally between the reforming and the combustion channels. Figure 8.2 shows where the four temperatures and gas samples were taken along the reactor length for each channels. In this chapter, methane conversion or temperature data at positions 1 to 4, refer to the location numbers on this figure. On the combustion channel, Part B, there is a Grafoil™ strip, for mechanical support, that divides the channel into two sub-channels. Average channel temperatures T_{ave} , reported in this chapter, represent the average of all four thermocouples readings. The average temperature on the reforming channel was used as the set point for temperature control, accomplished by a custom-made

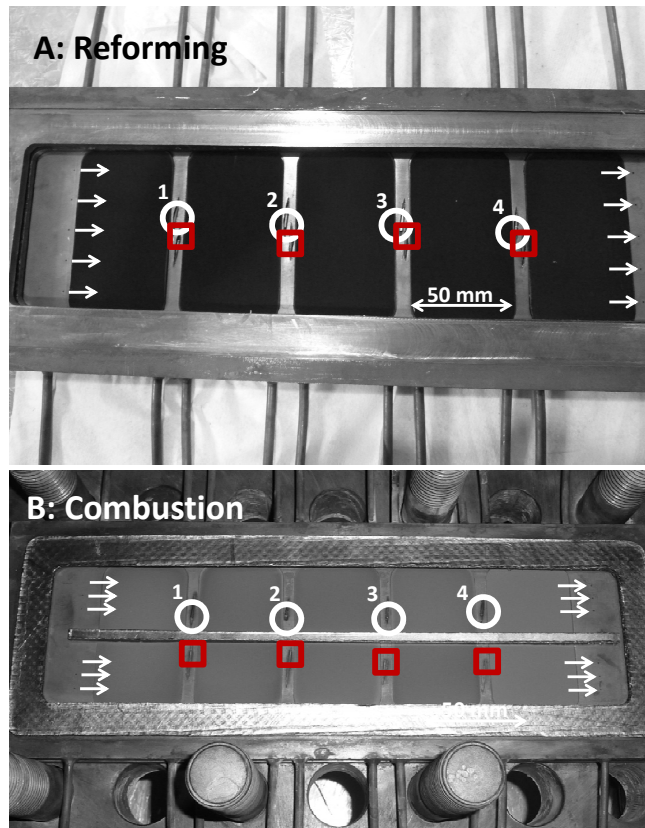


Figure 8.2: Top View of Thermocouple and Gas Sampling Locations for both Channels. A: Reforming Channel, B: Combustion Channel. Squares: Thermocouple locations; Circles: Gas sampling tube inlets; Arrows: Feed inlet and products outlet.

LabVIEW™ program.

Two gauge pressure transducers measured the pressure in both channels, at the first and last sampling points.

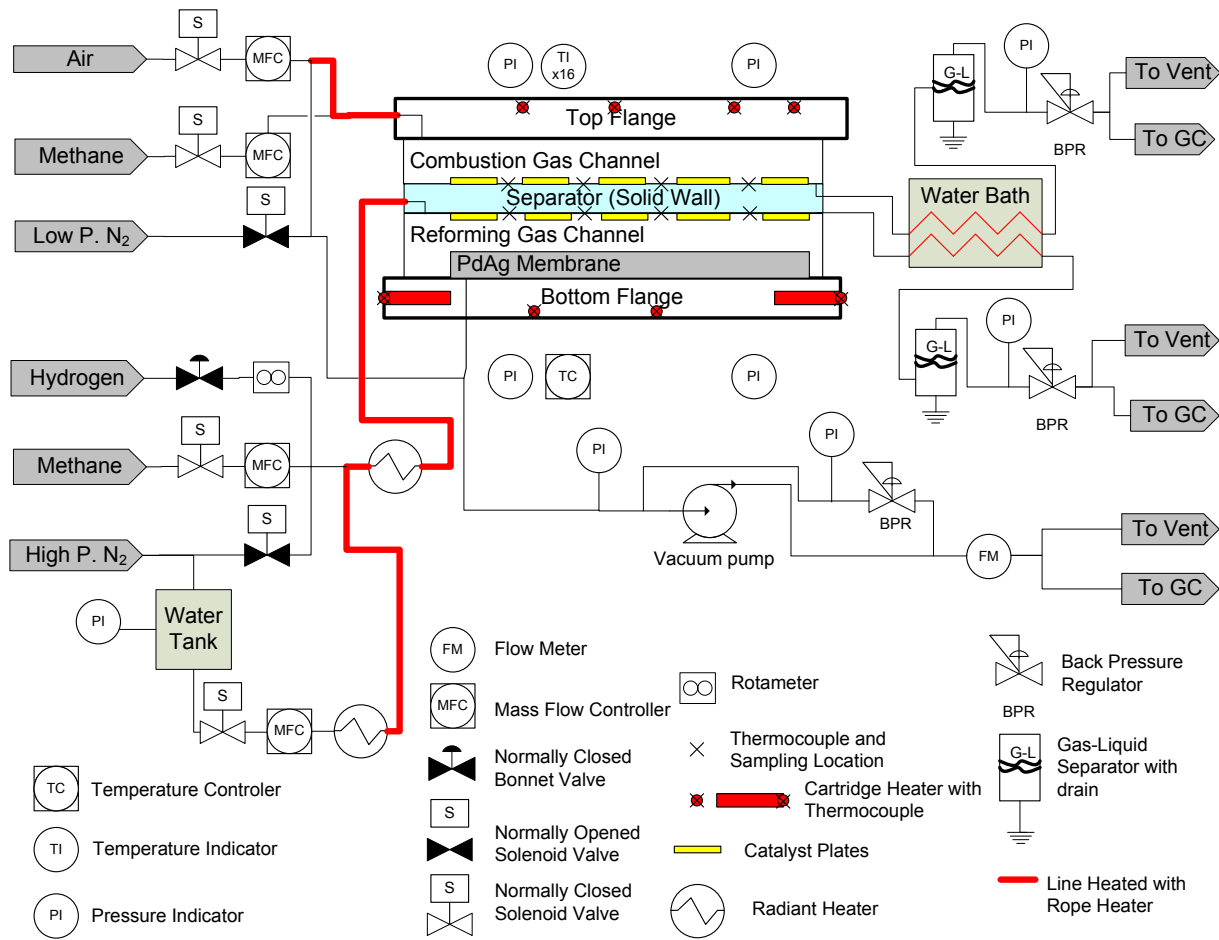


Figure 8.3: MCMR Process Flow Diagram. For detailed PI&D, see Appendix E.1.

8.2.2 Process Design

Figure 8.3 shows a simplified flow diagram of the MCMR unit, including some key control instruments. A detailed Process & Instrumentation Diagram (P&ID) is included in Appendix E.1. The functioning of the unit can be summarized as follows: For the reforming side, water is pressurized with N_2 and, after pre-heating to produce steam, it is mixed with CH_4 at the desired ratios. The H_2 line is only used for start-up and membrane testing purposes. For the combustion side, an air line is pre-heated with rope heaters, and CH_4 is mixed to the desired composition before entering the reactor. All feed streams are controlled with mass flow controllers, except for the H_2 , where the flow is adjusted when needed with the needle valve of a rotameter, previously calibrated. Downstream of the reactor, products are cooled by a water bath, and condensed water is removed with gas-liquid separators (see drawing in Appendix E.3). Gas products are split into two streams, one going to a Gas Chromatograph (GC), the second being vented. For the hydrogen permeate, two options are available, selected according to the desired permeate pressure: vane pump for vacuum, or back-pressure regulator for higher permeate pressure. Vacuum was generated with a 24V rotary vane pump (Clark Instrument, model no. 16987). Pressures in both channels were controlled by back-pressure regulators, located downstream of the gas-liquid separators.

In case of emergency shutdown, triggered manually or automatically by a flow, temperature or pressure alarm, the system is flushed with N_2 , while all other feed lines are isolated with solenoid valves. A detailed electrical and control diagram is found in Appendix E.2.

Gases in the experiments were purchased from Praxair: CH_4 (99% purity), H_2 (99,995+% purity), air (extra dry grade), and N_2 (99,995+% purity). Deionized water was utilized to produce the steam.

Figures 8.4 and 8.5 display images of the MCMR prototype, reactor skid, and process and control equipment.

The sampling of reforming gases was challenging, since water needed to be removed. However, non-insulated 1/16" (1.6 mm) lines (Fig. 8.5B) quickly cooled the gas to be sampled, and no external cooling was needed. Gases for sampling passed through a batch gas-liquid separator that needed to be flushed after each

sampling. 1 L tedlar bags, shown on Figure 8.5C, were filled and emptied twice to remove the previous sample gas, before keeping one sample. The bags were filled at a rate of ~ 0.5 L/min. It took ~ 30 min to sample all 8 sampling locations.

8.2.3 Catalyst Preparation

Coating methodologies and material employed are described in detail in Chapters 4 and 5. In brief, for commercial catalyst, Disperal P2 boehmite (Sasol) was mixed in distilled water with the commercial catalyst powder. Boehmite represented 15% of the total solid mass. The concentration of the catalyst powder was 0.25 mol/L (based on the molecular weight of alumina). The mixture was ball milled overnight, and the pH was adjusted with nitric acid to ~ 5 before and after the ball milling. The modified sol was air-spray coated onto a stainless or Fecralloy metal substrate, while being heated $> 100^\circ\text{C}$. The metal substrate was previously sand-blasted and calcined for Fecralloy. About 0.2-0.3 g of catalyst were coated on each metal plate, each measuring 50 mm x 88.5 mm. Once the masses of the catalyst coatings were judged acceptable, the samples were calcined overnight in static air at 650°C .

For lab-made catalyst, Baikalox CR125 $\gamma\text{-Al}_2\text{O}_3$ (Baikowski) was mixed in distilled water with the boehmite, which represented 40% of the total solid mass. The concentration of the $\gamma\text{-Al}_2\text{O}_3$ powder was 0.5 mol/L. After the air-spray coating and calcination, promoters were impregnated using a modified incipient wetness procedure, in which plates were flooded with the impregnation solution, and excess solution was removed after 2 min. The mixture was air dried for 2 h, and heated at 110°C overnight in static air. Impregnation solution concentrations are listed in Table 8.1. Support and promoters were steamed and heated under a pressure of 25 bar, and then maintained at 575°C for 24 h. Ru or Pd was then impregnated following the same procedure as for the promoters. Pd-based catalyst plates were calcined at 600°C in static air for 5.5 h and Ru-based catalyst plates were reduced in-situ. Catalyst compositions were estimated by weighing the plates after impregnation and heat treatment.

Tables 8.2 - 8.4 describe the catalyst samples employed for the MCMR for this chapter.

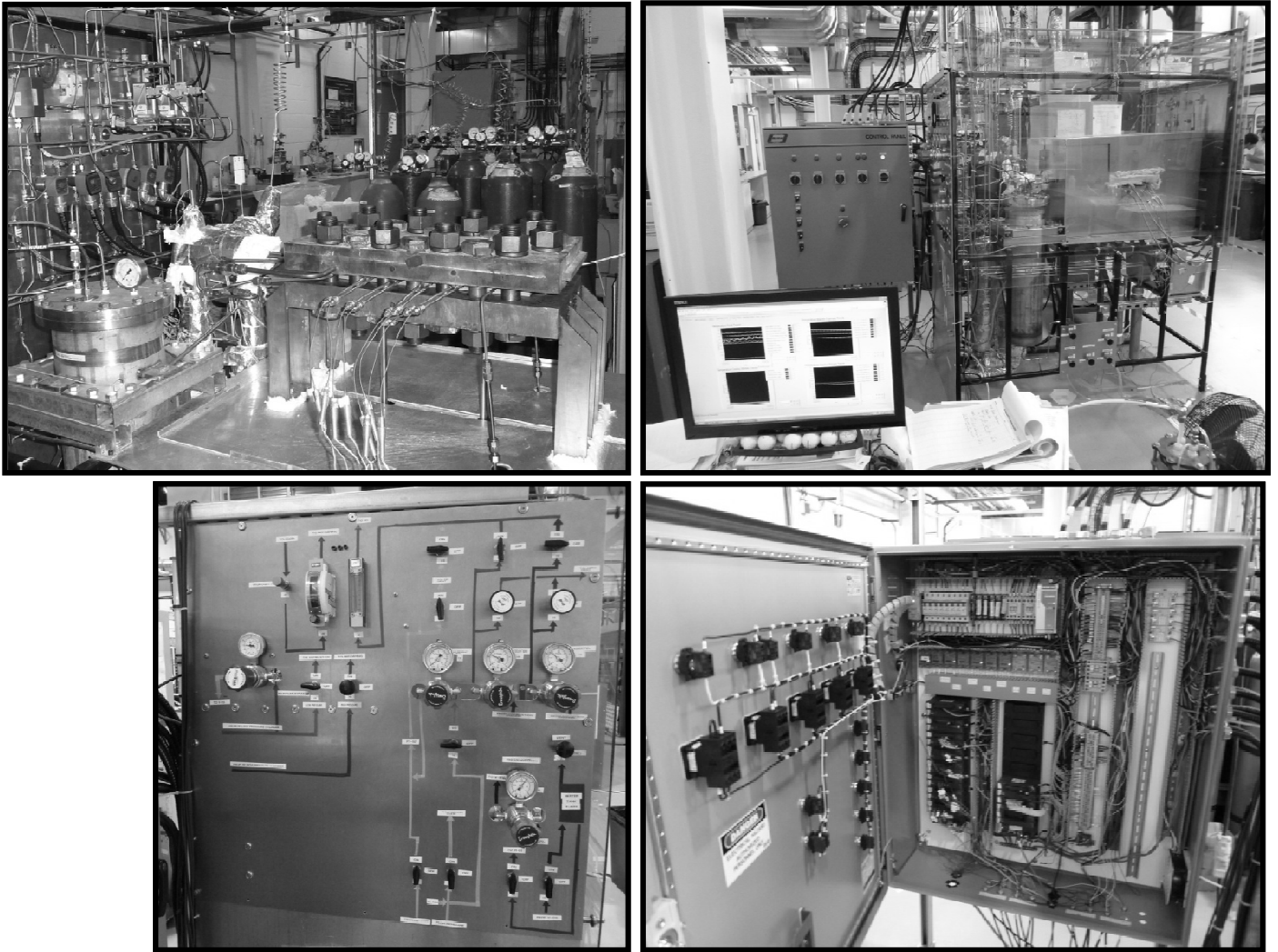


Figure 8.4: Reactor and Process Images I: (A) MCMR prototype on skid, without insulation; (B) MCMR with insulation and aluminum casing, electrical panel and monitor; (C) Front panel for pressure control; (D) Inside the electrical Panel.

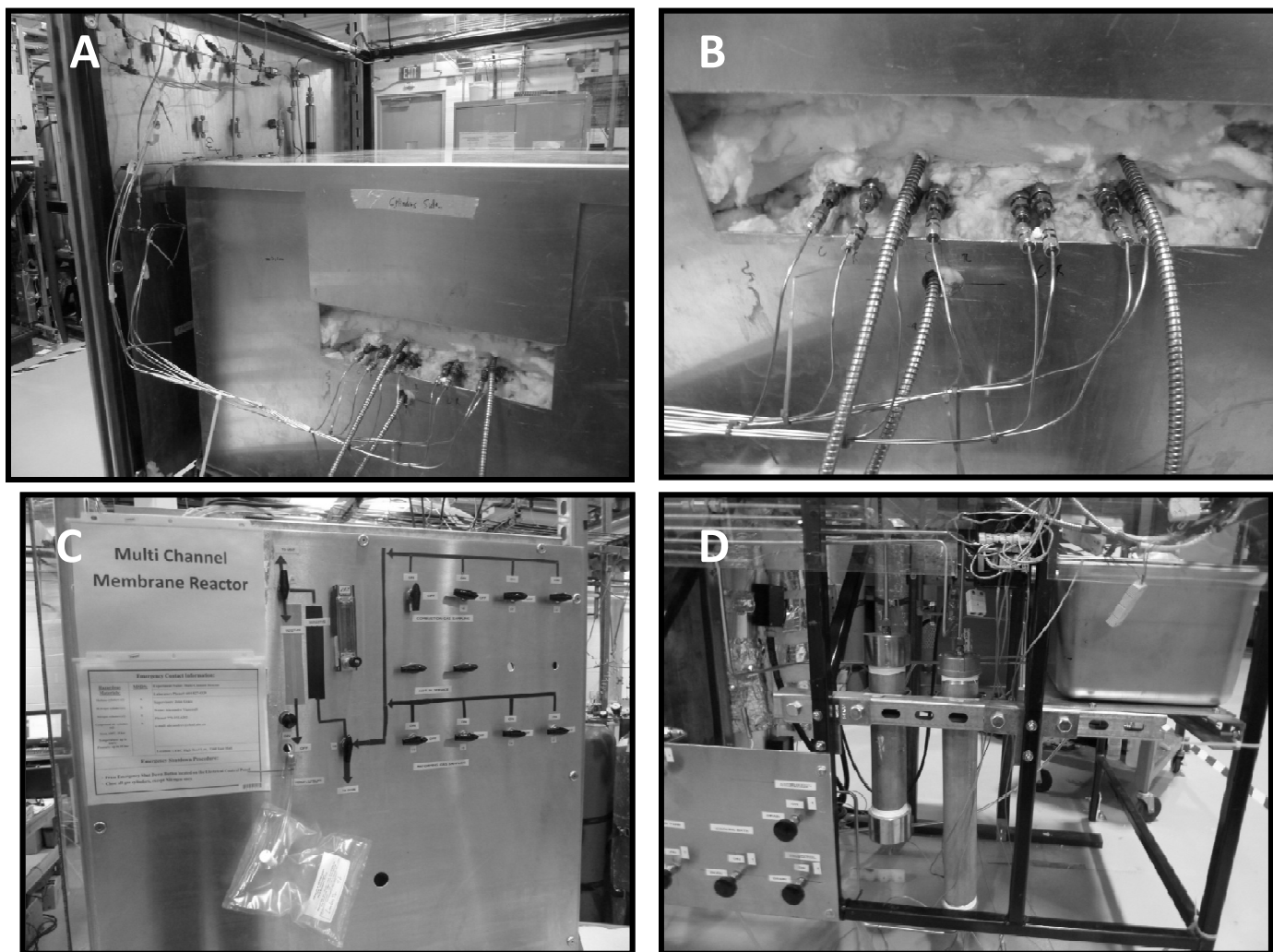


Figure 8.5: Reactor and Process Images II: (A) Sampling side of the MCMR; (B) Close-up on the sampling tube coming out of the reactor; (C) Sampling panel; (D) Water bath for products cooling and gas-liquid separators

Table 8.1: Impregnation Solutions and Desired Metal Contents for Catalysts used in MCMR

Desired Metal Content ^a wt%	Solution mol/L
Promoters	
La ₂ O ₃ 6%	La Nitr. 0.27
La ₂ O ₃ 4% MgO 4%	La Nitr. 0.18; Mg Nitr. 0.72
La ₂ O ₃ 4% MgO 2% MnO 2%	La Nitr. 0.18; Mg Nitr. 0.36; Mn Nitr. 0.28
Catalyst	
Pd 5%	Pd Nitr. Sol. Pd 4-5% w/w (Alfa Aesar, as received)
Ru 6%	Ru Nitr. 0.51

^aMeasured metal content can vary by $\pm 2\%$ from the desired value

Table 8.2: Catalyst Description for MCMR Experiment no.1, without Membrane

Catalyst on γ -Al ₂ O ₃ support	Plate Position	Mass Catalyst g	Ave. Coating Thickness μ m	Density of Catalyst Layer kg/m ³	Metal Support
Ru 7.5% La ₂ O ₃ 3.5% MgO 3.5%	1	0.342	236	327	Fecral- loy
Ru 5.6% La ₂ O ₃ 5% MgO 2.%	2	0.313	208	340	SS 310
Ru 8% La ₂ O ₃ 4% MnO 2% MgO 2%	3	0.299	217	312	Fecral- loy
Ru 8% La ₂ O ₃ 4% MnO 2% MgO 2%	4	0.286	210	308	SS 310
Ru 7% La ₂ O ₃ 6%	5	0.295	207	322	SS 310
<i>Total mass / Ave. Thickness / Ave. Density</i>		1.535	216	322	
Pd 5% (Alfa)	1	0.268	232	261	SS 310
Pd 5% (Alfa)	2	0.255	196	294	SS 310
Pd 5% (Alfa)	3	0.205	120	386	SS 304
Pd 5% (Alfa) (reused from run 0.9)	4	0.268	199	304	SS 304
Pd 5% (Alfa) (reused from run 0.9)	5	0.261	180	328	SS 304
<i>Total mass / Ave. Thickness / Ave. Density</i>		1.257	185	315	

Table 8.3: Catalyst Description for MCMR Experiment no.2, with Membrane

Catalyst on γ -Al ₂ O ₃ support	Plate Position	Mass Catalyst g	Ave. Coating Thickness μ m	Density of Catalyst Layer kg/m ³	Metal Support
Ru 8% La ₂ O ₃ 3% MnO 1.5% MgO 1.5%	1	0.306	220	315	Fecral-loy
Ru 6% La ₂ O ₃ 3% MgO 3%	2	0.316	211	338	SS 310
Ru 8% La ₂ O ₃ 5%	3	0.279	208	304	Fecral-loy
Ru 7% La ₂ O ₃ 4.5%	4	0.282	209	305	Fecral-loy
Ru 7% La ₂ O ₃ 6%	5	0.296	217	308	SS 310
<i>Total mass / Ave. Thickness / Ave. Density</i>		<i>1.479</i>	<i>213</i>	<i>314</i>	
Pd 5% (Alfa)	1	0.213	111	433	SS 304
Pd 5% (Alfa)	2	0.264	195	306	SS 310
Pd 5% (Alfa)	3	0.290	172	382	SS 304
Pd 5% (Alfa)	4	0.263	194	306	Fecral-loy
Pd 5% (Alfa)	5	0.287	205	317	SS 304
<i>Total mass / Ave. Thickness / Ave. Density</i>		<i>1.317</i>	<i>175</i>	<i>349</i>	

8.2.4 Reactor Assembly

The reforming catalyst plates were located on the lower side of the separator. In order to assemble them in the prototype, the following procedure was developed: the five reforming plates were deposited in the recesses of the separator. One gasket and the reforming frame were placed above the separator and plates (the gaskets were previously calcined at 400°C for 2 h, in an attempt to remove volatile sulfur compounds that could be present). Silicone glue was then applied onto the outside contour of the gasket. A flat heavy piece of metal was put on top of the separator and left overnight.

The next day, the reforming frame was removed and fitted with another gasket on the bottom flange, to install the dummy or Pd/Ag membrane, which also sits on a

Table 8.4: Catalyst Description for MCMR Experiment 3, with Membrane

Catalyst on γ -Al ₂ O ₃ support	Plate Position	Mass Catalyst g	Ave. Coating Thickness μ m	Density of Catalyst Layer kg/m ³	Metal Support
Ru 7.5% La ₂ O ₃ 5%	1	0.309	221	316	Fecralloy
Ru 7.5% La ₂ O ₃ 4% MgO 4%	2	0.294	214	310	Fecralloy
Ru 7% La ₂ O ₃ 4% MgO 4%	3	0.292	214	309	Fecralloy
Ru 6.5% La ₂ O ₃ 4.5% MgO 4.5%	4	0.325	228	321	Fecralloy
Ru 6% La ₂ O ₃ 3.5% MgO 3.5%	5	0.308	221	315	Fecralloy
<i>Total mass / Ave. Thickness / Ave. Density</i>		<i>1.528</i>	<i>220</i>	<i>314</i>	
Pd 5.5% La ₂ O ₃ 6%	1	0.263	200	297	Fecralloy
Pd 5.5% La ₂ O ₃ 4% MgO 4%	2	0.262	200	296	SS 310
Pd 4.5% La ₂ O ₃ 4% MgO 2% MnO 2%	3	0.278	207	303	SS 310
Pd 4.5 La ₂ O ₃ 3.5% MgO 3.5%	4	0.26	208	282	SS 310
Pd 5% (Alfa)	5	0.232	160	328	SS 304
<i>Total mass / Ave. Thickness / Ave. Density</i>		<i>1.295</i>	<i>195</i>	<i>301</i>	

gasket. To minimize feed by-pass under and along the sides of the membrane, strips of gasket were used to fill gaps as much as possible (See Figure 8.6). Despite these efforts, we estimated that between 13 to 23% of the feed by-passed the reforming channel. Details are provided in Section 8.2.8.

The separator, including the reforming plates and gaskets, were next placed on the reforming frame. The combustion plates were added, as well as Grafoil gasket and the Grafoil strip serving as mechanical support. The top flange was lowered carefully on to the top of the assembly. Bolts and nuts were greased with anti-

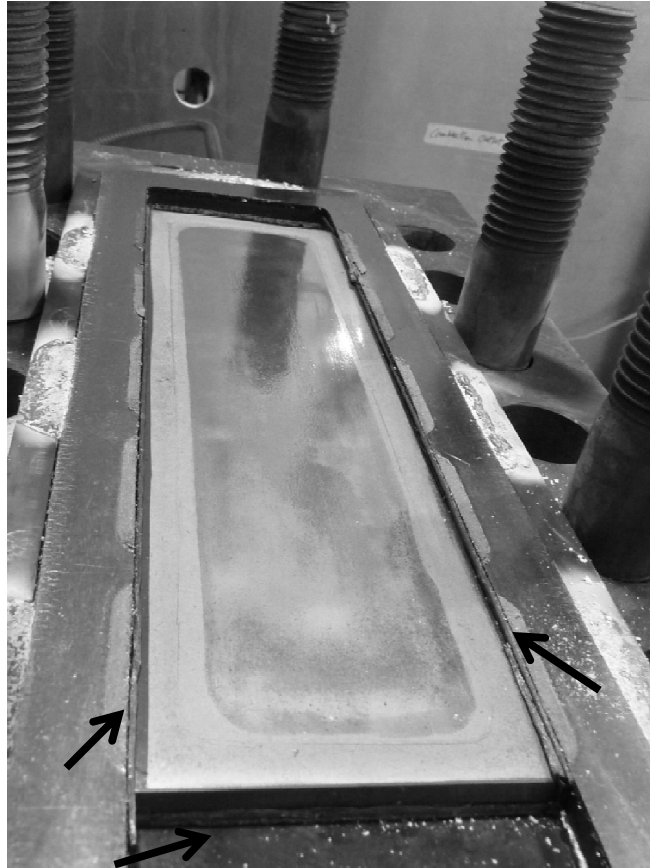


Figure 8.6: Pd/Ag Membrane Installed on Bottom Flange after Experiment no.3. Arrows indicate locations of gasket under the membrane and strips used on sides to fill gaps. They also indicate where feed by-passing is suspected to have occurred.

seize (Loctite, Metal Free Heavy Duty, no. 51606) and then tightened at 155 N-m. Feed, products and sampling connections were attached, and pressure tests on both channels were conducted. A layer of 150 to 200 mm of alumina fibre (Thermal Ceramics) was added to surround the reactor, as well as a 3.2 mm (1/8") thick aluminum casing, to contain the insulation material, and to reduce heat losses by radiation.

8.2.5 Start-up Procedure

Without Membrane

After assembly, the temperature of the reactor was increased at $\sim 1.6^{\circ}\text{C}/\text{min}$ from ambient to 350°C , at atmospheric pressure. With N_2 cylinders replacing methane, N_2 was injected at a rate of 0.26 and 0.13 nL/min into the reforming and combustion channels respectively. Those conditions were left overnight to provide time for some anti-seize grease to oxidize and the resulting smoke to dissipate.

The next day, the set point of the bottom and top flange heaters were increased to 500 and 555°C respectively. On the combustion side, N_2 flow was stopped, and air flow was started at 2.0 L/min. On the reforming side, N_2 flow was also stopped, and hydrogen flow was started at ~ 0.6 nL/min. Steam and air pre-heaters were started with skin temperature set points at 400 - 450°C .

Water flow was started at 0.18 kg/h. 45 to 60 min later, with the steam flow well established in the reactor, methane flow for reforming was started (0.5-1 nL/min) and the water flow was adjusted to reach the desired Steam-to-Carbon (S/C) molar ratio. Pressure was then increased gradually to 10-15 bar.

On the combustion side, air flow was increased to 5.5 - 6.5 nL/min, pressure was adjusted to 1-5 bar, and methane flow was started to obtain a concentration of 2-3.5% in air.

With Membrane

To preserve the membrane integrity, specific H_2 partial pressures are required when ramping the temperature. A hydrogen flow was then added to the procedure described above. The steps are listed in Table 8.5.

Table 8.5: Membrane Start-up Procedure

Steps	Temp. Set Point for Flanges Heaters (Bottom - Top) ^a	Pressure			Flow Rate		Note
		P_r	$P_{H_2,r}$	P_m	N ₂	H ₂	
	°C	bar	bar	bar	nL/min	nL/min	
1.	Ambient	4	0	1	0.2	0	
2.	(290 - 350)	4	0	1	0.2	0	Left overnight at those conditions
3.	Reactor Pressure increased to 6 bar with N ₂						
4.	(400 - 400)	6	0.05	1	14.5	0.1	
5.	(450 - 450)	6	0.10	1	6	0.1	
6.	(500 - 500)	6	0.3	1	3.8	0.2	
7.	(500 - 555)	6	0.8	1	1.3	0.2	
8.	(500 - 555)	6	6	1	0	10	Permeate test
8.	Reactor Pressure increased to 11 bar with H ₂						
9.	(500 - 555)	11		1	0	0.2	Steam start-up & methane start-up
10.	(500 - 555)	11		1	0	0	Normal operating conditions

^aMembrane sit on the bottom flange, where temperature was kept lower to insure membrane integrity.

8.2.6 Operation

Table 8.6 details the operating conditions during the experiments. Residence times and average velocities were respectively ~ 3 s and ~ 0.09 m/s in the reforming channel, and ~ 0.5 s and ~ 0.5 m/s in the combustion channel. Only the top flange cartridge heaters were utilized during the operation, to represent conditions where all heat transfer was coming from the combustion channel, as in a multi-channel assembly. Transverse temperature differences were small between the reforming and combustion channels, ~ 3 - 5°C . However, the top flange temperature could be as high as 610°C when the reforming channel was at 550°C . Axial temperature variations were generally less than 15°C in the channel. The heat losses to the surrounding were estimated by leaving the reactor at 550°C overnight, without any

Table 8.6: Experimental Operating Conditions

Exp. No.	Reforming Conditions				Per-meate	Combustion Conditions				Time of Stream	
	P_r	S/C	$F_{\text{CH}_4,ro}$	$T_{r,ave}$		P_m	P_c	$F_{\text{CH}_4,co}$	$y_{\text{CH}_4,co}$ (in air)		$T_{c,ave}$
	bar	mol/mol	nL/min	°C		bar	bar	nL/min	mol%		°C
1b	11.4	2.8	1.35	552	N/A	2.4	0.22	3.4	555	9.3	
1f	8.43	2.7	2.33	549	N/A	2.4	0.22	3.4	555	19.4	
2a	15.7	3.4	0.740	552	1.02	3.6	0.22	3.4	555	1.2	
2b	15.7	3.8	0.495	552	1.01	3.6	0.22	3.4	555	4.5	
2c	15.4	3.4	0.740	561	1.01	3.6	0.22	3.4	565	12.5	
2d	15.4	3.4	0.740	570	0.78	3.7	0.28	3.5	575	18.4	
3a	16.0	3.8	0.495	552	1.02	3.8	0.22	3.4	555	1.3	
3b	13.2	4.0	0.633	570	0.79	3.8	0.20	3.0	575	12.7	

gas flowing into the reactor. By measuring the time the cartridge heaters were on during one hour, knowing the total power installed (3kW), the heat losses were estimated to be at ~530 W. Comparatively, the heat of reaction for endothermic reforming reactions was ~60 W.

Pressure transducers were not able to detect pressure drops in the channels, since the drops were below or of the same order of magnitude as the instrument errors. Using Darcy-Weisbach equation for friction head loss in laminar flow regime, the pressure drop in both channels was estimated to be <3 Pa. Differential pressure transducers would be needed to measure accurately such small values.

8.2.7 Analytical Equipment

A GC was used to measure product gas compositions as described in Chapter 6.

To take images of coating surfaces, a Nikon Eclipse MA200 microscope was used, combined with a Nikon DS-Fi1 camera, with a resolution of 2560 x 1920 pixels.

To measure the coating thicknesses, a Positector 6000-1 thickness meter by

Defeslko, based on the eddy current principle, was used. Details of this method are provided in Chapter 4.

8.2.8 Modeling Parameters and Metrics

To compare the experimental results with predictions from the model presented in Chapter 2, some modifications were made on the catalyst layers and the membrane, as shown in Figure 8.7. Only part of the entire facial surface of the membrane plate could actually permeate hydrogen. The membrane contour is used to seal the membrane on the stainless support, and about 61% of the surface is active. In Figure 8.6, one can see a difference in foil polish appearance. The membrane center, with a mirror appearance, permeates hydrogen, whereas the frame does not. Also, in order to insert thermocouples and tubes for sampling, a gap existed between each of the catalyst plates. Therefore, membrane dead zone and no-catalyst zone corrections were added to the model. The model also allowed a distinct thickness for each plate. Tables 8.7 & 8.8 list the parameters utilized in the simulations.

We did not expect the catalyst layers to affect the laminar flow. Relative to channel imperfections, due to machining, gasket compression, and catalyst plates flatness, the catalyst layer thickness and surface roughness variations were negligible.

Methane Conversion, X_{CH_4}

Equation (6.13) from Chapter 6 was used to evaluate the methane conversion in both channels.

Specific Hydrogen Production, Y_{H_2}

Various performance indicators were defined in Chapter 3, including the specific hydrogen production indicators defined as the ratio between the mass flow of hydrogen extracted by the membrane and any of the reactor volume (*vol.react.*), mass of catalyst (kg_{cat}), or membrane area (*m.area*). For the reactor volume, we only included the internal volumes of the two channels, separator wall, and half the membrane support. This allowed our results to be compared with a Packed Bed Membrane Reactor (PBMR) and Fluidized Bed Membrane Reactor (FBMR).

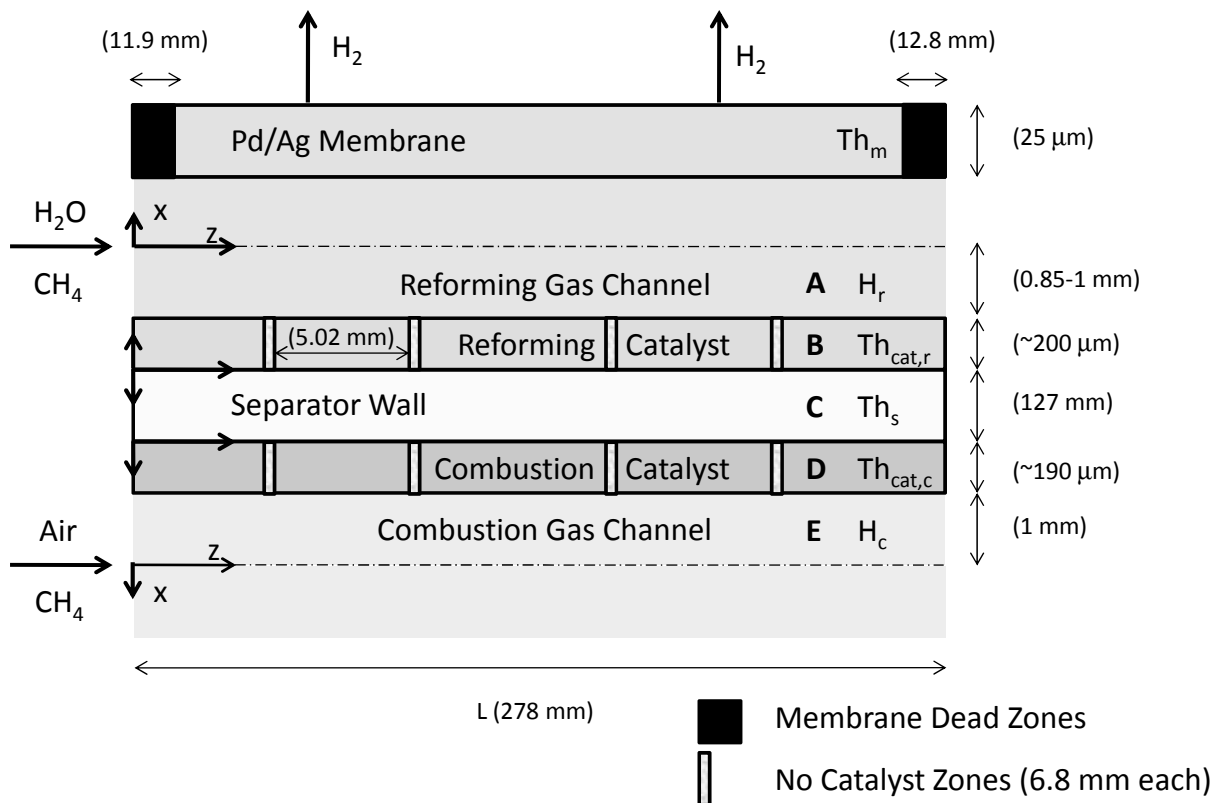


Figure 8.7: Schematic of MCMR Prototype for Simulations, Including Dimensions, Not to Scale. (Subscripts: Pd/Ag membrane m ; SMR channel r ; catalyst layer cat ; separator wall s ; MCC channel c .)

Temperature Profile

As discussed below, the methane conversion in the combustion channel underperformed the simulation predictions. For the experimental combustion methane flow, and the 2-D model with energy transfer developed in Chapter 2, temperatures would have quickly jumped, giving erroneous predictions. It is likely that flow distribution and catalyst deactivation caused the large discrepancies. Hence, the model could not be used to its full extent, and temperature profiles measured experimentally were imposed as input, instead of solving the energy balance. Second order polynomials were fitted to extrapolate the measured temperatures to the

Table 8.7: Parameters for Simulations Predictions, Part I. Physical properties options and solution parameters are the same as expressed in Table 3.2

Parameters (Symbols)	Values (Equations)	Units
Operating Parameters^a		
Reforming Feed H ₂ Content ($y_{H_2,ro}$)	0.001	mol/mol
Reforming Feed CO Content ($y_{H_2,ro}$)	0.001	mol/mol
Reforming Feed CO ₂ Content ($y_{H_2,ro}$)	0.001	mol/mol
Catalyst Parameters		
Pore Radius ($R_{pore,r}$)	9	nm
Pore Radius ($R_{pore,c}$)	4.5 (Alfa) - 9 (Lab-made)	nm
Pore Volume (v_r)	0.42	cm ³ /g
Pore Volume (v_c)	0.35 (Alfa) - 0.42 (Lab-made)	cm ³ /g
Porosity ($\epsilon_{cat,k}$)	See Eq. (6.12)	
Density ($\rho_{cat,k}$)	see Tables 8.2- 8.4	kg/m ³
Reforming Kinetics ^b	Jakobsen et al. (2010)	
Combustion Kinetics	n^{th} order (See Eq. (2.50))	
Reaction orders (α, β)	0.78, 0	
Pre-exponential Factor (A_4) ^b	1635 (Pd 1%) 4710 (Pd 5%)	kmol/(kg s bar ^{α})
Activation Energy (E_4)	88	kJ/mol

^aOperating parameters vary and are detailed in Table 8.6

^bSee Section 8.2.8.

channel inlet and outlet, and only the material balance equations were then solved.

Estimation of Membrane Effectiveness, η_m

From Eq. (2.22), η_m was evaluated by:

$$\eta_m = \frac{F_{H_2,m}/Area_m}{\frac{A_m}{Th_m} \exp\left(\frac{-E_m}{R_g T_{r,ave}}\right) \left(\sqrt{P_{H_2,r}} - \sqrt{P_{H_2,m}}\right)} \quad (8.1)$$

To evaluate the membrane area ($Area_m$), dead-zones (see Figure 8.7) were excluded to obtain an effective membrane surface of 0.020 m² (the full membrane surface being 0.022 m²). A_m , Th_m and E_m are listed in Table 8.8. The hydrogen perme-

Table 8.8: Parameters for Simulations Predictions, Part II. Physical properties options and solution parameters are the same as expressed in Table 3.2

Parameters (Symbols)	Values (Equations)	Units
Design Parameters		
Length (L)	0.251 - 0.278 ^a	m
Reforming Width (W_r)	0.081	m
Combustion Width (W_c)	0.074	m
Catalyst Thickness ($Th_{cat,k}$)	See Tables 8.2 - 8.4	μm
Ref. Gas Channel Half-Height (H_r)	Without memb. 1.0; with membrane 0.85;	mm
Comb. Gas Channel Half-Height (H_c)	1.0	m
Membrane Parameters		
Membrane Thickness (Th_m)	25	μm
Membrane Effectiveness (η_m)	0.56 (See Eq. (8.1) and Section 8.3.3)	
Pre-exponential Factor (A_m)	3.427e-5	mol/(s m bar ^{0.5})
Activation Energy (E_m)	9180	J/mol
Membrane Dead Zone	See Figure 8.7	

^aFor predictions with membrane, 5 plates, each 0.0502 m, and separated with a 6.75 mm gap, give a total length of 0.278 m.

ate flow ($F_{H_2,m}$), reforming channel average temperature ($T_{r,ave}$), reforming channel hydrogen partial pressure ($P_{H_2,r}$), and hydrogen permeate pressure $P_{H_2,m}$ were measured experimentally.

Estimation of Feed By-pass

Despite repeated attempts to eliminate the problem, the MCMR prototype had a design fault, with a portion of the reforming feed by-passing the channel by going under or beside the dummy and Pd/Ag membranes. It is probable that the by-passing caused the outlet conversion to be less than the measurements inside the reactor with the sampling tubes.

By mass balance, the following equation is obtained to estimate the extent of the

by-passing:

$$By-pass = \frac{X_{CH_4,out} - X_{CH_4,expected}}{X_{CH_4,expected}} \quad [mol/mol] \quad (8.2)$$

$X_{CH_4,out}$ is the measured outlet conversion. For experiments with membranes, we assumed that the $X_{CH_4,expected}$ should have been a conservatively-extrapolated 5% higher than the conversion measured after the 4th plate ($X_{CH_4,4}$):

$$X_{CH_4,expected} = X_{CH_4,4} * 1.05 \quad [mol/mol] \quad (8.3)$$

The by-pass estimate was used in two places: In some simulation predictions with the membrane, the reforming feed was multiplied by $(1-By-pass)$. Secondly, in the Parametric Study section below, the mole ratio of the hydrogen permeate ($F_{H_2,m}$) over the reforming methane fed $F_{CH_4,ro}$, was corrected as:

$$Ratio_{H_2,m/CH_4} = \frac{F_{H_2,m}}{F_{CH_4,ro}(1 - By-pass)} \quad (8.4)$$

Catalyst Coating Density, $\rho_{cat k}$

$\rho_{cat k}$ was evaluated by dividing the mass of catalyst, W_{cat} , by the area of the metal plate times the average thickness of the catalyst layer, $Th_{cat,k,ave}$:

$$\rho_{cat k} = \frac{W_{cat}}{0.0885 * 0.05058 * Th_{cat,k,ave}} \quad [kg/m^3] \quad (8.5)$$

Combustion Kinetics Modification

In Chapters 2 and 3, the kinetic model includes a term for the O_2 partial pressure, in order to avoid negative concentrations while solving the model. In Chapter 7, while evaluating combustion kinetic parameters, the effect of oxygen was neglected, since a large excess of oxygen ($\sim 240\%$) was employed. The literature usually also neglects the effect of oxygen for Pd catalysts (Lee and Trimm, 1995). However, at a high methane conversion $>80\%$, with Pd 5%, our model had diffi-

culty to converge. To cope with this issue, a multiplication factor was applied to the pre-exponential factor, A_4 . Above 80% methane conversion, A_4 was multiplied by 0.5, and above 95%, by 0.1.

Reforming Kinetics

In Chapter 2, three SMR kinetic models for Ru-based catalyst were presented. Preliminary simulations with Berman et al. (2005) and Wei and Iglesia (2004) models were judged not satisfactory for the MCMR prototype results. Berman et al. (2005) model largely underestimated the reaction rates and Wei and Iglesia (2004) model largely overestimated them. As shown in Chapter 6, Jakobsen et al. (2010) model could fit adequately our reaction rates in the packed bed micro-reactor. The reforming kinetics equations based on Jakobsen et al. (2010) were then utilized. However, for cases without membrane, when the methane conversion reached thermodynamic equilibrium, the model became unstable and the kinetic model was switched to the Xu and Froment (1989) model to complete the simulation.

8.3 Results and Discussion

8.3.1 Preliminary Results

Table 8.9 summarizes preliminary results obtained with the reforming channel. Only three of nine preliminary experiments were successful in producing hydrogen. Details are provided in Appendix C, as well as lessons learned during the reactor commissioning.

To summarize the reforming preliminary results, the commercial Ni-based RK-212 was not active in the MCMR, as well as catalysts whose support was not pre-aged by steam. In the preliminary experiments, the metal support was SS 304, and corrosion on the catalyst surface usually appeared a few weeks after the steaming step, or during the MCMR runs. As discussed in Chapter 6, it is suspected that iron oxide poisoned the catalyst, making it inactive. SS 310 and Fecralloy were therefore adopted for the experiments presented in this chapter. Finally, the methane conversion was improved with the addition of La_2O_3 (See Section C.2.2).

On the combustion side, the commercial oxidation catalyst converted methane,

Table 8.9: Summary of Preliminary Results for the Reforming Channel. See Appendix C for more details about the catalysts and experimental conditions.

Exp. Number ^a	Catalyst	Note Catalyst	Result	Problem
0.1	RK-212 with 20% boeh.	-	Not measured	Water in GC lines
0.2	Plates from Exp. 0.1 reused		CH ₄ conversion ≤3%	Catalyst not active
0.3	Ru (6.1wt%)/ γ-Al ₂ O ₃	γ-Al ₂ O ₃ support not steamed	CH ₄ conversion <1%	Catalyst support not stable
0.4	Ru (6-7%) MgO (5%, plate no.1 only)/ γ-Al ₂ O ₃	γ-Al ₂ O ₃ support steamed	Exp. partially successful, see Appendix C.2.2	Positive effect of pre-steaming
0.5	Ru 6-10% La ₂ O ₃ (4%, plate no.2 only)/ γ-Al ₂ O ₃		Exp. partially successful, see C.2.2	Positive effect of La ₂ O ₃
0.6	Ru (5-8%) La ₂ O ₃ (10-14%) ^b / γ-Al ₂ O ₃	Support steamed, catalyst 2 months old	CH ₄ conversion <5%	Catalyst poorly active, likely from rust
0.7	Ru 4-8% MnO (2% plate no.2) MgO (2-3% plates no.2 & 3) La ₂ O ₃ (3-7%)	Support steamed	Exp. partially successful, see Appendix C.2.2	Positive effect of La ₂ O ₃ observed
0.8	Same plates as Exp. 0.7	Catalyst ~3.5 months old	CH ₄ conversion <1%	Catalyst not active, likely from rust
0.9	Ru 4-10% La ₂ O ₃ (3-15%)/ γ-Al ₂ O ₃	Catalyst ~3.5 months old	CH ₄ conversion <5.5%	Catalyst poorly active, likely from rust

^aThese runs are separate from those covered in other tables of this chapter.

^b4th plate did not contain La₂O₃

but to a lower extent than predicted by the model. Results are again presented in Appendix C. In summary, a large channel height (9 mm) had a negative effect on the conversion. Pd 5% performed better than Pd 1%, but none of the commercial catalysts performed according to the model expectations. Some operating conditions led to faster deactivation, in particular higher methane concentration (4%), high temperature (565°C), and pressure above 3.2 bar.

8.3.2 Multi-Channel Reactor without Membrane

Figure 8.8 presents methane conversion and temperature profiles along the reactor for an experiment without a membrane. On the reforming side, the conversion quickly reached equilibrium, and the model adequately predicted the results.

On the combustion side, only the outlet conversion could be measured due to sampling issues caused by back-flow created by a short Grafoil strip for mechanical support (see Section “Lesson Learned” in Appendix C). Nevertheless, it is clear that the combustion conversion under-performed the expected results. One can see with the combustion model prediction (curve E) some singularities. Those are due to the variations in coating thicknesses (See Table 8.2).

For the Exp. no.1, the combustion conversion started at 90% and dropped to 40% after 21 h on stream. A large drop in conversion, 19% within 1 h, occurred when methane concentration in the feed was 4.1%, confirming previous observations that higher methane concentrations are associated with faster deactivation.

The methane conversion at the outlet of the reactor was a function of the thermodynamic equilibrium, and not of the kinetics. To test the model predictions without any membrane, the conversion at location no.1 (see Figure 8.2) was plotted as a function of the methane flow rates. Figure 8.9 shows the results, and despite some scatter in the experimental data, the trend adequately matches the simulations.

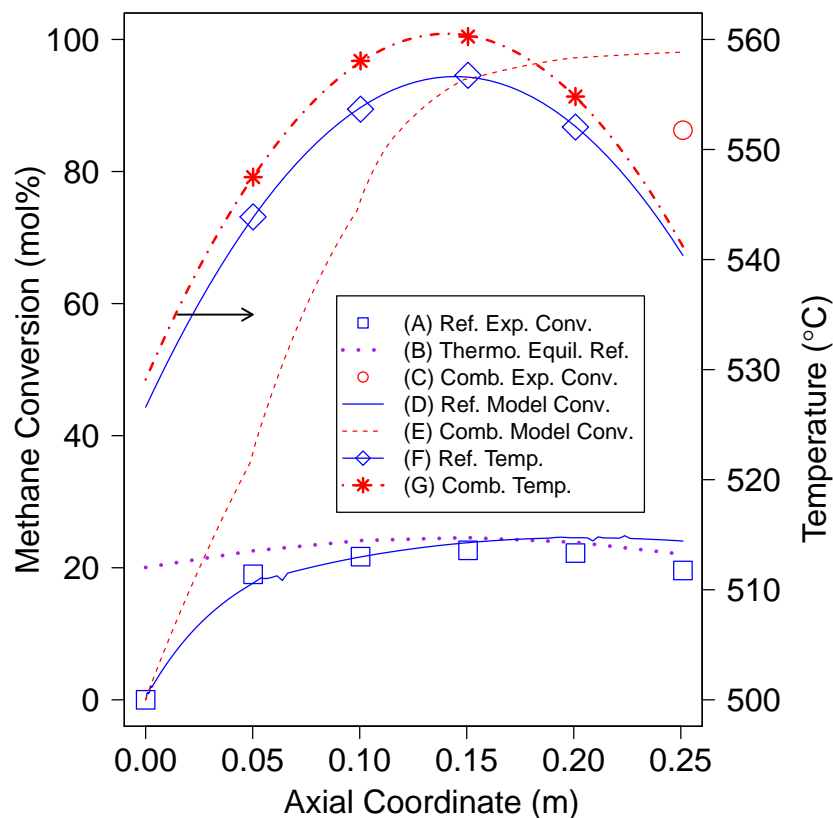


Figure 8.8: Conversion and Temperature Profiles for MCMR Run no.1a without Membrane. Operating Conditions: Reforming: CH_4 Flow: 1.35 nL/min, S/C: 2.8, P_r : 11.4 bar; Combustion: CH_4 Flow: 0.22 nL/min, 3.4% in air, P_c : 2.4 bar. Temperature data are fitted with a second order polynomial. Time on Steam: 9.3 h

8.3.3 Multi-Channel Reactor with Membranes

Effectiveness Factor

The membrane effectiveness factors were evaluated at the beginning of both Exp. 2 & 3, using Eq. (8.1). Results are presented in Table 8.10. η_m at $\sim 56\%$ is relatively low. However, the area taken includes zones on the sides of the membrane that do not permeate hydrogen. Taking the H_2 permeable area only, η_m would be closer to

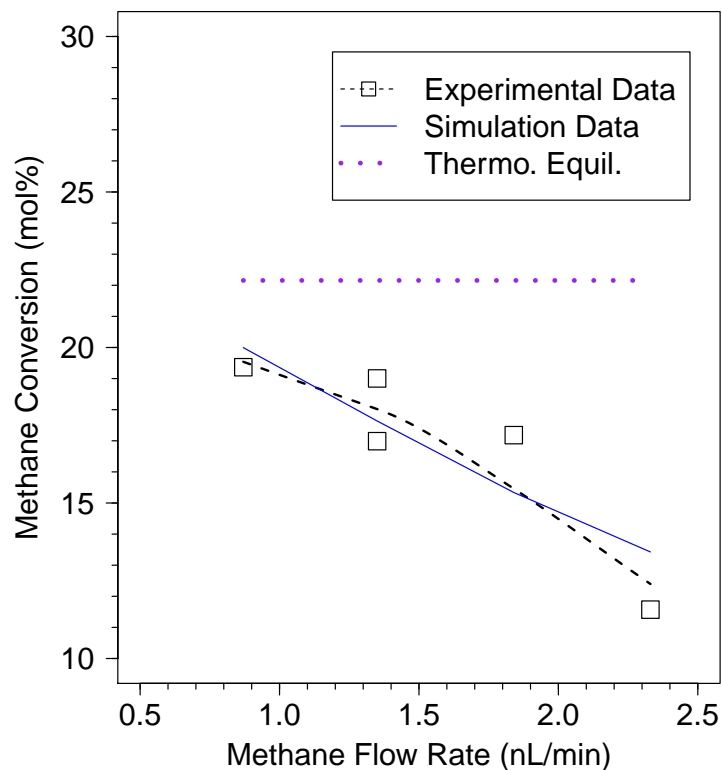


Figure 8.9: Methane Conversion versus Methane Flow Rate at Position no.1 for MCMR Exp. no.1, without Membrane. Operating Conditions Reforming: S/C: 2.7-2.9, P_r : 11.4 bar; Combustion: CH_4 Flow: 0.22 nL/min, 3.4-4.1% in air, P_c : 2.4 bar.

80%, which, according to the supplier, MRT, is a reasonable value.

Hydrogen Quality

The hydrogen permeate was tested for impurities. At the end of Exp. no.3, CO , CO_2 and CH_4 contents were 4, 21 and 27 ppm respectively, giving a hydrogen purity of 99.995%^a. Exp. no.3 reused the same membrane as Exp. no.2, suggesting

^aDue to being at the lower end of the scale of the analytical instrument, this is a best estimate. We believe that the purity is at level “4 nines”, i.e. 99.99%, but it is impossible to fully quantify the errors in the estimate.

Table 8.10: Membrane Effectiveness Calculations (membrane area estimated at 0.020 m²).

$P_{H_2,r}$ bar	P_m bar	$T_{ave,r}$ °C	H ₂ Flux mol/(m ² s)	η_m
Exp. no.2				
9.12	1.09	552	0.40	0.56
6.875	1.07	552	0.31	0.54
8.865	1.09	552	0.39	0.56
Exp. no.3				
7.12	1.07	548	0.32	0.56
7.19	1.07	549	0.33	0.56
7.06	2.04	550	0.25	0.57
7.06	2.04	550	0.25	0.57
Average				0.56

that the membrane start-up and cool-down procedure was successful in preserving the membrane integrity. Our GC was not calibrated for low ppm concentrations, and the accuracy of these results is uncertain. More tests with a GC calibrated for <10 ppm impurities and a dedicated sampling line for hydrogen permeate would be needed to confirm compliance with the hydrogen quality requirements for Proton Exchange Membrane Fuel Cells (PEMFCs) (see Table 1.2).

Dynamic Behaviour

Sohn et al. (2007) reported that MCRs respond promptly to dynamic changes in feed conditions. This observation was confirmed in our system. Figures 8.10 and 8.11 displays screenshots of flow and temperature trends, while methane flows were either being increased or started. On Figure 8.10 the permeate hydrogen increased immediately when the methane flow increased. The top row of Figure 8.11 displays channel temperature trends, and the arrows point towards the two thermocouples at the first location. Temperatures dropped and then increased with successive start-up of reforming and combustion flows. The bottom row displays the flange temperature for one thermocouple located inside a cartridge heater. The

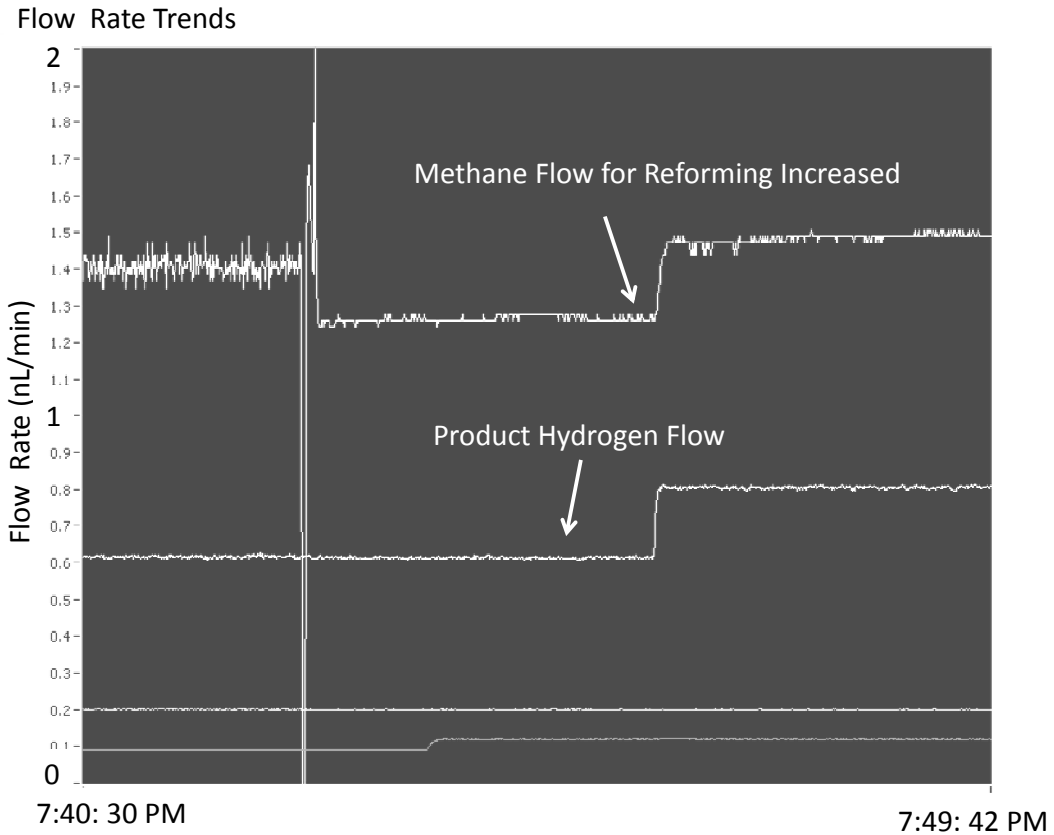


Figure 8.10: Process Response on H_2 Production to an Increase in CH_4 Flow: LabVIEWTM screenshot of permeate hydrogen and reforming methane flow rates.

temperature trend cycled as the heater was turned on and off. The heater turned off initially when the combustion methane flow started and the temperature dropped. However, heat losses to the surrounding exceeded the heat provided by the combustion, and heaters eventually returned to their heating cycles (not displayed on the Figure).

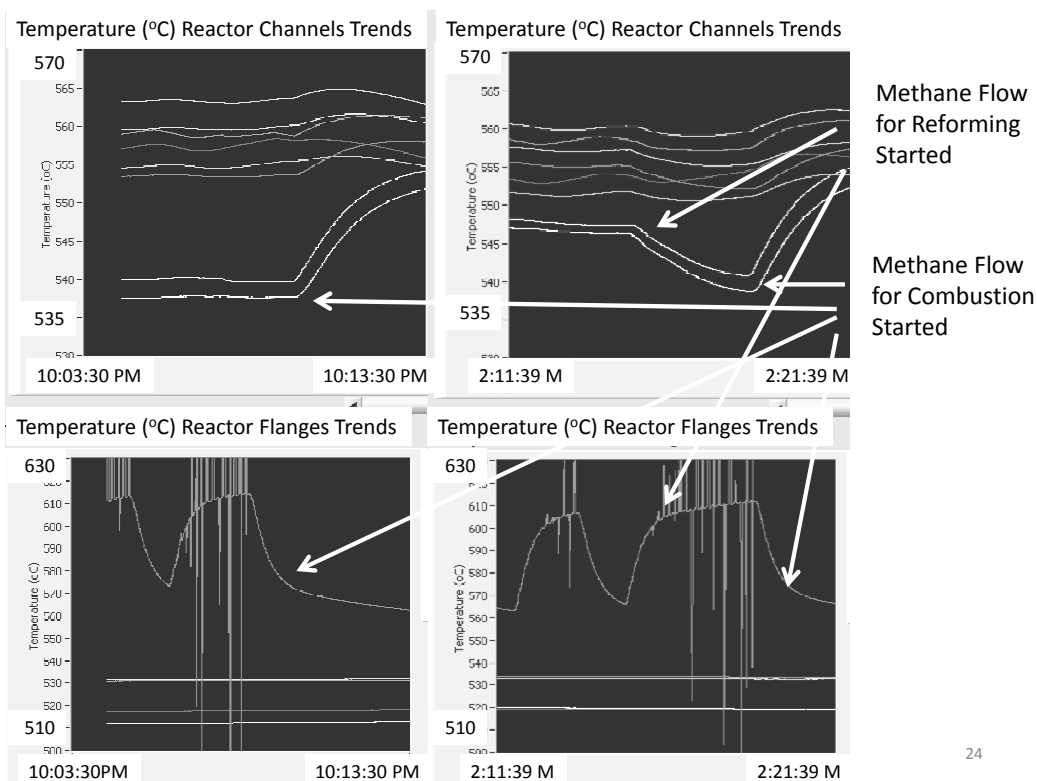


Figure 8.11: Process Response on Temperatures to the Start of Reforming and Combustion Methane Flows: LabVIEW™ screenshots of channel temperatures (top row) and flange temperatures (bottom row).

Methane Conversion and Temperature Profiles

Figure 8.12 presents methane conversion and temperature profiles along the reactor for Exp. no.3a with membrane. On the reforming side, the conversion quickly surpassed the equilibrium value, then peaked at the 4th position, above 80%, to finally drop 7% points at the outlet. Except for the outlet, the model slightly underestimates the conversion. Based on Eq. (8.2), it was estimated that the feed by-pass was 13% for this case. The simulations on the next figures below consider the feed by-passing.

On the combustion side, the experimental data confirmed that the combustion catalyst performance was less than expected from the model, even though the con-

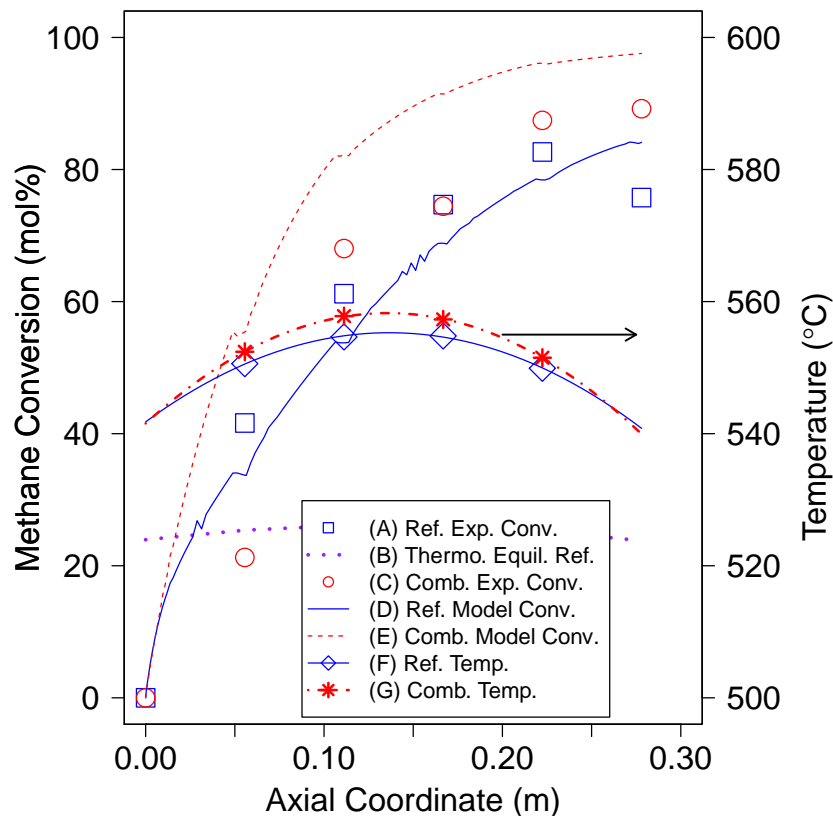


Figure 8.12: Conversion and Temperature Profiles for MCMR Exp. no.3a with Membrane. Operating Conditions: Reforming: CH_4 Flow: 0.495 nL/min, S/C: 3.8, P_r : 16.0 bar, P_m : 1.02 bar; Combustion: CH_4 Flow: 0.22 nL/min, 3.4% in air, P_c : 3.8 bar. Temperature data are fitted with a second order polynomial. Time on Steam: 1.3 h.

conversion almost reached 90%. One can observe kinks in both reforming and combustion model conversion curves. These are due to the no-catalyst zones (see Figure 8.7) and the variations in coating thicknesses (see Tables 8.3 & 8.4).

In Figure 8.13, several parameters were varied in an effort to explain the discrepancies between the experimental data and simulations. On the reforming side (Part A), wrong temperature readings were probably not the reason. However, multiplying the pre-exponential factor, A_1 by 2, or multiplying the feed flow rate

by (1-*By-pass*), both predicted well the first four experimental points. In Chapter 6, after a period of quick deactivation, the A_1 estimate was similar to that reported by Jakobsen et al. (2010). Since the deactivation rate of the catalyst was uncertain in the MCMR, A_1 was kept identical to the Jakobsen et al. (2010) value for further simulations below. The by-pass factor was utilized instead.

On the combustion side, Fig. 8.13B reveals that doubling the combustion flow rate could explain the lower-than-expected performances. A smaller pre-exponential factor, or wrong temperature readings could not explain the discrepancy. One could speculate that a flow distribution issue might be the problem for the combustion channel. Flow distribution is a common problem in MCR technologies, and Rebrov et al. (2011) reviewed various ways of improving flow distribution. 3-D Computational Fluid Dynamics (CFD) simulations might assist in testing this hypothesis.

Figure 8.14 presents methane conversion and temperature profiles along the reactor for Exp. no.3b with membrane. The learnings from the simulation presented in Figure 8.13 were applied. By multiplying the methane flow rate by (1 - the estimated by-pass factor), in this case 17%, the simulation predicted accurately the experimental data. However, for the combustion side, even multiplying the flow rate by 2 did not provide a match to the under-performing conversion data. This suggest that flow distribution was not the only problem. Instead, catalyst deactivation likely also played a role.

Some dimensionless numbers were evaluated for Experiment no.3b. Reynolds numbers were low in both channels, <40 , confirming laminar flow. Mass Peclet numbers for hydrogen (see Eq. (3.25)) at the entrance of the reforming channel and methane in the combustion channel were 631 and 4920 respectively. The Peclet number for hydrogen was <1000 , indicating some axial dispersion, neglected in the model. However, as shown in the previous figures, the reforming simulations predicted well the experimental data, and we did not see the benefit of adding second order axial dispersion terms at this stage.

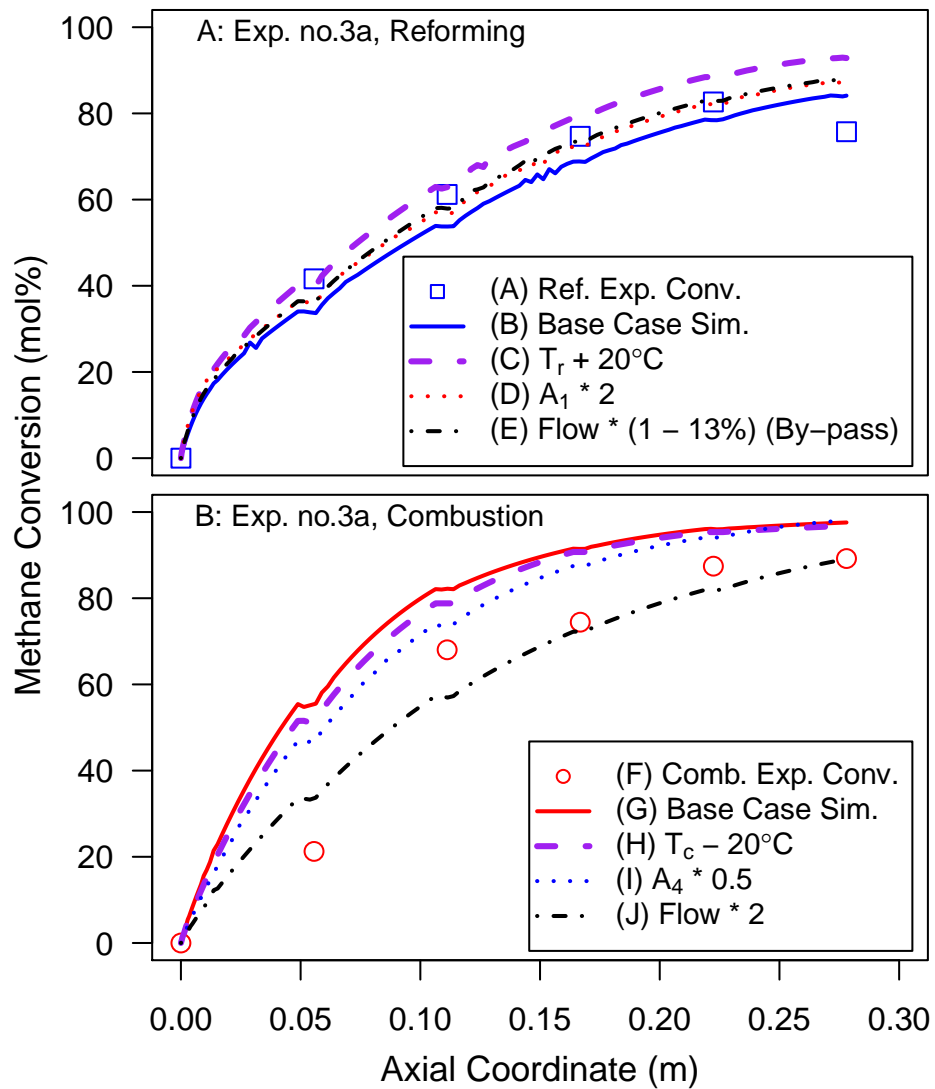


Figure 8.13: Sensitivity on Conversion Profiles for MCMR Run no.3a with Membrane. Operating conditions were detailed in Figure 8.12.

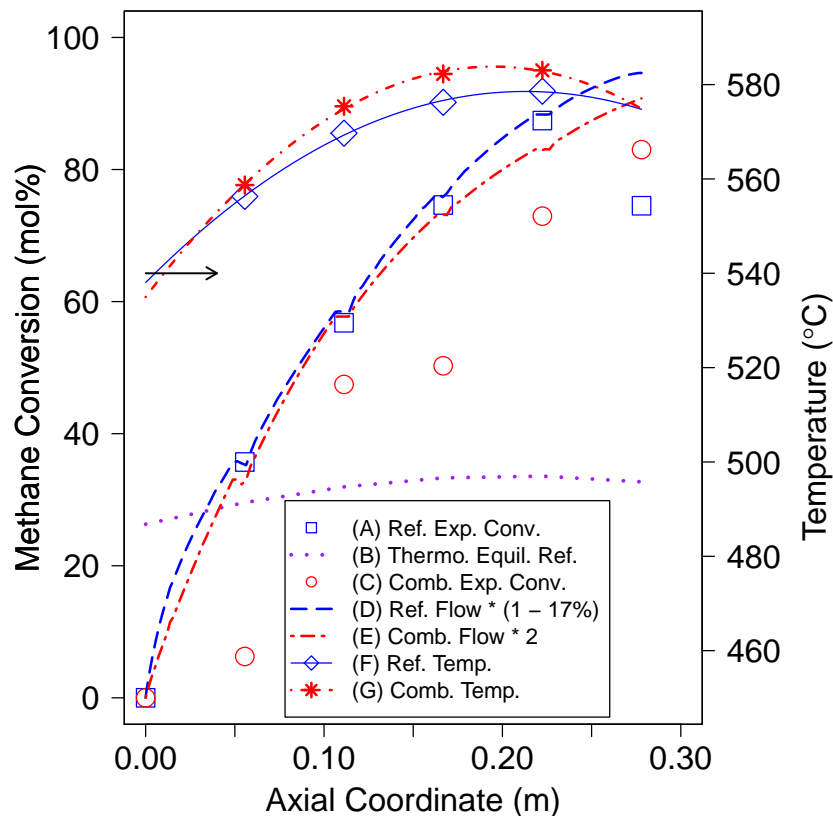


Figure 8.14: Conversion and Temperature Profiles for MCMR Exp. no.3b with Membrane. Operating Conditions: Reforming: CH₄ Flow: 0.63 nL/min, S/C: 3.98, P_r: 13.2 bar, P_m: 0.79 bar; Combustion: CH₄ Flow: 0.20 nL/min, 3.0% in air, P_c: 3.8 bar. Temperature data are fitted with a second order polynomial. Time on Steam: 12.7 h.

Parameters Study

Figure 8.15 displays several experimental data with simulation predictions, while varying one parameter at a time. For S/C experiments (Part A), experimental and simulation data showed an optimum point, but the experimental optimum occurred at slightly higher S/C than predicted.

In Part B, the model predicted well lower pressure experiments, but could not explain why the experimental hydrogen yield reached a peak and began to decrease

at higher pressure. The Jakobsen et al. (2010) kinetic model was developed at low pressure (1.3 bar). The Xu and Froment (1989) kinetic model was tried as well, where the data were up to 15 bar, but no peak was observed. It is uncertain at this stage whether the pressure effect results from an inaccurate kinetic model, strong deviation from ideal gas behaviour as assumed in the model, or feed by-pass increasing with increasing pressure. Kinetic experiments in the micro-reactor at higher pressures, and incorporating high pressure correlations for physical properties and equation of states in the model could be investigated in future.

In Part C, the methane flow rate effect was well predicted by the model. Our prototype is likely limited by the membrane flux, with the flow increase automatically lowering the hydrogen yield.

Performance Review

Table 8.11 summarizes several performance indicators with data obtained experimentally. We also compare the experimental results with predictions made in Chapter 3 and membrane reactor experimental work reported in the literature.

In term of methane conversion, the MCMR experimental results underperformed the best case scenario of Chapter 3 for various reasons: (1) The experiments were conducted at lower temperature than the simulation (average temp. of 550-570°C instead of a feed temperature of 600°C), slowing down the kinetics and the membrane flux, and lowering the SMR equilibrium conversion; (2) The prototype was shorter than the simulation (0.278 m instead of 0.3 m); (3) The vacuum pump on the experimental set-up did not give as high a vacuum as the simulation (0.8 instead of 0.7 bar); and (4) There was a design issue with appreciable feed by-passing.

Despite these deficiencies, the hydrogen yields per mass of catalyst were between one and two orders of magnitude higher than estimated for two FBMRs and one PBMR from the literature (Rakib et al., 2011; Mahecha-Botero et al., 2008; Tong et al., 2005). The hydrogen yields per reactor volume was about one order of magnitude higher than estimated (Rakib et al., 2011; Mahecha-Botero et al., 2008) for the FBMRs, confirming the technical potential for MCMR technology. The hydrogen yields per membrane area also performed well, considering that vacuum

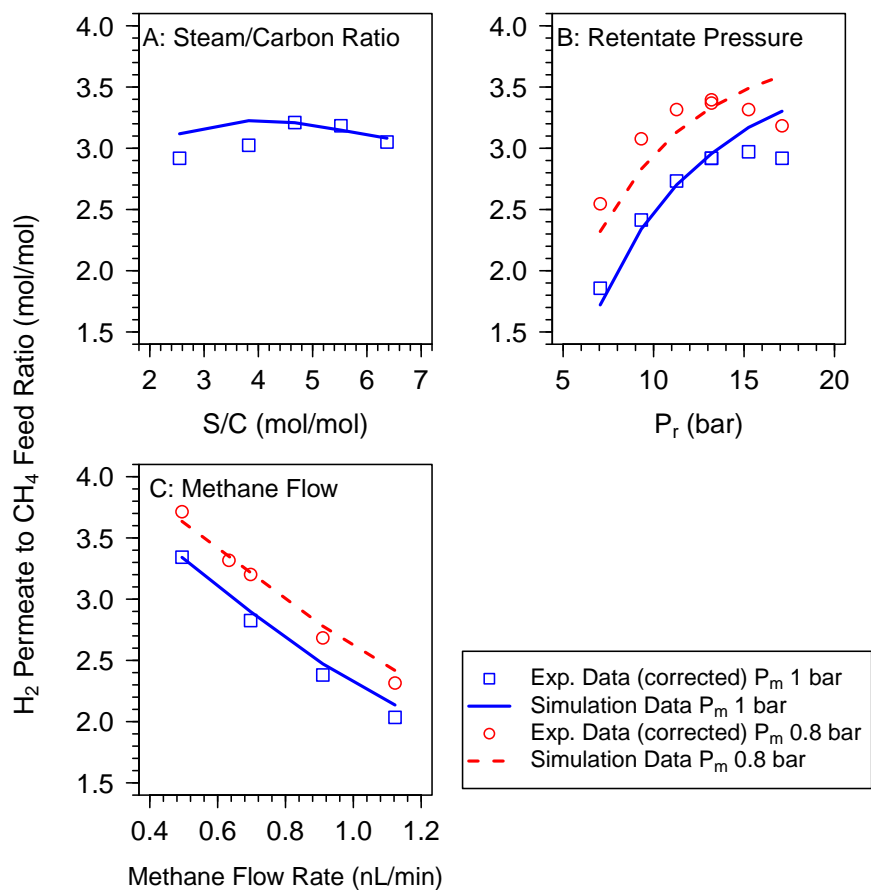


Figure 8.15: Parametric Study on Effect of Steam-to-Carbon Molar Ratio, Reforming Channel Pressure, and CH₄ Flow Rate, on H₂ Extracted to CH₄ Feed Ratio. Operating Conditions: A. CH₄ Flow: 0.495 nL/min, P_r: 15.8 bar, T_{ave,r}: 552°C; B. CH₄ Flow: 0.495 nL/min, S/C: 4.7, T_{ave,r}: 552°C; C. P_r: 13.2 bar, S/C: 3.5-4.4, T_{ave,r}: 570°C. Exp. data of H₂ Extracted to CH₄ Feed Ratio was corrected using Eq. (8.4), with feed by-pass of 13%. Time on Steam: 1.7-12.4 h.

Table 8.11: MCMR Experimental Results Compared with Early Simulations and Other Membrane Reactors. Membrane thickness for this work is 25 μm . See Table 8.6 for experimental conditions.

Exp. No.	X_{CH_4} ^a mol%	Ratio $\text{H}_2,\text{prod.}/\text{CH}_4$ mol/mol	Ratio $\text{H}_2,\text{m}/\text{CH}_4$ mol/mol	$F'_{\text{H}_2,\text{m}}$ kg/- day	$Y_{\text{H}_2,\text{vol.react.}}$ ^b kg/ (day m^3)	$Y_{\text{H}_2,\text{kg}_{\text{cat}}}$ kg/ (day kg_{cat})	$Y_{\text{H}_2,\text{m.area}}$ kg/ (day m^2)
1b	22.2	0.77	N/A	0.13 ^c	472	105	N/A
1f	24.1	0.72	N/A	0.21 ^c	766	170	N/A
2a	73.5	2.5	2.1	0.20	736	135	8.6
2b	87.3	2.9	2.4	0.15	562	103	6.6
2c	74.2	2.6	2.1	0.20	732	134	8.6
2d	91.2	2.9	2.5	0.23	861	153	10.1
3a	82.7	3.0	2.7	0.17	629	111	7.4
3b	87.4	2.94	2.90	0.23	860	152	10.1
Best Case Sim. ^d	91.5	3.68	3.12	0.51	1311	90.0	21.2
FBMR ^e	70	3.0	2.5	0.4	40	0.2	2
FBMR ^f	73	N/A	3.0	1.8	165	2.5	6.8
PBMR ^g	80	N/A	N/A	0.03	420	2	15

^aConversions in MCMR were taken at position no.4

^bFor the MCMR, the internal volumes of the two channels, separator wall, and half the membrane support were included.

^cNo membrane was present. Value is the hydrogen produced, $F'_{\text{H}_2,\text{prod.}}$. Hydrogen purity was $\sim 43\%$.

^dFrom Chapter 3, 600°C, 15 bar, 0.7 bar permeate, Th_m : 25 μm , reactor length 0.3 m (refer to chapter for other simulation parameters).

^e(Rakib et al., 2011) 500°C, 6 bar, 0.5 bar permeate side, Th_m : 25 μm , electric heating

^f(Mahecha-Botero et al., 2008) 550°C, 10 bar, 0.3 bar permeate side, Th_m : 25 μm , electrical heating

^g(Tong et al., 2005) 550°C, 3 bar, sweep flow equivalent to 0.3 bar, Th_m : 6 μm , electric heating

on the permeate side was less in our case than in the other reported work.

Improvement Potential for Reforming Channel

Table 8.12 presents options to improve the reforming results. As in Chapter 3, we looked at the effect of parameter changes on the minimum reactor length to

Table 8.12: Improvement Potential for the Reforming Channel

Parameter Modified	Value	Unit	Min. L to 90% X_{CH_4} (m)	% Change
Base Case: Exp. No.3b	-	-	0.277	-
Pressure Permeate P_m	0.4	bar	0.204	26
Membrane Thickness Th_m	12.5	μm	0.210	24
η_m	80%		0.237	14
Pre-exp. Factor A_1	x 1.5		0.254	8
Catalyst Thickness $Th_{cat,r}$	x 1.5	μm	0.263	5
No Membrane Dead Zone			0.275	0.5

reach 90% methane conversion. The top three improvements were related to the membrane, confirming that the permeation flux is currently the major factor limiting the conversion. The membrane catalyst effectiveness η_m could be improved by using the impermeable region of the membrane as a surface to seat the gasket. Increasing the vacuum with a better pump is also a realistic option. Decreasing the membrane thickness will depend on research advances in membrane technology and the hydrogen purity required.

Catalyst-related parameters in Table 8.12 generated less than 10% improvement. Therefore, at the current stage of the development of the technology, there is little incentive to improve the catalyst activity, but research should rather focus on catalyst stability.

8.4 Conclusions

A two-channel MCMR prototype was design, built and tested to produce pure hydrogen in a single vessel. Without any membrane, the reforming methane conversion quickly approached equilibrium and the model predicted the results adequately. With a membrane, the model underestimated the conversion. A design issue created by a portion of the feed by-passing the reforming channel accounted for at least part of the discrepancy. With a by-pass factor incorporated in the model, the reforming experimental results, for a wide range of flow, pressure and steam-

to-carbon ratio conditions, were adequately predicted. 87% methane conversion was achieved on the reforming side, and the extracted hydrogen-to-methane feed molar ratio reached 2.94.

On the combustion side, the experimental data fell below the model expectations. Even though methane conversion almost reached 90%, it is suspected that the flow distribution and catalyst deactivation caused significant discrepancies. Some operating conditions promoted higher deactivation decay, in particular higher methane concentration (4%), high temperature (565°C), and pressure above 3.2 bar. Research is needed to improve the combustion catalyst performance.

The hydrogen permeate was tested for impurities. CO content was estimated at 4 ppm, while hydrogen purity reached 99.995%.

The reactor responded promptly to dynamic changes in feed conditions, with the permeate hydrogen increasing immediately when the methane flow increased.

Even though the MCMR experimental results under-performed the best case scenario of the simulation performed in Chapter 3, hydrogen yields per mass of catalyst, were between one and two orders of magnitude higher than estimated for two FBMRs and one PBMR from the literature. The hydrogen yields per reactor volume were about one order of magnitude higher than estimated for the FBMRs.

Simulations suggested that the prototype was likely limited by the membrane flux. Lowering the permeate pressure, increasing membrane effectiveness and lowering membrane thickness should be adopted to improve the reactor performance.

Chapter 9

Overall Conclusions and Recommendations

9.1 Conclusions

A proof-of-concept Multi-Channel Membrane Reactor (MCMR) was designed, built, and operated for the decentralized production of hydrogen via Steam Methane Reforming (SMR). The concept alternates steam reforming gas channels to produce the hydrogen and Methane Catalytic Combustion (MCC) gas channels to provide the heat of reaction. A palladium-silver (Pd/Ag) membrane inside the reforming gas channel shifts the reaction equilibrium and produces pure hydrogen (99.995%) in a single compact vessel.

A 2-Dimensional (2-D), steady state model of the MCMR was first created, including all energy balances, mass balances, chemical kinetics and physical properties for a representative geometry including one reforming channel and one MCC channel. Most model assumptions were verified with dimensionless number calculations and back calculations of heat and mass transfer driving forces. Future model improvement would benefit from incorporation of second order heat transfer terms in the axial direction for the separator wall. Isothermal sensitivity analysis indicated that the H₂ membrane extraction is the major factor limiting reforming performance, whereas catalyst activity is the major factor limiting combustion performance. Non-isothermal simulation results predicted good heat transfer. Except

for the reactor entrance, transverse temperature variations within the computational domains could be kept below 10 K. Without rigorous optimization, it was possible to obtain methane conversion (>90%) without the formation of hot spots. Performance could be improved significantly by a combination of varying the pre-exponential factor (metal loading) and catalyst thickness along the length of the reactor, while increasing the methane flow rate to the combustion channel.

A method to coat both SMR and MCC catalysts on a metal support was developed. After many trials, the initial goal of producing coating with good adherence, measured by sonication, with coating layer thickness $>80\ \mu\text{m}$ was achieved. Air-spray hot substrate coating (hot spray) achieved thicknesses up to $240\ \mu\text{m}$ with $\gamma\text{-Al}_2\text{O}_3$, while adherence tests gave satisfactory results. Hot spray coating of commercial catalysts with $\gamma\text{-Al}_2\text{O}_3$ as carrier were successful as well. Pd/ $\gamma\text{-Al}_2\text{O}_3$ coatings were selected as the combustion catalyst for the MCMR prototype. A crack density test was devised as a non-destructive method to evaluate coating adherence, giving results consistent with the sonication test. Crack formation and coating delamination during impregnation were linked to the presence of white lines, precursors to cracks, on the coating surface, and to the absence of clusters. Cracks could be avoided by lowering carrier or commercial catalyst concentration in the modified sol, and by monitoring the rate of water evaporation during hot spray coating. La_2O_3 was an effective promoter to avoid carbon deposition during steaming. Rust appeared on most coatings where SS 304 was the support, and was suspected to deactivate the reforming catalyst. Rust diffusion was reduced by SS 310, and arrested completely by using Fecralloy as the metal support.

Micro-reactor activity experiments allowed various reforming and combustion catalysts to be tested for their suitability in the MCMR prototype. For reforming catalyst, a lab-made Ru $\sim 5\%$ $\gamma\text{-Al}_2\text{O}_3$ catalyst was selected for the MCMR. Aging of the support with steam was necessary to avoid total catalyst deactivation. The addition of MgO and La_2O_3 to the alumina improved the stability of the Ru catalyst. For combustion catalyst, commercial Pd 1% and 5% $\gamma\text{-Al}_2\text{O}_3$ catalysts (Alfa Aesar) as well as lab-made Pd 5% $\text{La}_2\text{O}_3\text{-MgO}/\gamma\text{-Al}_2\text{O}_3$, were found to be suitable for the MCMR prototype. Based on X-Ray Diffraction (XRD) and pore analyses, sources of deactivation were investigated. For the reforming Ru-based catalyst, pore sintering was a deactivation mechanism, with a phase change from

γ -Al₂O₃ to α -Al₂O₃, and average pore size increasing during MCMR operation. For the combustion catalyst, pore sintering was also found to be the major source of deactivation for the two commercial Pd catalysts, while metal sintering was more important for the lab-made Pd La₂O₃–MgO catalyst.

Kinetic parameters were estimated. For reforming Ru-based catalyst, the pre-exponential factor was similar to that reported by Jakobsen et al. (2010). For combustion, the Pd 1% (Alfa) catalyst activation energy, E_4 , was estimated to be 88 kJ/mol, while the reaction order for methane α was 0.78. The pre-exponential factor for commercial Pd 1% catalyst was about three times smaller than for the commercial and lab-made Pd 5% catalysts tested.

A MCMR prototype was designed, built and tested. Without a membrane, the reforming methane conversion quickly reached equilibrium and the 2-D model predicted adequately the results. With a Pd/Ag membrane, except for the outlet conversion, the model slightly underestimated the conversion. A design fault allowed a portion of the feed to by-pass the reforming channel. Incorporating a by-pass correction factor in the model, the reforming experimental results, for a wide range of flow, pressure and steam-to-carbon ratio conditions, were generally predicted adequately. 87% methane conversion was achieved on the reforming side, and the extracted hydrogen-to-methane feed molar ratio reached 2.94. CO content was estimated at 4 ppm. On the combustion side, the experimental conversions were consistently less than predicted by the models. Even though some methane conversions reached almost 90%, it is suspected that flow distribution and catalyst deactivation were causing the large discrepancies.

Hydrogen yields per mass of catalyst, were between one and two orders of magnitude higher than estimated for two Fluidized Bed Membrane Reactors (FBMRs) and one Packed Bed Membrane Reactor (PBMR) from the literature. The hydrogen yields per reactor volume was about one order of magnitude higher than estimated for the FBMRs, confirming the technical potential for the technology.

9.2 Recommendations

The MCMR concept is promising, producing pure hydrogen in two experimental sets, over a total period exceeding 34 hours. However, scale-up, long-term catalyst

activity, energy efficiency, membrane longevity, and economical viability have yet to be proven. The next steps should be directed towards a pre-commercial prototype, designed to recover the heat, minimize emissions, and operate several months without servicing.

Recommendations are divided in to general and specific ones, the latter extracted from the main document.

9.2.1 General Recommendations

The improvement of the MCMR concept requires a multi-disciplinary approach. Expertise should be sought in:

- Mechanical Engineering: To improve flow distribution in channels, expanding the number of channels, eliminating feed by-passing, designing a heat exchanger to recover products heat, and facilitating the assembly and disassembly;
- Catalysis: To improve stability of the catalysts, in order to maintain high activity for at least several months;
- Materials Engineering: To develop thinner, robust membranes adapted to the MCMR;
- Process Engineering: To recover reforming product gases as a fuel for the combustion channel.

9.2.2 Specific Recommendations

Specific recommendations are summarized as follows:

- Reactor Modeling
 - Include 2nd order terms for heat transfer in the transverse direction. A more powerful simulation software than MATLABTM should be considered, e.g. gPROMsTM or ANSYSTM;
 - Consider adding hydrogen axial dispersion to the model;
 - Conduct 3-D Computational Fluid Dynamics (CFD) flow simulations on the feed distribution, and investigate options to improve the design;

- A catalyst model could be improved to reflect a more realistic pore configuration, as shown in Figure 6.9;
- Review physical properties and equations of state for higher pressure >12 bar;
- Model flow distribution between multiple plates and channels.
- Catalyst Coating
 - Automate the coating process to improve catalyst coating uniformity;
 - Heat treatment for Fecralloy could be optimized. For instance, Jia et al. (2007) showed that oxidation at 900°C created a larger number of alumina whiskers on the surface than oxidation at 1000°C;
 - Optimize coating parameters to reduce the number of clusters on the coating surface, while maintaining adherence, optimal layer structure and active area;
 - Investigate electrostatic-spray-assisted vapour deposition, to reduce the amount of material losses while coating, as suggested by Choy (2003);
 - Consider alternatives to γ -Al₂O₃ as carrier, since phase change to α -Al₂O₃ was observed;
 - Design and build specific equipment to steam at high pressure (>20 bar) carrier plates and pre-reduce the catalyst plates.
- Reforming Catalyst
 - Select and optimize promoter contents;
 - The literature shows advantages of bi-metallic catalysts (Jeong et al., 2006; Zhou et al., 2009). For instance Ni combined with Ru, Rh, or Pt could be tried;
 - Improve experimental procedures to test stability in order to improve the repeatability of the experiments;
 - Perform kinetic estimations at higher pressures.
- MCC
 - A better understanding of CO formation is needed;

- The effect of water should be studied, since the inhibition on the reaction rate is likely (Ciuparu et al., 2001);
- Find better promoters and/or supports to improve the stability of the oxidation catalysts;
- Catalysts, combining Pd with Pt and Rh could be tried.
- MCMR Process
 - Investigate the potential of using the reforming product gas, after water removal, as fuel for the combustion channel. Conversion in the reforming could be optimized in such a way that the exhaust gas would contain enough energy to supply all the heat required, avoiding excessive methane conversion in the reforming channel, while achieving higher overall methane conversion (including the combustion channel);
 - Improve ventilation around the unit to eliminate smoke coming from insulating materials and anti-seize oxidation during start-up;
 - The back pressure regulator on the reforming side was not working properly and pressure was not as stable as it should be. The regulator size may be the issue. It should be changed for future experiments;
 - To test hydrogen permeate impurities, the Gas Chromatograph (GC) should be calibrated for <10 ppm impurities, and a H₂ dedicated sampling line should be installed;
 - Install a better vacuum pump in order to reach lower permeate pressure;
 - A differential pressure transducer should be installed to measure pressure drop in the gas channels.
- MCMR Design (in addition to the General Recommendations above)
 - To enhance the hydrogen flux, use the impermeable region of the membrane as a surface to seat gaskets;
 - Find a way to make the seals resistant to heat cycles.
- Membrane (in addition to the General Recommendations above)
 - Test membrane long term longevity in MCMR;
 - Develop membrane resistant to higher temperatures (>600°C).

References

- Adhikari, S. and Fernando, S. (2006). Hydrogen membrane separation techniques. *Industrial & Engineering Chemistry Research*, 45(3):875–881.
- Adris, A. M., Lim, C. J., and Grace, J. R. (1994). The fluidized bed membrane reactor (FBMR) system: a pilot scale experimental study. *Chemical Engineering Science*, 49:5833–5843.
- Adris, A. M., Pruden, B. B., Lim, C. J., and Grace, J. R. (1996). On the reported attempts to radically improve the performance of the steam reforming reactor. *Canadian Journal of Chemical Engineering*, 74:177–186.
- Agrafiotis, C., Tsetsekou, A., and Ekonomakou, A. (1999). The effect of particle size on the adhesion properties of oxide washcoats on cordierite honeycombs. *Journal of Materials Science Letters*, 18(17):1421–1424.
- Ahmad, Z. K. (2011). Catalytic combustion of methane on commercial palladium based catalysts. Master's thesis, University Of British Columbia.
- Alfadhel, K. and Kothare, M. V. (2005). Modeling of multicomponent concentration profiles in membrane microreactors. *Industrial & Engineering Chemistry Research*, 44(26):9794–9804.
- Ally, J. and Pryor, T. (2007). Life-cycle assessment of diesel, natural gas and hydrogen fuel cell bus transportation systems. *Journal of Power Sources*, 170(2):401.
- American Motor Honda Co. (2012). FCX-Clarity Fuel cell electric vehicle. Accessed on May 24th, 2012, <http://automobiles.honda.com/fcx-clarity/>.
- Arena, B. J. (1992). Deactivation of ruthenium catalysts in continuous glucose hydrogenation. *Applied Catalysis A: General*, 87(2):219 – 229.

- Arzamendi, G., Dieguez, P., Montes, M., Odriozola, J., Sousa-Aguiar, E. F., and Gandia, L. (2009). Methane steam reforming in a microchannel reactor for GTL intensification: A computational fluid dynamics simulation study. *Chemical Engineering Journal*, 154(1-3):168 – 173.
- Babicki, M. and Hall, A. (2003). PSA technology hits the fast lane. *Chemical Processing*.
- Baratti, R., Tronci, S., Zafir, M., and Graviilidis, A. (2003). Optimal catalyst distribution in catalytic plate reactors. *International Journal of Chemical Reactor Engineering*, 1:A58.
- Barbieri, G., Brunetti, A., Tricoli, G., and Drioli, E. (2008). An innovative configuration of a Pd-based membrane reactor for the production of pure hydrogen: Experimental analysis of water gas shift. *Journal of Power Sources*, 182(1):160 – 167.
- Barbieri, G., Violante, V., Maio, F. P. D., Criscuoli, A., and Drioli, E. (1997). Methane steam reforming analysis in a palladium-based catalytic membrane reactor. *Industrial & Engineering Chemistry Research*, 36:3369–3374.
- Basile, A., Gallucci, F., Iulianelli, A., and Tosti, S. (2008). Co-free hydrogen production by ethanol steam reforming in a Pd-Ag membrane reactor. *Fuel Cells*, 8(1):62–68.
- Basile, A., Gallucci, F., and Paturzo, L. (2005). Hydrogen production from methanol by oxidative steam reforming carried out in a membrane reactor. *Catalysis Today*, 104:251–259.
- Berman, A., Karn, R. K., and Epstein, M. (2005). Kinetics of steam reforming of methane on Ru/Al₂O₃ catalyst promoted with mn oxides. *Applied Catalysis A: General*, 282(1-2):73–83.
- Berndt, C. C. and Lin, C. K. (1993). Measurement of adhesion for thermally sprayed materials. *Journal of Adhesion Science and Technologies*, 7(12):1235–1264.
- Besra, L. and Liu, M. (2007). A review on fundamentals and applications of electrophoretic deposition (EPD). *Progress in Materials Science*, 52(1):1–61.
- Bird, R., Stewart, W., and Lightfoot, E. (2002). *Transport Phenomena*. John Wiley & Sons, New York, 2nd edition.

- Boyd, D. A. (2007). *Internally circulating fluidized bed membrane reactor for high-purity hydrogen production*. PhD thesis, University of British Columbia, Vancouver, BC.
- Boyd, T., Grace, J. R., Lim, J. C., and Adris, A. M. (2005). Hydrogen from an internally circulating fluidized bed membrane reactor. *International Journal of Chemical Reactor Engineering*, 3(A58).
- Bozo, C., Guilhaume, N., Garbowski, E., and Primet, M. (2000). Combustion of methane on CeO₂–ZrO₂ based catalysts. *Catalysis Today*, 59:33–45.
- Brinker, J. C. and Scherer, G. W. (1990). *Sol-gel science: the physics and chemistry of sol-gel processing*. Academic Press, San Diego, CA.
- California Fuel Cell Partnership (2012). Department of Energy Targets. Accessed on May 25th 2012, <http://cafcp.org/progress/technology/doetargets>.
- Carberry, J. J., Dudokovic, M. P., Froment, G. F., Grace, J. R., Hendrix, C. D., Kenney, C. N., Mears, D. E., and Shah, Y. T. (1987). *A Practical Guide to Catalyst Testing*. Number 4186TE. Catalytica, Mountain View, CA.
- Chalker, P. R., Bull, S. J., and Rickerby, D. S. (1991). A review of the methods for the evaluation of coating-substrate adhesion. *Materials Science and Engineering*, A 140:583–592.
- Chang, H.-F., Pai, W.-J., Chen, Y.-J., and Lin, W.-H. (2010). Autothermal reforming of methane for producing high-purity hydrogen in a Pd/Ag membrane reactor. *International Journal of Hydrogen Energy*, 35(23):12986 – 12992.
- Chauhan, S., Kumar, D., and Srivastava, V. K. (2009). Modeling catalytic combustion of methane during the warm-up period of the converter. *Chemical Product and Process Modeling*, 4(1):Article 44.
- Chen, Y., Wang, Y., Xu, H., and Xiong, G. (2007a). Integrated one-step PEMFC-grade hydrogen production from liquid hydrocarbons using Pd membrane reactor. *Industrial & Engineering Chemistry Research*, 46(17):5510–5515.
- Chen, Z. and Elnashaie, S. (2004). Steady-state modeling and bifurcation behavior of circulating fluidized bed membrane reformer/regenerator for the production of hydrogen for fuel cells from heptane. *Chemical Engineering Science*, 59:3965–3979.

- Chen, Z., Grace, J. R., Lim, C. J., and Li, A. (2007b). Experimental studies of pure hydrogen production in a commercialized fluidized-bed membrane reactor with SMR and ATR catalysts. *International Journal of Hydrogen Energy*, 32:2359–2366.
- Chen, Z., Yan, Y., and Elnashaie, S. S. (2003). Novel circulating fast fluidized-bed membrane reformer for efficient production of hydrogen from steam reforming of methane. *Chemical Engineering Science*, 58(19):4335–4349.
- Cheng, Y., Pena, M., and Yeung, K. (2009). Hydrogen production from partial oxidation of methane in a membrane reactor. *Journal of the Taiwan Institute of Chemical Engineers*, 40(3):281 – 288.
- Choy, K. L. (2003). Chemical vapour deposition of coatings. *Progress in Materials Science*, 48(2):57–170.
- Choy, K. L. and Seh, H.-K. (2000). Fabrication of Ni–Al₂O₃-based reforming catalyst using flame-assisted vapour deposition. *Materials Science and Engineering A: Structural Materials: Properties, Microstructure and Processing*, 281(1-2):253–258.
- Cini, P., Blaha, S. R., Harold, M. P., and Venkataraman, K. (1991). Preparation and characterization of modified tubular ceramic membranes for use as catalyst supports. *Journal of Membrane Science*, 55(1-2):199–225.
- Ciuparu, D., Katsikis, N., and Pfefferle, L. (2001). Temperature and time dependence of the water inhibition effect on supported palladium catalyst for methane combustion. *Applied Catalysis A: General*, 216:209 – 215.
- CNW (2010). Number of gas stations in Canada continues to decline. Accessed on May 31st, 2012, <http://www.newswire.ca/en/story/763099/number-of-gas-stations-in-canada-continues-to-decline>.
- Colella, W. G., Jacobson, M. Z., and Golden, D. M. (2005). Switching to a U.S. hydrogen fuel cell vehicle fleet: The resultant change in emissions, energy use, and greenhouse gases. *Journal of Power Sources*, 150(2005):150–181.
- Colussi, S., Gayen, A., Camellone, M. F., Boaro, M., Llorca, J., Fabris, S., and Trovarelli, A. (2009). Nanofaceted Pd-O sites in Pd-Ce surface superstructures: Enhanced activity in catalytic combustion of methane. *Heterogeneous Catalysis*, 48:8481 – 8484.

- Coronel, L., Munera, J., Lombardo, E., and Cornaglia, L. (2011). Pd based membrane reactor for ultra pure hydrogen production through the dry reforming of methane. experimental and modeling studies. *Applied Catalysis A: General*, 400(1-2):185 – 194.
- Cristiani, C., Valentini, M., Merazzi, M., Neglia, S., and Forzatti, P. (2005). Effect of ageing time on chemical and rheological evolution in γ -Al₂O₃ slurries for dip-coating. *Catalysis Today*, 105(3-4):492–498.
- Damle, A., Richardson, C., Powers, T., Love, C., and Acquaviva, J. (2008). Demonstration of a pilot-scale membrane reactor process for hydrogen production. *ECS Transactions*, 12(1):499–510.
- Damle, A. S. (2009). Hydrogen production by reforming of liquid hydrocarbons in a membrane reactor for portable power generation - experimental studies. *Journal of Power Sources*, 186(1):167 – 177.
- Davis, M. and Davis, R. (2003). *Fundamentals of Chemical Reaction Engineering*. McGraw-Hill, New York.
- De Falco, M., Salladini, A., and Iaquaniello, G. (2011). Reformer and membrane modules for methane conversion: Experimental assessment and perspectives of an innovative architecture. *ChemSusChem*, 4(8):1157–1165.
- Deshmukh, S., Heinrich, S., Mörl, L., van, M. S., and Kuipers, J. (2007). Membrane assisted fluidized bed reactors: Potentials and hurdles. *Chemical Engineering Science*, 62(1-2):416–436.
- Deshpande, K., Meldon, J. H., Schmidt, M. A., and Jensen, K. F. (2010). SOI-supported microdevice for hydrogen purification using palladium-silver membranes. *Journal of Microelectromechanical Systems*, 19(2):402–409.
- Dincer, I. (2007). Environmental and sustainability aspects of hydrogen and fuel cell systems. *International Journal of Energy Research*, 31:29–55.
- Earth System Research Laboratory (2012). Trends in atmospheric carbon dioxide. U.S. Department of Commerce - National Oceanic and Atmospheric Administration - Global Monitoring Division, Accessed on June 12th, 2012, http://www.esrl.noaa.gov/gmd/ccgg/trends/mlo_data.
- eBullion Guide (2012). Ruthenium price history - Ruthenium price chart for the last 30 days. Accessed: May 8th 2012, <http://www.ebullionguide.com/price-chart-ruthenium-last-30-days.aspx>.

- Elnashaie, S. and Adris, A. (1989). Fluidized bed steam reformer for methane. In J.R. Grace, L. S. and Bergougnou, M., editors, *Fluidization VI*, pages 319–326. Engineering Foundation, New York.
- Elnashaie, S. S., Adris, A. M., Al-Ubaid, A. S., and Soliman, M. A. (1990). On the non-monotonic behaviour of methane-steam reforming kinetics. *Chemical Engineering Science*, 45(2):491–501.
- Elnashaie, S. S. and Garhyan, P. (2003). *Conservation Equations and Modeling of Chemical and Biochemical Processes*. Marcel Dekker, New York.
- Enger, B. C., Walmsley, J., Bjorgum, E., Lodeng, R., Pfeifer, P., Schubert, K., Holmen, A., and Venvik, H. J. (2008). Performance and SEM characterization of Rh impregnated microchannel reactors in the catalytic partial oxidation of methane and propane. *Chemical Engineering Journal*, 144(3):489 – 501.
- Environment Canada (2012). National Inventory Report 1990-2010: Executive Summary. Technical report, Government of Canada, Minister of the Environment.
- Farrauto, R. J. and Bartholomew, C. H. (1997). *Fundamentals of Industrial Catalytic Processes*. Blackie Academic & Professional, London.
- Ferrari, B., Sanchez-Herencia, A. J., and Moreno, R. (2006). Nickel-alumina graded coatings obtained by dipping and EPD on nickel substrates. *Journal of the European Ceramic Society*, 26(12):2205–2212.
- Ferreira-Aparicio, P. and Benito, M. J. (2005). New trends in reforming technologies: from hydrogen industrial plants to multifuel microreformers. *Catalysis Reviews - Science and Engineering*, 47:491–588.
- Fogler, H. S. (2004). *Elements of Chemical Reaction Engineering*. Prentice-Hall, Upper Saddle River, NJ, 4th edition.
- Franz, A. J., Jensen, K. F., and Schmidt, M. A. (2000). Palladium membrane microreactors. In W, E., editor, *3rd International Conference on Microreaction Technology, New Orleans, LA, April 18-21, 1999*, pages 267–276.
- Frauhammer, J., Eigenberger, G., Hippel, L., and Arntz, D. (1999). A new reactor concept for endothermic high-temperature reactions. *Chemical Engineering Science*, 54(15-16):3661 – 3670.
- Fuelcells.org (2012a). U.S. Hydrogen Fuelling Stations. Accessed on May 31st, 2012, from <http://www.fuelcells.org/resources/charts/>.

- Fuelcells.org (2012b). Worldwide Hydrogen Fueling Stations. Accessed on May 31st, 2012, from <http://www.fuelcells.org/resources/charts/>.
- Galuszka, J., Pandey, R., and Ahmed, S. (1998). Methane conversion to syngas in a palladium membrane reactor. *Catalysis Today*, 46(2-3):83 – 89.
- Gao, D., Zhang, C., Wang, S., Yuan, Z., and Wang, S. (2008). Catalytic activity of Pd/Al₂O₃ toward the combustion of methane. *Catalysis Communications*, 9(15):2583–2587.
- Germani, G., Stefanescu, A., Schuurman, Y., and van Veen, A. C. (2007). Preparation and characterization of porous alumina-based catalyst coatings in microchannels. *Chemical Engineering Science*, 62(18-20):5084.
- Gielens, F., Tong, H., Vorstman, M., and Keurentjes, J. (2007). Measurement and modeling of hydrogen transport through high-flux Pd membranes. *Journal of Membrane Science*, 289(1-2):15–25.
- Gitzen, W. H., editor (1970). *Alumina as a Ceramic Material*. American Ceramic Society, Columbus, Ohio.
- Goto, S., Tagawa, T., Assabumrungrat, S., and Praserthdam, P. (2003). Simulation of membrane microreactor for fuel cell with methane feed. *Catalysis Today*, 82(1-4):223 – 232.
- Grace, J. R., Elnashaie, S. S., and Lim, C. J. (2005). Hydrogen production in fluidized beds with in-situ membranes. *International Journal of Chemical Reactor Engineering*, 3:Article A41.
- Granovskii, M., Dincer, I., and Rosen, M. A. (2006). Life cycle assessment of hydrogen fuel cell and gasoline vehicles. *International Journal of Hydrogen Energy*, 31(3):337.
- Groppi, G., Ibashi, W., Valentini, M., and Forzatti, P. (2001). High-temperature combustion of CH₄ over PdO/Al₂O₃: kinetic measurements in a structured annular reactor. *Chemical Engineering Science*, 56(3):831.
- Guo, J., Lou, H., Zhao, H., Wang, X., and Zheng, X. (2004). Novel synthesis of high surface area MgAl₂O₄ spinel as catalyst support. *Materials Letters*, 58:1920–1923.
- Haldor Topsøe (2009). Topsøe HTCR Compact Hydrogen Units. Commercial brochure, Kongens Lyngby, Denmark.

- Harale, A., Hwang, H. T., Liu, P. K., Sahimi, M., and Tsotsis, T. T. (2010). Design aspects of the cyclic hybrid adsorbent-membrane reactor (HAMR) system for hydrogen production. *Chemical Engineering Science*, 65(1):427–435.
- Hawthorne, H., Neville, A., Troczynski, T., Hu, X., Thammachart, M., Xie, Y., Fu, J., and Yang, Q. (2004). Characterization of chemically bonded composite sol-gel based alumina coatings on steel substrates. *Surface and Coatings Technology*, 176(2):243 – 252.
- Hellman, A., Resta, A., Martin, N. M., Gustafson, J., Trincherro, A., Carlsson, P.-A., Balmes, O., Felici, R., van Rijn, R., Frenken, J. W. M., Andersen, J. N., Lundgren, E., and Grönbeck, H. (2012). The active phase of palladium during methane oxidation. *The Journal of Physical Chemistry Letters*, 3:678–682.
- Hwang, K.-R., Ryi, S.-K., Lee, C.-B., Lee, S.-W., and Park, J.-S. (2011). Simplified, plate-type Pd membrane module for hydrogen purification. *International Journal of Hydrogen Energy*, 36(16):10136 – 10140.
- IHS Chemical (2003). Small-Scale Hydrogen Production.
- Intergovernmental Panel on Climate Change (2007). Climate Change 2007: Synthesis Report. Technical report, Geneva, Switzerland.
- International Energy Agency (2007). IEA Energy Technology Essentials - Hydrogen Production & Distribution. Technical report.
- Ismagilov, Z., Podyacheva, O., Solonenko, O., Pushkarev, V., Kuz'min, V., Ushakov, V., and Rudina, N. (1999). Application of plasma spraying in the preparation of metal-supported catalysts. *Catalysis Today*, 51:411 – 417.
- Iulianelli, A., Liguori, S., Longo, T., Tosti, S., Pinacci, P., and Basile, A. (2010). An experimental study on bio-ethanol steam reforming in a catalytic membrane reactor. part II: Reaction pressure, sweep factor and WHSV effects. *International Journal of Hydrogen Energy*, 35(7):3159–3164.
- Jakobsen, J. G., Jorgensen, T. L., Chorkendorff, I., and Sehested, J. (2010). Steam and CO₂ reforming of methane over a Ru/ZrO₂ catalyst. *Applied Catalysis A: General*, 377(1-2):158–166.
- Jeong, J. H., Lee, J. W., Seo, D. J., Seo, Y., Yoon, W. L., Lee, D. K., and Kim, D. H. (2006). Ru-doped Ni catalysts effective for the steam reforming of methane without the pre-reduction treatment with H₂. *Applied Catalysis A: General*, 302(2):151–156.

- Jia, J., Zhou, J., Zhang, J., Yuan, Z., and Wang, S. (2007). The influence of preparative parameters on the adhesion of alumina washcoats deposited on metallic supports. *Applied Surface Science*, 253:9099–9104.
- Kanuri, S. (2011). Energy Reinvented - Presentation on Stationary Fuel Cells - UTC Power. Accessed on June 1st, 2012, <http://www.fuelcellseminar.com/media/9000/hrd33b-1%20kanuri.pdf>.
- Karakaya, M. and Avci, A. K. (2011). Microchannel reactor modeling for combustion driven reforming of iso-octane. *International Journal of Hydrogen Energy*, 36:6569 – 6577.
- Karnik, S., Hatalis, M., and Kothare, M. (2003). Towards a palladium micro-membrane for the water gas shift reaction: microfabrication approach and hydrogen purification results. *Journal of Microelectromechanical Systems*, 12(1):93 – 100.
- Keurentjes, J. T. F., Gielens, F. C., Tong, H. D., van Rijn, C. J. M., and Vorstman, M. A. G. (2004). High-flux palladium membranes based on microsystem technology. *Industrial & Engineering Chemistry Research*, 43:4768–4772.
- Kikuchi, E. (2000). Membrane reactor application to hydrogen production. *Catalysis T*, 56:97–101.
- Kolios, G., Frauhammer, J., and Eigenberger, G. (2002). Efficient reactor concepts for coupling of endothermic and exothermic reactions. *Chemical Engineering Science*, 57:1505 – 1510.
- Kolios, G., Gritsch, A., Glockler, B., Sorescu, G., and Frauhammer, J. (2004). Novel reactor concepts for thermally efficient methane steam reforming: Modeling and simulation. *Industrial & Engineering Chemistry Research*, 43(16):4796–4808.
- Kusakabe, K., Mizoguchi, H., and Eda, T. (2006). Methane steam reforming in a zirconia membrane reactor. *Journal of Chemical Engineering of Japan*, 39(4):444–447.
- Laosiripojana, N. and Assabumrungrat, S. (2005). Methane steam reforming over Ni/CeZrO₂ catalyst: Influences of CeZrO₂ support on reactivity, resistance toward carbon formation, and intrinsic reaction kinetics. *Applied Catalysis A: General*, 290(2005):200–211.
- Lee, J. H. and Trimm, D. L. (1995). Catalytic combustion of methane. *Fuel Processing Technology*, 42(2-3):339–359.

- Li, H., Guo, Y., Zhou, L., Chen, J., Sakurai, M., and Kameyama, H. (2009). Plate-type anodic alumina supported ruthenium catalysts for steam reforming of kerosene: Influence of calcination on catalysts reactivity. *Journal of Chemical Engineering of Japan*, 42(12):937–943.
- Lide, D. R., editor (2004). *CRC Handbook of Chemistry and Physics*. CRC Press, Boca Raton, FL, 85th ed edition.
- Lin, W.-H., Hsiao, C.-S., and Chang, H.-F. (2008). Effect of oxygen addition on the hydrogen production from ethanol steam reforming in a Pd-Ag membrane reactor. *Journal of Membrane Science*, 322(2):360 – 367.
- Linde Group (2012). Hydrogen recovery by pressure swing adsorption. Accessed on June 1st, 2012, http://www.linde-engineering.com/en/process_plants/adsorption_plants/hydrogen_recovery_by_pressure_swing_adsorption/index.html.
- Liu, C.-J., Vissokov, G. P., and Jang, B. W.-L. (2002). Catalyst preparation using plasma technologies. *Catalysis Today*, 72:173 – 184.
- Lyubovsky, M. and Pfefferle, L. (1999). Complete methane oxidation over Pd catalyst supported on α -alumina. influence of temperature and oxygen pressure on the catalyst activity. *Catalysis Today* 47, 47:29–44.
- MacLean, H. L. and Lave, L. B. (2003). Evaluating automobile fuel/propulsion system technologies. *Progress in Energy and Combustion Science*, 29(1):1–69.
- Mahecha-Botero, A., Boyd, T., Grace, J. R., Lim, C. J., Gulamhusein, A., Wan, B., Kurokawa, H., and Shirasaki, Y. (2011a). In-situ CO₂ capture in a pilot-scale fluidized-bed membrane reformer for ultra-pure hydrogen production. *International Journal of Hydrogen Energy*, 36(6):4038 – 4055.
- Mahecha-Botero, A., Boyd, T., Gulamhusein, A., Comyn, N., Lim, C. J., Grace, J. R., Shirasaki, Y., and Yasuda, I. (2008). Pure hydrogen generation in a fluidized-bed membrane reactor: Experimental findings. *Chemical Engineering Science*, 63(10):2752 – 2762.
- Mahecha-Botero, A., Boyd, T., Gulamhusein, A., Grace, J. R., Lim, J., Shirasaki, Y., Kurokawa, H., and Yasuda, I. (2011b). Catalytic reforming of natural gas for hydrogen production in a pilot fluidized-bed membrane reactor: Mapping of operating and feed conditions. *International Journal of Hydrogen Energy*, 17:10727–10736.

- Mahecha-Botero, A., Grace, J. R., Lim, C. J., Elnashaie, S., Boyd, T., and Gulamhusein, A. (2009). Pure hydrogen generation in a fluidized bed membrane reactor: Application of the generalized comprehensive reactor model. *Chemical Engineering Science*, 64(17):3826 – 3846.
- Meille, V. (2006). Review on methods to deposit catalysts on structured surfaces. *Applied Catalysis A: General*, 2006(315):1–17.
- Meille, V., Pallier, S., Bustamante, G. V. S. C., Roumanie, M., and Reymond, J.-P. (2005). Deposition of γ -Al₂O₃ layers on structured supports for the design of new catalytic reactors. *Applied Catalysis A: General*, 286(2):232–238.
- Mishra, A. and Prasad, R. (2011). A review on preferential oxidation of carbon monoxide in hydrogen rich gases. *Bulletin of Chemical Reaction Engineering & Catalysis*, 6(1):1–14.
- Mori, N., Nakamura, T., Sakai, O., Iwamoto, Y., and Hattori, T. (2008). CO-free hydrogen production by membrane reactor equipped with CO methanator. *Industrial & Engineering Chemistry Research*, 47(5):1421–1426.
- Naqvi, S. (2007). Hydrogen production. PEP Report 32C, SRI Consulting, Menlo Park, CA.
- National Academy of Engineering (2004). The hydrogen economy: Opportunities, costs, barriers, and R&D needs. Technical Report ISBN 0-309-09163-2, National Research Council.
- National Research Council (2008). Transitions to Alternative Transportation Technologies - A Focus on Hydrogen. Technical report, Washington, D.C.
- Nielsen, J. R. and Hansen, J. (1993). CO₂-reforming of methane over transition metals. *Journal of Catalysis*, 144(1):38 – 49.
- Nomura, M., Seshimo, M., Aida, H., Nakatani, K., Gopalakrishnan, S., Sugawara, T., Ishikawa, T., Kawamura, M., and ichi Nakao, S. (2006). Preparation of a catalyst composite silica membrane reactor for steam reforming reaction by using a counterdiffusion CVD method. *Industrial & Engineering Chemistry Research*, 45:3950–3954.
- O’Connell, M., Kolb, G., Schelhaas, K.-P., Wichert, M., Tiemann, D., Pennemann, H., and Zapf, R. (2011). Towards mass production of microstructured fuel processors for application in future distributed energy generation systems: A review of recent progress at IMM. *Chemical Engineering Research and Design*, 90(1):11–18.

- Ogden, J. (2001). Review of small stationary reformers for hydrogen production. Technical Report 64, Center for Energy and Environmental Studies, Princeton University.
- Ozawa, Y., Tochihara, Y., Nagai, M., and Omi, S. (2003). PdO/Al₂O₃ in catalytic combustion of methane: stabilization and deactivation. *Chemical Engineering Science*, 58:671 – 677.
- Papadias, D. D., Lee, S. H., Ferrandon, M., and Ahmed, S. (2010). An analytical and experimental investigation of high-pressure catalytic steam reforming of ethanol in a hydrogen selective membrane reactor. *International Journal of Hydrogen Energy*, 35(5):2004 – 2017.
- Park, G.-G., Yim, S.-D., Yoon, Y.-G., Lee, W.-Y., Kim, C.-S., Seo, D.-J., and Eguchi, K. (2005). Hydrogen production with integrated microchannel fuel processor for portable fuel cell systems. *Journal of Power Sources*, 145(2):702 – 706.
- Park, S.-J., Lee, D.-W., Yu, C.-Y., Lee, K.-Y., and Lee, K.-H. (2008). Hydrogen production from a DME reforming-membrane reactor using stainless steel-supported Knudsen membranes with high permeability. *Journal of Membrane Science*, 318(1-2):123 – 128.
- Patil, C. S., van Sint Annaland, M., and Kuipers, J. (2007). Fluidised bed membrane reactor for ultrapure hydrogen production via methane steam reforming: Experimental demonstration and model validation. *Chemical Engineering Science*, 62(11):2989 – 3007.
- Peela, N. R., Mubayi, A., and Kunzru, D. (2009). Washcoating of γ -alumina on stainless steel microchannels. *Catalysis Today*, 147:S17–S23.
- Poling, B. E., Prausnitz, J. M., and O'Connell, J. P. (2000). *The Properties of Gases and Liquids*. McGraw-Hill, New York, 5th edition.
- Pourbaix, M. (1974). *Atlas of electrochemical equilibria in aqueous solutions*. National Association of Corrosion Engineers.
- Rakib, M. A. and Alhumaizi, K. I. (2005). Modeling of a fluidized bed membrane reactor for the steam reforming of methane: Advantages of oxygen addition for favorable hydrogen production. *Energy & Fuels*, 19:2129–2139.
- Rakib, M. A., Grace, J. R., Lim, C. J., and Elnashaie, S. S. (2011). Modeling of a fluidized bed membrane reactor for hydrogen production by steam reforming of

hydrocarbons. *Industrial & Engineering Chemistry Research*, 50(6):3110–3129.

REB Research (2012). REBresearch Me100 Hydrogen Generator. Accessed on May 30th, 2012, http://www.rebresearch.com/hydrogen_generators.html.

Rebrov, E. V., Schouten, J. C., and de Croon, M. H. (2011). Single-phase fluid flow distribution and heat transfer in microstructured reactors. *Chemical Engineering Science*, 66(7):1374 – 1393.

Reyes, S. and Jensen, K. F. (1986). Percolation concepts in modelling of gas-solid reactions-II. application to char gasification in the diffusion regime. *Chemical Engineering Science*, 41(2):345 – 354.

Ryi, S.-K., Li, A., Lim, C. J., and Grace, J. R. (2011). Novel non-alloy Ru/Pd composite membrane fabricated by electroless plating for hydrogen separation. *International Journal of Hydrogen Energy*, 36(15):9335 – 9340.

Ryi, S. K., Park, J. S., Cho, S. H., and Kim, S. H. (2006a). Fast start-up of microchannel fuel processor integrated with an igniter for hydrogen combustion. *Journal of Power Sources*, 161(2):1234 – 1240.

Ryi, S.-K., Park, J.-S., Kim, S.-H., Cho, S.-H., Kim, D.-W., and Um, K.-Y. (2006b). Characterization of Pd–Cu–Ni ternary alloy membrane prepared by magnetron sputtering and Cu-reflow on porous nickel support for hydrogen separation. *Separation and Purification Technology*, 50:82–91.

SAE International (2011). Hydrogen fuel quality for fuel cell vehicles. Standard J2719 SEP2011.

Sandler, S. (1999). *Chemical and Engineering Thermodynamics*. John Wiley & Sons, New York, 3rd edition.

Schäfer, A., Heywood, J. B., and Weiss, M. A. (2006). Future fuel cell and internal combustion engine automobile technologies: A 25-year life cycle and fleet impact assessment. *Energy*, 31(12):2064–2087.

Schaper, H., Doesburg, E., and Reijen, L. V. (1983). The influence of lanthanum oxide on the thermal stability of gamma alumina catalyst supports. *Applied Catalysis*, 7:211–220.

Seris, E., Abramowitz, G., Johnston, A., and Haynes, B. (2008). Scaleable, microstructured plant for steam reforming of methane. *Chemical Engineering Journal*, 135, Supplement 1(0):S9 – S16.

- Seshan, K., editor (2002). *Handbook of Thin-Film Deposition Processes and Techniques*. Noyes Publications, Norwich, NY.
- Sherwood, T. K., Pigford, R. L., and Wilke, C. R. (1975). *Mass Transfer*. McGraw-Hill, New York.
- Shigarov, A. B., Fadeev, S. I., and Kirillov, V. A. (2009). Modeling of a heat-integrated catalytic reformer/combustor of methane: Fine balancing between hot spots and extinction. *Chemical Engineering & Technology*, 32(9):1367–1375.
- Sidwell, R. W., Zhu, H., Kibler, B. A., Kee, R. J., and Wickham, D. T. (2003). Experimental investigation of the activity and thermal stability of hexaaluminate catalysts for lean methane-air combustion. *Applied Catalysis A: General*, 255(2):279–288.
- Simakov, D. S. A. and Sheintuch, M. (2009). Demonstration of a scaled-down autothermal membrane methane reformer for hydrogen generation. *International Journal of Hydrogen Energy*, 34(21):8866–8876.
- Simsek, E., Avci, A. K., and Önsan, Z. I. (2011). Investigation of catalyst performance and microstructured reactor configuration for syngas production by methane steam reforming. *Catalysis Today*, 178:157–163.
- Sohn, J. M., Byun, Y. C., Cho, J. Y., Choe, J., and Song, K. H. (2007). Development of the integrated methanol fuel processor using micro-channel patterned devices and its performance for steam reforming of methanol. *International Journal of Hydrogen Energy*, 32(18):5103 – 5108.
- SRI Consulting (2010). Hydrogen. Technical report.
- Stefanescu, A., van Veen, A. C., Mirodatos, C., Beziat, J. C., and Duval-Brunel, E. (2007). Wall coating optimization for microchannel reactors. *Catalysis Today*, 125(1-2):16–23.
- Su, C., Jin, T., and Kuraoka, K. (2005). Thin palladium film supported on SiO₂-modified porous stainless steel for a high-hydrogen-flux membrane. *Industrial & Engineering Chemistry Research*, 44:3053–3058.
- Terribile, D., Trovarelli, A., de Leitenburg, C., Primavera, A., and Dolcetti, G. (1999). Catalytic combustion of hydrocarbons with Mn and Cu-doped ceria-zirconia solid solutions. *Catalysis Today*, 47:133–140.

- Thaicharoensutcharittham, S., Meeyoo, V., Kitiyanan, B., Rangsunvigit, P., and Rirkosomboon, T. (2009). Catalytic combustion of methane over NiO/Ce_{0.75}Zr_{0.25}O₂ catalyst. *Catalysis Communications*, 10(5):673–677.
- Thybo, S., ren Jensen, S., Johansen, J., Johannessen, T., Hansen, O., and Quaade, U. J. (2004). Flame spray deposition of porous catalysts on surfaces and in microsystems. *Journal of Catalysis*, 223(2):271–277.
- Tong, J. and Matsumura, Y. (2006). Pure hydrogen production by methane steam reforming with hydrogen-permeable membrane reactor. *Catalysis Today*, 111:147–152.
- Tong, J., Matsumura, Y., Suda, H., and Haraya, K. (2005). Experimental study of steam reforming of methane in a thin (6 μm) Pd-based membrane reactor. *Industrial & Engineering Chemistry Research*, 44(5):1454–1465.
- Tonkovich, A., Kuhlmann, D., Rogers, A., McDaniel, J., Fitzgerald, S., Arora, R., and Yuschak, T. (2005). Microchannel technology scale-up to commercial capacity. *Chemical Engineering Research and Design*, 83(6):634 – 639.
- Tonkovich, A., Perry, S., Wang, Y., Qiu, D., LaPlante, T., and Rogers, W. (2004). Microchannel process technology for compact methane steam reforming. *Chemical Engineering Science*, 59(22-23):4819 – 4824.
- Tonkovich, A. L. Y., Yang, B., Perry, S. T., Fitzgerald, S. P., and Wang, Y. (2007). From seconds to milliseconds to microseconds through tailored microchannel reactor design of a steam methane reformer. *Catalysis Today*, 120(1):21 – 29.
- Tosti, S., Borgognoni, F., and Santucci, A. (2010). Multi-tube Pd-Ag membrane reactor for pure hydrogen production. *International Journal of Hydrogen Energy*, 35(20):11470 – 11477.
- Tsuru, T., Morita, T., Shintani, H., Yoshioka, T., and Asaeda, M. (2008). Membrane reactor performance of steam reforming of methane using hydrogen-permselective catalytic SiO₂ membranes. *Journal of Membrane Science*, 316(1-2):53 – 62.
- Tsuru, T., Shintani, H., Yoshioka, T., and Asaeda, M. (2006). A bimodal catalytic membrane having a hydrogen-permselective silica layer on a bimodal catalytic support: Preparation and application to the steam reforming of methane. *Applied Catalysis A: General*, 302:78–85.

- Tsuru, T., Yamaguchi, K., Yoshioka, T., and Asaeda, M. (2004). Methane steam reforming by microporous catalytic membrane reactors. *Separations*, 59(11):2794–2805.
- Twigg, M. V., editor (1997). *Catalyst Handbook*. Manson Publishing, London, UK, 2nd edition.
- UTC Power (2012). Purecell model 400. Accessed on June 2nd, 2012, <http://www.utcpower.com/products/purecell400>.
- Vaccaro, S., Malangoney, L., and Ciambelliz, P. (2010). Modelling of a catalytic micro-reactor coupling endothermic methane reforming and combustion. *International Journal of Chemical Reactor Engineering*, 8:Article A51.
- Valentini, M., Groppi, G., Cristiani, C., Levi, M., Tronconi, E., and Forzatti, P. (2001). The deposition of $\gamma\text{-Al}_2\text{O}_3$ layers on ceramic and metallic supports for the preparation of structured catalysts. *Catalysis Today*, 69(1-4):307–314.
- Varady, M. J., McLeod, L., Meacham, J. M., Degertekin, F. L., and Fedorov, A. G. (2007). An integrated MEMS infrastructure for fuel processing: hydrogen generation and separation for portable power generation. *Journal of Micromechanics and Microengineering*, 17:S257–S264.
- Venkataraman, K., Wanat, E. C., and Schmidt, L. D. (2003). Steam reforming of methane and water-gas shift in catalytic wall reactors. *American Institute of Chemical Engineers Journal*, 49(5):1277–1284.
- Waldron, W. and Sircar, S. (2000). Parametric study of a pressure swing adsorption process. *Adsorption*, 6:179–188.
- Wang, G., Ogden, J. M., and Sperling, D. (2008). Comparing air quality impacts of hydrogen and gasoline. *Transportation Research Part D: Transport and Environment*, 13(7):436 – 448.
- Wei, J. and Iglesia, E. (2004). Reaction pathways and site requirements for the activation and chemical conversion of methane on Ru-based catalysts. *Journal of Physical Chemistry B*, 108(22):7262.
- Wilhite, B. A., Schmidt, M. A., and Jensen, K. F. (2004). Palladium-based micromembranes for hydrogen separation: Device performance and chemical stability. *Industrial & Engineering Chemistry Research*, 43:7083–7091.
- Wilhite, B. A., Weiss, S. E., Ying, J. Y., Schmidt, M. A., and Jensen, K. F. (2006). High-purity hydrogen generation in a microfabricated 23 wt% Ag-Pd

membrane device integrated with 8:1 LaNi_{0.95}Co_{0.05}O₃/Al₂O₃ catalyst. *Advanced Materials*, 18(13):1701–1704.

Xebec Absorption (2012). H₂solutions - hydrogen purification. Commercial brochure. Accessed on June 1st, 2012, http://www.xebecinc.com/pdf/e_H2X_brochure.pdf.

Xu, J. and Froment, G. F. (1989). Methane steam reforming, methanation and water-gas shift. I. intrinsic kinetics. *AIChE Journal*, 35(1):88–96.

Yu, C.-Y., Lee, D.-W., Park, S.-J., Lee, K.-Y., and Lee, K.-H. (2009). Study on a catalytic membrane reactor for hydrogen production from ethanol steam reforming. *International Journal of Hydrogen Energy*, 34(7):2947 – 2954.

Yuan, J., Ren, F., and Sunden, B. (2007). Analysis of chemical-reaction-coupled mass and heat transport phenomena in a methane reformer duct for PEMFCs. *International Journal of Heat and Mass Transfer*, 50(3-4):687 – 701.

Zanfir, M. and Gavriilidis, A. (2002). Parametric sensitivity in catalytic plate reactors with first-order endothermic-exothermic reactions. *Chemical Engineering Journal*, 86(3):277 – 286.

Zanfir, M. and Gavriilidis, A. (2003). Catalytic combustion assisted methane steam reforming in a catalytic plate reactor. *Chemical Engineering Science*, 58(17):3947 – 3960.

Zanfir, M. and Gavriilidis, A. (2004). Influence of flow arrangement in catalytic plate reactors for methane steam reforming. *Chemical Engineering Research and Design*, 82(2):252 – 258.

Zhai, X., Ding, S., Cheng, Y., Jin, Y., and Cheng, Y. (2010). CFD simulation with detailed chemistry of steam reforming of methane for hydrogen production in an integrated micro-reactor. *International Journal of Hydrogen Energy*, 35(11):5383 – 5392.

Zhang, X., Hu, H., Zhu, Y., and Zhu, S. (2006). Methanol steam reforming to hydrogen in a carbon membrane reactor system. *Industrial & Engineering Chemistry Research*, 45(24):7997–8001.

Zhou, L., Guo, Y., Sakurai, M., and Kameyama, H. (2009). Study of porous anodic alumina supported plate-type catalysts during daily start-up and shut-down operation of methane steam reforming. *Applied Catalysis A: General*, 364(1-2):101–107.

Zou, G., Wang, Z., Sun, M., Luo, X., and Wang, X. (2011). A novel solid-gas process to synthesize LaMnO_3 perovskite with high surface area and excellent activity for methane combustion. *Journal of Natural Gas Chemistry*, 20(3):294 – 298.

Zou, J., Huang, J., and Ho, W. S. W. (2007). CO_2 -selective water gas shift membrane reactor for fuel cell hydrogen processing. *Industrial & Engineering Chemistry Research*, 46(8):2272–2279.

Ztek Corporation (2005). High performance steam reforming. Accessed on June 12th, 2012, <http://www.ztekcorporation.com/hpsr.htm>.

Appendix A

Supplementary Coating Results

Many coating experiments were unsuccessful, and several were not included in Chapter 4. This Appendix presents results with catalyst coatings not selected for further investigation. Refer to Chapter 4 for the material and methods descriptions.

A.1 Brush Coating Results

Using the brush coating technique, Figure A.1 shows adherence and thickness results with $\gamma\text{-Al}_2\text{O}_3$, $\alpha\text{-Al}_2\text{O}_3$ (Part A) and RK-212 (Part B).

On Part A, one can observe the relation between the carrier concentration and the thickness. The thickness is generally proportional to the carrier concentration, but that parameter cannot be increased indefinitely. For CR125 ($\gamma\text{-Al}_2\text{O}_3$), at the highest carrier concentration, mass losses are above the acceptable limit of 20 wt%. For A-16 ($\alpha\text{-Al}_2\text{O}_3$), increasing carrier concentration after 7 mol/L did not increase the thickness, but mass losses were acceptable. Higher carrier concentration generally led to a more viscous modified sol, and then, a thicker film and thicker coating. However, above a certain concentration, the modified sol became too viscous and coating was difficult. Not shown on the plots, the standard deviation for the five thickness measurements on each plate was usually $\sim 4\text{-}6\ \mu\text{m}$.

Figure 4.4 Part A shows an SEM image of a Ni-MgO/ $\gamma\text{-Al}_2\text{O}_3$ sample obtained by brush coating. The effect of the metal substrate roughness is still visible on the coating surface. Figure A.4A.1 shows image of a $\gamma\text{-Al}_2\text{O}_3$ sample. The brush

sweep can be clearly seen. On the same figure, plate picture were taken after being subjected to the sonication test.

On Figure A.1B, it can be seen that brush coating of the commercial catalyst RK-212 was more challenging than with γ -Al₂O₃ and α -Al₂O₃. Very few samples achieved their adherence target. The largest particles performed the worst, but no reproducible sol recipe was found with smaller particle sizes.

Brush coating was of limited success. Since good adherence, but insufficient thickness, was obtained with some modified sol, multi-layer brush coating was investigated next.

A.2 Multi-layer Brush Coating

Figure A.2 shows the average coating thickness progression after addition of coating layers. $\sim 40 \mu\text{m}$ for γ -Al₂O₃ and $\sim 45 \mu\text{m}$ for α -Al₂O₃ coatings were obtained after five layers. Not shown on the plot, a sol containing MgAl₂O₄ was also tried, but after seven layers, the estimated coating thicknesses were still $< 20 \mu\text{m}$.

Three γ -Al₂O₃ plates were put in the sonic bath after the fifth layer. Adherences were all acceptable, with 2.3, 15.7 and 10.3% mass losses.

Since it requires about one day of work per layer of coating, and even though we believed that multi-layer coating could eventually achieve coatings of $\sim 80 \mu\text{m}$ thickness with acceptable adherence, this technique was overly time consuming, and therefore abandoned.

A.3 Dip Coating

Figure A.3 shows thickness and adherence results using the dip coating method. Similar to the brush coating method, the coating thickness is generally proportional to the carrier concentration. Although some samples showed thickness $> 80 \mu\text{m}$, adherence quality was unsatisfactory. Not shown on the plots, the standard deviation for the five thickness measurements on each plate ranged from 2-11 μm , with an average at $\sim 6 \mu\text{m}$. Figure A.4 Part C.1 shows a sample obtained by dip coating. Part C.2 shows the extensive mass losses after sonication.

Since the adherence criteria was not met on Figure A.3 at higher coating thicknesses, dip coating was rejected for further investigation.

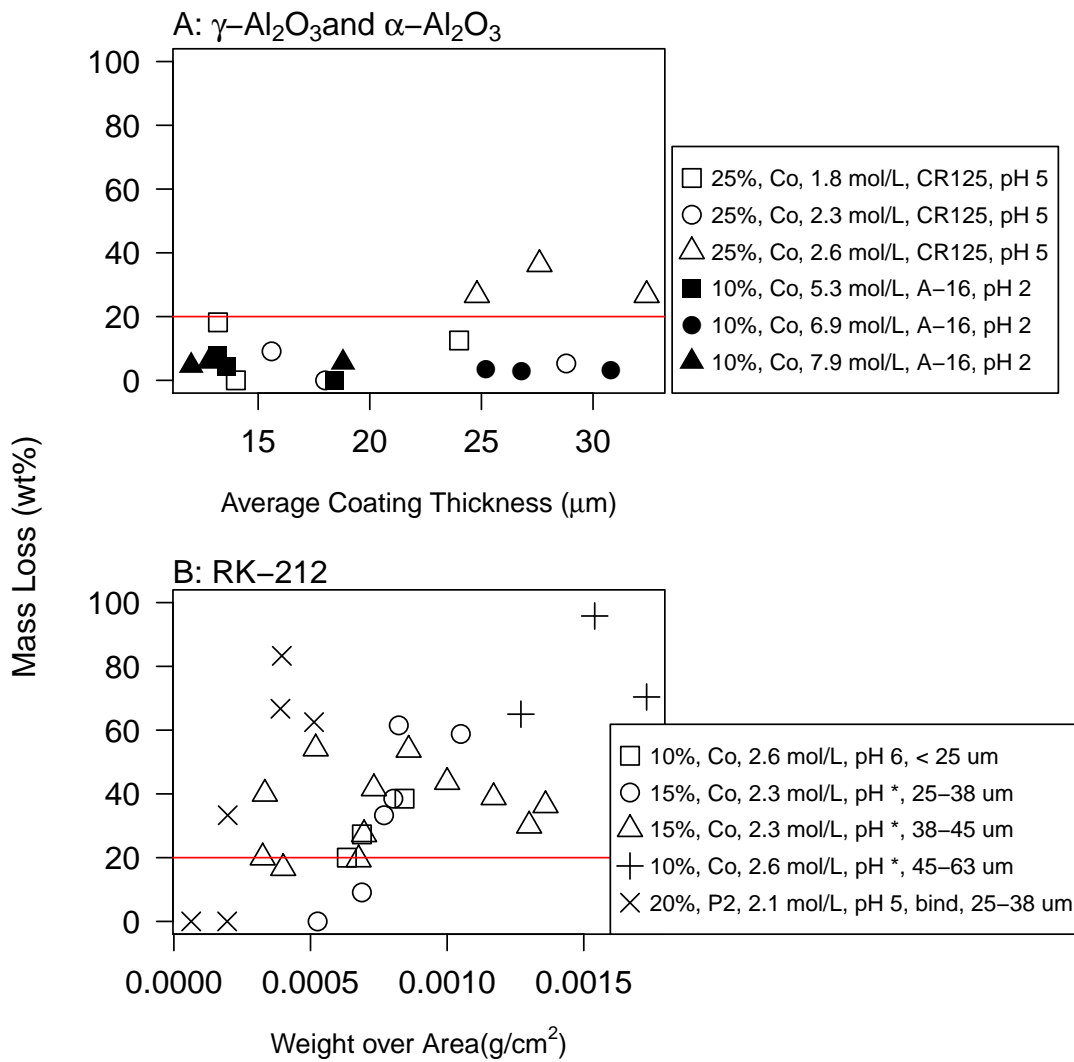


Figure A.1: Brush Coating of $\gamma\text{-Al}_2\text{O}_3$, $\alpha\text{-Al}_2\text{O}_3$ and RK-212 Modified Sol:
 A: $\gamma\text{-Al}_2\text{O}_3$ and $\alpha\text{-Al}_2\text{O}_3$, Mass Loss vs Average Thickness; B: RK-212, Mass Loss vs Weight over Area (pH * = final pH not measured).
 Line representing the 20% mass loss limit is shown.

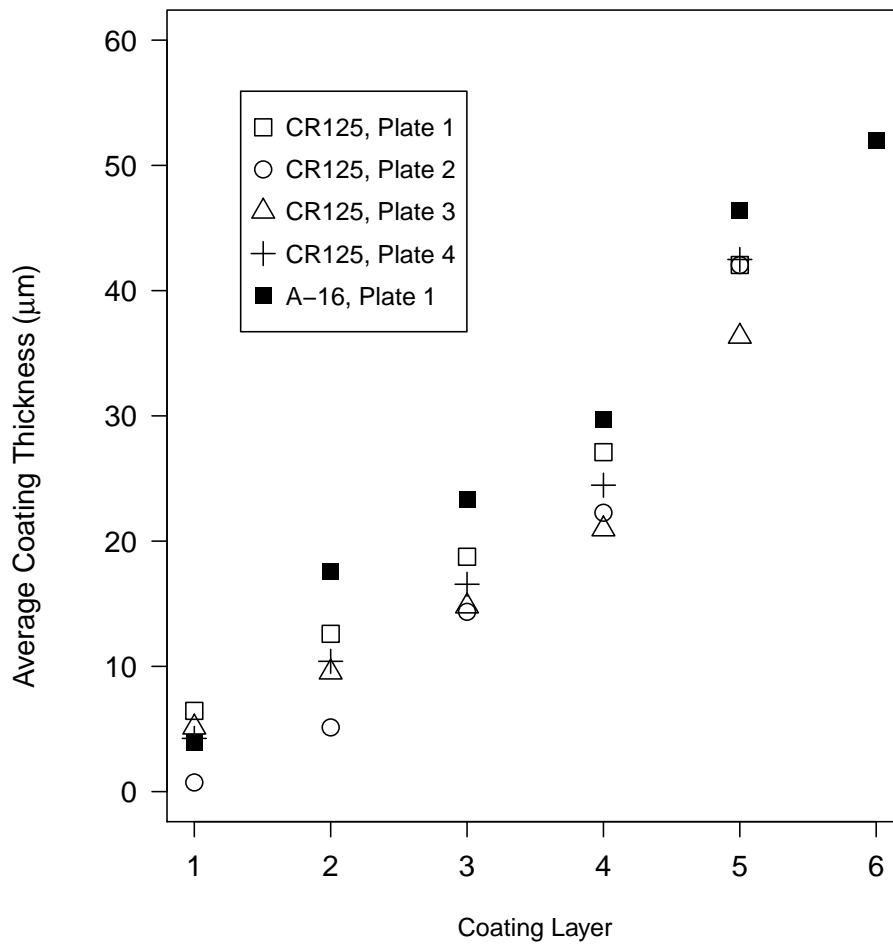


Figure A.2: Multi-Layer Brush Coating of $\gamma\text{-Al}_2\text{O}_3$ and $\alpha\text{-Al}_2\text{O}_3$ Modified Sol, Average Thickness vs Coating Layer. Sol parameters: Ni 15% MgO 5%/ $\gamma\text{-Al}_2\text{O}_3$, 57% boeh., Co, 0.31 mol/L, CR125, pH not measured; Ni 11% MgO 5%/ $\alpha\text{-Al}_2\text{O}_3$, 21% boeh., Co, 1.55 mol/L, A-16, pH not measured.

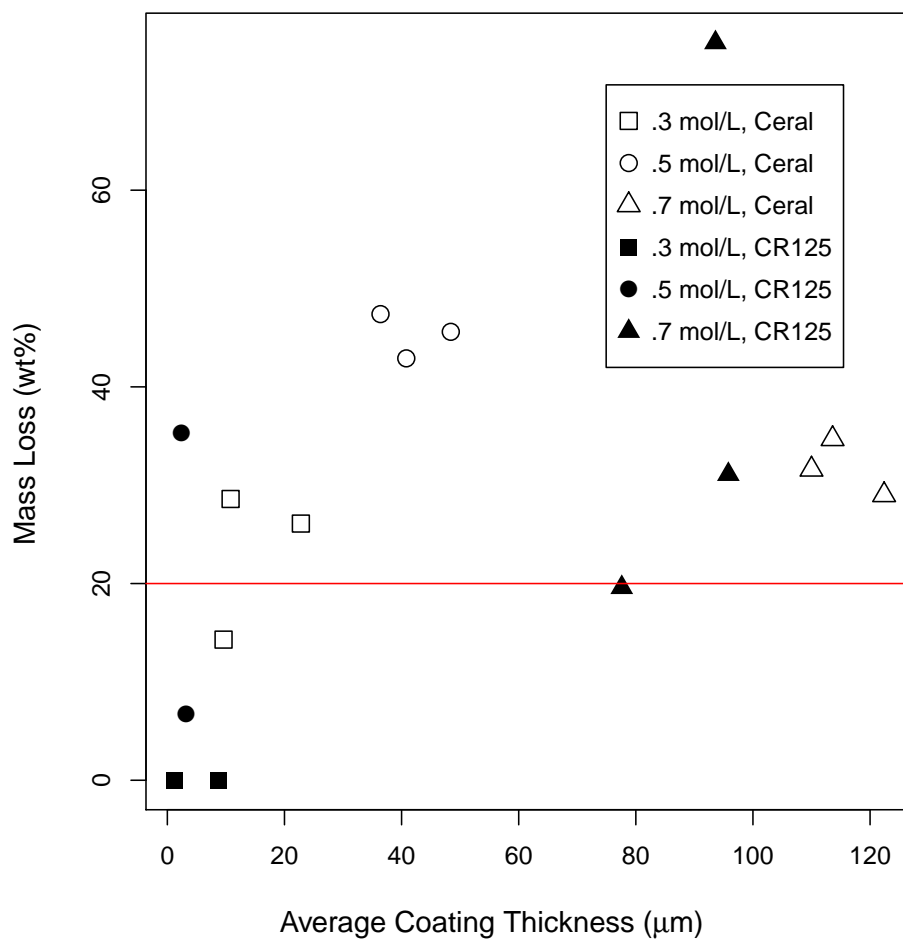


Figure A.3: Dip Coating of γ -Al₂O₃ and α -Al₂O₃ Modified Sol Including Metal Precursors to Obtain Ni 15% MgO 5% / γ -Al₂O₃, or α -Al₂O₃: Mass Loss vs Average Thickness. Withdrawal speed: 3.7 mm/s; α -Al₂O₃ modified sol: 10% boeh., P2, pH 4; γ -Al₂O₃ modified sol: 25% boeh., P2, pH 4. Line representing the 20% mass loss limit is shown.

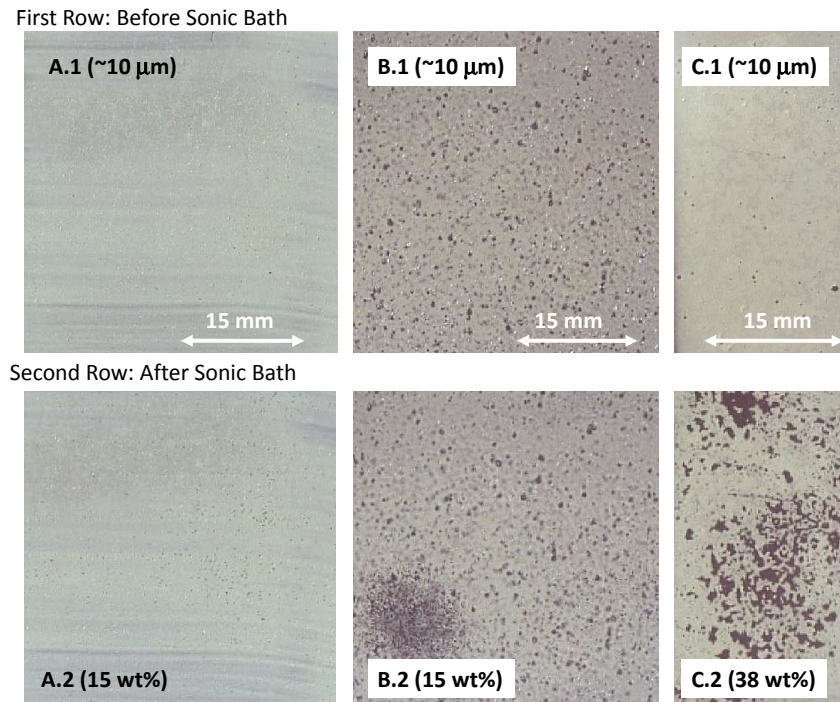


Figure A.4: Scanned Images of Brush, Cold Spray and Dip Coating Samples, before and after Sonication (top row: thickness, bottom row: mass loss after sonication): A. Brush Coating: γ - Al_2O_3 (25% boeh., 2.7 mol/L, pH 2); B. Cold Spray: Ni 11%-MgO 5%/ α - Al_2O_3 (30% boeh., 2.1 mol/L, pH 2); C. Dip Coating: Ni 15%-MgO 5%/ α - Al_2O_3 (10% boeh., 1.6 mol/L, pH 4).

A.4 Cold Substrate Air Spray Coating (Cold Spray)

Attempts with cold spray coating were unsuccessful. In order to be used with the air-spray gun, the viscosity of the modified sol must be kept low by adjusting the carrier concentration. For α - Al_2O_3 , concentration had to be ≤ 2 mol/L. However, at low carrier concentration, a very thin coating layer was obtained between each sweep. In order to obtain a 40+ μm thick film, considerable time (>40 min) was needed to spray & air-dry all layers. Furthermore, visual inspection showed poor coating uniformity (see Figure A.4 B.1). Screen testing using ethanol instead of water as solvent for the modified sol was also tried, but uniformity was no better.

The coating thickness standard deviation within a plate was as high as 17 μm for a 60 μm coating. For those reasons, cold spray coating was discontinued.

A.5 Hot Spray Coating Including Metal Precursors

As shown in Chapter 4 (see Figure 4.1), catalyst and promoter precursors could either be introduced directly in the modified sol or by impregnation, after the coating and calcination of the carrier. In this section, we report results where catalyst and promoter precursors were introduced in the modified sol.

Figure A.5 shows hot spray coating results for Ni-based catalyst with $\gamma\text{-Al}_2\text{O}_3$ as carrier. In Part A, only one set of samples gave acceptable results (30% boeh., P2, 1.08 mol/L, pH 4). In Part B, water was substituted for methanol as the solvent. Optical microscope images with methanol were encouraging, since this eliminated cracks (see Figure A.6). However, the absence of cracks did not result in an improvement in the adherence, as seen in Figure A.5 Part B. These results indicate the fundamental role played by water on the bonding process.

Figure A.7 shows coating results for Ni-based catalysts with $\alpha\text{-Al}_2\text{O}_3$, MgAl_2O_4 or $\text{CeO}_2\text{-ZrO}_2$ as carriers. Results were not encouraging. Most samples failed the adherence quality test at larger coating thicknesses. For $\alpha\text{-Al}_2\text{O}_3$ tests, Dispersal boehmite (P0) was also tried, but coarse cracks were visible after calcination and no thickness measurements were taken.

Appendix B.3 demonstrates that the introduction of metal precursors with the modified sol did not lead to active and stable catalysts. Because of the poor activity, combined with poor adherence results, spray coating, including metal precursors, was not investigated further.

A.6 Hot Spray Coating of Commercial Catalyst: Supplementary Results

Figure A.8 shows results with the Ni-based RK-212 catalyst. Part A shows attempts to coat this catalyst with sieved particles $<45 \mu\text{m}$. Results were negative, with most samples not meeting the bonding quality requirement, regardless of the modified sol parameters. Part B shows results with particles size $\ll 25 \mu\text{m}$, where the results were better. Many samples had acceptable adherence in this case, but

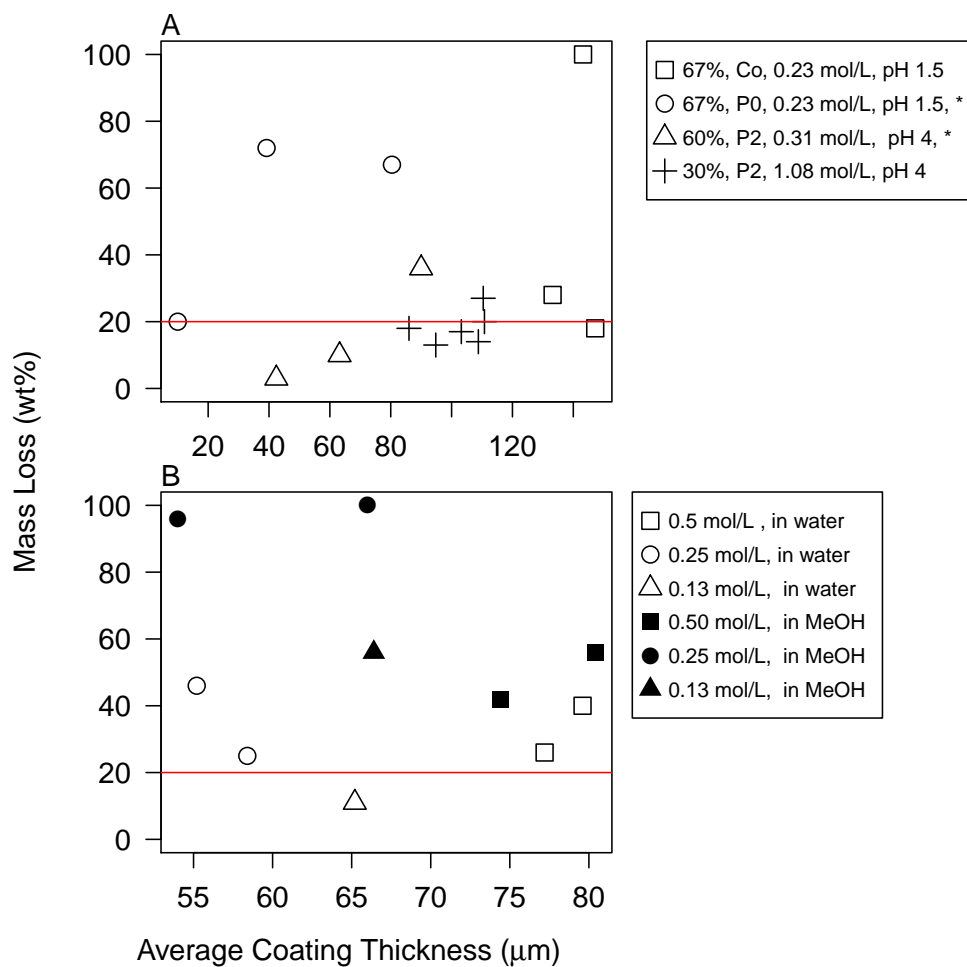


Figure A.5: Hot Spray Coating of $\gamma\text{-Al}_2\text{O}_3$ Modified Sol Including Metal Precursors, Mass Loss vs Average Thickness: A. Ni 15% MgO 5% CaO 0-1.5% K_2O 0-1.5% / $\gamma\text{-Al}_2\text{O}_3$, various sol parameters, with water as solvent (* Ni-MgO only); B. Ni 15% MgO 4% CaO 2% K_2O 2% / $\gamma\text{-Al}_2\text{O}_3$, Comparison between water and methanol as solvent for the sol (30% boeh., P2, pH 4).

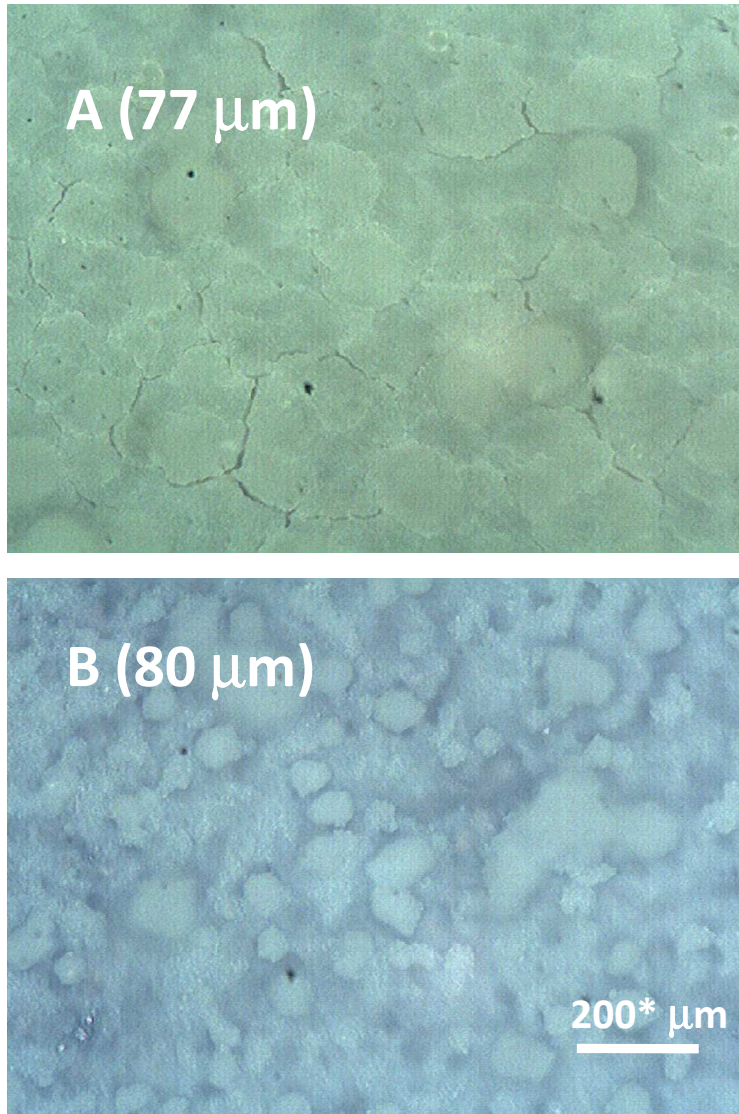


Figure A.6: Hot Spray Coating Optical Images with Methanol vs Water as Solvent for Modified Sol. Catalyst: Ni 11%-MgO 4% CaO 2% K₂O 2% / γ -Al₂O₃ (Coating Thickness): A. Water as solvent; B. Methanol as solvent, * approximative dimension.

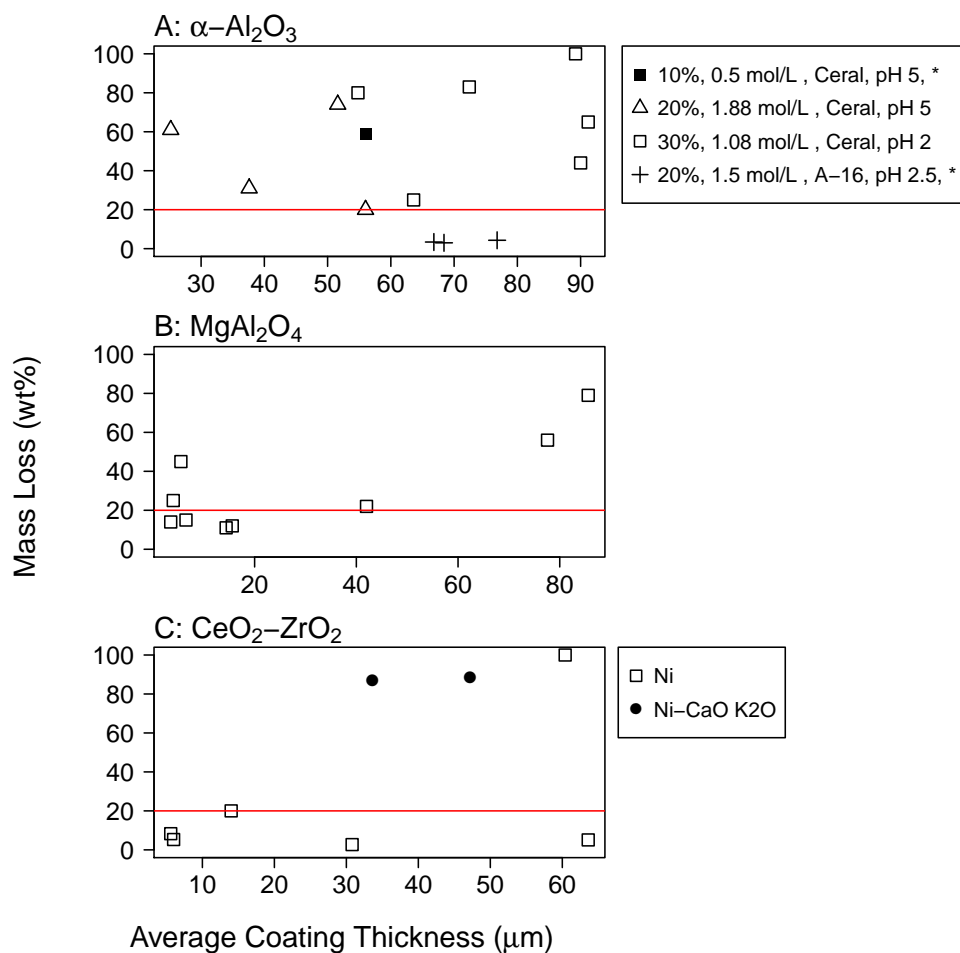


Figure A.7: Hot Spray Coating of $\alpha\text{-Al}_2\text{O}_3$, MgAl_2O_4 and $\text{CeO}_2\text{-ZrO}_2$ Modified Sol Including Metal Precursors, Mass Loss vs Average Thickness: A. Ni 12-15% MgO 4-5% CaO 0-2% K_2O 0-2%/ $\alpha\text{-Al}_2\text{O}_3$ (* Ni-MgO only) B. Ni 15%/ MgAl_2O_4 (46% boeh., 0.5 mol/L, pH 1-2); C. Ni 15% CaO 0-2% K_2O 0-2%/ $\text{CeO}_2\text{-ZrO}_2\text{-}\gamma\text{-Al}_2\text{O}_3$ (25% boeh., 0.4 mol CeO_2 /L, pH 1). Line representing the 20% mass loss limit is shown.

more work would be needed at thicknesses $\geq 80 \mu\text{m}$.

In Part A, black squares corresponds to coating samples without boehmite. Even though samples with 5% and 10% boehmite did not yield acceptable coating quality, the adherence improvement on the graph is noticeable, indicating the importance of boehmite in the bonding process. One can also see that binder did not help the coating process.

Some effects of acid addition can be observed in Part B. RK-212 has a strong alkalinity. Without addition of acid, the pH was 11.8. Samples without acid, as well as samples with formic acid at pH of 8.5, were unsuccessful. Many samples with nitric acid (default acid) at pH 8 had acceptable adherence. Since alumina is slightly acidic in water, these results with RK-212 were the first to show acceptable adherence with alkaline pH. Also in Part B, 8 of 10 samples $>50 \mu\text{m}$ had boehmite content $\geq 20\%$. High boehmite content is not necessarily desirable, since it dilutes the commercial catalyst and can potentially blocks active sites, as reported by Meille (2006).

As shown in Appendix B.2, RK-212 stability and activity were not satisfactory for our MCMR application. For this reason, even though there were some encouraging results with particles $\ll 25 \mu\text{m}$, we did not conduct further tests with RK-212.

Ruthenium-based commercial catalyst was next considered as an alternative to RK-212. Figure A.9 shows coating results for a commercial Ru 5% catalyst. In Part A, it can be seen that multiple samples were successfully coated to a thickness $>80 \mu\text{m}$ with acceptable adherence. Results suggested that pH 5 could lead to less variation than pH 6.5. More testing would be needed to find the optimal boehmite content.

As mentioned in Appendix B.4, coated Ru 5% catalyst activity and stability were noticeably inferior to fresh catalyst (received from the supplier). The nitric acid was likely to be responsible for the losses in activity and stability. Figure A.9B shows various attempts to replace nitric acid. More clarity was obtained regarding what did not work. First, acid is necessary, results without it being clear failures. Using P3 boehmite, which contains acetate instead of nitrate, did not work either with formic or acetic acid. Some samples were successful with formic acid using P2 boehmite, but reproducibility was poor. We will see in Appendix B.4 that P2

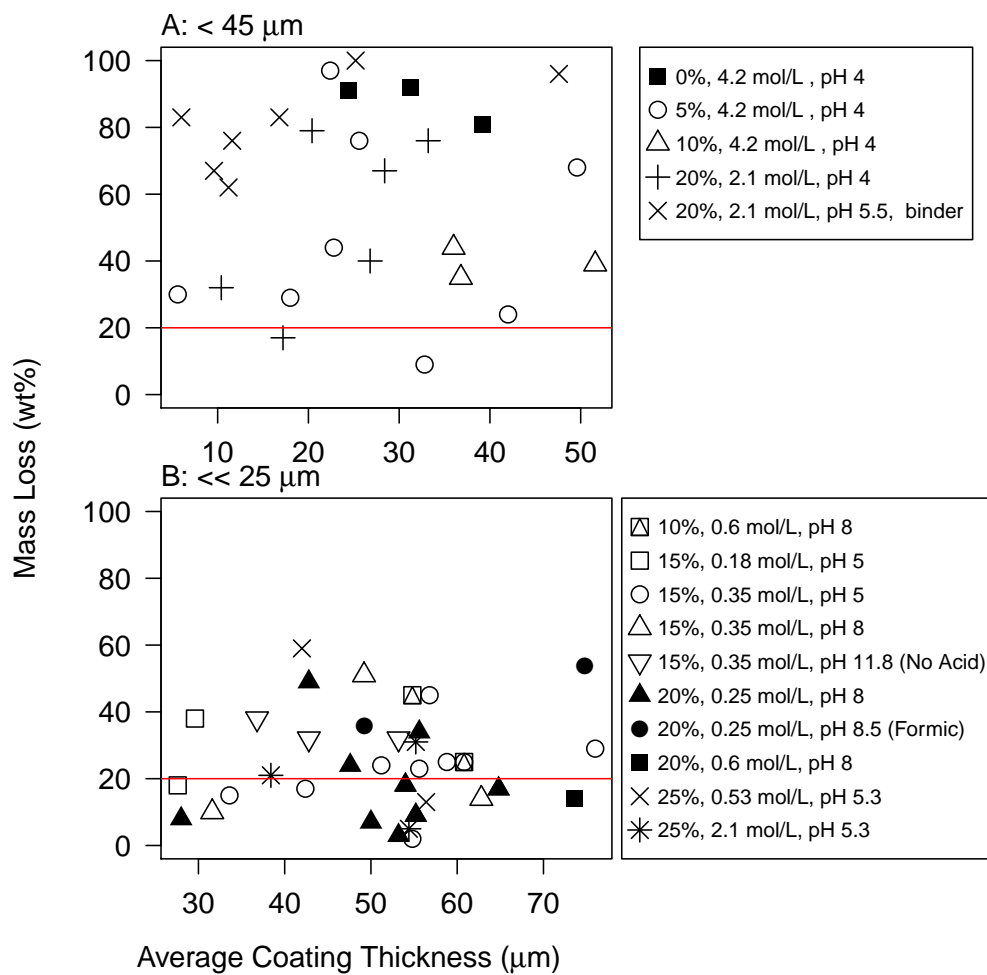


Figure A.8: Hot Spray Coating of Commercial RK-212 Catalyst, Mass Loss vs Average Thickness: A. Sieved particles size of <45 μm ; B. Particle sizes estimated to be $\ll 25 \mu\text{m}$. Line representing the 20% mass loss limit is shown.

boehmite is not necessarily bad for Ru catalyst. More tests would be needed with the combination of P2 boehmite and formic acid. However, as shown in Chapter 6, we finally decided to produce our own Ru-based catalyst, allowing us to pre-steam the carrier and add promoters. Ru-based commercial catalyst coating was therefore not investigated further.

A.7 Thickness vs Mass Data

For catalyst plates with Fecralloy, the thickness meter was not functional due to the magnetic property of the alloy. To estimate the thickness, linear regression was performed with thickness versus mass of catalyst data. The catalyst plates from MCMR Exp. no.1, 2 & 3, were used to generate the plot. Those coatings had SS 310 as metal support, and were made of the same modified sol as the samples on Fecralloy (see Figure A.10).

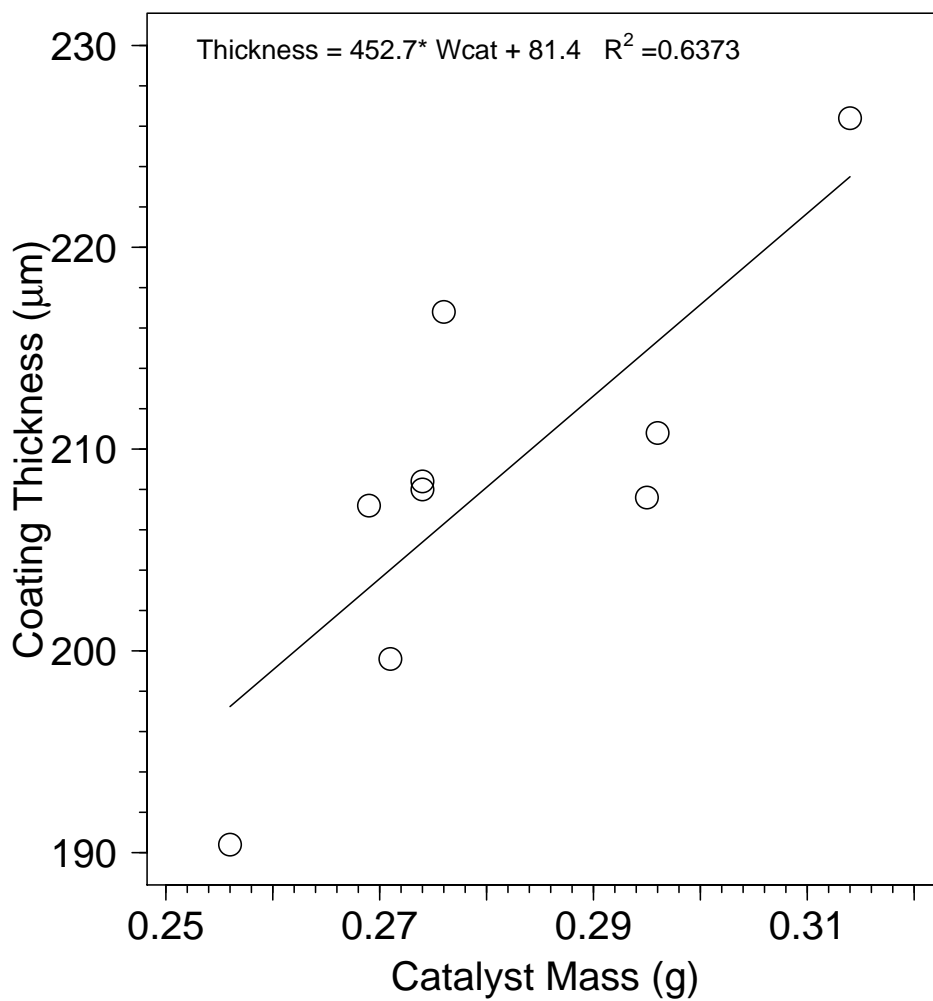


Figure A.10: Coating Thickness vs Mass of Catalyst. Modified sol: 40% boeh., γ -Al₂O₃ 0.5 mol L, pH 5, adjusted with nitric acid.

Appendix B

Stability of Reforming Catalysts: Supplementary Results

Many reforming catalysts tested in the micro-reactor were rejected for various reasons, and several of them were not included in Chapter 6. This Appendix presents those results. Refer to Chapter 6 for material and method descriptions.

B.1 Preliminary Stability Test

The first reforming stability tests were related to early coating attempts, as explained in Chapter 4 and Appendix A. Crushed RK-212, RK-212 with boehmite, lab-made Ni catalyst, and commercial Ru catalyst were tested first. Physical properties of the commercial catalysts are presented in Table B.1.

B.2 RK-212

Figure B.1 Part A shows results of stability tests with crushed RK-212 at various operating conditions and catalyst loadings (see Table B.2). None of the conditions studied showed long term stability.

Figure B.1 Part B reveals the importance of catalyst loading with respect to deactivation. Low catalyst loading data showed strong deactivation, while high catalyst loading led to negligible deactivation, with stable conversion near the predicted equilibrium value.

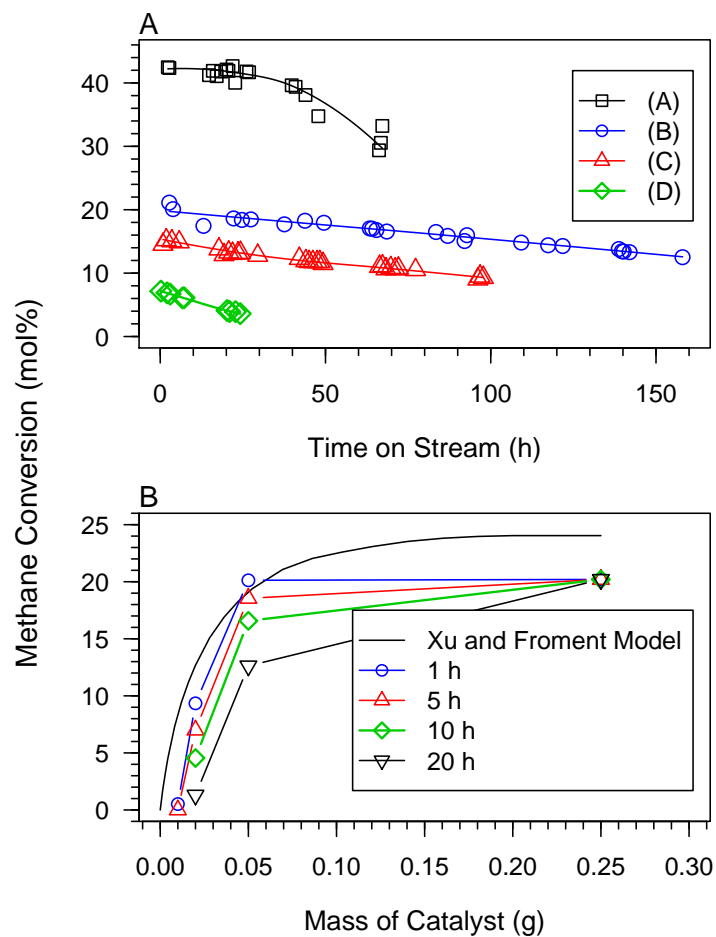


Figure B.1: Stability of RK-212: Effect of Operating Conditions and Catalyst Loading. (A) Methane Conversion vs Time on Stream. Catalyst: RK-212 after crushing. Catalyst loadings varied from 0.05 to 0.2 g, as given in Table B.2, where other operating parameters are also tabulated; (B) Methane Conversion vs Mass of Catalyst. Catalyst: RK-212 with 20 wt% boeh. Operating parameters: 550°C, 10.6 bar, S/C: 4, H/C: 0.5, CH₄ Flow: 105 Nml/min.

Table B.1: Surface Area, Pore Volume, Average Pore Size, and Metal Dispersion of Commercial Reforming Catalysts

	Surface Area	Pore Volume	Ave. Pore Dia.	Metal Dispersion
	m ² /g	cm ³ /g	nm	mol %
RK-212 (after crushing, $D_{p,ave} \ll 25 \mu\text{m}$)	14.3	0.06	19.1	0.77%
RK-212 with 20% boehmite (fresh)	59.4	0.18	10.3	-
Ru 5%/ $\gamma\text{-Al}_2\text{O}_3$ (Alfa) (as received)	225	1.27	19.7	17%
Ru 5%/ $\gamma\text{-Al}_2\text{O}_3$ (Alfa) with 15% boeh. (fresh, average of two samples)	158	0.67	16.4	-

Table B.2: Stability of RK-212: Operating Conditions for Figure B.1 Part A.

Legend Code	Mass Catalyst (g)	CH ₄ flow (Nml/min)	H ₂ O/CH ₄ (mol/mol)	H ₂ /CH ₄ (mol/mol)	Temperature (°C)	Pressure (bar)
A	0.12	100	4	0.5	550	11
B	0.05	100	4	1	550	6
C	0.2	100	3.5	1.35	550	
D	0.1	112	3.5	1	550	5

Figure B.2 shows the effects of the coating process on the catalyst activity and stability. It can be seen that the coating method decreased the initial activity and increased the rate of deactivation. Neither catalyst showed signs of residual long-term activity.

Our first test with the MCMR prototype was performed with RK-212 (see Chapter 8). After an unsuccessful first trial, the coated RK-212 catalyst was scratched off the plates and tested in the micro-reactor. Conversion was nil. With all these poor results, the RK-212 catalyst was rejected for further testing.

B.3 Early Lab-made Ni catalyst

One option with the initial coating procedure, explained in Appendix A.5, was to insert metal catalyst and promoter precursors directly into the modified sol. We

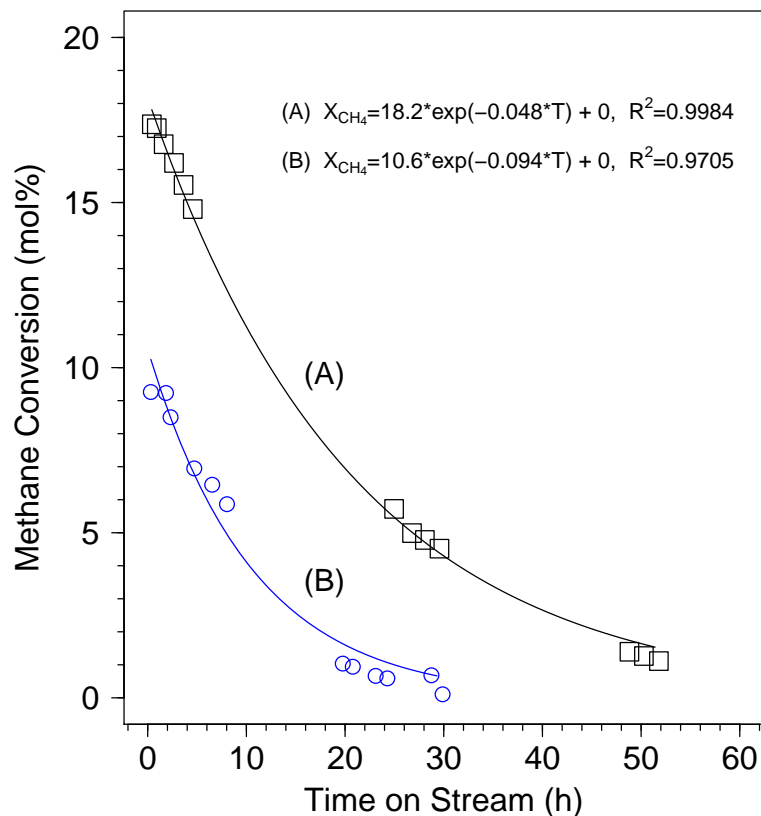


Figure B.2: Stability of RK-212: Comparing Crushed with Coated Catalyst: Methane Conversion vs Time on Stream. S/C: 4, H/C: 0.4, CH₄ Flow: 100 Nml/min; Catalyst loading: 0.02 g. (A) RK-212 powder after crushing; (B) RK-212 with 20 wt% boeh., pH 8 adjusted with nitric acid, calcined in air at 650°C overnight.

tested on the micro-reactor 0.05 g of a NiO 15% MgO 5% / α -Al₂O₃ catalyst. Methane conversion was nil. Slightly better results were obtained with 0.2 g of a NiO 15% / CeO₂-ZrO₂, with an initial conversion of 3.3% at 600°C, 11 bar. Nevertheless, this catalyst, was under-performing, even relative to RK-212.

Figure B.3 helps to explain why lab-made Ni catalysts under-performed compared to RK-212. A high temperature \sim 750°C would be needed to reduce the lab-made catalyst, instead of \sim 440°C for RK-212. Reducing at 750°C could cre-

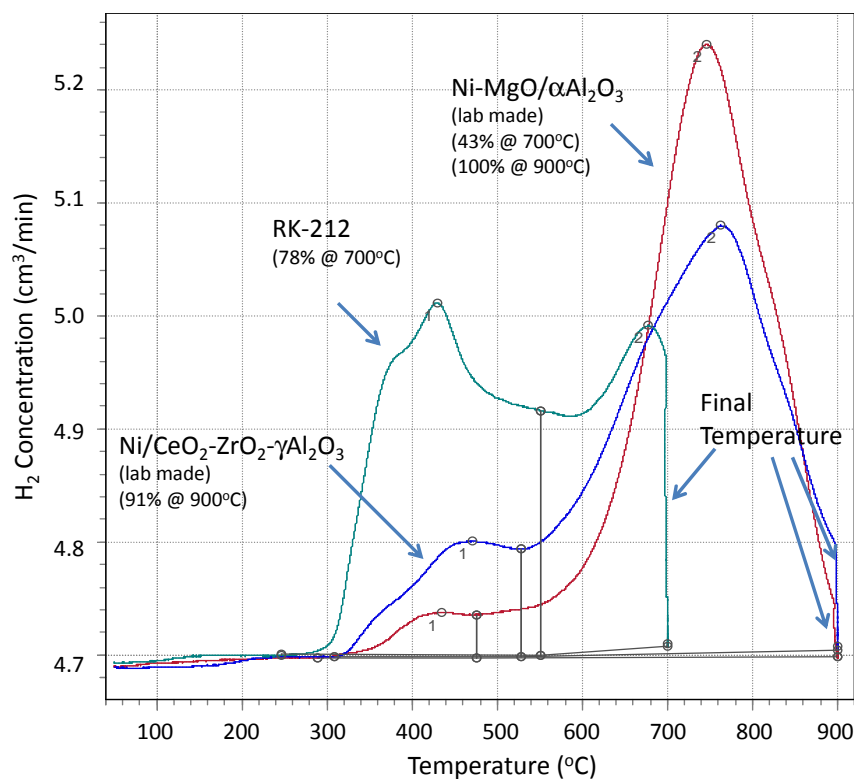


Figure B.3: TPR diagrams of Ni-based Catalysts (% reduction @ reduction temperature). See Section 6.2.7 for procedure description.

ate issues with the MCMR. If the reduction was performed in-situ, a temperature of 750°C would damage the Pd/Ag membrane. With the poor catalyst activity of lab-made Ni catalysts, combined with poor coating results mentioned in Appendix A.5, the catalyst strategy, consisting in inserting metal precursors with the modify sol, was not investigated further.

B.4 Commercial Ru 5%/ γ -Al₂O₃ Catalyst

After the poor results obtained with both lab-made and commercial Ni-based catalysts, we started investigating Ru-based catalysts. The first attempts were made with a Ru 5%/ γ -Al₂O₃ from Alfa Aesar.

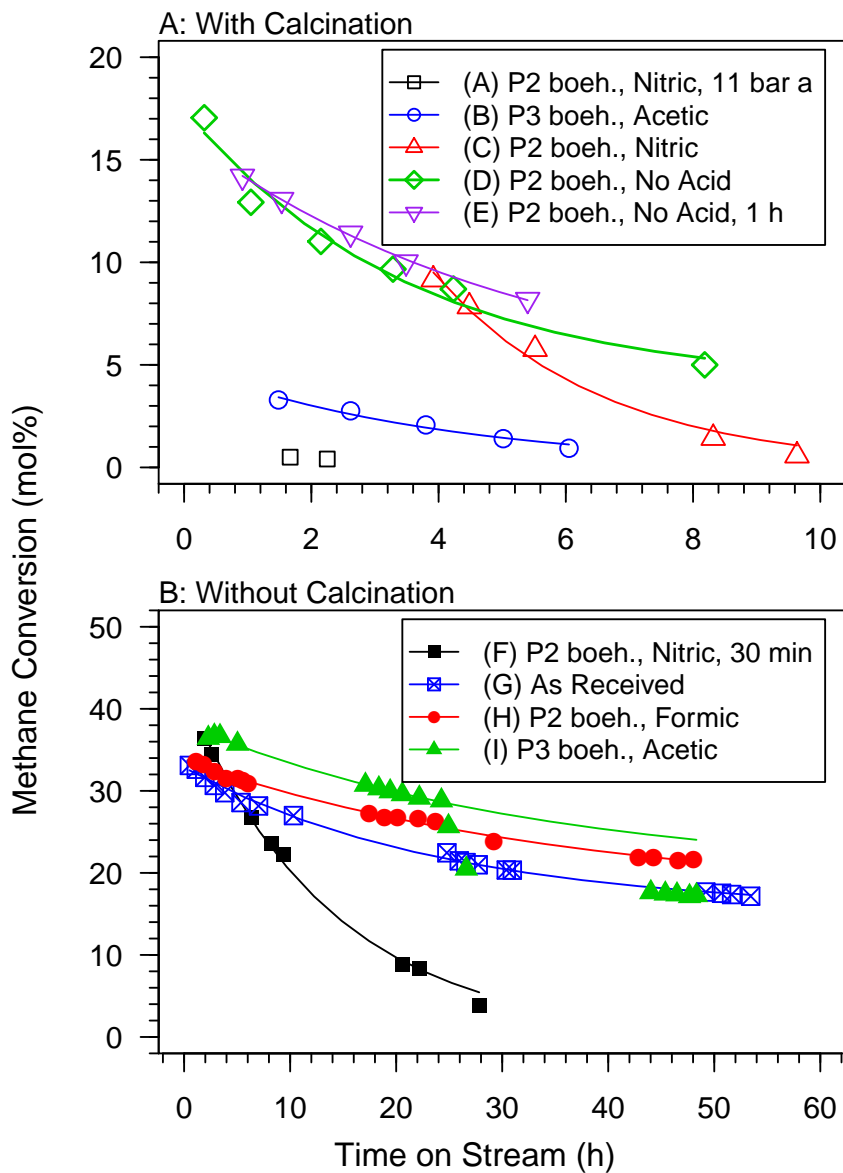


Figure B.4: Stability of Commercial Ru 5%/ γ -Al₂O₃ (Alfa): Methane Conversion vs Time on Stream. Reforming Conditions: 550°C, 11 bar, S/C: 2.5, H/C: 0, CH₄ Flow: 100 Nml/min; Catalyst loading: 0.02 g; Modified Sol: 15% boeh., 0.25 mol/L. Data fitted with Eq. (6.14). See Table B.3 shows change in modified sol parameters and start-up/ reduction conditions.

Table B.3: Stability Conditions of Ru 5% (Alfa): Modified Sol Parameters and Reduction/Start-up Conditions for Figure B.4

Label	Boeh.	Acid (pH)	Calcination ^a (Y/N)	Start-up Changes ^b
A	P2	Nitric (6)	Y	11 bar
B	P3	Acetic (6)	Y	No change
C	P2	Nitric (6)	Y	No change
D	P2	No Acid ^c	Y	No change
E	P2	No Acid ^c	Y	1 h
F	P2	Nitric (6)	N	30 min
G	As Received		N	No change
H	P2	Formic (6)	N	600°C, 1 h
I	P3	Acetic (6)	N	1.5 h

^aNormal calcination: calcined overnight in static air at 600°C.

^bNormal start-up/reduction: catalyst reduced overnight at 550°C, 1.01 bar, with 42 Nml/min H₂.

^cpH not measured

Table B.4: Curve Fitting Related to Figure B.4, and Eq. (6.14) for Stability of Ru 5% (Alfa)

Label	a	b	c	a+c	R ²
A	Activity too low				
B	4.92	0.245	0	4.92	0.97
C	42.4	0.382	0	42.4	0.98
D	13.5	0.282	4.0	17.5	0.97
E	12.7	0.187	3.5	16.2	0.999
F	42.3	0.0737	0	42.3	0.995
G	17.5	0.0410	15.4	32.9	0.996
H	16.8	0.0272	16.9	33.7	0.994
I	18.5	0.0298	19.7	38.2	0.996

Figures B.4 A & B show stability and activity results for the Ru 5% (Alfa) catalyst. The modified sol and start-up parameters are listed in Table B.3. Exponential curve fitting data are presented in Table B.4.

The samples submitted to calcination in air (Figure B.4 Part A) during the coating procedure suffered both from loss of activity and stronger deactivation, compared to samples that were not calcined in air (Part B). The problem could come from formation of Ruthenium tetroxide (RuO_4), which has a melting point of 40°C , and could be volatile during calcination. Another explanation could be that calcination sintered the Ru metal sites, as suggested in Section 6.3.5, with lab-made Ru catalyst. Another interesting, but failed experiment, is portrayed by curve (A). Here the catalyst was reduced by mistake overnight at 11 bar instead of 1 bar. The result was a complete loss of activity.

Samples using nitric acid, curves (A), (C) and (F), showed stronger deactivation than samples with no acid, acetic acid or formic acid. Curves (H) and (I) gave similar similar results to those “as received” catalyst. We also observe that both boehmites, P2 and P3, did not adversely affect activity, and that overnight reduction was unnecessary, 1 h at 600°C was sufficient.

The explanation behind the negative effect of nitric acid on the catalyst activity is unclear. The electrochemical equilibrium diagram (Pourbaix, 1974) indicates that nitric acid could corrode Ru in aqueous solution. The possibility that corrosion might introduce irreversible changes to the Ru oxidation state was tested with X-Ray Diffraction (XPS) surface analyses. The test results were inconclusive, with Ru peaks hidden by carbon peaks. Carbon peaks are inevitable when catalyst has been in contact with dust particles in ambient air. The Ru corrosion could also have provoked sintering of Ru metal sites, but there were not enough samples to perform CO-sorption analysis. However, the commercial Ru-based catalyst was less active and stable than the lab-made Ru-based catalyst (see Chapter 6). For this reason, as well as some difficulty in coating commercial catalyst with acetic or formic acid, no further testing and analysis with Ru 5% (Alfa) were performed.

Appendix C

MCMR Supplementary Results

C.1 Lessons Learned During Reactor Commissioning

Many issues occurred during the commissioning of the reactor. Some of the issues are illustrated in Figures C.1, C.2, and C.3.

- The reforming product gas-liquid separator had originally a drain trap functioning on thermodynamic principle. The trap was found to be unsafe, with a little dirt preventing the trap from sealing, causing a sudden pressure drop on the reforming side. Two bonnet valves in series were installed to replace it.
- A computer, with a custom-made LabVIEW program, controlled the temperatures and set the flow rates. The computer was disconnected from Internet or other networks, because automatic software updates could trigger automatic reboot of the computer, causing automatic shut down of the unit.
- Heat cycles were an issue for the MCMR. Metal expansion and contraction weaken the seal, and gasket burst had occurred (see Fig. C.1A) on one occasion. Temperatures of the reactor should not be lowered in sleeping mode; only feed gases should be shut off.
- SS wool used inside steam pre-heaters oxidized (Fig. C.1B) causing rust to be introduced in the MCMR during the pre-aging of the catalyst support C.2A&B). The wool was therefore changed to alumina beads.

- Thermocouples installed inside cartridges heaters were not reliable. Electrical noise from the heaters prevented continuous reading of the thermocouples, which therefore could not be used for temperature control.
- Anti-seize must be chosen carefully. Bolts and nuts seized during an early experimental run (Fig. C.1C). The anti-seize was changed to one more suitable for higher temperatures. Nuts were changed to Stainless Steel (SS) 316, and bolts were kept to SS 304, to reduce the possibility of galling.
- Grafoil gaskets without SS insert were not resistant to the operating conditions, as shown in Fig. C.1D.
- Grafoil gaskets decomposed with heat. Carbon formation was visible on combustion catalyst after runs. A flow of air or nitrogen was applied during start-up, shut down or sleeping mode, to avoid the problem.
- To maximize oxidation catalyst exposure to the feed, in some experiments, the Grafoil strips were reduced in length, only covering the middle three plates (see Fig. C.2C). This configuration caused issues with gas sampling, where back-flow from the second half of the channel occurred, creating erroneous conversion results. The strip should cover all catalyst plates. Another issue occurred when the Grafoil was too long. Figure C.3 presents three images of the catalyst plates after Exp. no.3. A thin layer of carbon was deposited on the first plate, likely from the gasket. The catalyst of the dark region was scratched off and analyzed for carbon content. Even though carbon was visible, its amount was below the detection limit of the analyzer.
- The design provided the option of feeding air from the top flange, while methane was fed through the separator. However, methane decomposition occurred in the feeding area of the separator, causing flow distribution issues. Figures C.2D.1 & D.2 show carbon formation on one side of the plates.

C.2 Preliminary Results

Preliminary results from the MCMR experiments are detailed here. For information on material and methods, refer to Chapter 8. Active catalysts used in this section are detailed in Tables C.1 - C.3. Table C.4 lists simulation parameters that differ from Tables 8.7 & 8.8.

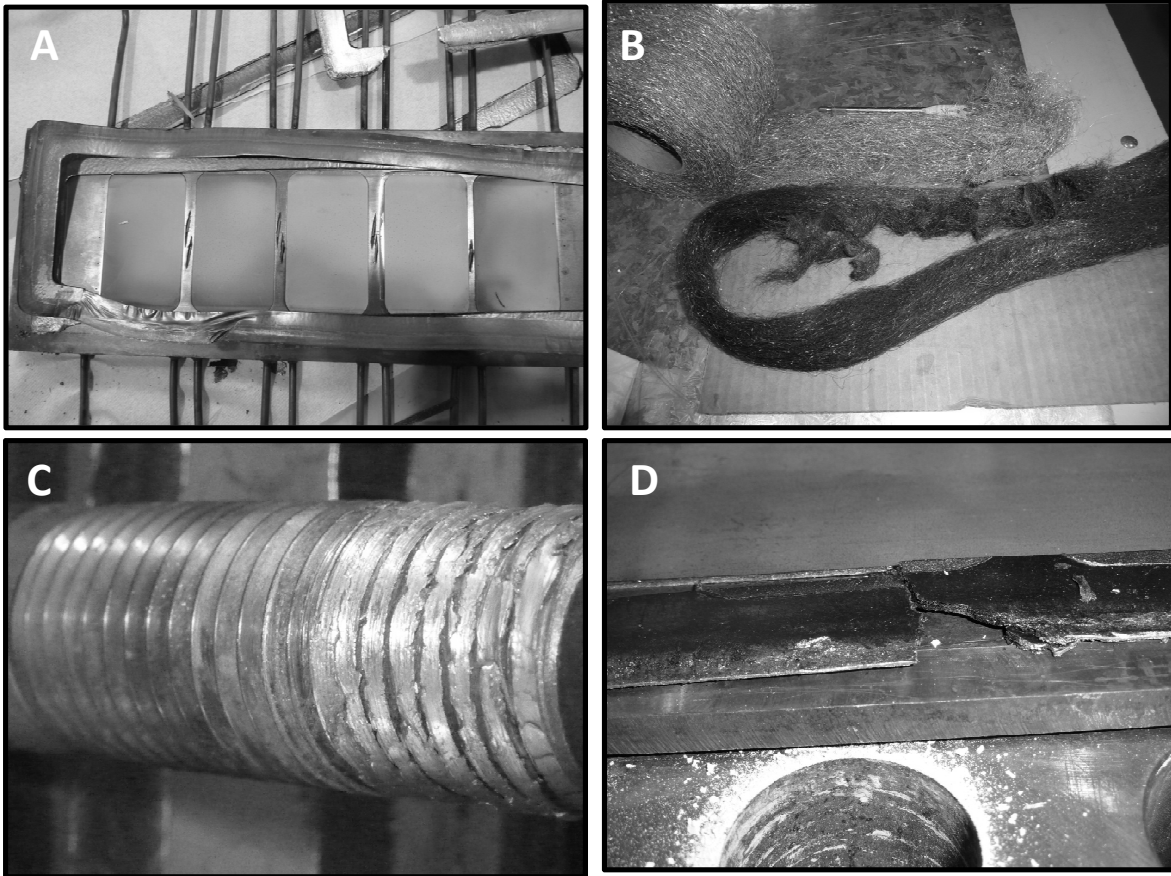


Figure C.1: Issues Encountered with MCMR, Part I: (A) Gasket burst due to heat cycle; (B) SS wool oxidized in steam pre-heater; (C) Galling of bolts with nuts, resulting in stripping of bolt threads while removing nuts; (D) Wrong gasket used: Grafoil without SS foil insert.

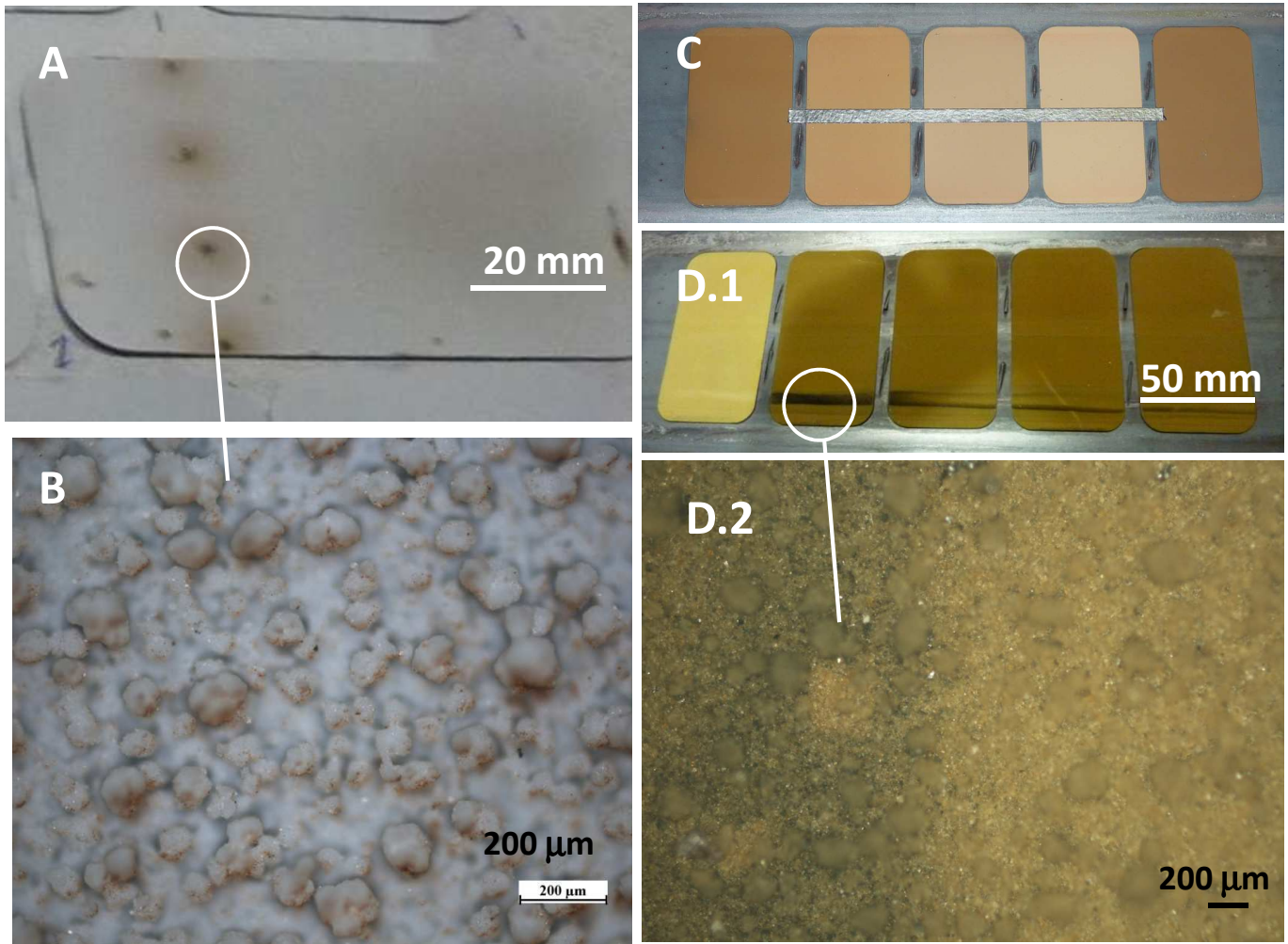


Figure C.2: Issues encountered with MCMR, Part II: (A) Rust deposition on $\gamma\text{-Al}_2\text{O}_3$ plates from rusty wool inside steam pre-heater; (B) Optical microscope image of (A); (C) Grafoil strip skipping first and last plates, causing issues with gas sampling; (D) Flow distribution issue, with feed not reaching the combustion channel properly, causing carbon formation.

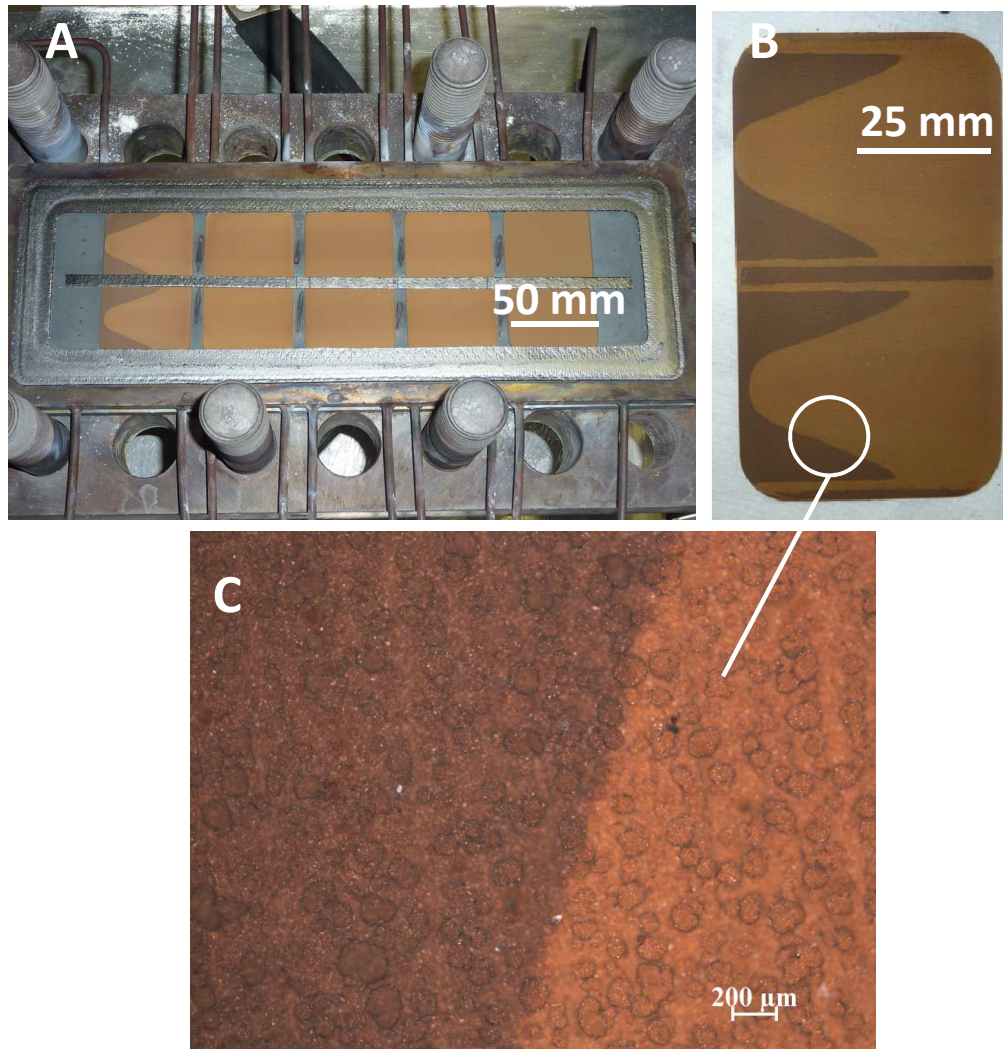


Figure C.3: Issues Encountered with MCMR, Part III: (A) Combustion plates after Exp. no.3. (B) Flow distribution issue causing carbon formation. (C) Optical microscope image of (B).

Table C.1: Catalyst Description for MCMR Preliminary Experiments, Part I. Metal support is SS 304. No membrane was used. Experiments Numbering is consistent with Table 8.9.

Catalyst on γ -Al ₂ O ₃ support	Plate Position	Mass Catalyst g	Ave. Coating Thickness μm	Density Catalyst Layer kg/m ³
Experiment no.0.3				
Pd 1% (Alfa)	1	0.22	166	300
Pd 1% (Alfa)	2	0.23	164	319
Pd 1% (Alfa)	3	0.24	170	321
Pd 1% (Alfa)	4	0.38	157	546
Pd 1% (Alfa)	5	0.32	148	489
<i>Total mass / Ave. Thickness / Ave. Density</i>		1.39	161	395
Experiment no.0.4				
Ru 6% MgO 5%	1	0.237	87	617
Ru 6%	2	0.324	147	499
Ru 6%	3	0.289	121	541
Ru 7%	4	0.326	147	500
Ru 7%	5	0.276	130	480
<i>Total mass / Ave. Thickness / Ave. Density</i>		1.452	126	527
Pd 1% (Alfa)	1	0.293	160	413
Pd 5% (Alfa)	2	0.172	85	458
Pd 5% (Alfa)	3	0.224	122	415
Pd 5% (Alfa)	4	0.236	152	350
Pd 5% (Alfa)	5	0.204	126	367
<i>Total mass / Ave. Thickness / Ave. Density</i>		1.129	129	401

C.2.1 Combustion Preliminary Results

First attempts with the MCMR prototype failed to produce hydrogen in the reforming channel. We instead collected data with only the combustion channel performing.

Figure C.4 shows the influence of the channel height. In the first part of the graph, the reactor included the combustion frame, which created a 9 mm channel height. Outlet values were lower than intermediate sampling values, since gas sam-

Table C.2: Catalyst Description for MCMR Preliminary Experiments, Part II. Metal support is SS 304. No membrane was used. Experiments Numbering is consistent with Table 8.9.

Catalyst on γ -Al ₂ O ₃ support	Plate Position	Mass Catalyst g	Ave. Coating Thickness μ m	Density Catalyst Layer kg/m ³
Experiment no.0.5				
Ru 10%	1	0.266	149	403
Ru 8% La ₂ O ₃ 4%	2	0.272	133	462
Ru 8%	3	0.27	123	496
Ru 7%	4	0.354	148	541
Ru 6%	5	0.317	136	525
<i>Total mass / Ave. Thickness / Ave. Density</i>		1.479	138	485
Pd 1% (Alfa) (all plates reused from Exp. no.0.4)	1	0.293	160	413
Pd 5% (Alfa)	2	0.172	85	458
Pd 5% (Alfa)	3	0.224	122	415
Pd 5% (Alfa)	4	0.236	152	350
Pd 5% (Alfa)	5	0.204	126	367
<i>Total mass / Ave. Thickness / Ave. Density</i>		1.129	129	401

ples were taken near the bottom of the channel, where the conversions were higher. After removing the combustion frame, the intermediate points became lower than at the outlet. Experimental data were under-performing the model predictions.

In Figure C.5, the palladium content in the last four plates was increased from 1% to 5%. Initially, the conversion was higher than in Figure C.4. Since we observed performance improvement going from 9 mm to 2 mm with the channel height, a thinner gasket was tried to give a 1 mm channel height. The conversion deteriorated, but this was due to the carbon in the feed line that disturbed the flow distribution. After experiencing this issue, the methane feed was pre-mixed with air to avoid thermal decomposition. The same catalyst was used a third time, but suffered permanent deactivation. Experimental data again fell below model predictions in this Figure.

Figure C.6 shows several operating conditions where a rapid loss of activity

Table C.3: Catalyst Description for MCMR Preliminary Experiments, Part III. Metal support is SS 304. No membrane was used. Experiments Numbering is consistent with Table 8.9.

Catalyst on γ -Al ₂ O ₃ support	Plate Position	Mass Catalyst g	Ave. Coating Thickness μ m	Density Catalyst Layer kg/m ³
Experiment no.0.6				
Ru 8% La ₂ O ₃ 4% (reused)	1	0.272	133	463
Ru 8% La ₂ O ₃ 10%	2	0.342	149	518
Ru 6% La ₂ O ₃ 12%	3	0.286	120	537
Ru 9%	4	0.255	144	400
Ru 5% La ₂ O ₃ 14%	5	0.204	89	519
<i>Total mass / Ave. Thickness / Ave. Density</i>		1.359	127	487
Pd 1% (Alfa)	1	0.256	166	349
Pd 5% (Alfa) (light)	2	0.262	162	366
Pd 5% (Alfa) (dark)	3	0.268	199	304
Pd 5% (Alfa) (light)	4	0.284	173	371
Pd 5% (Alfa) (dark)	5	0.261	180	328
<i>Total mass / Ave. Thickness / Ave. Density</i>		1.331	176	344
Experiment no.0.7				
Ru 5% La ₂ O ₃ 7%	1	0.326	195	377
Ru 4.2% MgO 3% La ₂ O ₃ 3%	2	0.421	226	421
Ru 8% MnO 2% MgO 2% La ₂ O ₃ 4%	3	0.262	147	403
Ru 5% La ₂ O ₃ 7%	4	0.344	194	401
Ru 8% La ₂ O ₃ 7%	5	0.318	187	384
<i>Total mass / Ave. Thickness / Ave. Density</i>		1.671	190	397
Pd 5% (Alfa) (dark) (all plate reused from Exp. 0.6, but in different order)	1	0.256	199	290
Pd 5% (Alfa) (light)	2	0.262	162	366
Pd 5% (Alfa) (dark)	3	0.268	180	337
Pd 5% (Alfa) (light)	4	0.284	173	371
Pd 1% (Alfa)	5	0.261	166	355

Table C.4: Simulation Parameters for Preliminary Results

Parameters (Symbols)	Values (Equations)	Units
Catalyst Parameters		
Pore Volume (v_r)	0.49 (γ -Al ₂ O ₃ only); 0.42 (with La ₂ O ₃)	cm ³ /g
Density ($\rho_{cat,k}$)	see Tables C.1 - C.3	kg/m ³
Reforming Kinetics	Xu and Froment (1989)	
Design Parameters		
Length (L)	0.251	m
Reforming Width (W_r)	0.081	m
Combustion Width (W_c)	0.074	m
Catalyst Thickness ($Th_{cat,k}$)	See Tables C.1 - C.3	μ m
Separator Wall Thickness (Th_s)	0.0127	m
Reforming Gas Channel Half-Height (H_r)	2;	mm
Combustion Gas Channel Half-Height (H_c)	0.5 - 1 - 4.5	mm

was observed. The amount of data is insufficient to conclude the exact conditions that affect the stability. However experiments involving higher methane concentration (4%), temperature at 565°C and pressure above 3.2 bar were more likely to generate higher deactivation decay. The negative effect of higher pressure was also observed in Chapter 7.

C.2.2 Reforming Preliminary Results

Figure C.7 shows the first experiments that produced hydrogen. Outlet conversion was less than the equilibrium conversion, but intermediate points were above or at equilibrium. The outlet suffered from feed by-passing, as explained in Chapter 8, and the catalyst slowly deactivated.

Figure C.8 presents the second experiments that produced hydrogen. Two changes were made from the first experiments: (1) the second plate contained La₂O₃, and (2) it was attempted to correct the feed by-pass by filling gap below and beside the dummy membrane with Grafoil. The by-pass appeared to be only corrected at lower flow rate (0.52 nL/min). The conversion at the second position was high, suggesting a positive effect of La₂O₃. The reforming catalyst slowly

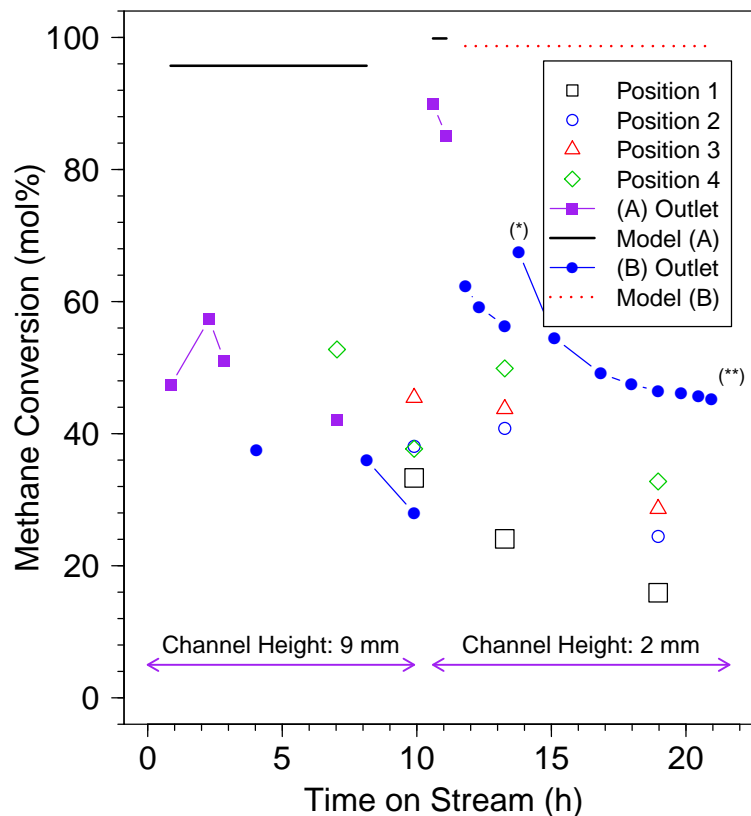


Figure C.4: Combustion Methane Conversion versus Time on Stream, for MCMR Exp. no.0.3. Operating Conditions: (A) CH₄ Flow: 0.10 nL/min, 3.5% in air, P_c : 6.0 bar, $T_{ave,c}$: 550°C. (B) CH₄ Flow: 0.10 nL/min, 3.0% in air, P_c : 6.0 bar, $T_{ave,c}$: 550°C.

deactivated again.

Figure C.9, Parts A & B present methane conversion and temperature profiles along the reactor length (axial coordinate) for experiments no.0.4 and 0.5. The conversions at the first location are well below model predictions, but approached equilibrium at the second location. On the combustion side, as mentioned above, the experimental data under-performed the model predictions. There was little difference between the temperatures on the reforming and combustion sides, because both top and bottom flange heaters were on.

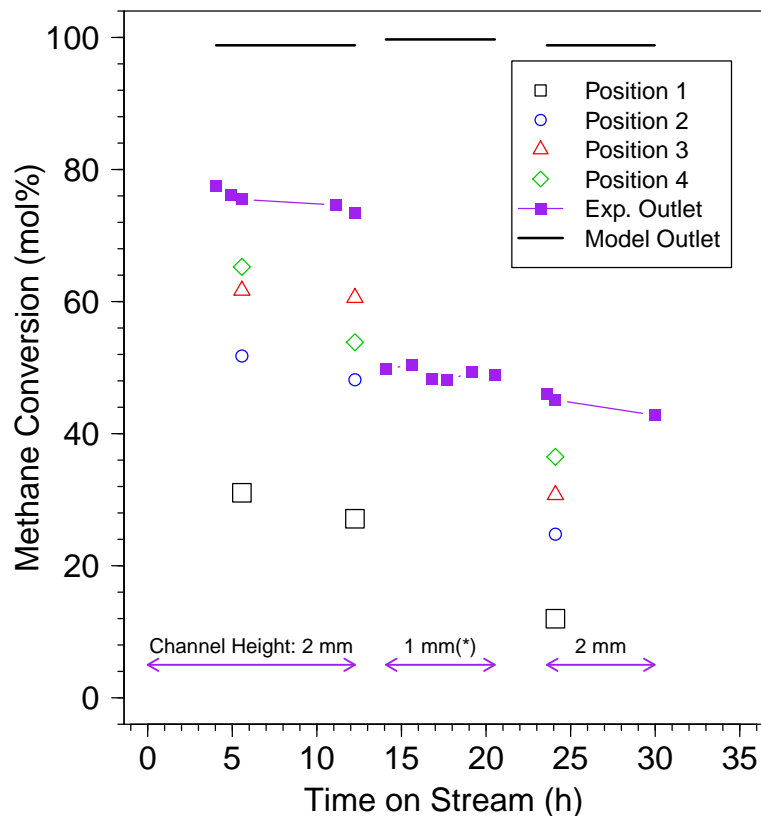


Figure C.5: Combustion Methane Conversion versus Time on Stream, for MCMR Exp. no.0.4 and 0.5. Operating Conditions: (A) CH₄ Flow: 0.20 nL/min, 3.0% in air, P_c : 3.6 bar. $T_{ave,c}$: 550°C.

Figure C.10 displays methane conversion and temperature profiles along the reactor length for Exp. no.0.7. For the first time, all reforming plates had La₂O₃ as promoter, and the effect was visible with the conversion at the first point, matching for the first time the model predictions. The bottom flange heaters were shut down, and transversal temperature difference emerged: ~3°C difference between the combustion and reforming channel at locations 2 and 3. The conversion dropped at the outlet, showing the difficulty to stop by-passing at higher flow rates.

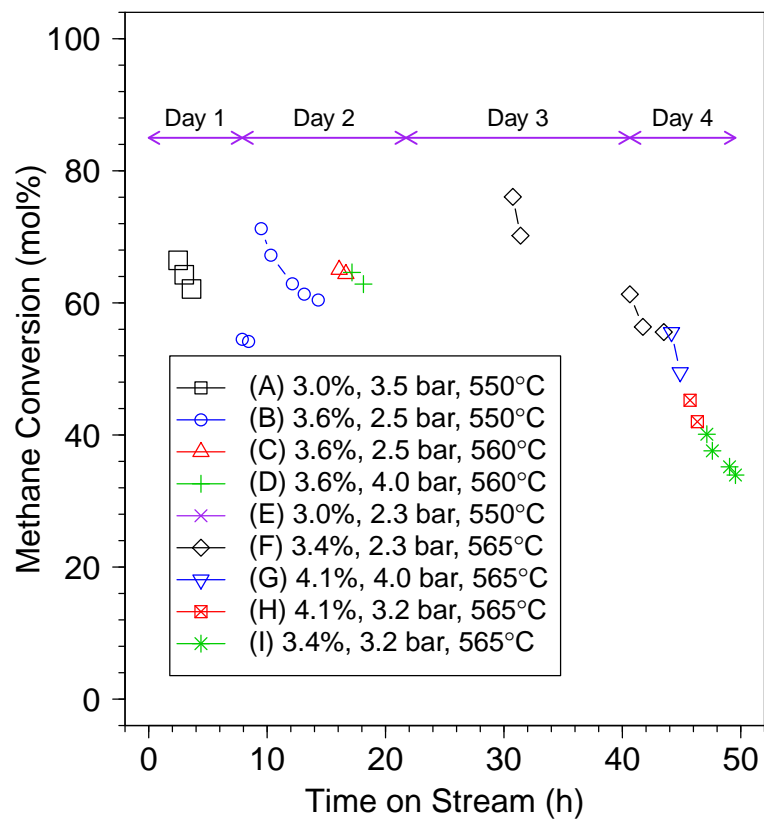


Figure C.6: Combustion Methane Conversion versus Time on Stream, for MCMR Exp. no.0.6 and 0.7. CH₄ Flow: 0.20 nL/min, other operation conditions are detailed in Legend. Channel height: 1mm.

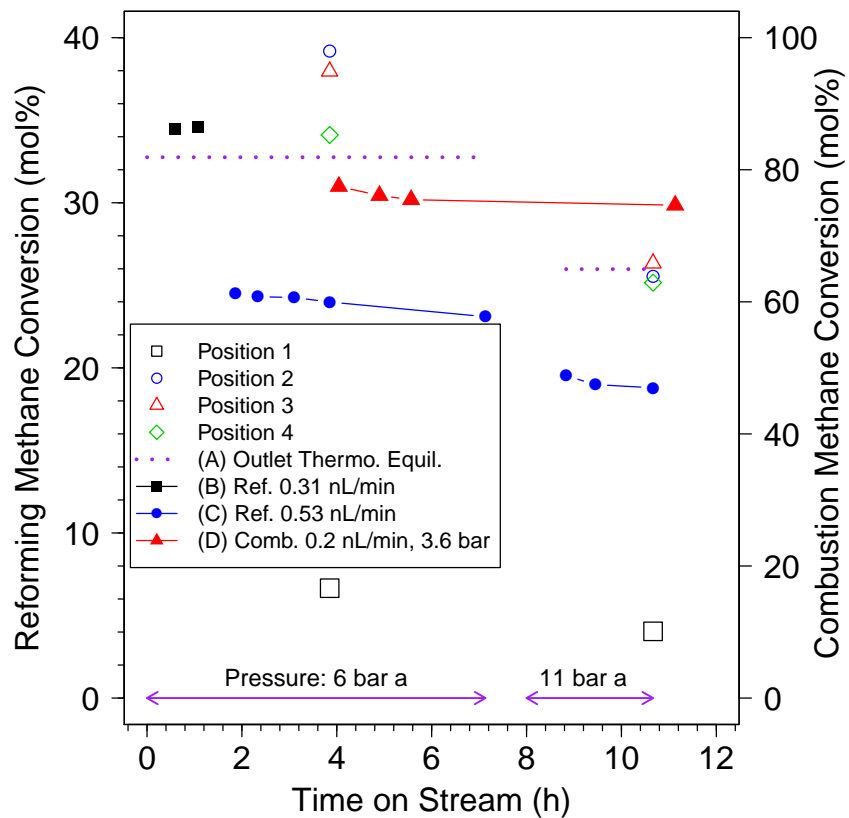


Figure C.7: Reforming Methane Conversion versus Time on Stream, for MCMR Exp. no.0.4. Reforming Operating Conditions: S/C: 4.4 $T_{ave,r}$: 550°C. Other operating conditions are detailed on Figure. Channel Height: 4 mm.

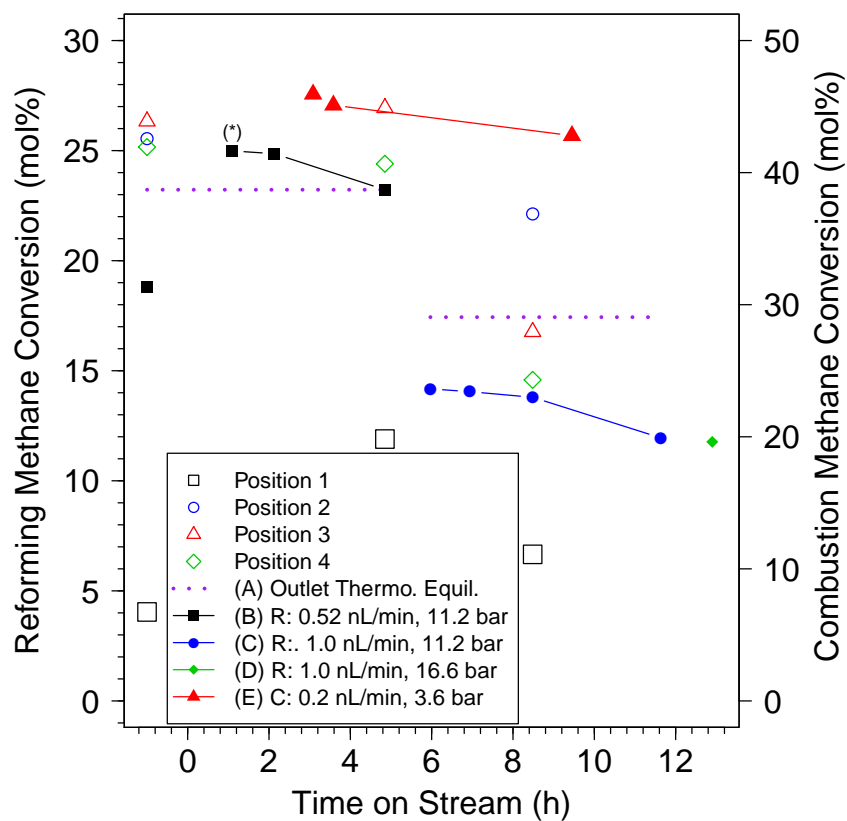


Figure C.8: Reforming Methane Conversion versus Time on Stream, for MCMR Exp. no.0.5. Reforming Operating Conditions: S/C : 4.7 (B) - 2.5 (C&D). $T_{ave,r}$: 550°C. Other operating conditions are detailed on Figure. Channel Height: 4 mm. (*) By-pass corrected. The first set of data on the left side are from Exp. no.0.4. In legend, R = reforming, C = combustion.

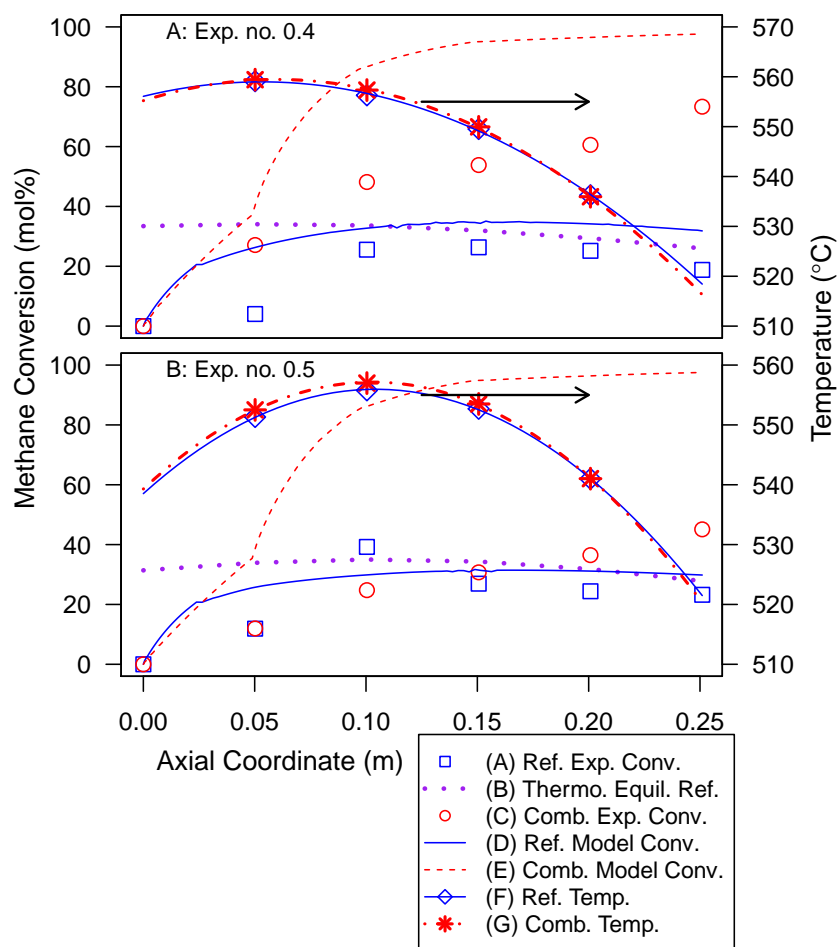


Figure C.9: Conversion and Temperature Profiles for MCMR Exp. no.0.4 and 0.5. Operating Conditions: (A. Exp. no.0.4) Reforming: CH₄ Flow: 0.53 nL/min, S/C: 4.4, P_r : 11.0 bar; Combustion: CH₄ Flow: 0.20 nL/min, 3.0%, P_c : 2.5 bar. Time on Steam: 10.6 h. (B. Exp. no.0.5) Reforming: CH₄ Flow: 0.53 nL/min, S/C: 4.7, P_r : 11.2 bar; Combustion: CH₄ Flow: 0.20 nL/min, 3.0% in air, P_c : 3.6 bar. Time on Steam: (ref.) 4.9 h, (comb.) 24.1 h. Temperature data are fitted with a second order polynomial.

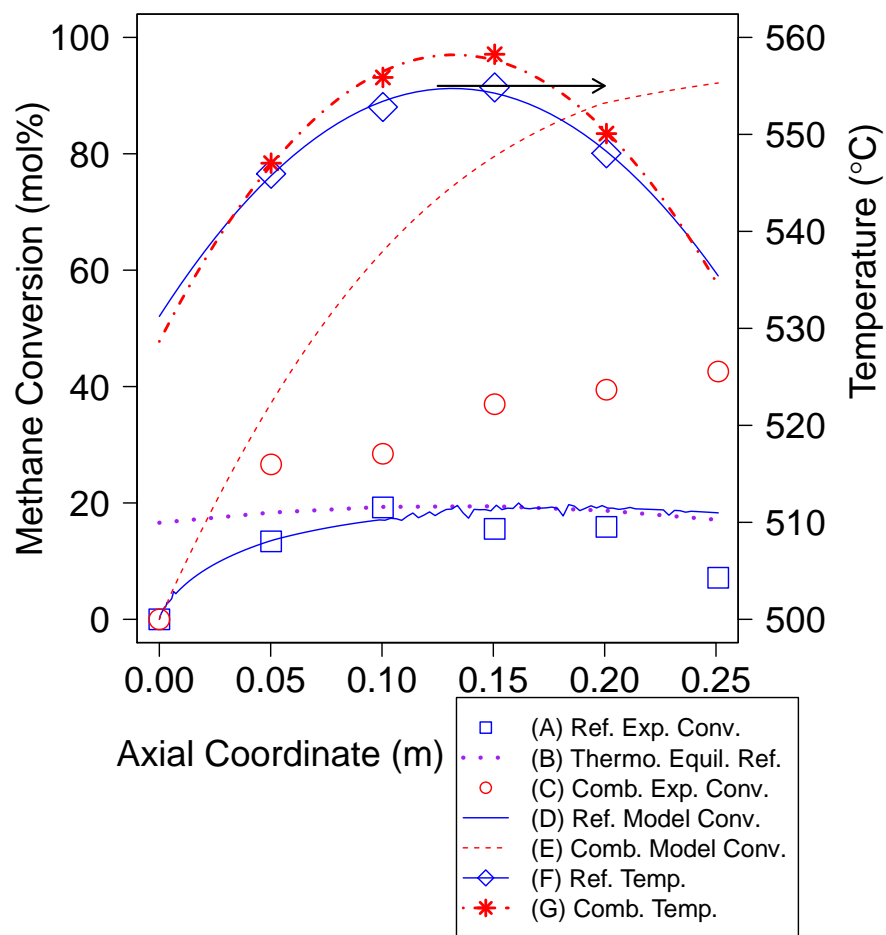


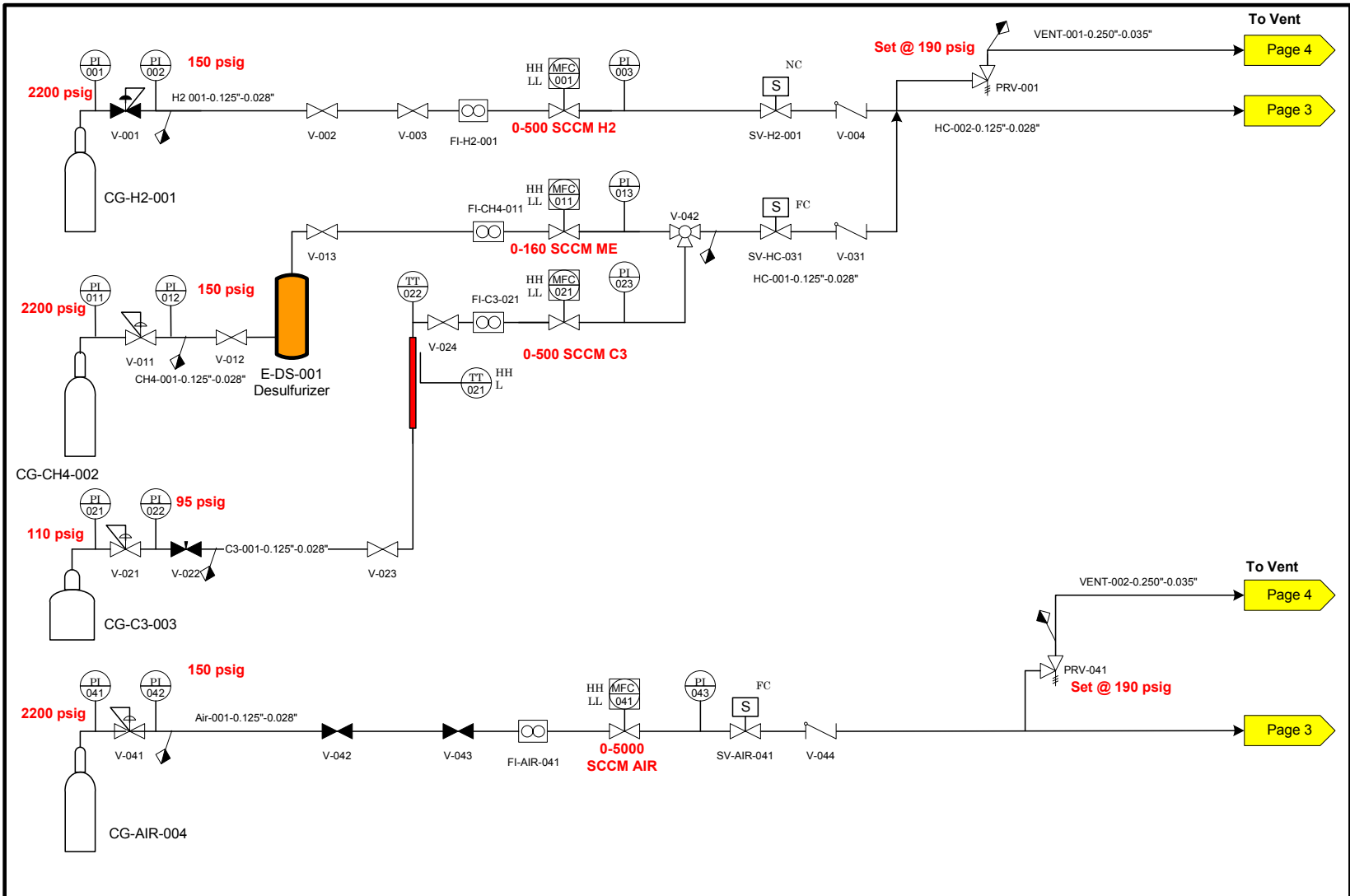
Figure C.10: Conversion and Temperature Profiles for MCMR Exp. no.0.7. Operating Conditions: Reforming: CH₄ Flow: 1.01 nL/min, S/C: 2.5, P_r : 16.4 bar; Combustion: CH₄ Flow: 0.20 nL/min, 3.0%, P_c : 2.0 bar. Time on Steam: (ref.) 10 h, (comb.) 30 h. Temperature data are fitted with a second order polynomial.

Appendix D

Micro-Reactor Supplementary Information

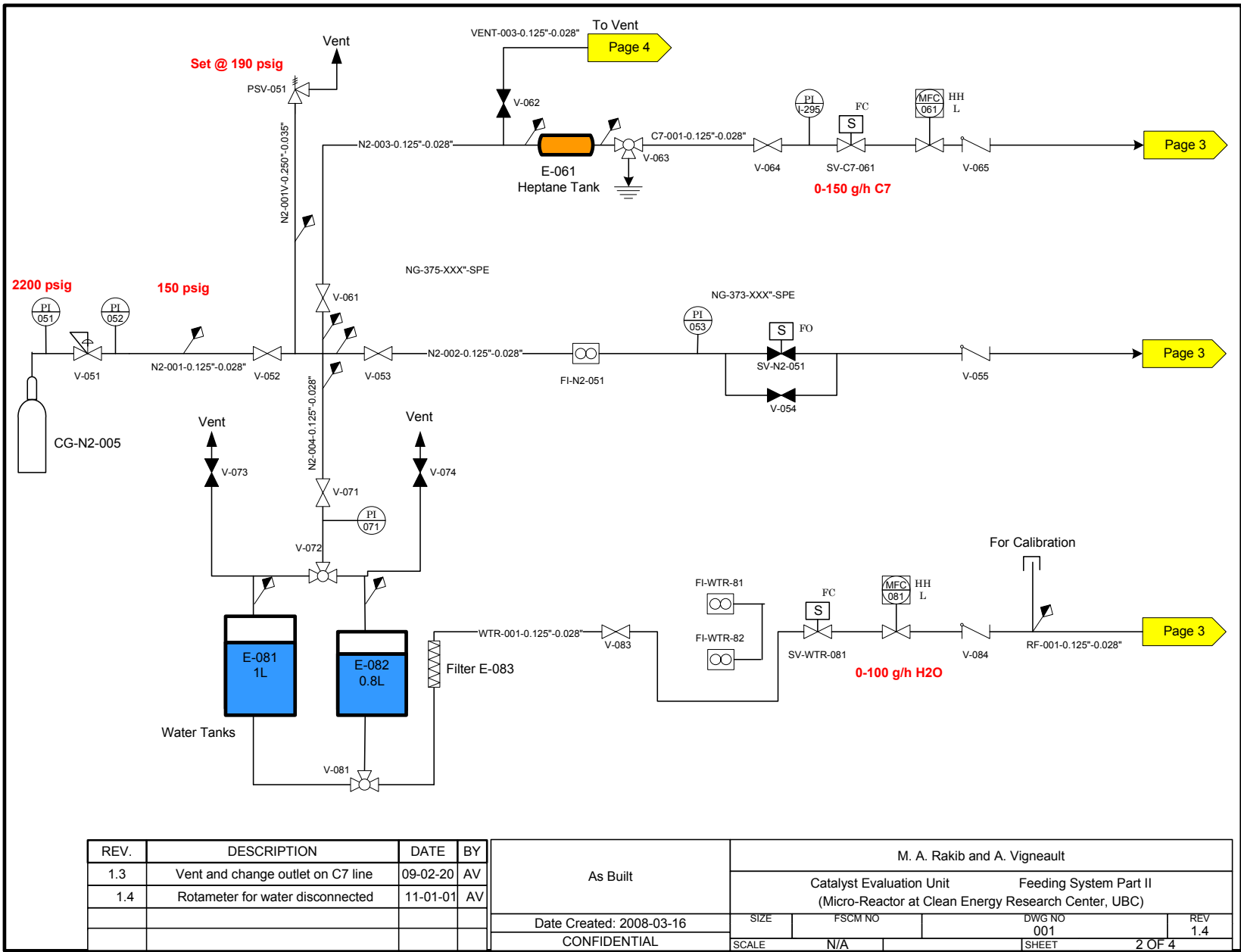
D.1 Micro-Reactor PI&D

293



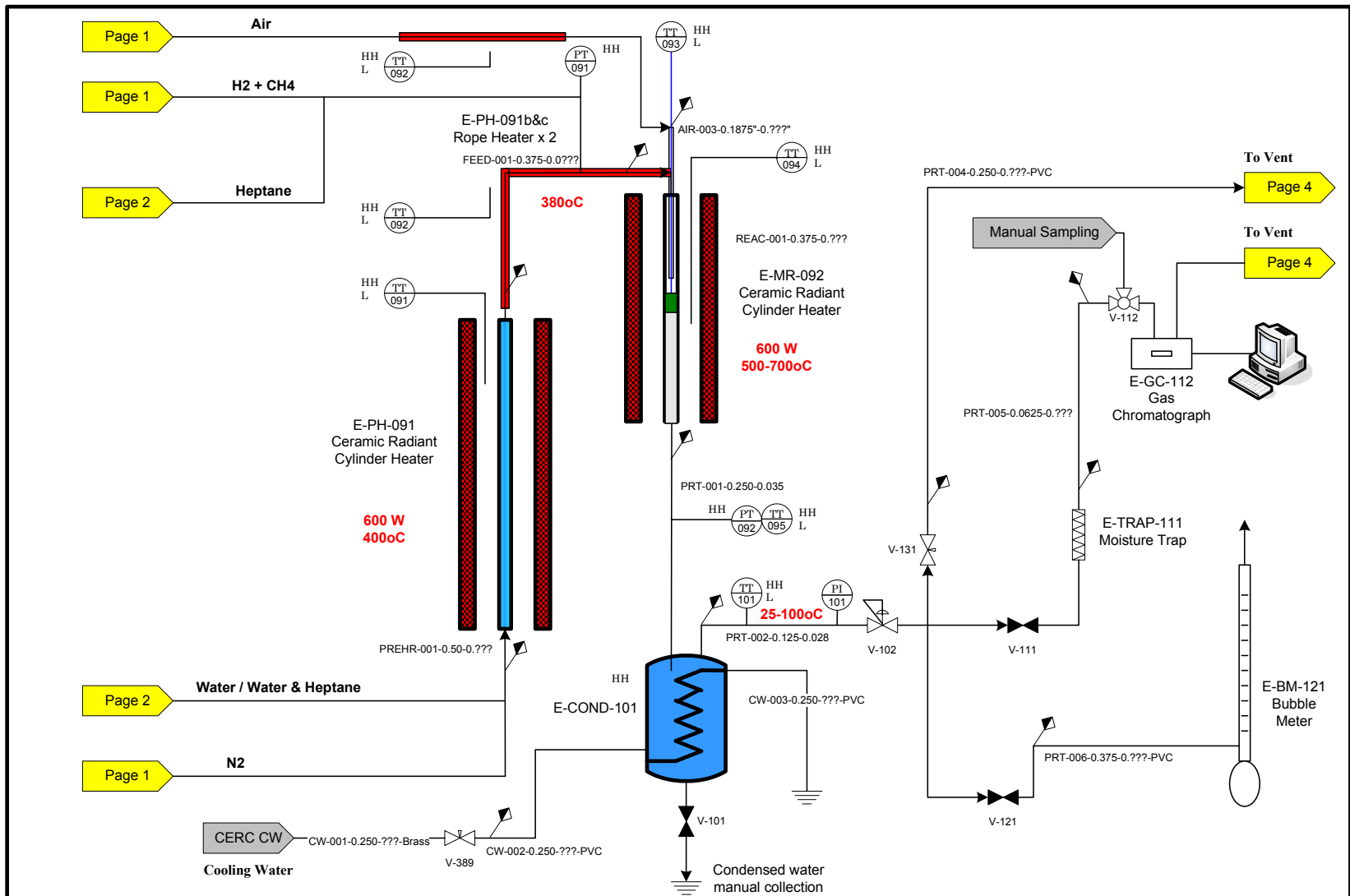
REV.	DESCRIPTION	DATE	BY	M. A. Rakib and A. Vigneault				
2.2	Flow rates and pressure updates	09-02-20	AV	As built				
				Catalyst Evaluation Unit Feeding System Part I (Micro-Reactor at Clean Energy Research Center, UBC)				
				Date Created: 2008-03-16	SIZE	FSCM NO	DWG NO	REV
				CONFIDENTIAL	SCALE	N/A	001	2.2
							SHEET	1 OF 4

294



REV.	DESCRIPTION	DATE	BY	M. A. Rakib and A. Vigneault			
1.3	Vent and change outlet on C7 line	09-02-20	AV	As Built			
1.4	Rotameter for water disconnected	11-01-01	AV				
Date Created: 2008-03-16				SIZE	FSCM NO	DWG NO	REV
CONFIDENTIAL				SCALE	N/A	001	1.4
				SHEET		2 OF 4	

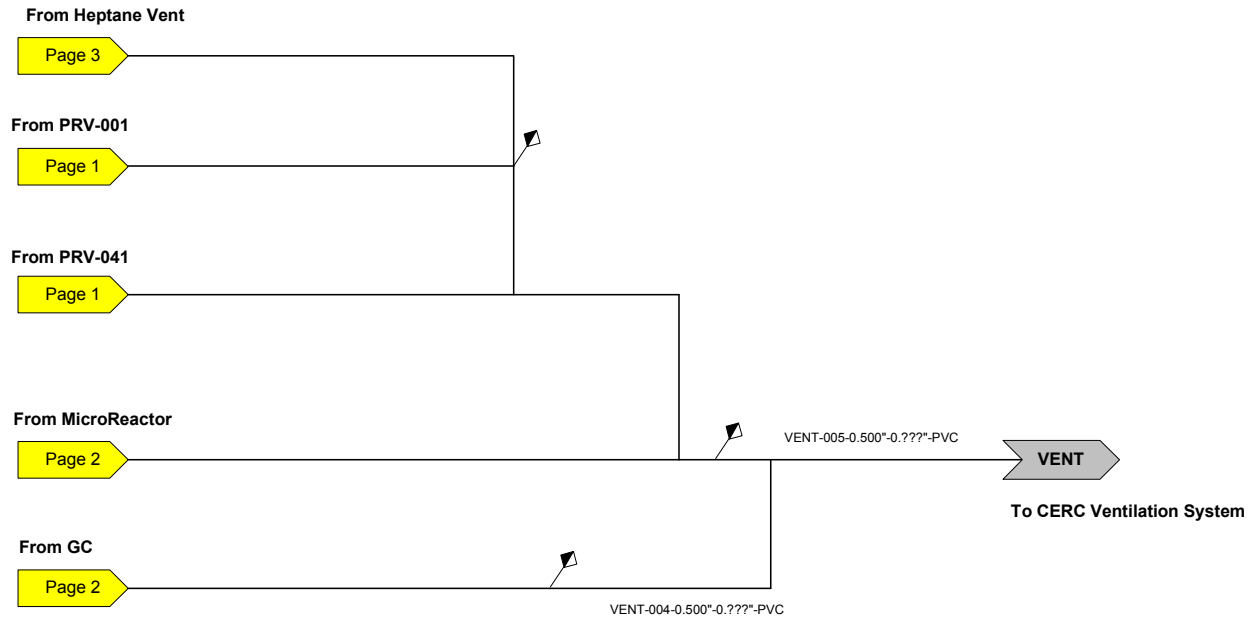
295



REV.	DESCRIPTION	DATE	BY
1.2	Rope heater added on Air line	09-02-20	AV
1.3	V-131 changed for Bonnet Valve	11-01-01	AV

As Built		M. A. Rakib and A. Vigneault			
		Catalyst Evaluation Unit MicroReactor (Micro-Reactor at Clean Energy Research Center, UBC)			
Date Created: 2008-03-16		SIZE	FSCM NO	DWG NO	REV
CONFIDENTIAL		SCALE	N/A	001	1.3
		SHEET		3 OF 4	

296

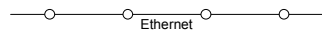


REV.	DESCRIPTION	DATE	BY	M. A. Rakib and A. Vigneault				
1.2	Add heptane vent line	09-02-20	AV	As built	Catalyst Evaluation Unit Vent (Micro-Reactor at Clean Energy Research Center, UBC)			
					SIZE	FSCM NO	DWG NO	REV
				Date Created: 2008-03-16		001	1.2	
				CONFIDENTIAL	SCALE	N/A	SHEET	4 OF 4

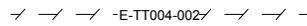
D.2 Micro-Reactor Electrical and Control Diagram

Wires

Wire denomination:
 E-Device code name- number wire line: specs (ampereage used) AC, DC current lines
 AC / DC



Ethernet



Thermocouple



Emergency Push Button



Ground



Overload Switch



AC Power Source



Solid State Relay



Switch in Contactor

Connectors



Outlet



DC + Terminal Block



DC - / commun Terminal Block



AC + Terminal Blocks



AC - Terminal Blocks



Ethernet



Quick Connect for Thermocouple



Manual Switch (Salzer)



Light



Fuse



Coil in contactor



Heater



Pump

E-112

Instrument



Flow control valve/ Mass Flow Meter

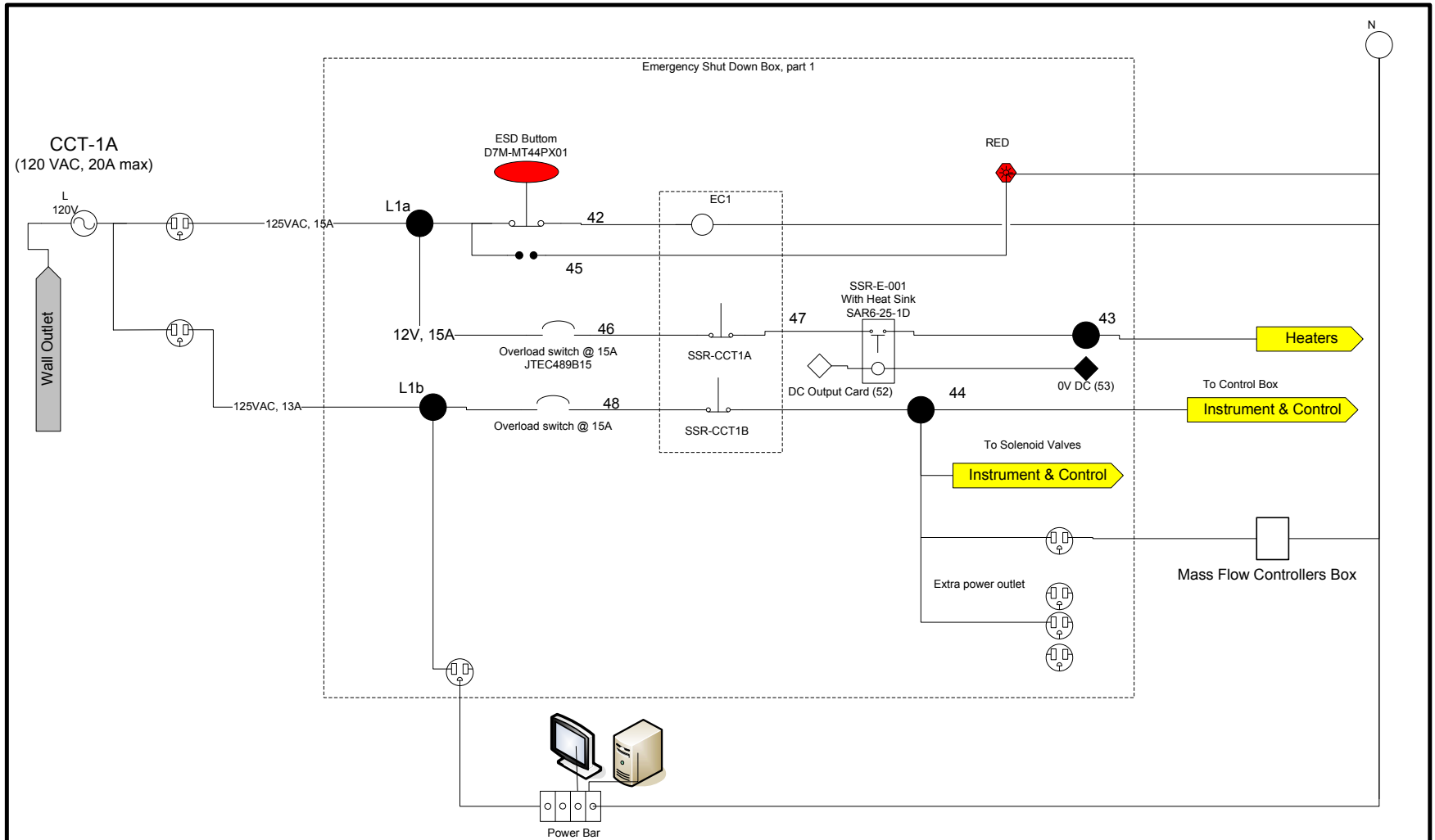


Pressure Transducer



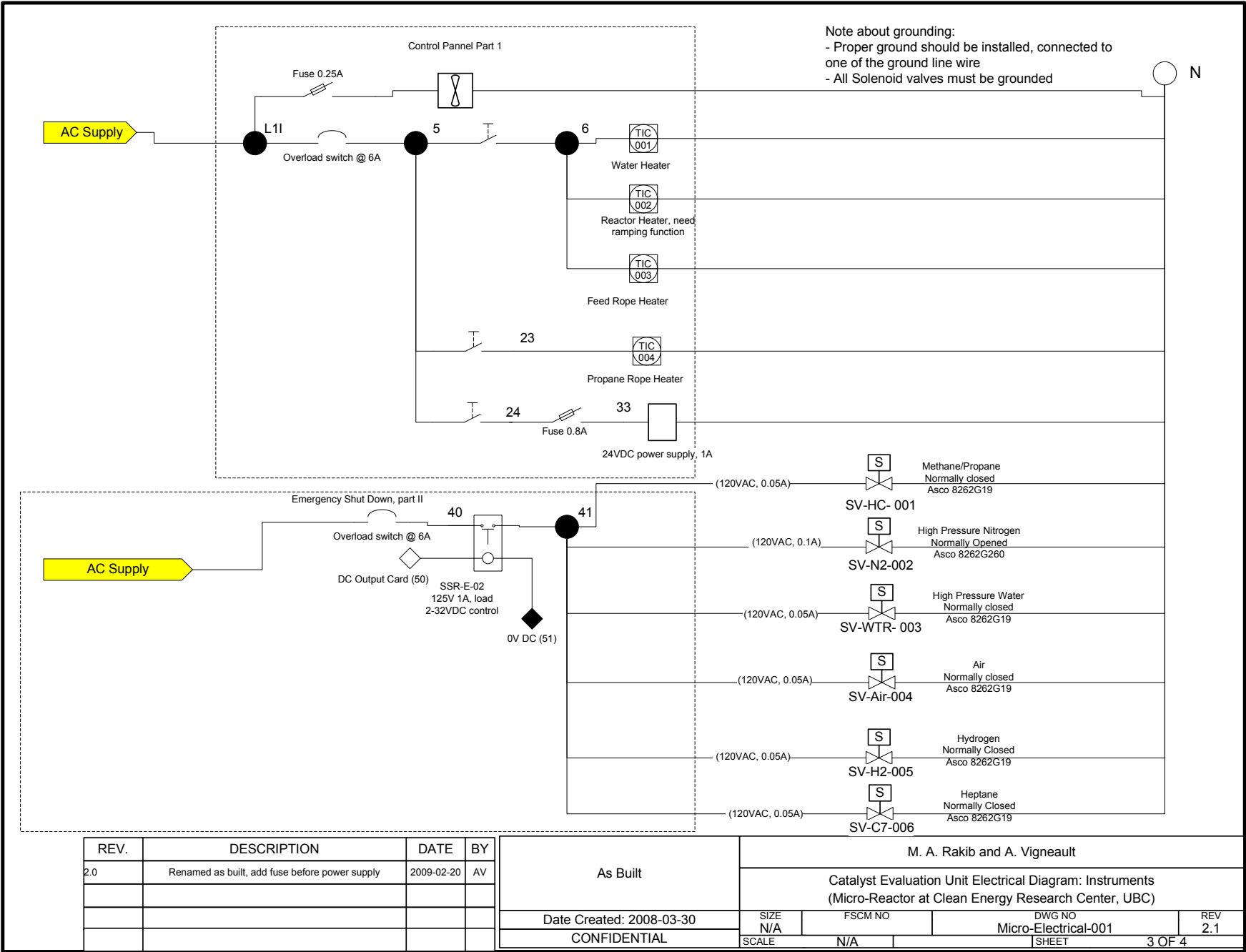
Temperature Indicator & Controller

REV.	DESCRIPTION	DATE	BY	M. A. Rakib and A. Vigneault ing. jr.				
2.2	Name updates	2009-02-20	AV	As built				
				Electrical Connections Multi Channel Reactor: LEGEND				
				Created: 2008-03-30	SIZE	FSCM NO	DWG NO	REV
				CONFIDENTIAL	SCALE	N/A	002	2.2
							SHEET	1 OF 4



REV.	DESCRIPTION	DATE	BY	M. A. Rakib and A. Vigneault				
1.2	Change names, reconnected red light	2009-02-20	AV	As Built				
				Catalyst Evaluation Unit Electrical Diagram: AC Supply (Micro-Reactor at Clean Energy Research Center, UBC)				
				Date created: 2008-03-30	SIZE N/A	FSCM NO	DWG NO Micro-Electrical-001	REV 1.2
				CONFIDENTIAL	SCALE	N/A	SHEET	2 OF 4

300

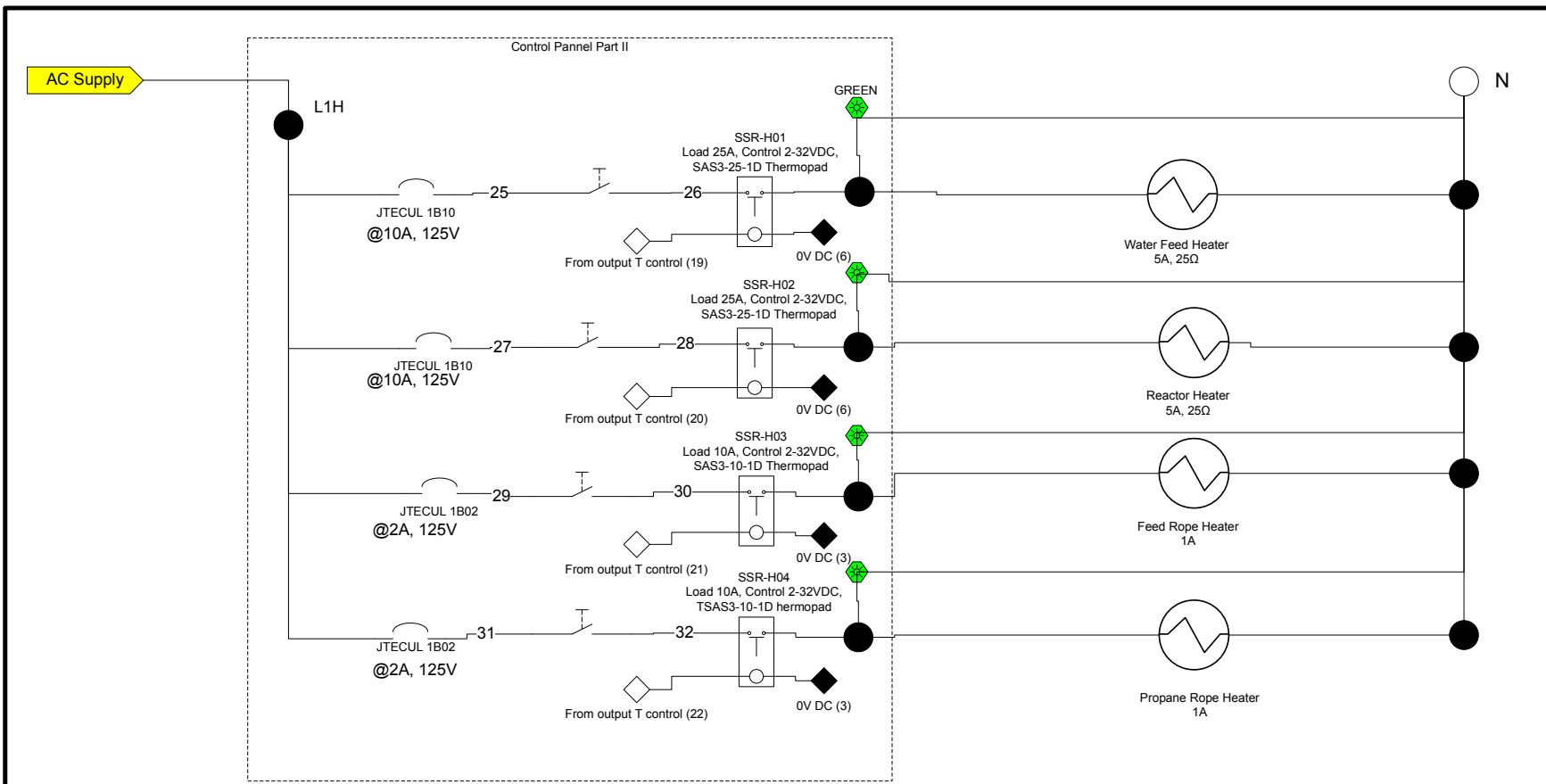


REV.	DESCRIPTION	DATE	BY
2.0	Renamed as built, add fuse before power supply	2009-02-20	AV

As Built
Date Created: 2008-03-30
CONFIDENTIAL

M. A. Rakib and A. Vigneault			
Catalyst Evaluation Unit Electrical Diagram: Instruments (Micro-Reactor at Clean Energy Research Center, UBC)			
SIZE N/A	FSCM NO N/A	DWG NO Micro-Electrical-001	REV 2.1
SCALE	N/A	SHEET	3 OF 4

301



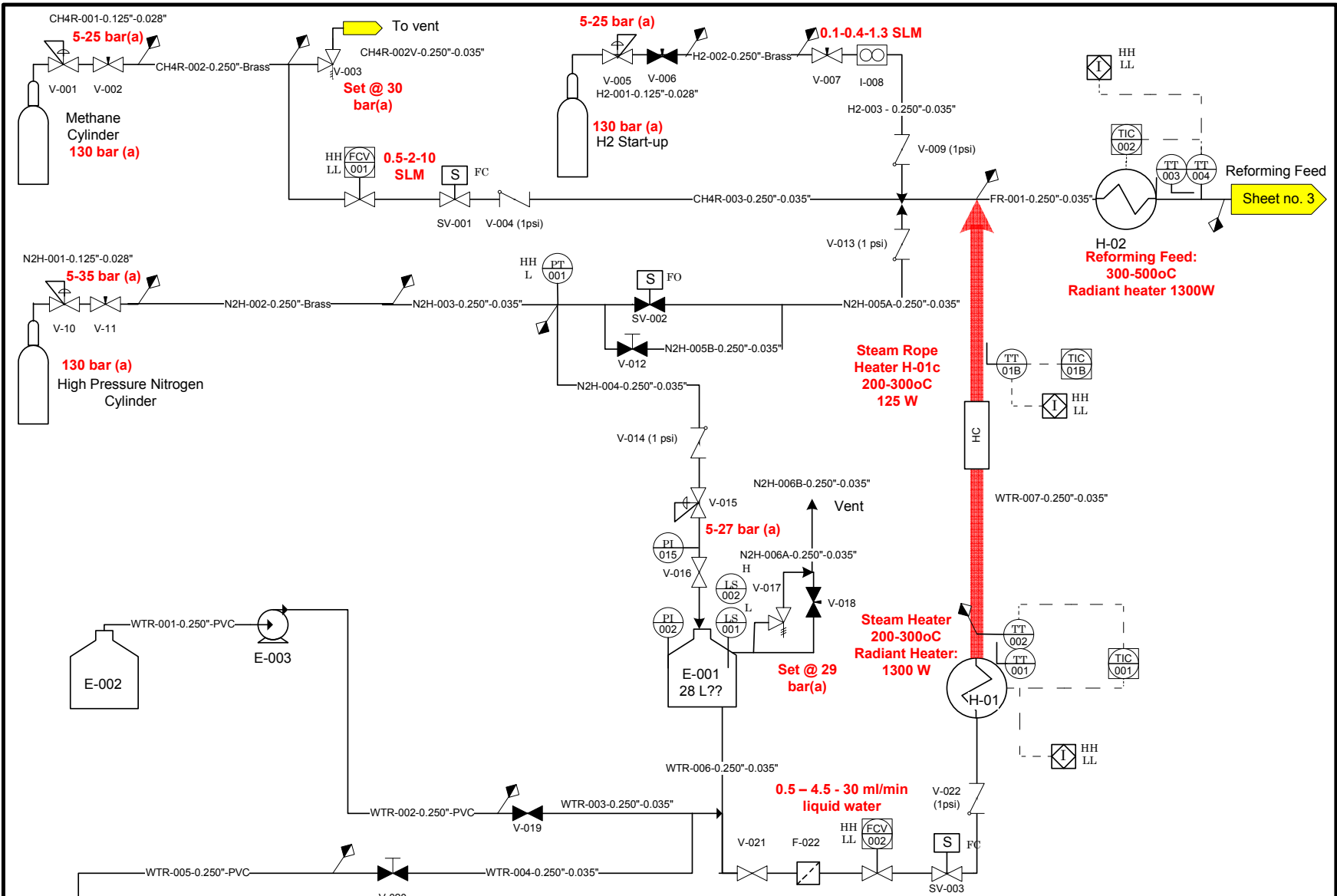
REV.	DESCRIPTION	DATE	BY	M. A. Rakib and A. Vigneault					
2.0	Renamed as built, change fuses to breakers	20080616	AV	Preliminary					
									Catalyst Evaluation Unit Electrical Diagram: Heaters (Micro-Reactor at Clean Energy Research Center, UBC)
				Last update: 2008-06-16		SIZE N/A	FSCM NO	DWG NO Micro-Electrical-001	REV 2
				CONFIDENTIAL		SCALE	N/A	SHEET	4 OF 4

Appendix E

Multi-Channel Reactor Supplementary Information

E.1 MCMR PI&D

303

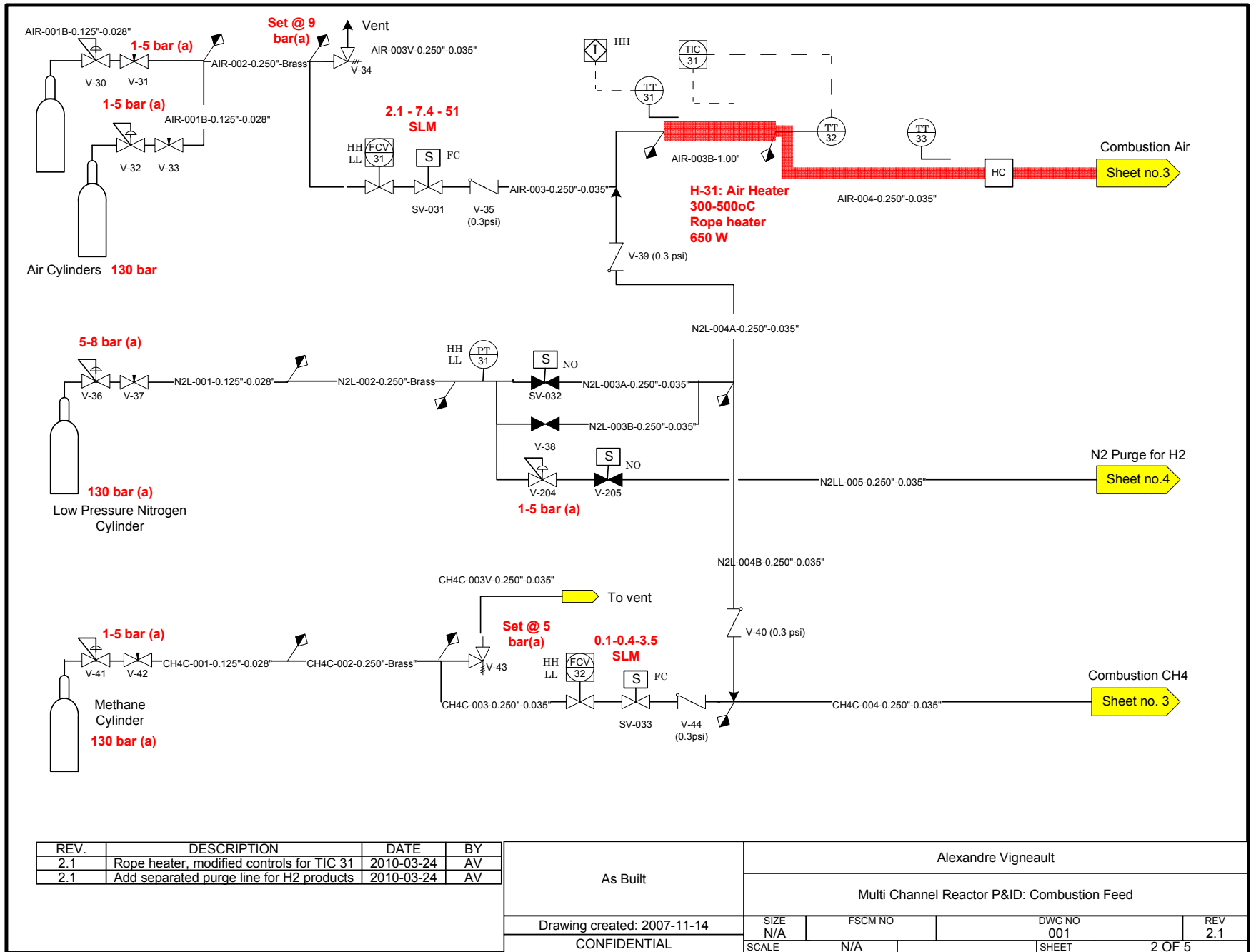


Sheet no. 3

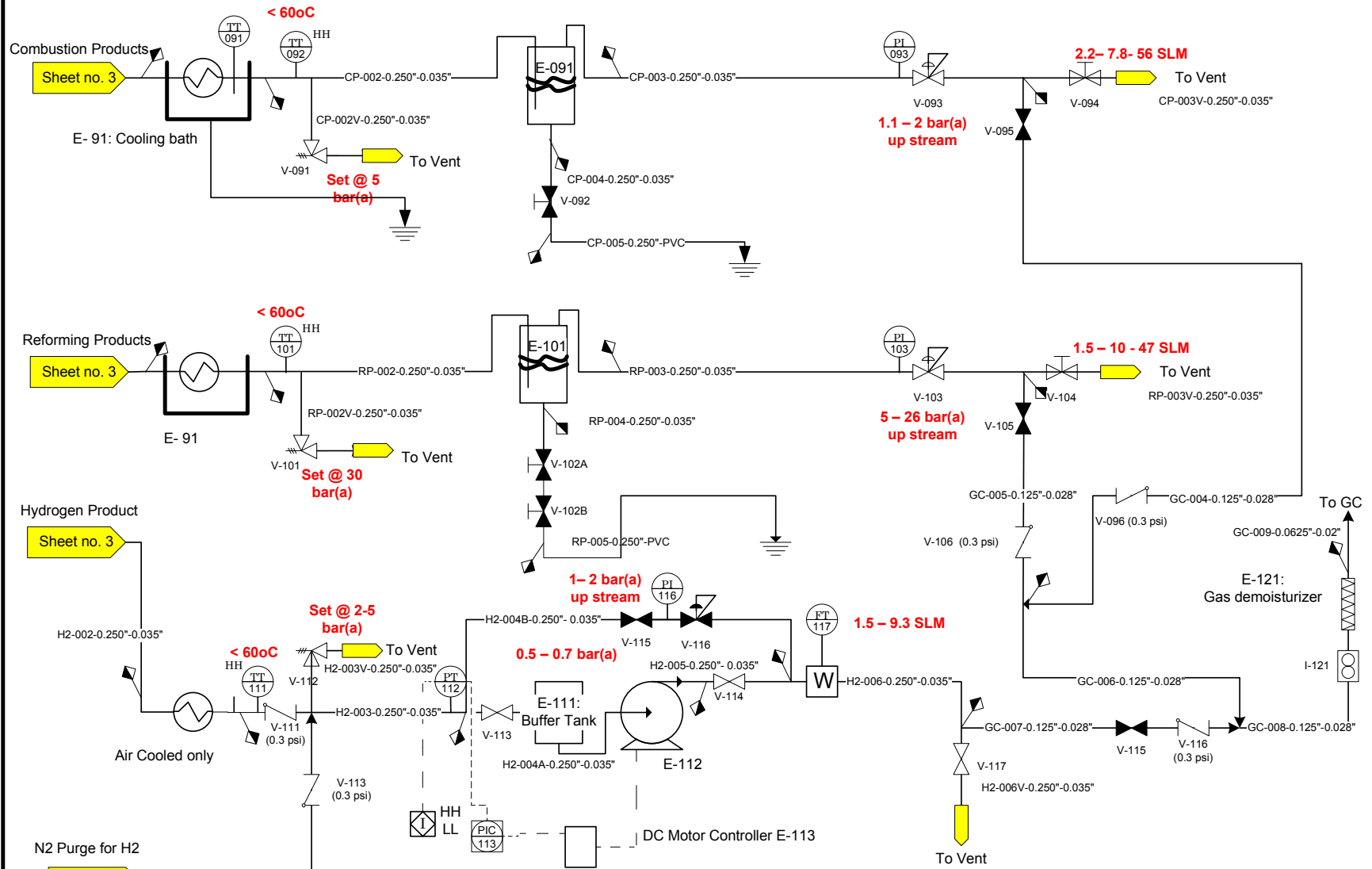
REV.	DESCRIPTION	DATE	BY
2.1	Steam rope heater added	2010-03-24	AV

As Built		Alexandre Vigneault		
Multi Channel Reactor: Reforming Feed				
Drawing created: 2007-11-14		SIZE N/A	FSCM NO	DWG NO 001
CONFIDENTIAL		SCALE N/A	SHEET	REV 2.1
				1 OF 5

304



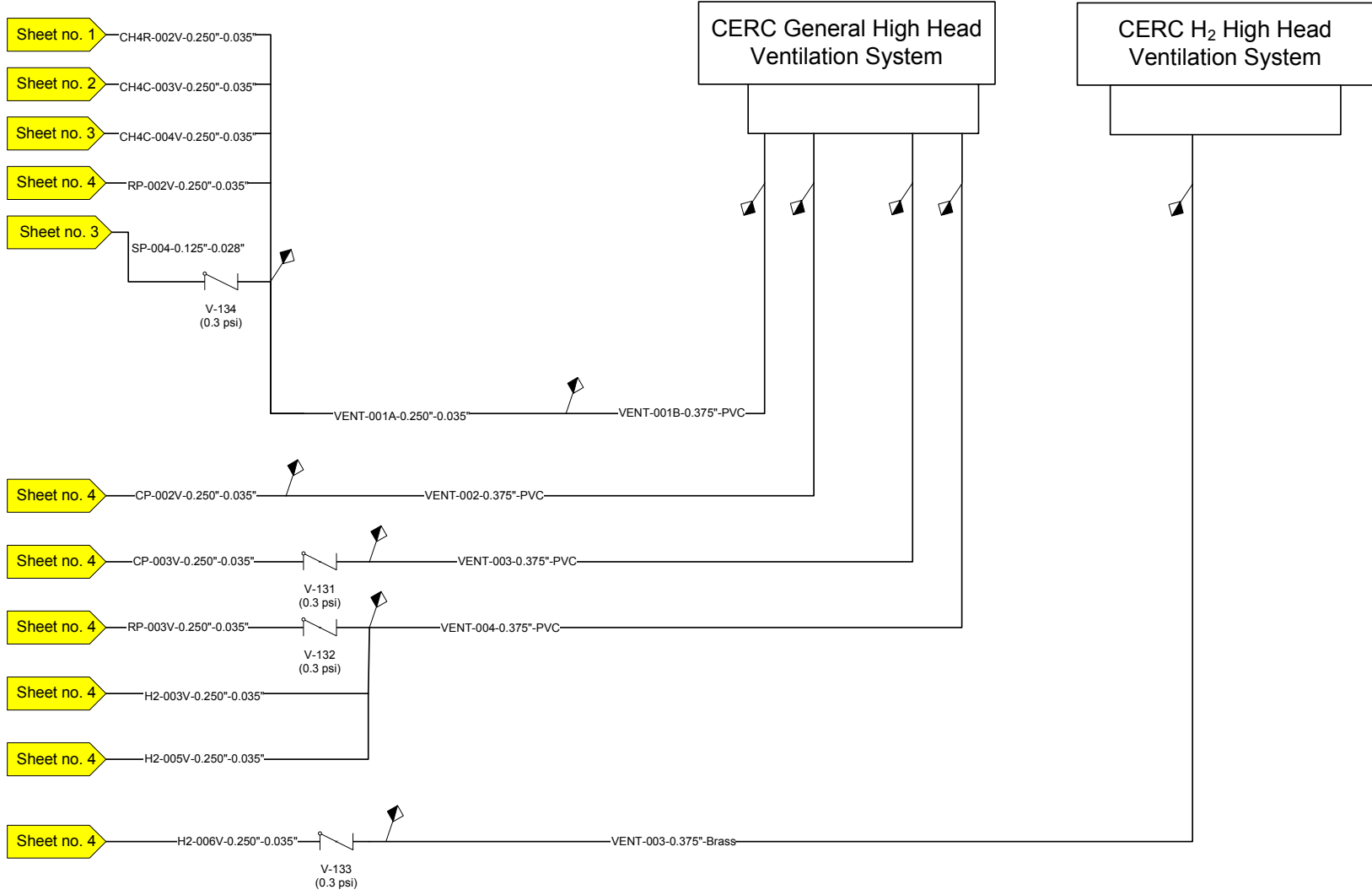
306



REV.	DESCRIPTION	DATE	BY
2.1	Outlet valves changed for bonnet type	2010-03-25	AV
2.2	Drain trap removed (not working)	2011-01-01	AV

As Built		Alexandre Vigneault			
		Multi-Channel Reactor: Products			
Drawing created: 2007-11-15		SIZE N/A	FSCM NO	DWG NO 001	REV 2.1
CONFIDENTIAL		SCALE	N/A	SHEET	4 OF 5

307



REV.	DESCRIPTION	DATE	BY
2.1	SP-004 line added	2010-03-25	AV

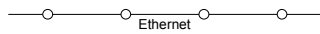
As Built	Alexandre Vigneault			
	Multi-Channel Reactor: Venting			
Drawing created: 2007-11-15	SIZE N/A	FSCM NO	DWG NO 001	REV 2.1
CONFIDENTIAL	SCALE	N/A	SHEET	5 OF 5

E.2 MCMR Electrical Diagram

309

Wires

Wire denomination:
 E-Device code name- number wire line: specs (ampereage used) AC, DC current lines
 AC / DC



Ethernet



Thermocouple



Emergency Push Button



Ground



Overload Switch



AC Power Source

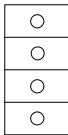
Connectors



Wall Outlet



AC Connector/junctions



Connector Block



DC +



DC - / common



Ethernet



Terminal Block



Quick Connect for Thermocouple



SSR: Solid State Relay
 MR: Mechanical Relay



Switch in Contactor



Manual Switch



Light



Fuse



Coil in contactor



Fan

Instrument



Flow control valve/ Mass Flow Meter



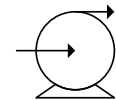
Pressure Transducer



Thermocouple



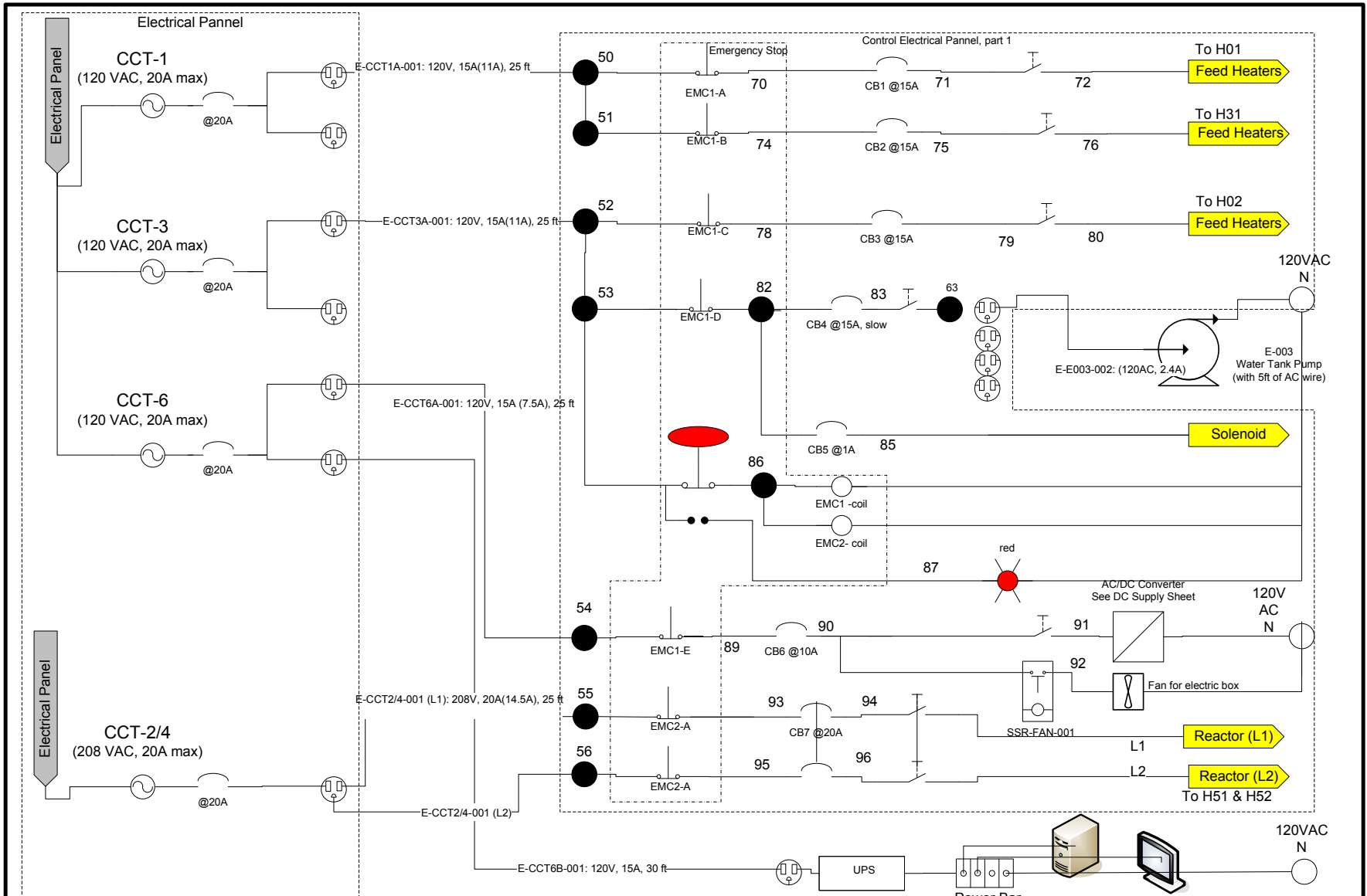
Heater



Pump

E-112

REV.	DESCRIPTION	DATE	BY	Alexandre Vigneault				
				Preliminary				
				Electrical Connections Multi Channel Reactor: LEGEND				
				Last update: 2008-05-05	SIZE	FSCM NO	DWG NO	REV
				CONFIDENTIAL	SCALE	N/A	002	3
							SHEET	1 OF 16

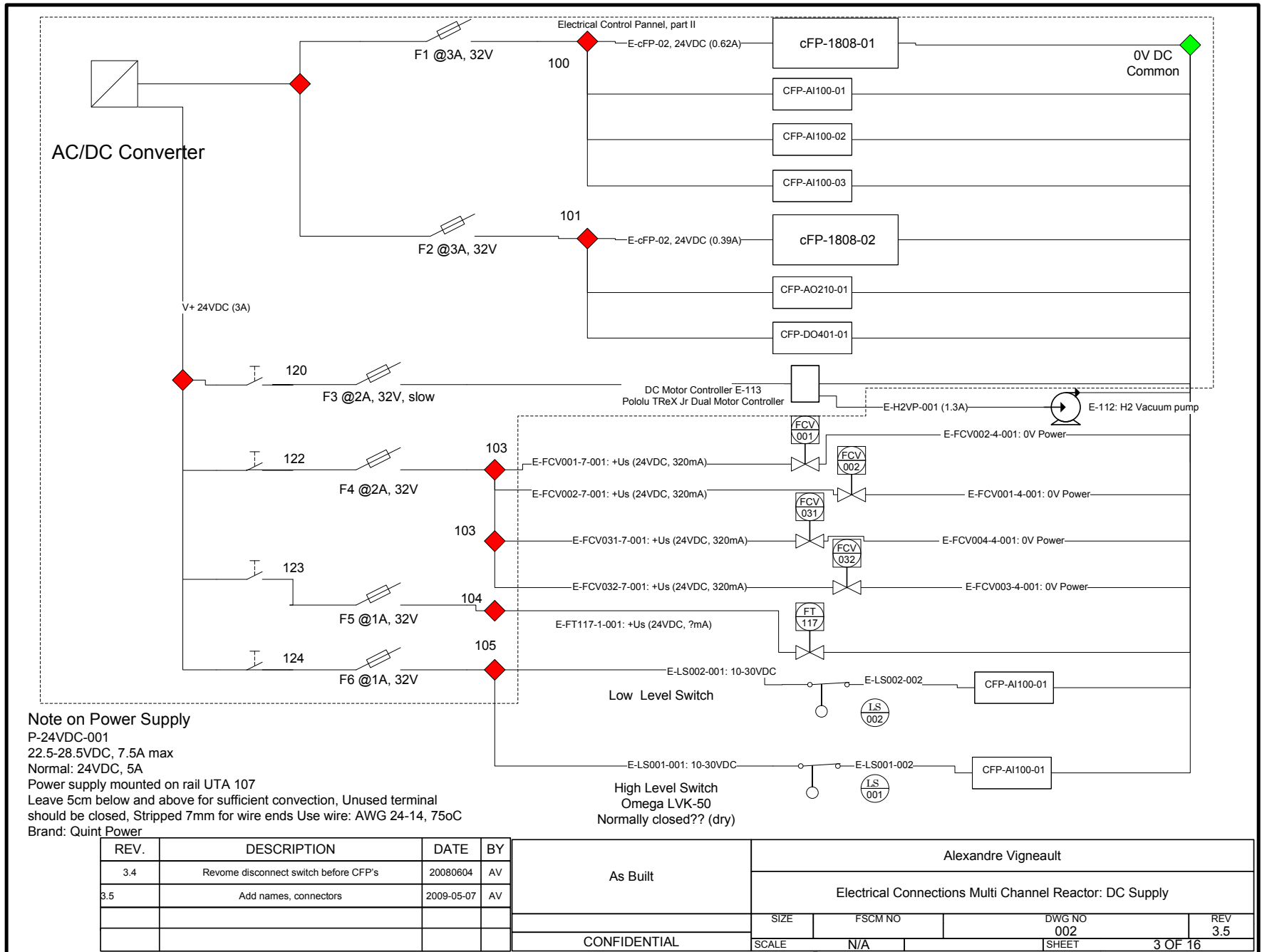


REV.	DESCRIPTION	DATE	BY
3.4	Remove CCT-1b, 3b, replace fuse by breakers, fix L1, L2	2009-05-05	AV

As Built		Alexandre Vigneault			
		Electrical Connections Multi Channel Reactor: AC Supply			
SIZE	FSCM NO	DWG NO	REV		
		002	3.4		
SCALE	N/A	SHEET	2 OF 16		

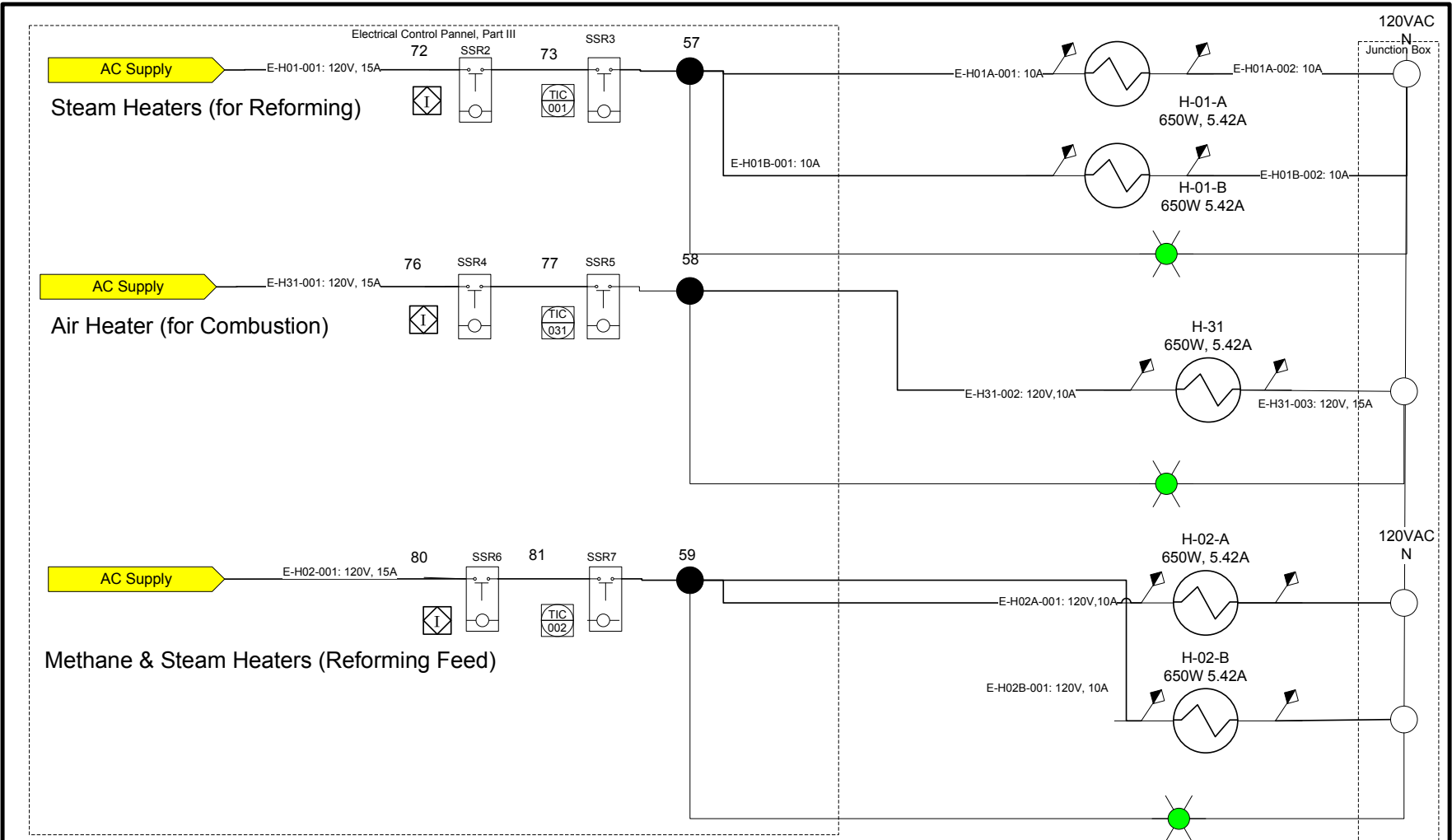
CONFIDENTIAL

311



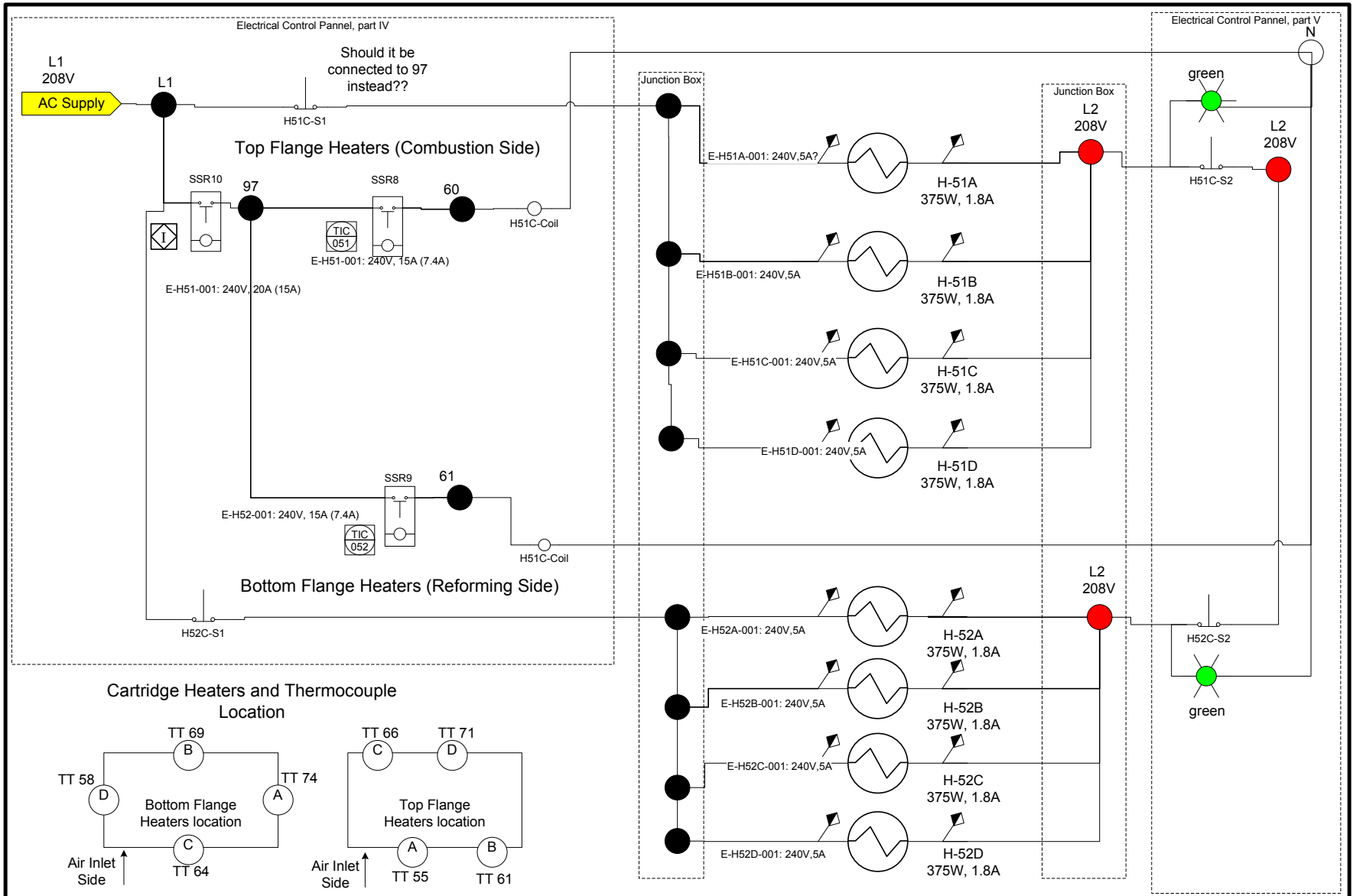
As Built				Alexandre Vigneault			
CONFIDENTIAL				Electrical Connections Multi Channel Reactor: DC Supply			
SIZE	FSCM NO	DWG NO	REV				
SCALE	N/A	002	3.5	SHEET 3 OF 16			

312

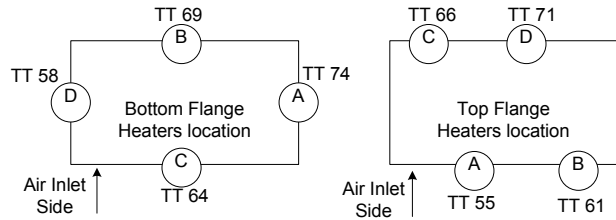


REV.	DESCRIPTION	DATE	BY	Alexandre Vigneault			
3.2	Renaming relays, change all MR of SSR	20080604	AV	Electrical Connections Multi Channel Reactor: H01 & H31			
3.3	Remove junctions boxes, name connectors	2009-05-09	AV				
				SIZE	FSCM NO	DWG NO	REV
						001	3.3
				CONFIDENTIAL	SCALE	N/A	SHEET 4 OF 16

313



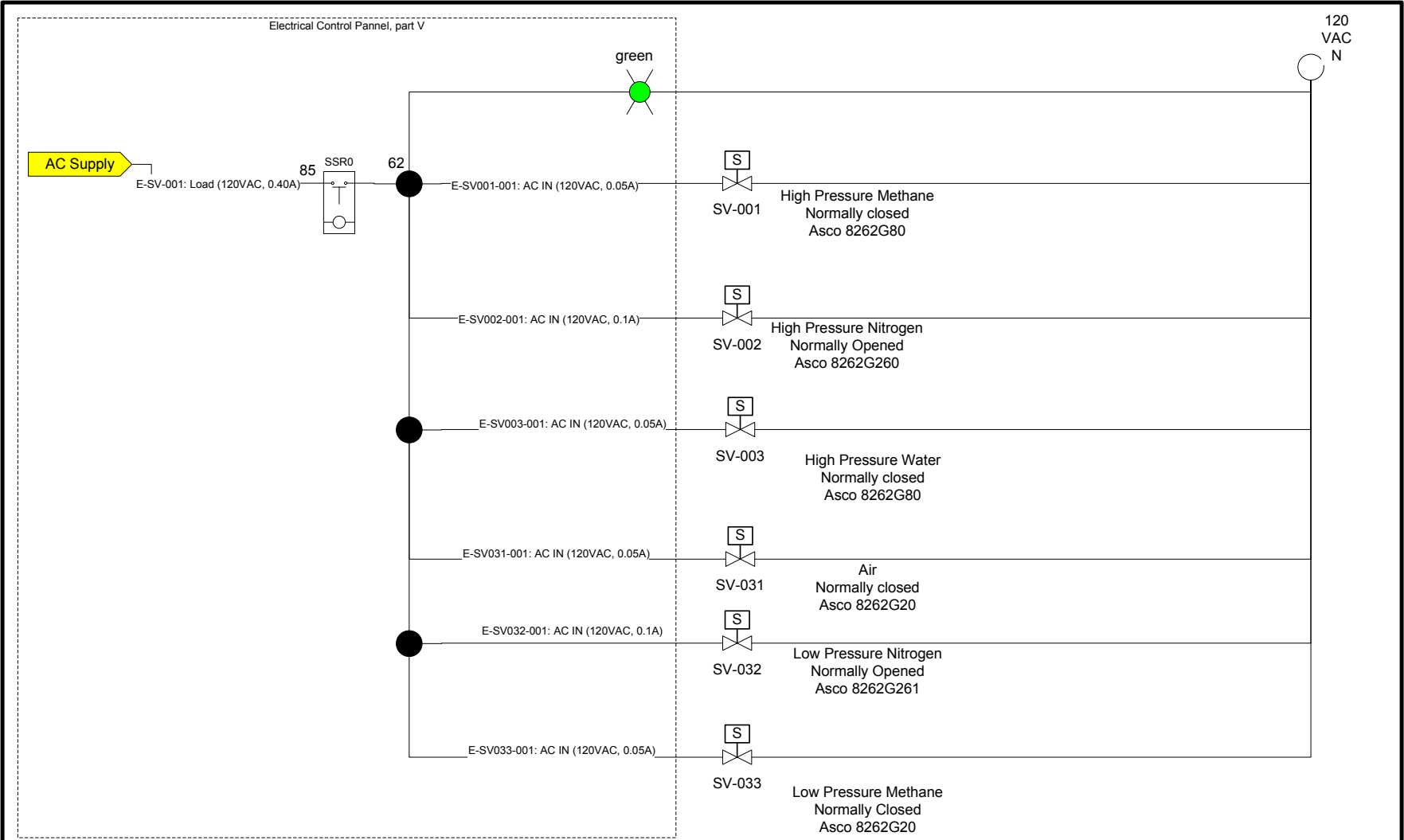
Cartridge Heaters and Thermocouple Location



REV.	DESCRIPTION	DATE	BY
4.2	Renaming relays, change MR to SSR	2008-06-04	AV
4.3	Add 2 contactors, in order to control the lights	2009-05-13	AV

As Built	Alexandre Vigneault			
	Electrical Connections Multi Channel Reactor: Reactor Heaters			
CONFIDENTIAL	SIZE	FSCM NO	DWG NO	REV
	SCALE	N/A	001	4.3
			SHEET	5 OF 16

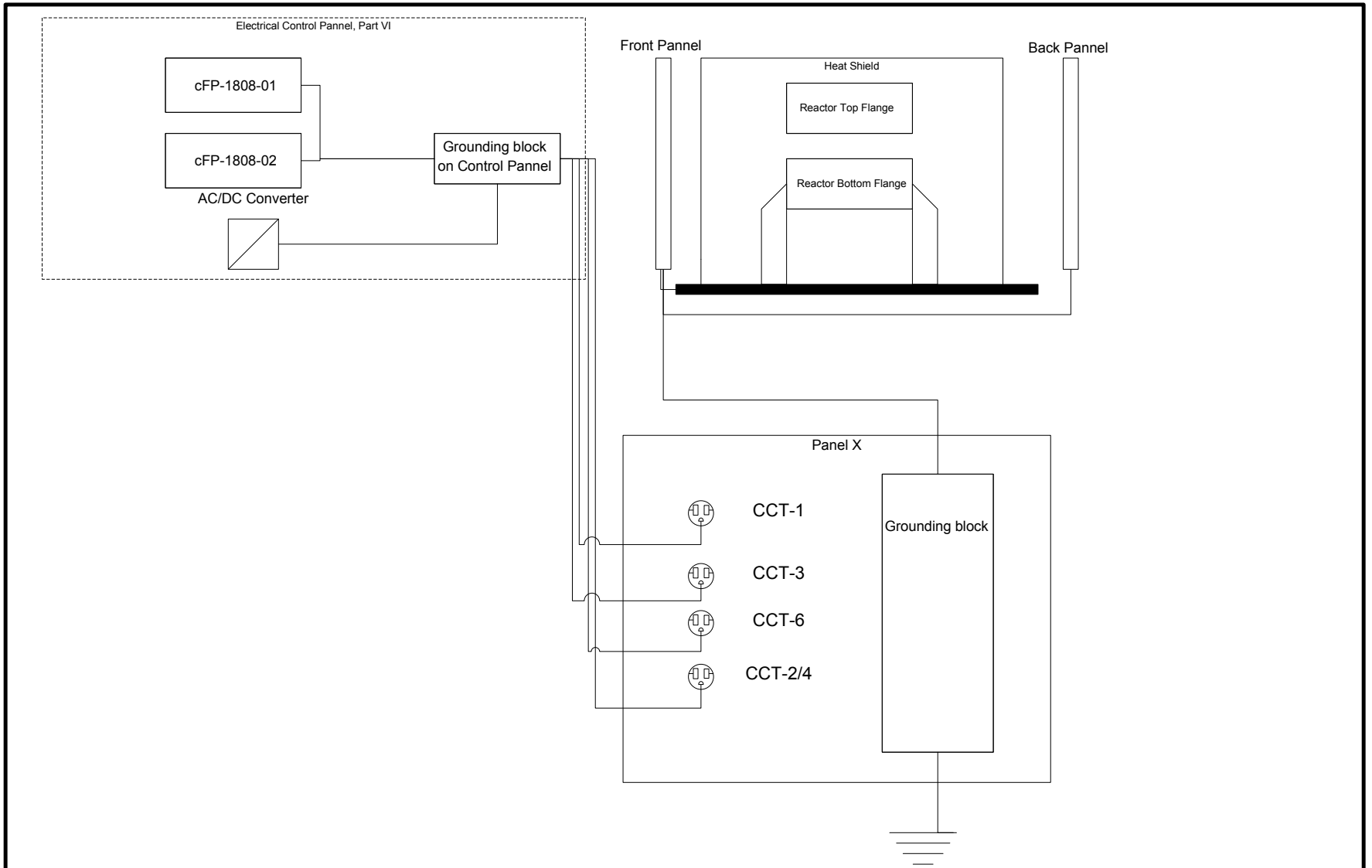
314



REV.	DESCRIPTION	DATE	BY	Alexandre Vigneault			
3.1	Add Pilot Light	2009-05-13	AV	As Built			
				Electrical Connections Multi Channel Reactor: Solenoid Valves			
				SIZE	FSCM NO	DWG NO	REV
						002	3.1
				SCALE	N/A	SHEET	6 OF 16

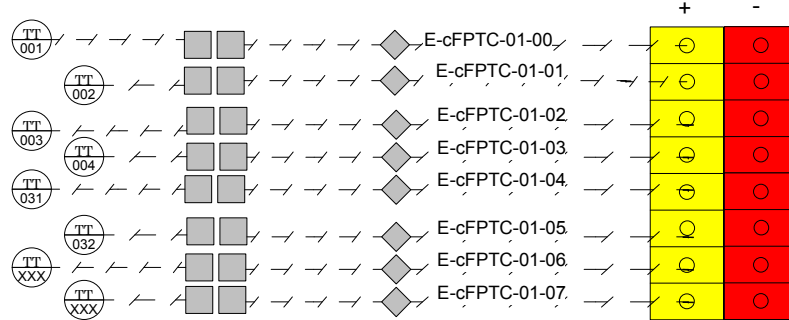
CONFIDENTIAL

315

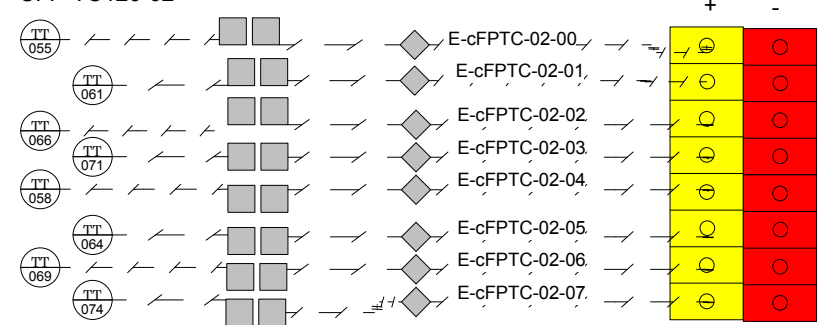


REV.	DESCRIPTION	DATE	BY	Alexandre Vigneault			
3	Rewiring as Built	2009-05-13	AV	As Built			
				Electrical Connections Multi Channel Reactor: Grounding			
				SIZE	FSCM NO	DWG NO	REV
				CONFIDENTIAL	N/A	002	3
				SCALE		SHEET	7 OF 16

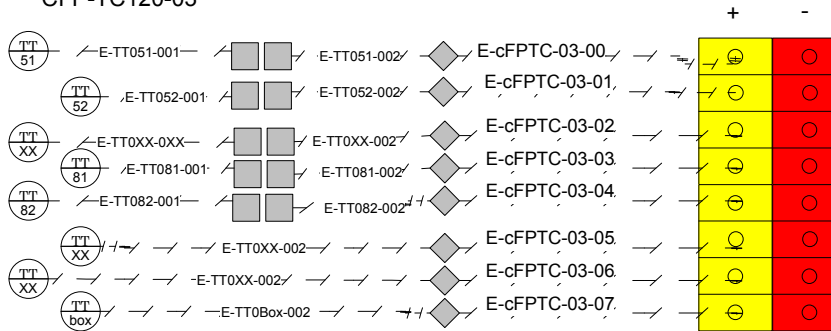
CFP-TC120-01



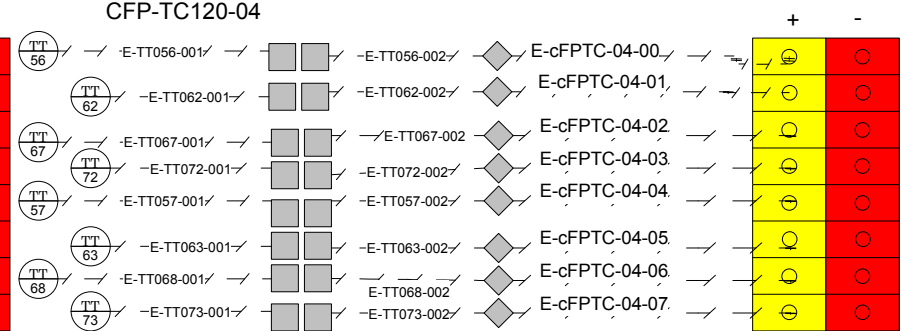
CFP-TC120-02



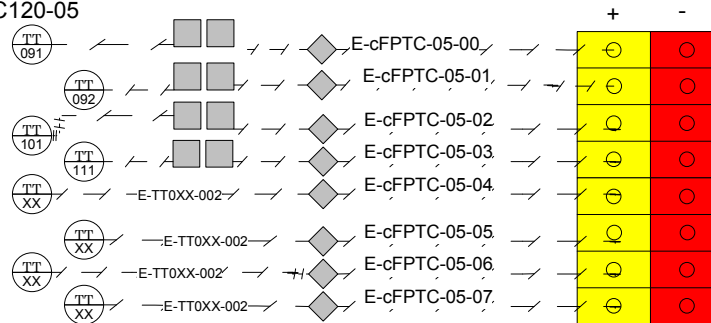
CFP-TC120-03



CFP-TC120-04



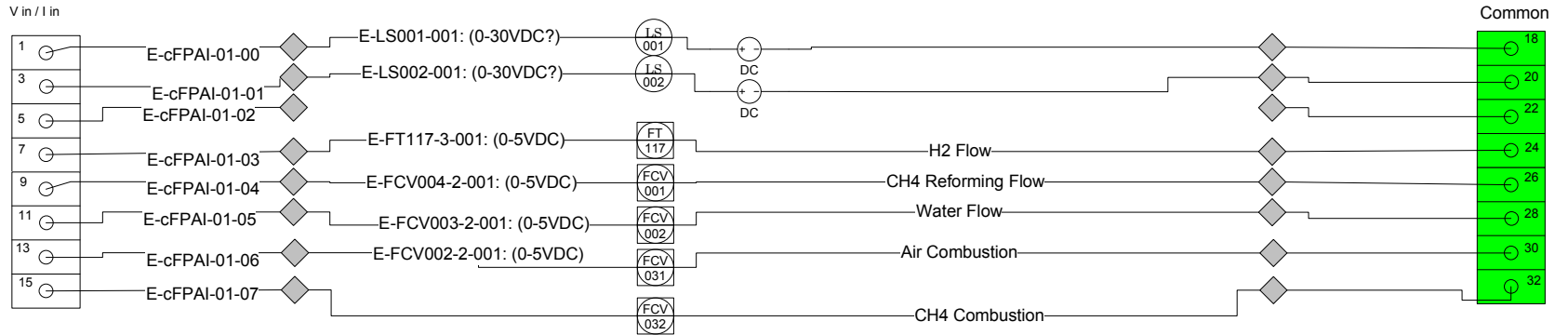
CFP-TC120-05



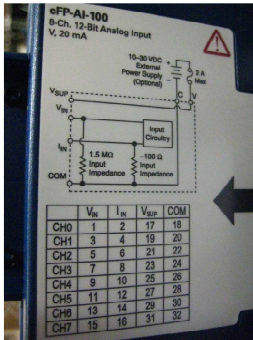
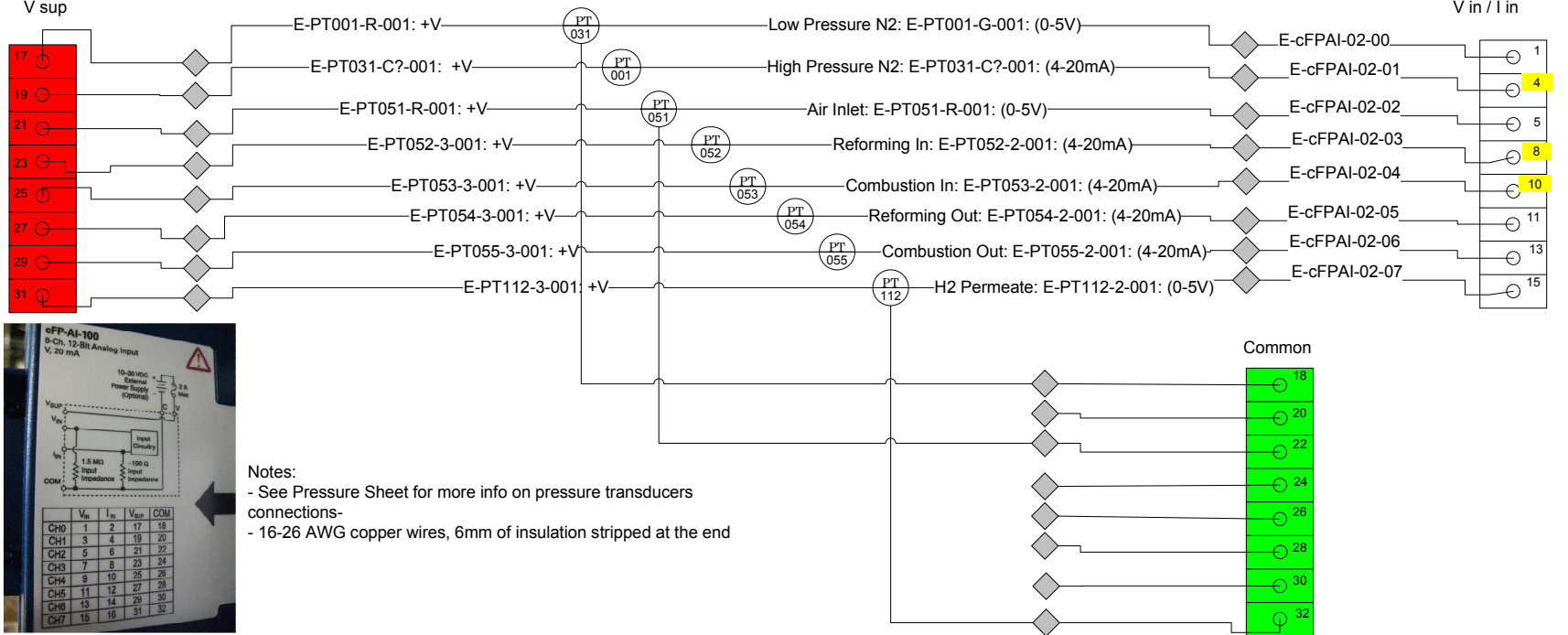
All thermocouples are type K
 For the sake of simplicity, one of two wires are shown for thermocouple wires
 Each thermocouple comes with a 80" wire

REV.	DESCRIPTION	DATE	BY	Alexandre Vigneault			
2.1	Removed TT 000, add quick connect connectors	2009-05-13	AV	As Built			
				Electrical Connections Multi Channel Reactor: Thermocouple Input			
				SIZE	FSCM NO	DWG NO	REV
				SCALE	N/A	002	2.1
				CONFIDENTIAL		SHEET	8 OF 16

CFP-AI100-03 (Interface 1 Bank 8)



CFP-AI100-02 (Interface 1 Bank 6)



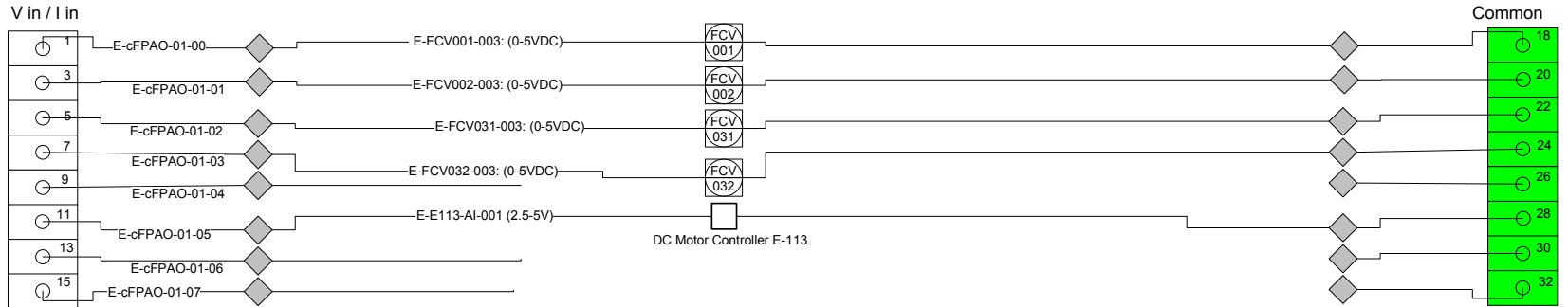
Notes:
 - See Pressure Sheet for more info on pressure transducers connections-
 - 16-26 AWG copper wires, 6mm of insulation stripped at the end

317

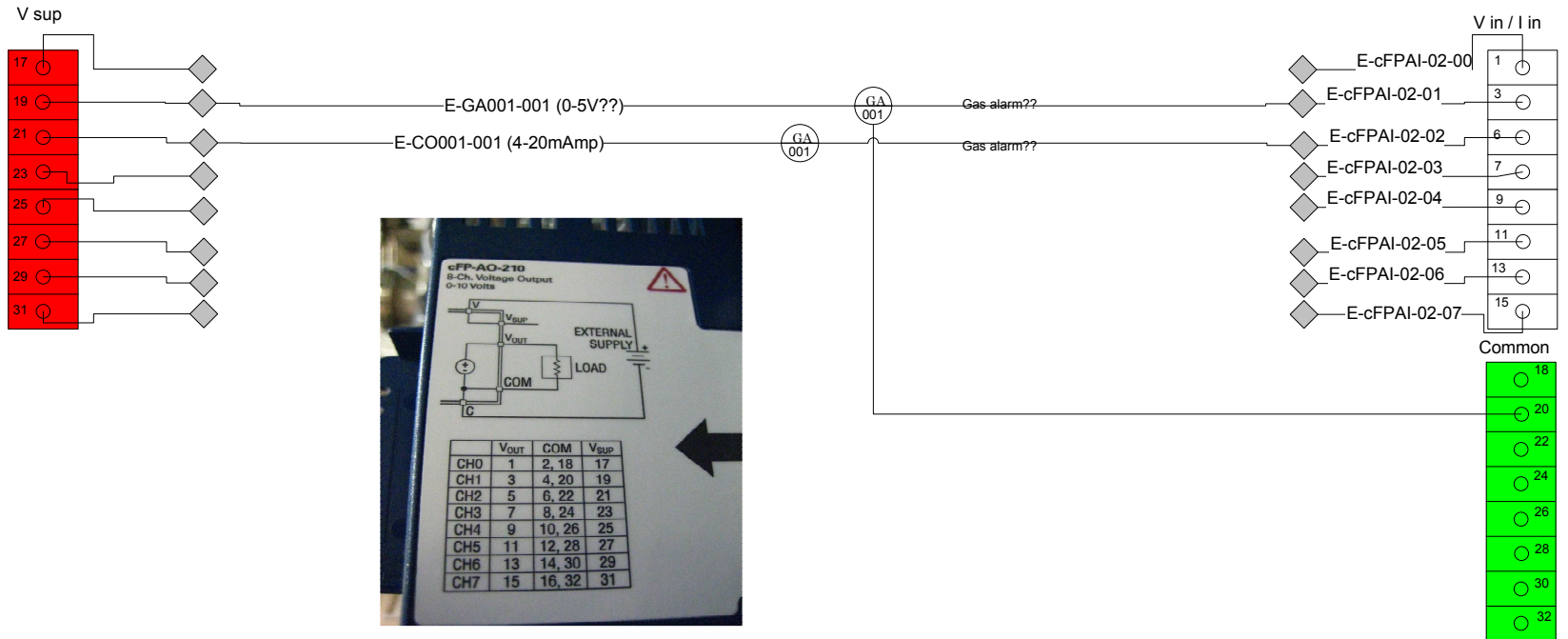
REV.	DESCRIPTION	DATE	BY	Alexandre Vigneault			
2.1	Fix PT 001- 031 positions	2009-05-12	AV	As Built			
				Electrical Connections Multi Channel Reactor: Analog I/O			
				SIZE	FSCM NO	DWG NO	REV
				SCALE	N/A	002	2.1
						SHEET	9 OF 16

CONFIDENTIAL

CFP-AO210-01 (Interface 2 Bank 3)



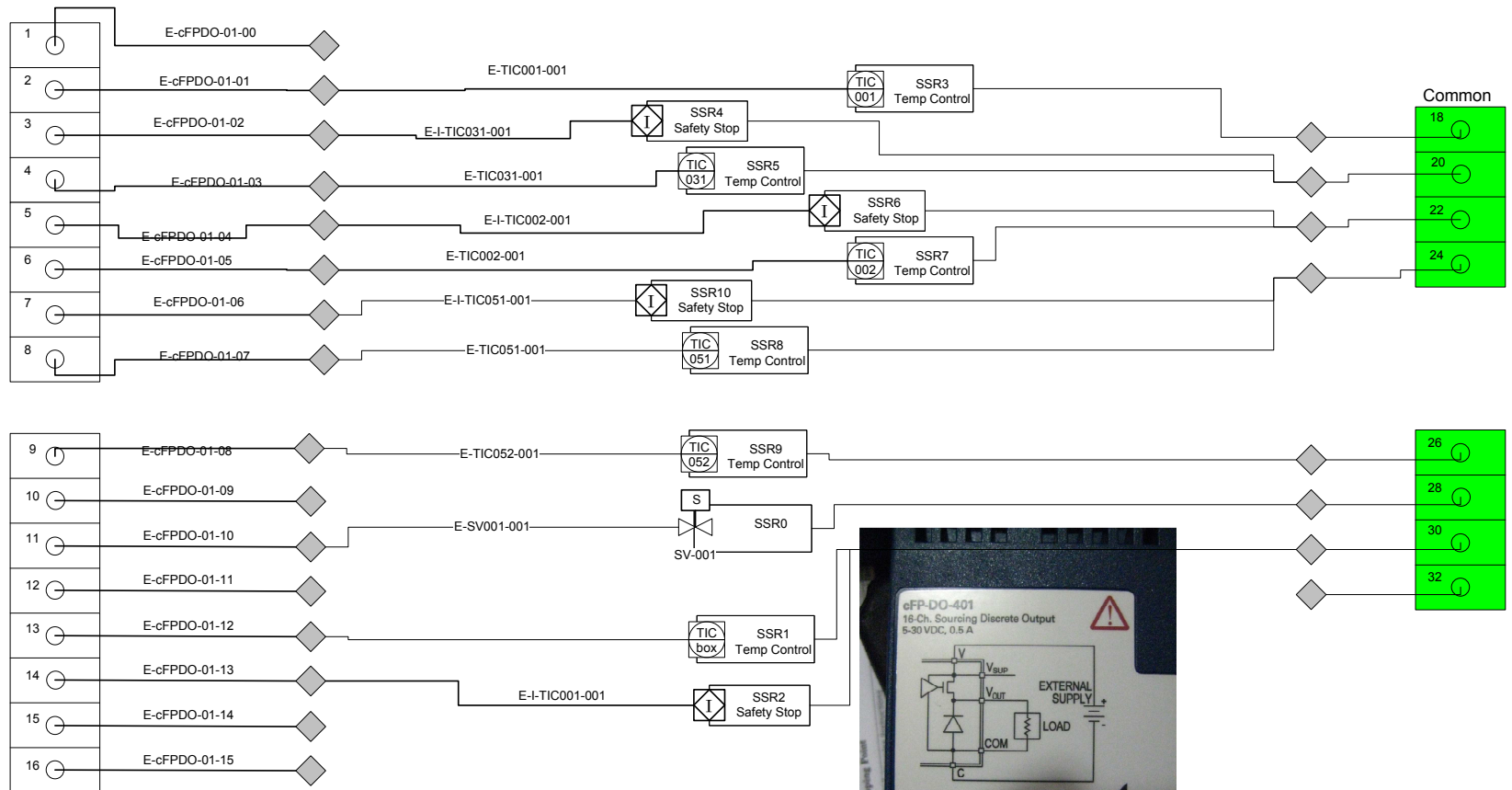
CFP-AI100-02 (Interface 1 Bank 7)



318

REV.	DESCRIPTION	DATE	BY	Alexandre Vigneault					
				Preliminary					
				Electrical Connections Multi Channel Reactor: Analog I/O					
				Last update: 2009-05-13		SIZE	FSCM NO	DWG NO	REV
				CONFIDENTIAL		SCALE	N/A	002	2.1
						SHEET		10 OF 16	

cFP-DO401-01 (Interface 2, Bank 2)



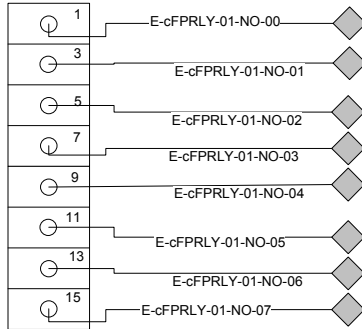
319

REV.	DESCRIPTION	DATE	BY
4.2	Rewiring COM side, name editing, adding one SSR TIC 052	20080604	AV
4.3	Switch SSR2 (ch no. 0 broken), rename SSR's	2009-05-12	AV

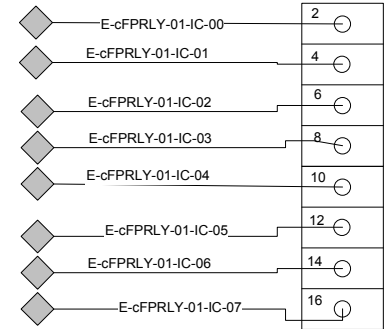
As Built	Alexandre Vigneault			
	Electrical Connections Multi Channel Reactor: Digital Output			
	SIZE	FSCM NO	DWG NO	REV
			002	4.3
CONFIDENTIAL	SCALE	N/A	SHEET	11 OF 16

cFP-RLY421-01

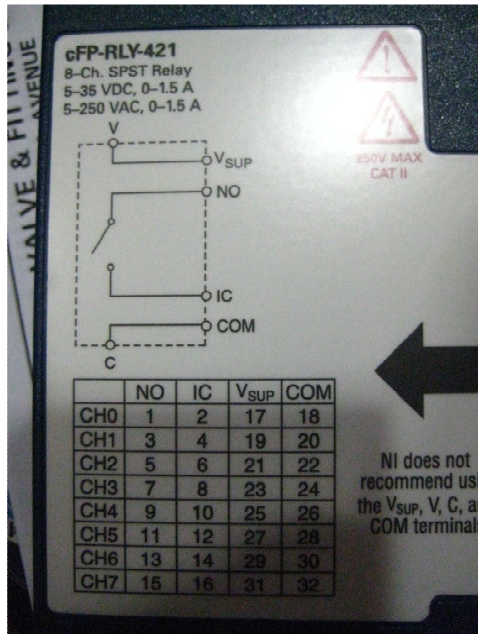
NO +



IC -

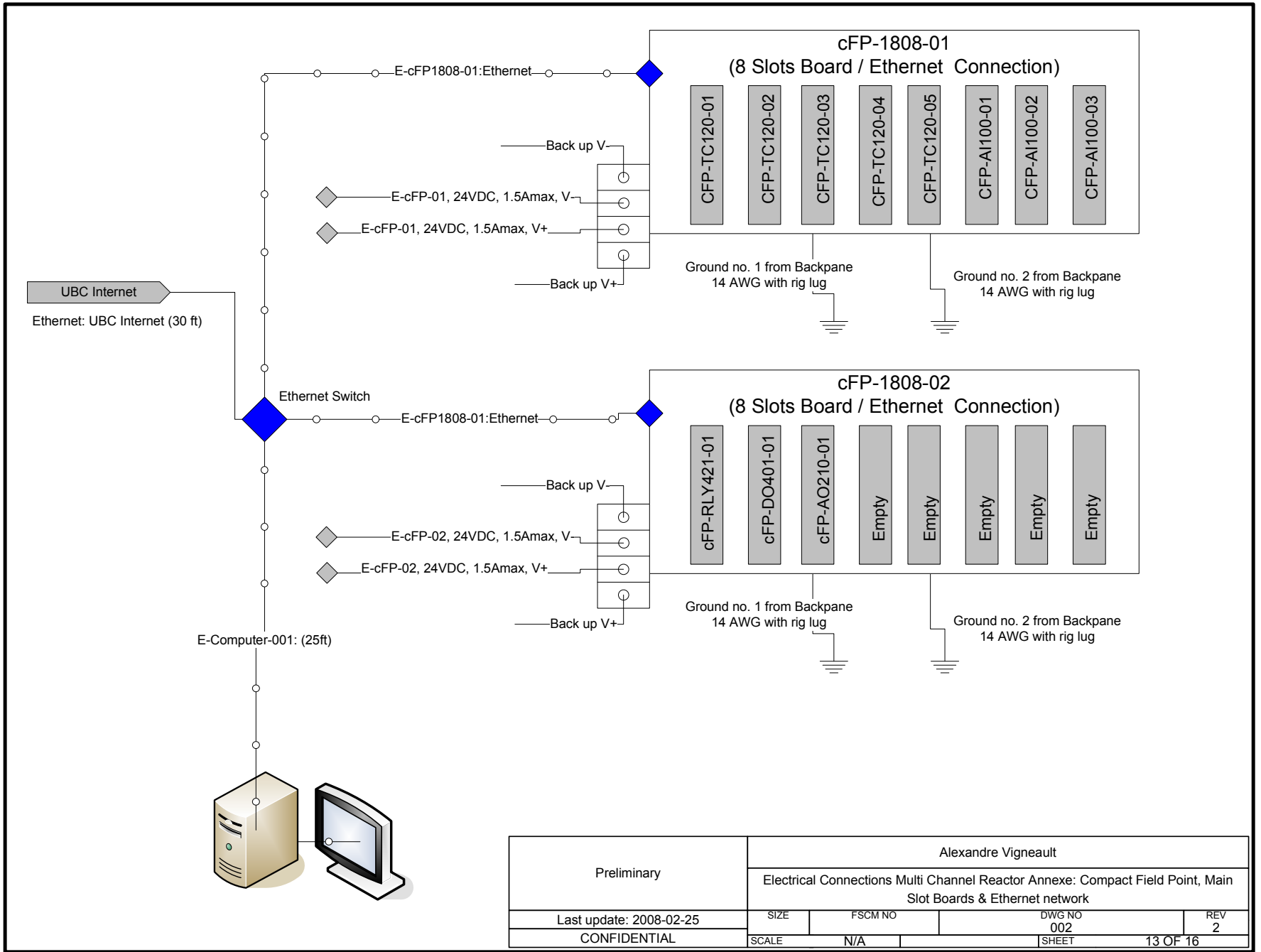


320

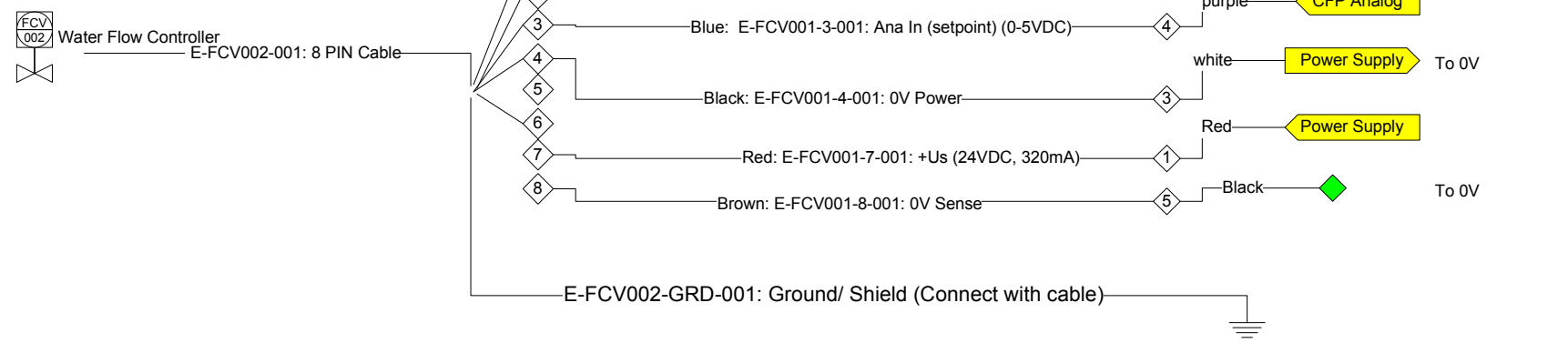
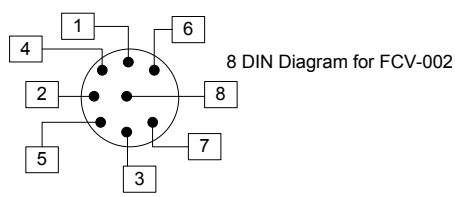
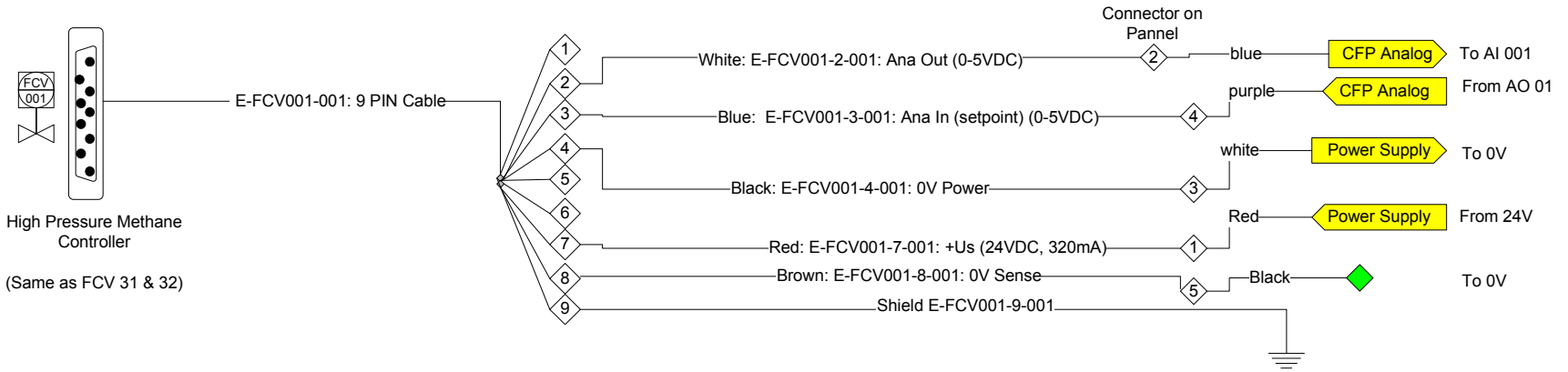


Preliminary	Alexandre Vigneault			
	Electrical Connections Multi Channel Reactor: Relays			
Last update: 2009-05-13	SIZE	FSCM NO	DWG NO 002	REV 3
CONFIDENTIAL	SCALE	N/A	SHEET	12 OF 16

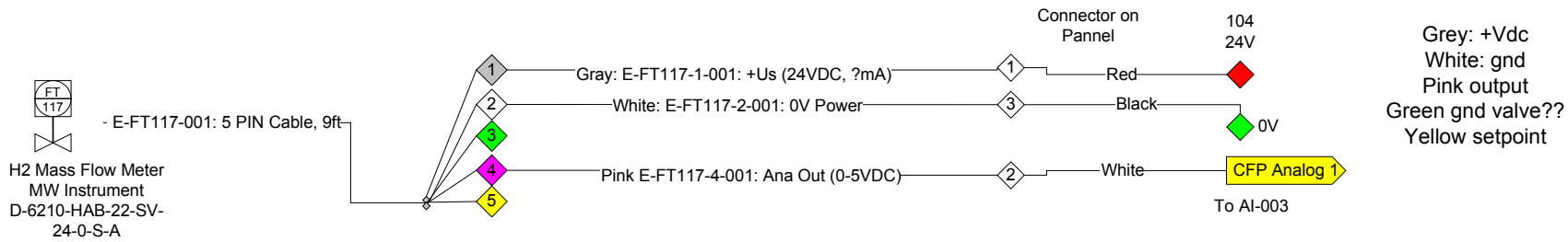
321



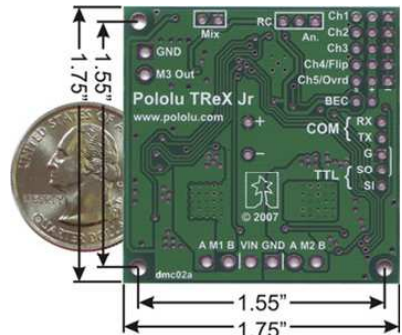
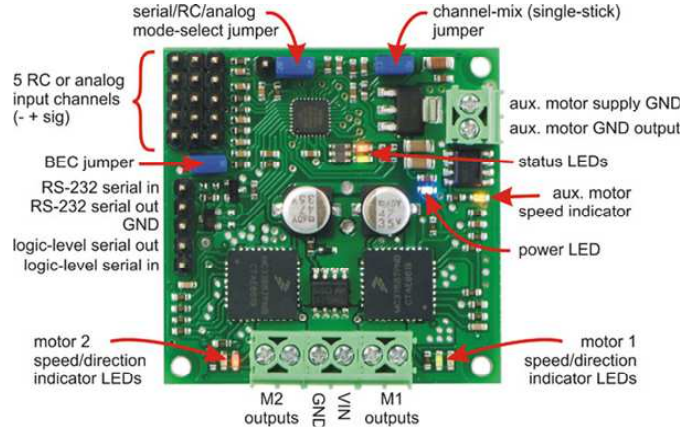
Preliminary	Alexandre Vigneault			
	Electrical Connections Multi Channel Reactor Annexe: Compact Field Point, Main Slot Boards & Ethernet network			
Last update: 2008-02-25	SIZE	FSCM NO	DWG NO 002	REV 2
CONFIDENTIAL	SCALE	N/A	SHEET	13 OF 16



As Built	Alexandre Vigneault			
	Electrical Connections Multi Channel Reactor Annexe: Mass Flow Controllers Wiring 1&2			
Last update: 2009-05-13	SIZE	FSCM NO	DWG NO 002	REV 1.1
CONFIDENTIAL	SCALE	N/A	SHEET	14 OF 16

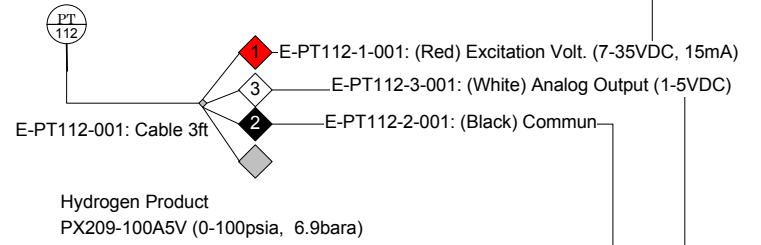
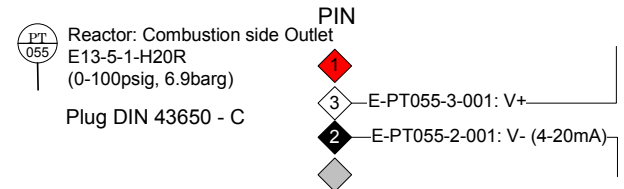
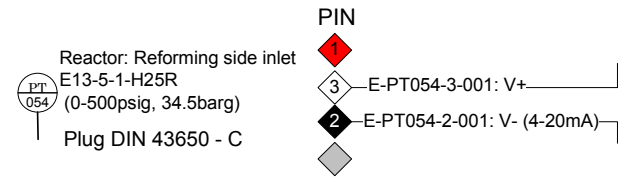
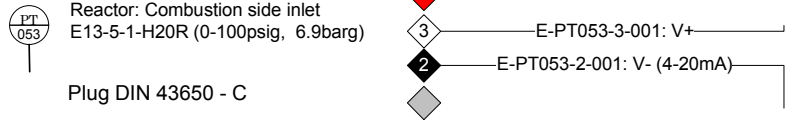
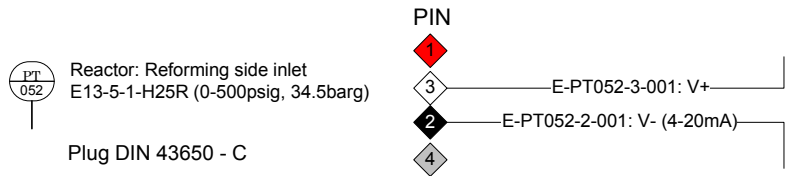
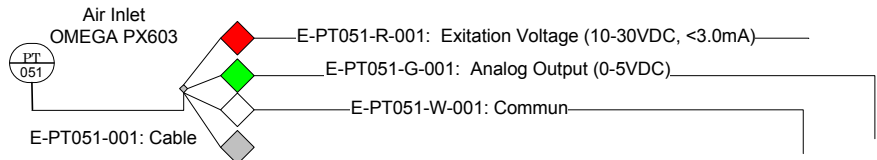
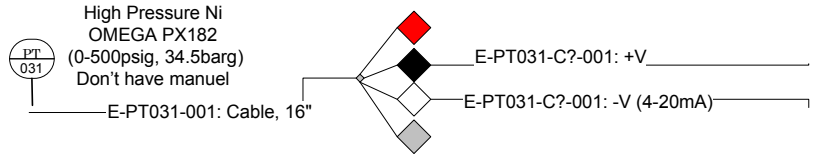
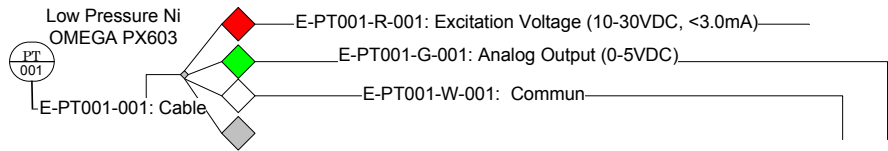


Control Motor for H2 pump



323

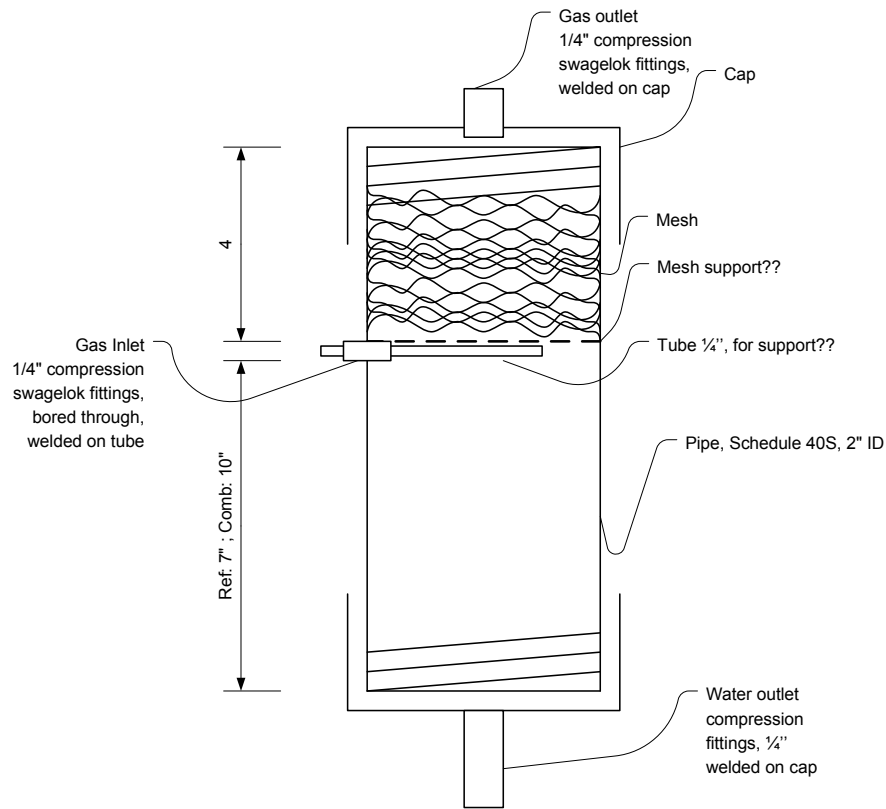
As Built	Alexandre Vigneault			
	Electrical Connections Multi Channel Reactor Annexe: H2 Flow Meter & H2 Pressure Controller			
Last update: 2009-05-13	SIZE	FSCM NO	DWG NO	REV
CONFIDENTIAL	SCALE	N/A	002	2.1
			SHEET	15 OF 16



As Built	Alexandre Vigneault			
	Electrical Connections Multi Channel Reactor Annexe: Pressure Transducers			
Last update: 2008-02-25	SIZE	FSCM NO	DWG NO	REV
CONFIDENTIAL	SCALE	N/A	002	2
			SHEET	16 OF 16

E.3 MCMR Process Part Mechanical Drawings

326

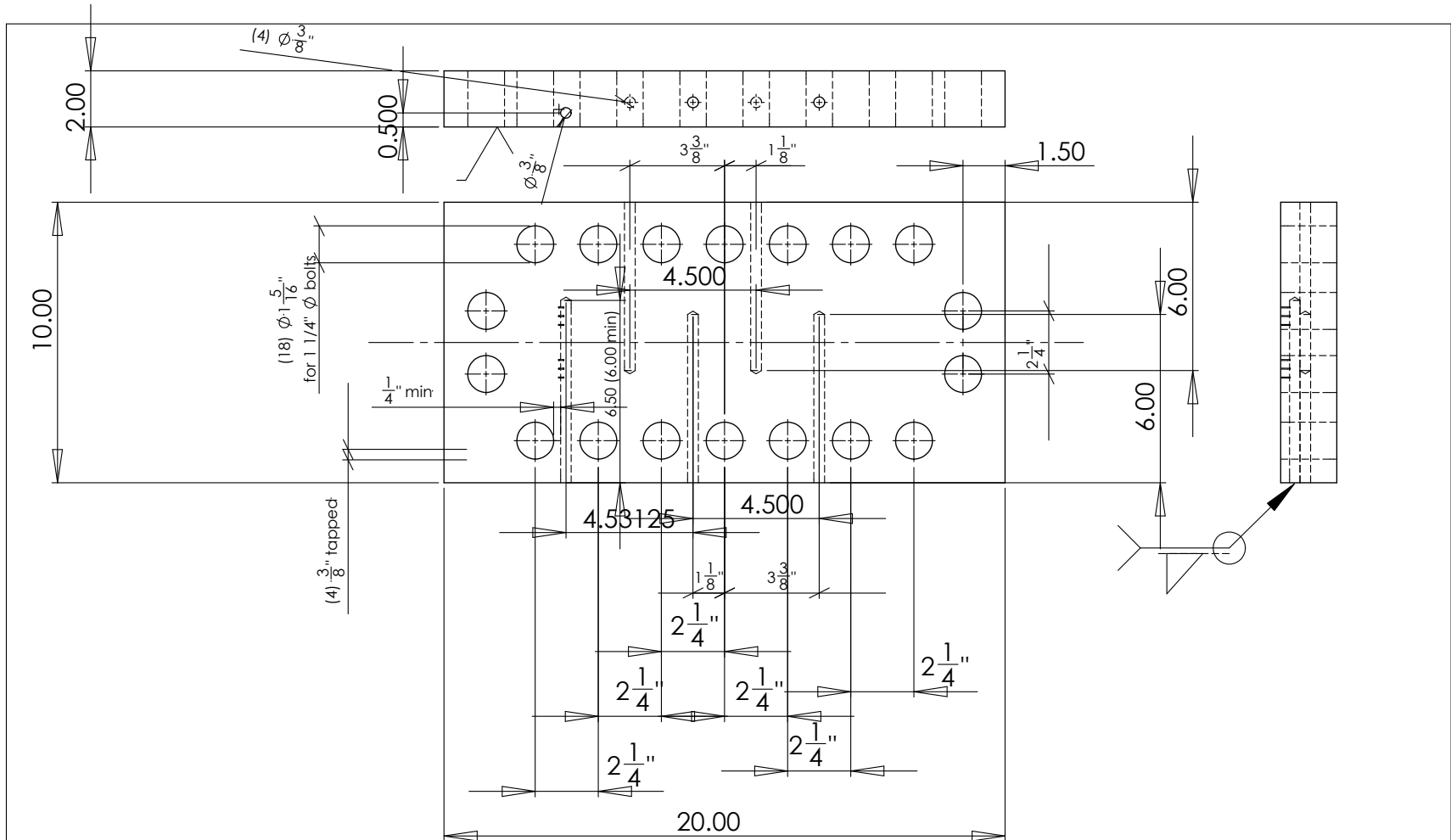


Pipe Material: Seamless SS
 Tolerance: xx"
 Dimensions in inches

Preliminary	Department of Chemical and Biological Engineering University of British Columbia			
	Gas water separator			
Alexandre Vigneault ing. Jr.	SIZE	FSCM NO	DWG NO GasWaterSeparator_20070801	REV 1
Confidential	SCALE	No scale	August 1st 2007	SHEET Pr1 OF 1

E.4 MCMR Mechanical Drawings

328



PROPRIETARY AND CONFIDENTIAL
 THE INFORMATION CONTAINED IN THIS DRAWING IS THE SOLE PROPERTY OF <INSERT COMPANY NAME HERE>. ANY REPRODUCTION IN PART OR AS A WHOLE WITHOUT THE WRITTEN PERMISSION OF <INSERT COMPANY NAME HERE> IS PROHIBITED.

		UNLESS OTHERWISE SPECIFIED:		NAME	DATE	July 18, 2007	
		DIMENSIONS ARE IN INCHES		DRAWN		TITLE:	
		TOLERANCES:		CHECKED			
		FRACTIONAL ±		ENG APPR.			
		ANGULAR: MACH ± BEND ±		MFG APPR.			
		TWO PLACE DECIMAL ±		Q.A.			
		THREE PLACE DECIMAL ±		COMMENTS:		SIZE DWG. NO. REV	
		INTERPRET GEOMETRIC TOLERANCING PER:				A top flange 03	
		MATERIAL				SHEET 1 OF 2	
		SS 304					
		FINISH					
NEXT ASSY	USED ON	APPLICATION		DO NOT SCALE DRAWING			

5

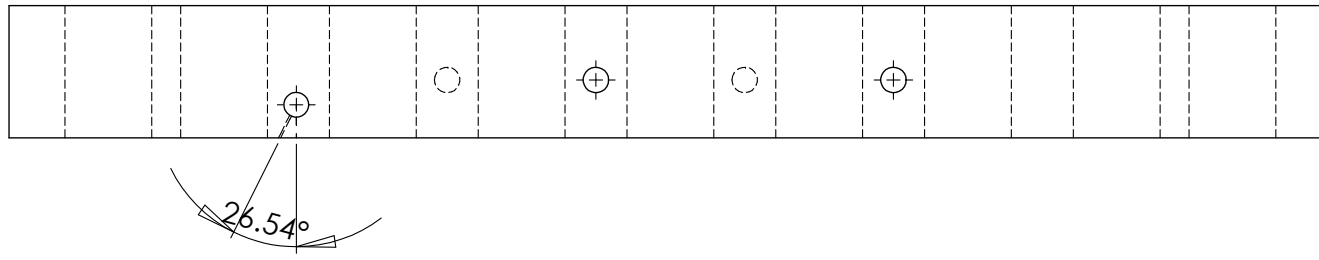
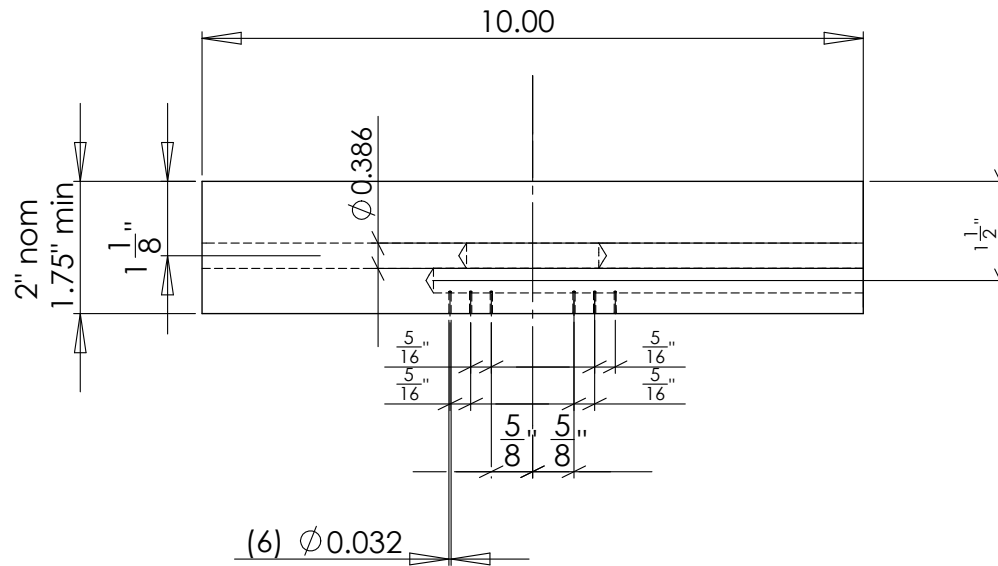
4

3

2

1

329



PROPRIETARY AND CONFIDENTIAL
 THE INFORMATION CONTAINED IN THIS DRAWING IS THE SOLE PROPERTY OF <INSERT COMPANY NAME HERE>. ANY REPRODUCTION IN PART OR AS A WHOLE WITHOUT THE WRITTEN PERMISSION OF <INSERT COMPANY NAME HERE> IS PROHIBITED.

		UNLESS OTHERWISE SPECIFIED:		NAME	DATE	July 18, 2007		
		DIMENSIONS ARE IN INCHES	DRAWN			TITLE:		
		TOLERANCES: 0.020	CHECKED					
		FRACTIONAL ±	ENG APPR.					
		ANGULAR: MACH ± BEND ±	MFG APPR.					
		TWO PLACE DECIMAL ±	Q.A.					
		THREE PLACE DECIMAL ±	COMMENTS:			SIZE	DWG. NO.	REV
		INTERPRET GEOMETRIC TOLERANCING PER:				A	top flange	03
		MATERIAL						
		SS 304						
NEXT ASSY	USED ON	FINISH						
APPLICATION		DO NOT SCALE DRAWING						SHEET 2 OF 2

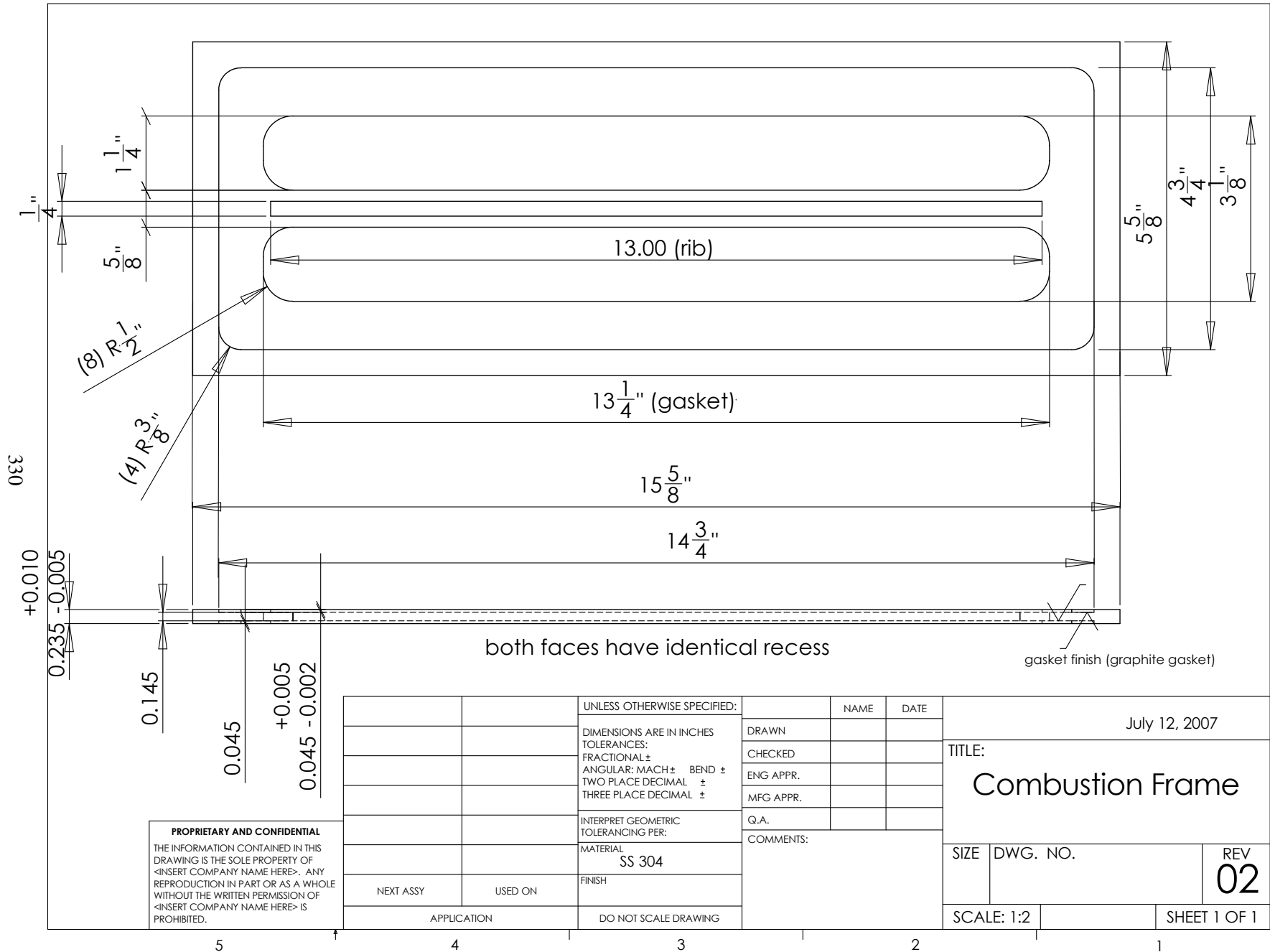
5

4

3

2

1



both faces have identical recess

gasket finish (graphite gasket)

PROPRIETARY AND CONFIDENTIAL
 THE INFORMATION CONTAINED IN THIS DRAWING IS THE SOLE PROPERTY OF <INSERT COMPANY NAME HERE>. ANY REPRODUCTION IN PART OR AS A WHOLE WITHOUT THE WRITTEN PERMISSION OF <INSERT COMPANY NAME HERE> IS PROHIBITED.

		UNLESS OTHERWISE SPECIFIED:	NAME	DATE
		DIMENSIONS ARE IN INCHES	DRAWN	
		TOLERANCES:	CHECKED	
		FRACTIONAL ±	ENG APPR.	
		ANGULAR: MACH ± BEND ±	MFG APPR.	
		TWO PLACE DECIMAL ±	Q.A.	
		THREE PLACE DECIMAL ±	COMMENTS:	
		INTERPRET GEOMETRIC TOLERANCING PER:		
		MATERIAL		
		SS 304		
NEXT ASSY	USED ON	FINISH		
APPLICATION		DO NOT SCALE DRAWING		

July 12, 2007

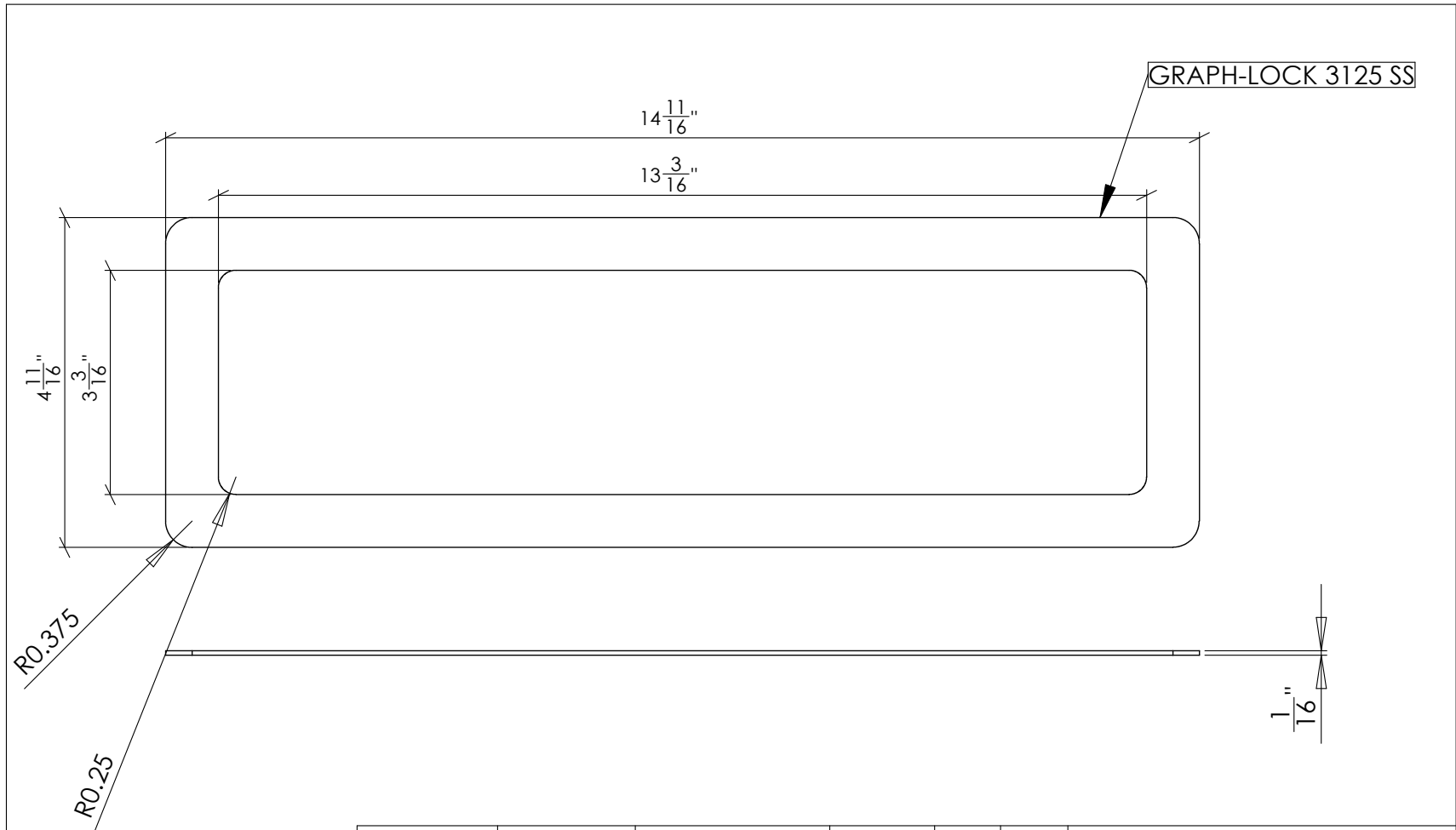
TITLE:
Combustion Frame

SIZE	DWG. NO.	REV 02
------	----------	------------------

SCALE: 1:2 SHEET 1 OF 1

5 4 3 2 1

331



PROPRIETARY AND CONFIDENTIAL
 THE INFORMATION CONTAINED IN THIS DRAWING IS THE SOLE PROPERTY OF <INSERT COMPANY NAME HERE>. ANY REPRODUCTION IN PART OR AS A WHOLE WITHOUT THE WRITTEN PERMISSION OF <INSERT COMPANY NAME HERE> IS PROHIBITED.

		UNLESS OTHERWISE SPECIFIED:		NAME	DATE	July 12, 2007		
		DIMENSIONS ARE IN INCHES				TITLE:		
		TOLERANCES:						
		FRACTIONAL: ± 0.005						
		ANGULAR: MACH \pm BEND \pm						
		TWO PLACE DECIMAL \pm				SIZE	DWG. NO.	REV
		THREE PLACE DECIMAL \pm				A	gasket	01
		INTERPRET GEOMETRIC TOLERANCING PER:				SCALE 1:2		
		MATERIAL				SHEET 1 OF 1		
		Graphoil						
		FINISH						
		DO NOT SCALE DRAWING						
		APPLICATION						
		NEXT ASSY	USED ON					

5

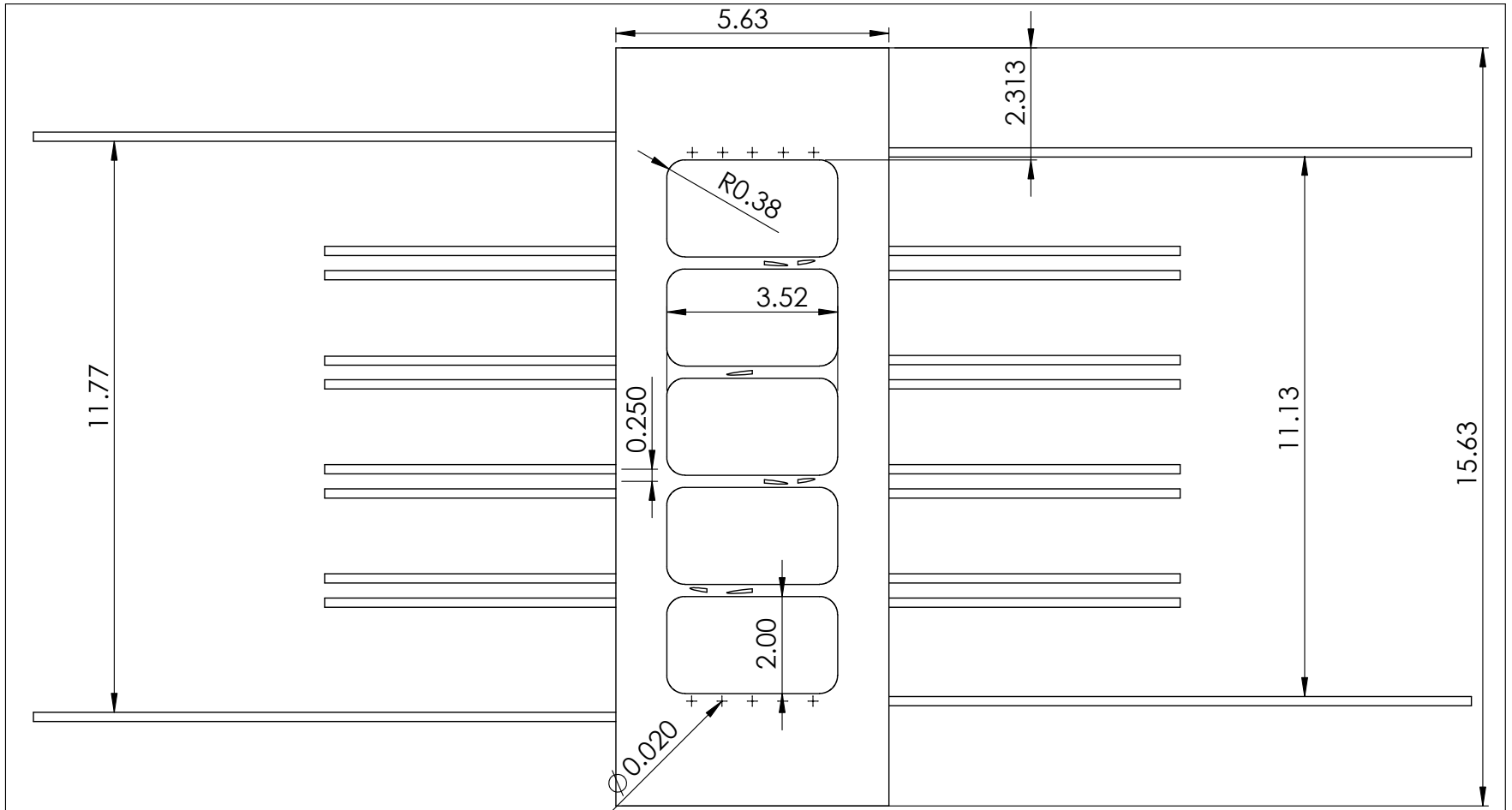
4

3

2

1

332

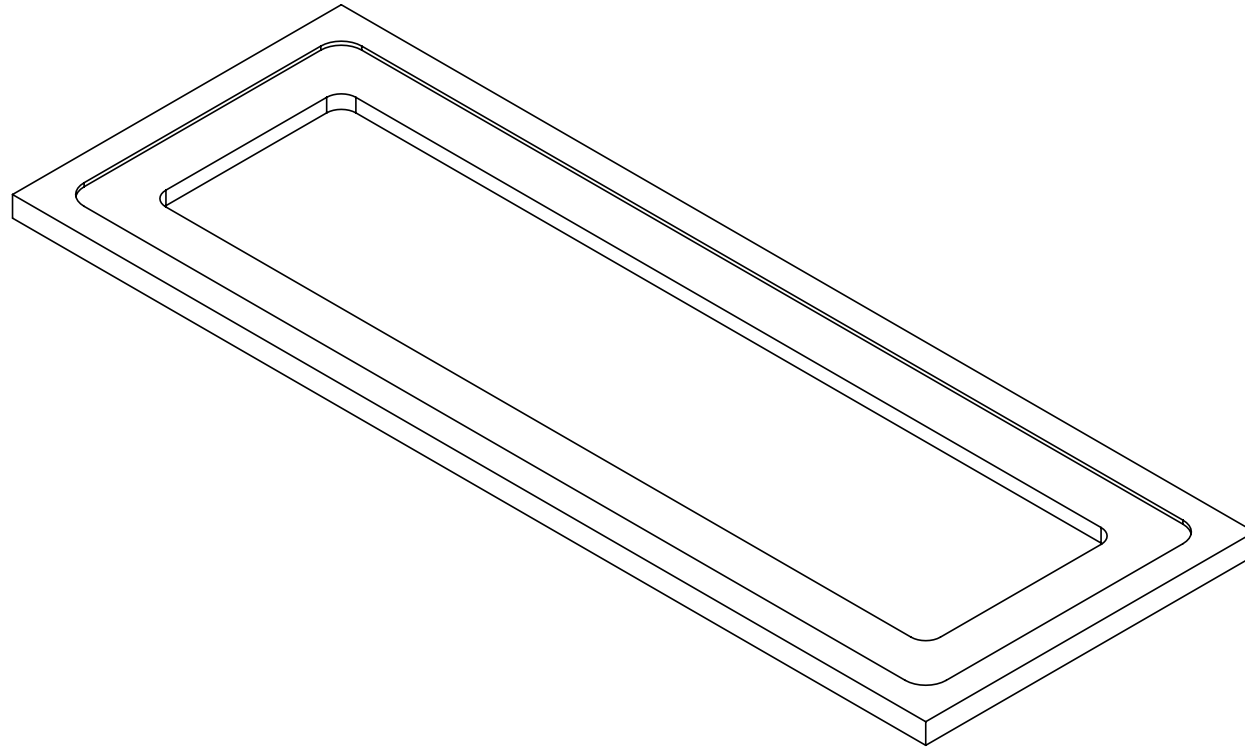


PROPRIETARY AND CONFIDENTIAL
 THE INFORMATION CONTAINED IN THIS DRAWING IS THE SOLE PROPERTY OF <INSERT COMPANY NAME HERE>. ANY REPRODUCTION IN PART OR AS A WHOLE WITHOUT THE WRITTEN PERMISSION OF <INSERT COMPANY NAME HERE> IS PROHIBITED.

		UNLESS OTHERWISE SPECIFIED:		NAME	DATE	July, 30, 2007	
		DIMENSIONS ARE IN INCHES		DRAWN		TITLE: Separator Preliminary	
		TOLERANCES:		CHECKED			
		FRACTIONAL ±		ENG APPR.			
		ANGULAR: MACH ± BEND ±		MFG APPR.			
		TWO PLACE DECIMAL ±		Q.A.		SIZE DWG. NO. REV	
		THREE PLACE DECIMAL ±		COMMENTS:		SCALE: 1:5 SHEET 1 OF 1	
		INTERPRET GEOMETRIC TOLERANCING PER:					
		MATERIAL					
		SS 304					
		FINISH					
NEXT ASSY		USED ON					
APPLICATION		DO NOT SCALE DRAWING					

5 4 3 2 1

334



PROPRIETARY AND CONFIDENTIAL
 THE INFORMATION CONTAINED IN THIS DRAWING IS THE SOLE PROPERTY OF <INSERT COMPANY NAME HERE>. ANY REPRODUCTION IN PART OR AS A WHOLE WITHOUT THE WRITTEN PERMISSION OF <INSERT COMPANY NAME HERE> IS PROHIBITED.

		UNLESS OTHERWISE SPECIFIED:		NAME	DATE	UBC: CHBE		
		DIMENSIONS ARE IN INCHES	DRAWN					TITLE:
		TOLERANCES:	CHECKED			Reforming Frame Iso view		
		FRACTIONAL <MOD-PM>	BEND <MOD-PM>					
		ANGULAR: MACH <MOD-PM>	BEND <MOD-PM>					
		TWO PLACE DECIMAL <MOD-PM>	MFG APPR.			SIZE	DWG. NO.	REV
		THREE PLACE DECIMAL <MOD-PM>				A		
		INTERPRET GEOMETRIC TOLERANCING PER:	Q.A.			SCALE: 1: 2		SHEET 2 OF 2
		MATERIAL	COMMENTS:					
		ERROR!:Material						
NEXT ASSY	USED ON	FINISH						
		ERROR!:Finish						
	APPLICATION	DO NOT SCALE DRAWING						

5

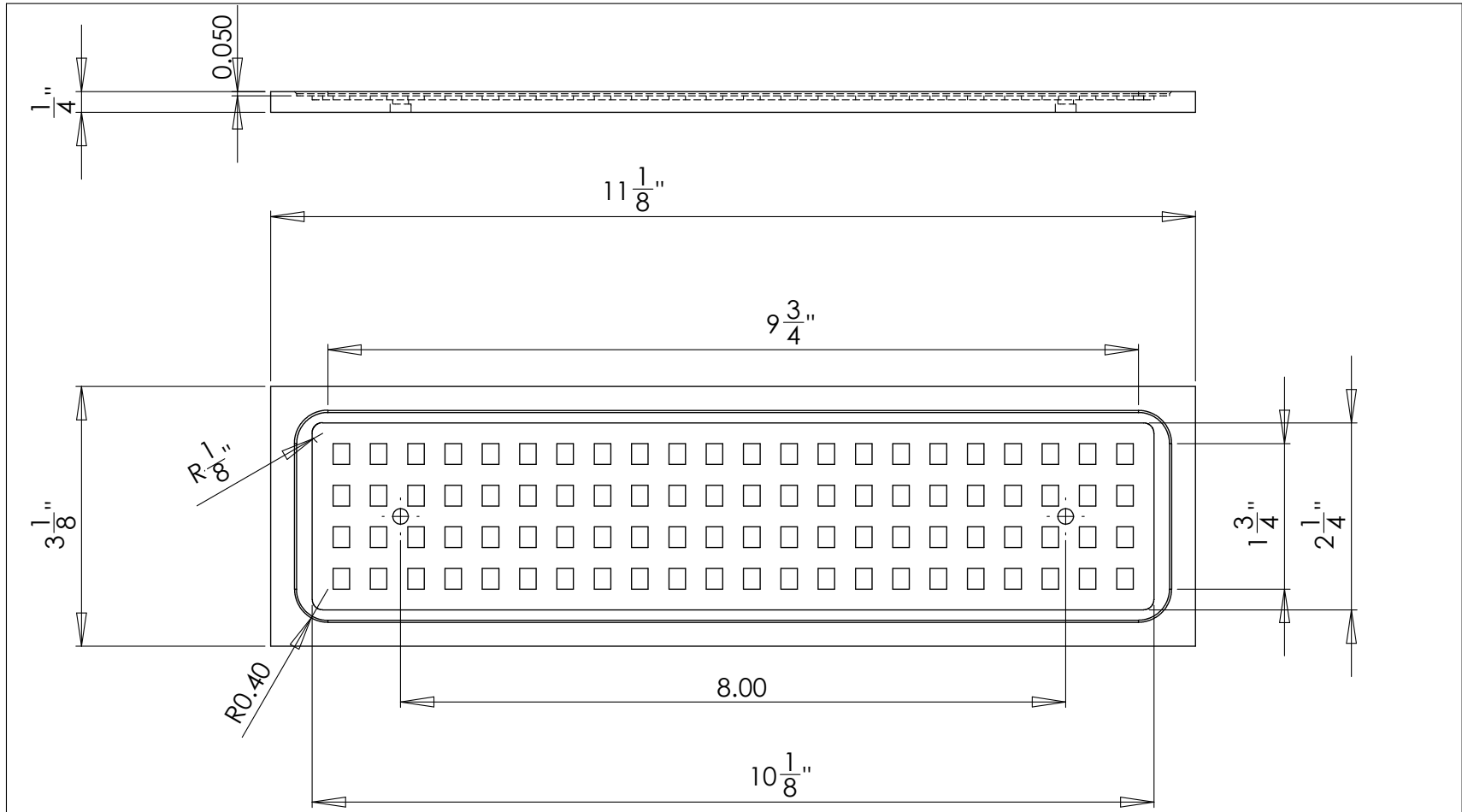
4

3

2

1

335



PROPRIETARY AND CONFIDENTIAL
 THE INFORMATION CONTAINED IN THIS DRAWING IS THE SOLE PROPERTY OF <INSERT COMPANY NAME HERE>. ANY REPRODUCTION IN PART OR AS A WHOLE WITHOUT THE WRITTEN PERMISSION OF <INSERT COMPANY NAME HERE> IS PROHIBITED.

		UNLESS OTHERWISE SPECIFIED:	NAME	DATE	July 12, 2007	
		DIMENSIONS ARE IN INCHES	DRAWN		TITLE:	
		TOLERANCES:	CHECKED			
		FRACTIONAL ±	ENG APPR.			
		ANGULAR: MACH ± BEND ±	MFG APPR.			
		TWO PLACE DECIMAL ±	Q.A.			
		THREE PLACE DECIMAL ±	COMMENTS:			
		INTERPRET GEOMETRIC TOLERANCING PER:			SIZE	DWG. NO.
		MATERIAL			A	membrane
NEXT ASSY	USED ON	FINISH			REV 01	
APPLICATION		DO NOT SCALE DRAWING			SHEET 1 OF 1	

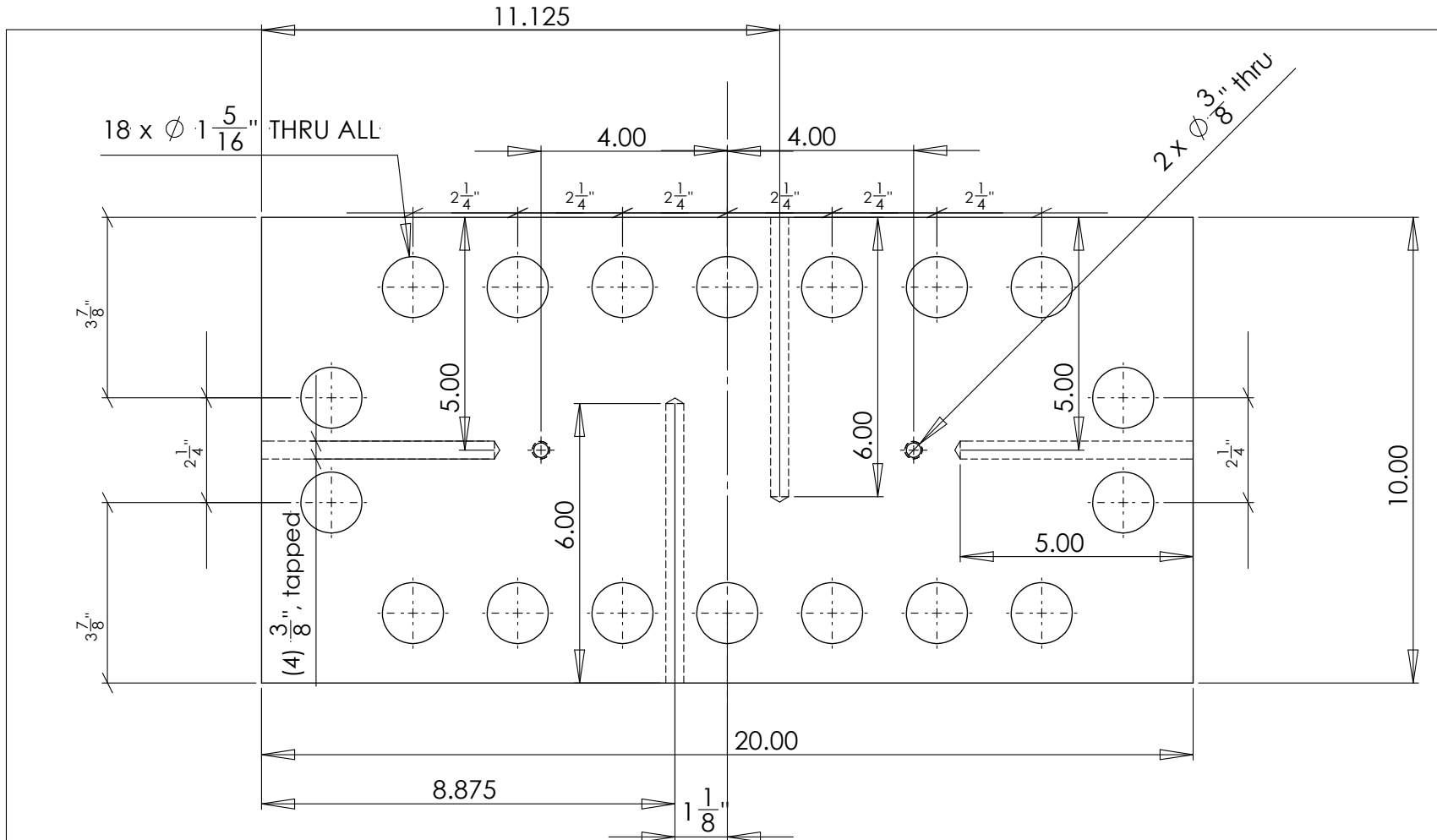
5

4

3

2

1



336

PROPRIETARY AND CONFIDENTIAL
 THE INFORMATION CONTAINED IN THIS DRAWING IS THE SOLE PROPERTY OF <INSERT COMPANY NAME HERE>. ANY REPRODUCTION IN PART OR AS A WHOLE WITHOUT THE WRITTEN PERMISSION OF <INSERT COMPANY NAME HERE> IS PROHIBITED.

		UNLESS OTHERWISE SPECIFIED:		NAME	DATE	July 18, 2007	
		DIMENSIONS ARE IN INCHES		DRAWN		TITLE: Preliminary	
		TOLERANCES:		CHECKED			
		FRACTIONAL ±		ENG APPR.			
		ANGULAR: MACH ± BEND ±		MFG APPR.			
		TWO PLACE DECIMAL ±		Q.A.			
		THREE PLACE DECIMAL ±		COMMENTS:		SIZE	DWG. NO.
		INTERPRET GEOMETRIC TOLERANCING PER:				A	bottom flange
		MATERIAL				REV	02
NEXT ASSY	USED ON	FINISH				SHEET 1 OF 2	
APPLICATION		DO NOT SCALE DRAWING					

5

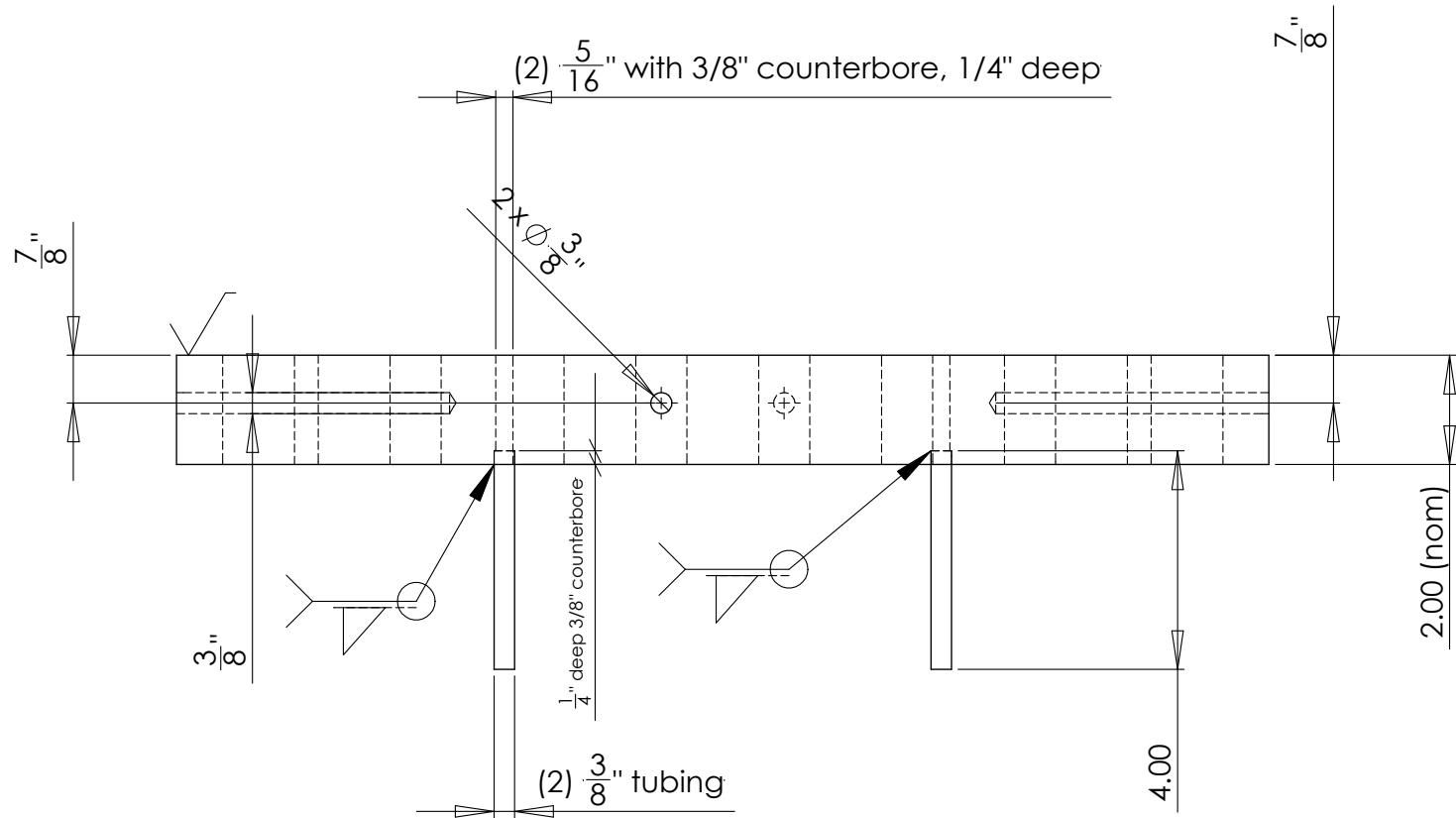
4

3

2

1

337



PROPRIETARY AND CONFIDENTIAL
 THE INFORMATION CONTAINED IN THIS DRAWING IS THE SOLE PROPERTY OF <INSERT COMPANY NAME HERE>. ANY REPRODUCTION IN PART OR AS A WHOLE WITHOUT THE WRITTEN PERMISSION OF <INSERT COMPANY NAME HERE> IS PROHIBITED.

		UNLESS OTHERWISE SPECIFIED:		NAME	DATE	July 18, 2007		
		DIMENSIONS ARE IN INCHES	DRAWN			TITLE: Preliminary		
		TOLERANCES:	CHECKED					
		FRACTIONAL \pm	ENG APPR.					
		ANGULAR: MACH \pm BEND \pm	MFG APPR.					
		TWO PLACE DECIMAL \pm	Q.A.					
		THREE PLACE DECIMAL \pm	COMMENTS:			SIZE	DWG. NO.	REV
		INTERPRET GEOMETRIC TOLERANCING PER:				A	bottom flange	02
		MATERIAL						
		SS 304						
		FINISH						
NEXT ASSY	USED ON							
APPLICATION		DO NOT SCALE DRAWING						SHEET 2 OF 2

5

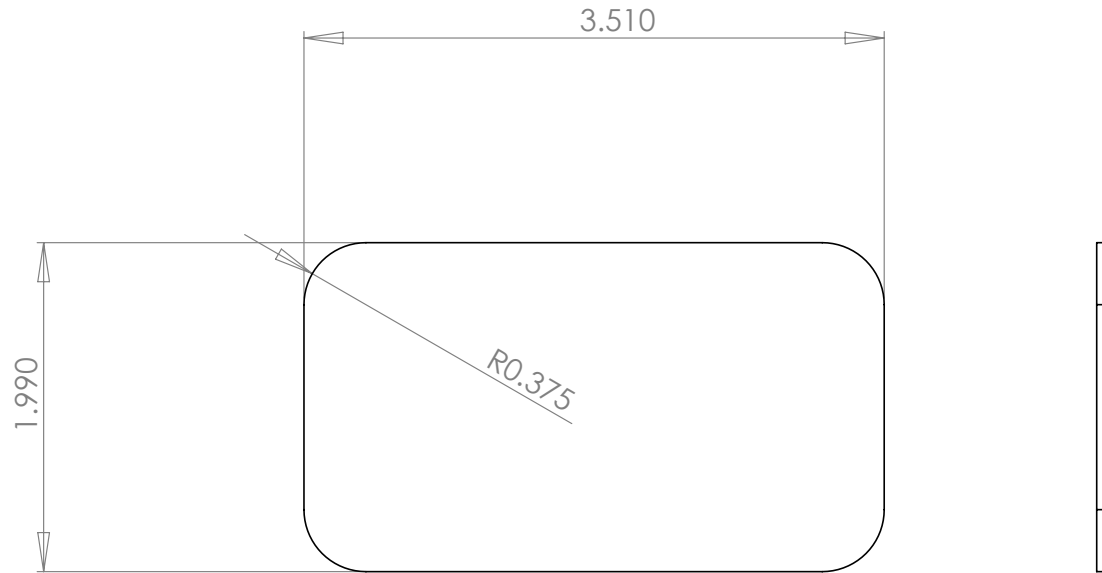
4

3

2

1

338



Note: Make as many coupons as you can from two sheets of metals (material provided):
 First one is 1ft x 3ft, material is SS 310, 24 gauge
 Second is 19.68 in x 7.87 in x (200mm x 500mm) Fecralloy (Fe-Cr-Al alloy), 0.5 mm thick
 Tolerance is - 0.010" (we can't go higher than specified dimensions)
 Please remove the tabs after the water jet cutting, plates need to stay flat. A bent corner will make the coupons useless.

PROPRIETARY AND CONFIDENTIAL
 THE INFORMATION CONTAINED IN THIS DRAWING IS THE SOLE PROPERTY OF <INSERT COMPANY NAME HERE>. ANY REPRODUCTION IN PART OR AS A WHOLE WITHOUT THE WRITTEN PERMISSION OF <INSERT COMPANY NAME HERE> IS PROHIBITED.

		UNLESS OTHERWISE SPECIFIED:		NAME	DATE	UBC- CHBE		
		DIMENSIONS ARE IN INCHES TOLERANCES: FRACTIONAL: -.010 ANGULAR: -.010	DRAWN					TITLE:
			CHECKED			Metal Coupons		
			ENG APPR.					
			MFG APPR.			SIZE	DWG. NO.	REV
		INTERPRET GEOMETRIC TOLERANCING PER: - 0.01	Q.A.			A		1.1
		MATERIAL stainless	COMMENTS:			SCALE: 1:1		
	NEXT ASSY	USED ON	FINISH no finish					
	APPLICATION		DO NOT SCALE DRAWING					

5

4

3

2

1

Appendix F

MATLAB Program

The MATLAB program can be downloaded here: <https://www.dropbox.com/s/zhjxfr9o45zwqcf/VigneaultSimulationFiles.zip>